

# Dynamic stability of thin-walled structures : a semi-analytical and experimental approach

**Citation for published version (APA):**

Mallon, N. J. (2008). *Dynamic stability of thin-walled structures : a semi-analytical and experimental approach*. [Phd Thesis 1 (Research TU/e / Graduation TU/e), Mechanical Engineering]. Technische Universiteit Eindhoven. <https://doi.org/10.6100/IR637287>

**DOI:**

[10.6100/IR637287](https://doi.org/10.6100/IR637287)

**Document status and date:**

Published: 01/01/2008

**Document Version:**

Publisher's PDF, also known as Version of Record (includes final page, issue and volume numbers)

**Please check the document version of this publication:**

- A submitted manuscript is the version of the article upon submission and before peer-review. There can be important differences between the submitted version and the official published version of record. People interested in the research are advised to contact the author for the final version of the publication, or visit the DOI to the publisher's website.
- The final author version and the galley proof are versions of the publication after peer review.
- The final published version features the final layout of the paper including the volume, issue and page numbers.

[Link to publication](#)

**General rights**

Copyright and moral rights for the publications made accessible in the public portal are retained by the authors and/or other copyright owners and it is a condition of accessing publications that users recognise and abide by the legal requirements associated with these rights.

- Users may download and print one copy of any publication from the public portal for the purpose of private study or research.
- You may not further distribute the material or use it for any profit-making activity or commercial gain
- You may freely distribute the URL identifying the publication in the public portal.

If the publication is distributed under the terms of Article 25fa of the Dutch Copyright Act, indicated by the "Taverne" license above, please follow below link for the End User Agreement:

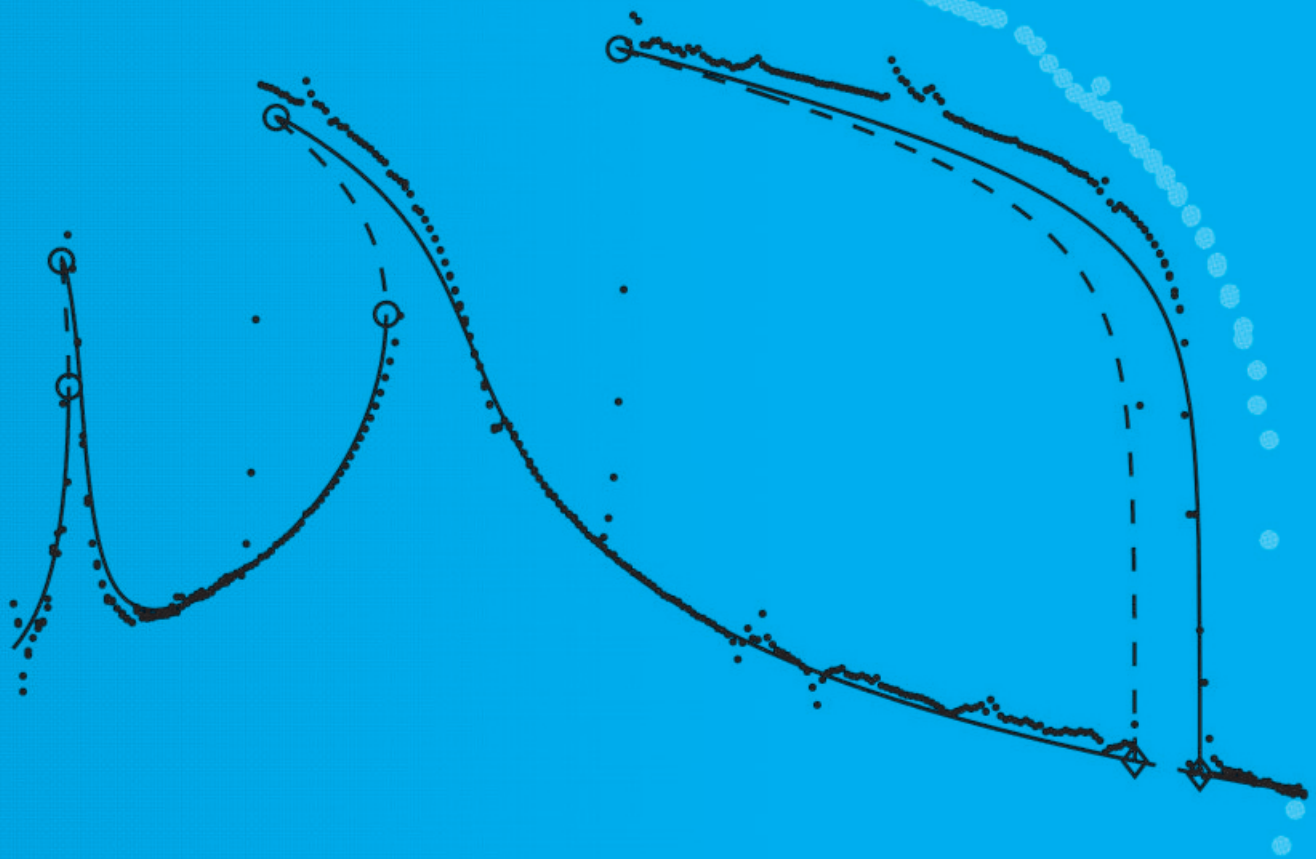
[www.tue.nl/taverne](http://www.tue.nl/taverne)

**Take down policy**

If you believe that this document breaches copyright please contact us at:

[openaccess@tue.nl](mailto:openaccess@tue.nl)

providing details and we will investigate your claim.



# Dynamic stability of thin-walled structures

A semi-analytical and experimental approach

Niels Mallon



*Dynamic stability of thin-walled  
structures: a semi-analytical and  
experimental approach*

Niels Mallon



This research was financially supported by the Dutch Technology Foundation STW (EWO.5792).

A catalogue record is available from the Eindhoven University of Technology Library.

ISBN 978-90-386-1374-1

Typeset by the author with the L<sup>A</sup>T<sub>E</sub>X 2<sub>ε</sub> documentation system.

Cover design by Sikko Hoogstra.

Printed by PrintPartners Ipskamp BV, Enschede, The Netherlands.

*Dynamic stability of thin-walled  
structures: a semi-analytical and  
experimental approach*

PROEFSCHRIFT

ter verkrijging van de graad van doctor aan de  
Technische Universiteit Eindhoven,  
op gezag van de Rector Magnificus, prof.dr.ir. C.J. van Duijn,  
voor een commissie aangewezen door het College voor  
Promoties in het openbaar te verdedigen op  
donderdag 2 oktober 2008 om 16.00 uur

door

Niels Johannes Mallon

geboren te Boxmeer

Dit proefschrift is goedgekeurd door de promotor:

prof.dr. H. Nijmeijer

Copromotor:

dr.ir. R.H.B. Fey

# Contents

<b>Notations</b>	<b>5</b>
<b>1 Introduction</b>	<b>7</b>
1.1 Objectives . . . . .	11
1.2 Outline of the thesis . . . . .	11
<b>2 Preliminaries</b>	<b>13</b>
2.1 Semi-analytical approach . . . . .	13
2.1.1 Modelling steps . . . . .	14
2.2 Stability of structures . . . . .	19
2.2.1 Static buckling . . . . .	19
2.2.2 Dynamic buckling . . . . .	26
2.3 Computational tools . . . . .	34
<b>3 Dynamic buckling of a shallow arch under shock loading</b>	<b>37</b>
3.1 Modelling of the arch . . . . .	38
3.1.1 Initial shape . . . . .	40
3.1.2 Discretization and equations of motion . . . . .	41
3.2 Static Buckling . . . . .	43
3.3 Dynamic Pulse Buckling . . . . .	47
3.3.1 Approach . . . . .	47
3.3.2 Perfect arch ( $e = 0$ ) . . . . .	49
3.3.3 Imperfect arch ( $e \neq 0$ ) . . . . .	54
3.3.4 Other arches . . . . .	56
3.4 Conclusions . . . . .	59
<b>4 Periodic Excitation of a Buckled Beam</b>	<b>61</b>
4.1 Modelling of the beam structure . . . . .	62
4.1.1 Three discretization cases . . . . .	64
4.1.2 Finite element model . . . . .	66
4.2 Static and modal analysis . . . . .	66
4.2.1 Static Equilibrium . . . . .	67
4.2.2 Modal Analysis . . . . .	68
4.3 Nonlinear Dynamic Analysis . . . . .	69
4.3.1 Steady-State Behaviour . . . . .	70
4.3.2 Influence of Parameters . . . . .	76
4.4 Comparison with Transient FEA . . . . .	78
4.5 Conclusions . . . . .	82

<b>5</b>	<b>Dynamic stability of a base-excited thin beam with top mass</b>	<b>85</b>
5.1	Equation(s) of motion . . . . .	87
5.2	Static and modal analysis . . . . .	90
5.3	Steady-state analysis . . . . .	93
5.4	Convergence of steady-state results . . . . .	104
5.5	Conclusions . . . . .	107
<b>6</b>	<b>Experiments with a base-excited thin beam with top mass</b>	<b>109</b>
6.1	Experimental setup . . . . .	111
6.2	Semi-analytical model . . . . .	112
6.3	Results . . . . .	113
6.4	Conclusions . . . . .	127
<b>7</b>	<b>Dynamic stability of a base-excited thin cylindrical shell with top mass</b>	<b>129</b>
7.1	Modelling approach . . . . .	132
7.1.1	Equations of motion . . . . .	136
7.2	Static and modal analysis . . . . .	138
7.2.1	FE model . . . . .	139
7.2.2	Static analysis . . . . .	140
7.2.3	Modal Analysis . . . . .	143
7.3	Dynamic analysis . . . . .	146
7.3.1	Model without companion modes and without axially asymmetrical modes (16-DOF) . . . . .	147
7.3.2	Model with companion modes but without axially asymmetrical modes (26-DOF) . . . . .	156
7.3.3	Model with axially asymmetrical modes but without companion modes (31-DOF) . . . . .	156
7.3.4	Influence circumferential wave number $n$ . . . . .	157
7.4	Conclusions . . . . .	163
<b>8</b>	<b>Experiments with a base-excited thin cylindrical shell with top mass</b>	<b>165</b>
8.1	Experimental setup . . . . .	167
8.2	Semi-analytical model . . . . .	171
8.3	Modal and buckling analysis . . . . .	172
8.4	Numerical steady-state analysis . . . . .	174
8.5	Experimental steady-state analysis . . . . .	185
8.6	Conclusions . . . . .	193
<b>9</b>	<b>Conclusions/Recommendations</b>	<b>195</b>
9.1	Conclusions . . . . .	195
9.2	Recommendations . . . . .	199



---

<b>A Modelling of the electrodynamic shaker</b>	<b>201</b>
A.1 The coupled shaker-structure model . . . . .	210
<b>B Stepped sine procedure</b>	<b>213</b>
<b>C In-plane fields cylindrical shell model</b>	<b>215</b>
C.1 Solving the in-plane fields . . . . .	215
C.2 Expressions in-plane fields for $N = M = 1$ . . . . .	219
<b>Summary</b>	<b>233</b>
<b>Samenvatting</b>	<b>235</b>
<b>Acknowledgments</b>	<b>237</b>
<b>Curriculum vitae</b>	<b>239</b>



## *Notations*

$f_{,x}$	First partial derivative of $f$ with respect to $x$
$f_{,xx}$	Second partial derivative of $f$ with respect to $x$
$\dot{x}$	First time derivative of $x$
$\ddot{x}$	Second time derivative of $x$
$t$	Time

### Abbreviations

<i>CF</i>	cyclic fold bifurcation
DOF	degree of freedom
ELV	expendable launch vehicle
FE	finite element
FEA	finite element analysis
FEM	finite element method
FRF	frequency response function
<i>NS</i>	Neimark-Sacker bifurcation
<i>PD</i>	period doubling bifurcation
PDE	partial differential equation
PSD	power spectral density
MEMS	micro electro mechanical system
ODE	ordinary differential equation
SUT	structure under test



## Introduction

A structure can be classified as "thin-walled" if its thickness is much smaller than its other dimensions. In general, thin-walled structures possess a very high in-plane stiffness while their out-of-plane stiffness is very low. This property makes thin-walled structures very suitable for two purposes. Firstly, if the structure is designed such that the loading assesses mainly the in-plane stiffness, load-carrying constructions with very high stiffness-to-mass ratios can be achieved. Due to this property, thin-walled structures are used extensively in building and civil engineering constructions, aircraft, aerospace, shipbuilding and other industries. Secondly, the out-of-plane flexibility property of thin-walled structures allows to make mechanisms with relative large displacements while staying in the elastic domain. Applications can, for example, be encountered in suspension systems [138], deployable structures [125] and in Micro-Electro-Mechanical-Systems [114; 115].

The design of thin-walled structures encompasses a number of challenges. Firstly, thin-walled structures under compressive loading may become unstable, that is they buckle. Buckling often occurs at stresses much lower than the yield stress making the buckling strength one of the key design criteria. Secondly, thin-walled structures may be sensitive to geometrical imperfections (small deviations from the nominal shape) and loading imperfections. This can result in significant reductions of the maximum load carrying capacity of the imperfect structure with respect to the perfect one. Finally, out-of-plane displacements can rapidly become very large (in comparison with the thickness of the structure) resulting in the fact that geometrical nonlinearities can no longer be neglected during the analysis.

Although there are still some open issues, the analysis of the (nonlinear) response and buckling of thin-walled structured subjected to static loading (i.e. the situation in which transient inertia and damping forces may be neglected) is well established in engineering science [66]. However, in practise thin-walled structures are often subjected not only to a static load but also to a dynamic load. The resistance of structures liable to buckling, to withstand time-dependent loading is addressed as the *dynamic stability* of these structures. The term dynamic stability will be further elucidated in Section 2.2. Now, two examples of dynamically loaded thin-walled structures will be discussed.

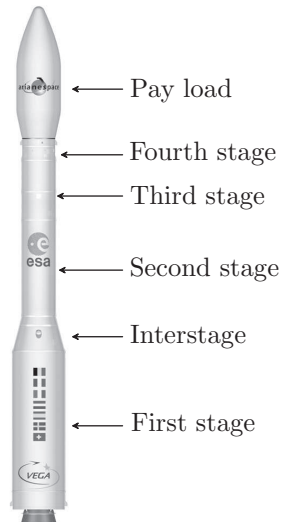


Figure 1.1: Vega launcher (courtesy ESA).

The first example comes from aerospace engineering and considers the case where a thin-walled structure acts as a (light-weight) load-carrying construction. The Vega is an expendable launch vehicle (ELV), used to place satellites into an orbit around the Earth, see Fig. 1.1. The satellite (the pay load) is placed in the top of the ELV and in four steps the vehicle is brought into the atmosphere. During each step, one stage of the ELV is ignited and after its fuel is burned it is separated from the rest of the vehicle using pyrotechnic charges. The first and second stage of the Vega are interconnected using a conical thin-walled interstage, see Fig. 1.2. The interstage has a maximum diameter of approximately 3 [m] and is constructed from curved aluminium panels with a thickness of approximately 6 [mm] in combination with ring stiffeners for extra stability [134]. A simplification of the mechanical loading of the interstage during the launch is shown in Fig. 1.3, i.e. the structure carries a rigid top mass (resembling the mass of the upper part of the launch vehicle) while being subjected to a base acceleration (resembling the longitudinal acceleration of the launch vehicle). During a typical launch, the longitudinal acceleration shows various static levels (with peak values up to  $5.5 \cdot g$ , where  $g = 9.81 \text{ [m/s}^2\text{]}$  denotes the gravitation constant) with on top significant dynamic fluctuations (order  $1 \cdot g$ ) and shocks [9; 137]. The combination of the base acceleration and the top mass results in a (time-varying) compressive loading of the thin-walled interstage. Consequently, dynamic buckling of the interstage, but obviously

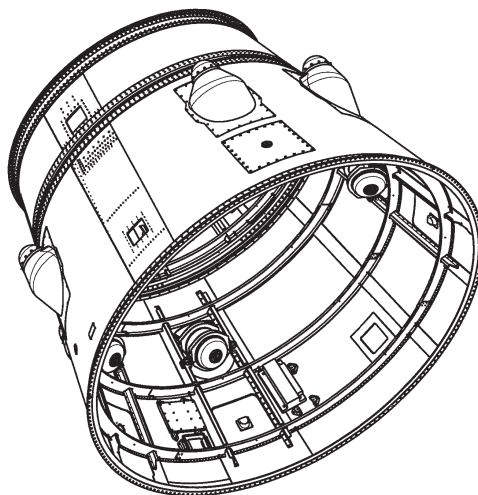


Figure 1.2: Vega interstage (courtesy Dutch Space BV).

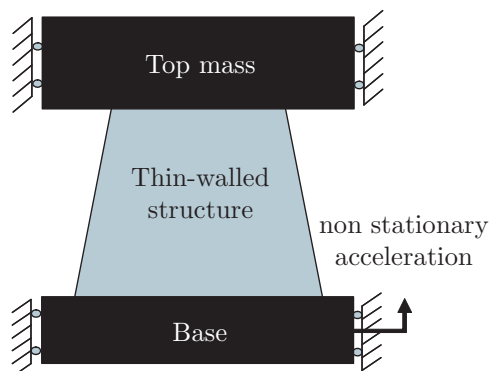


Figure 1.3: Simplification of the mechanical loading of the interstage during the launch.

also of other parts, is one of main issues during the design of such a launcher.

The next example illustrates how the (out-of-plane) flexibility property of thin-walled structures can be exploited to realize a flexible mechanism for adaptive optics on micro scale. In Fig. 1.4, a 3D self assembled microplate suspended in two buckled beams is depicted [115]. The microplate has size  $380 \times 250$  [ $\mu\text{m}$ ]

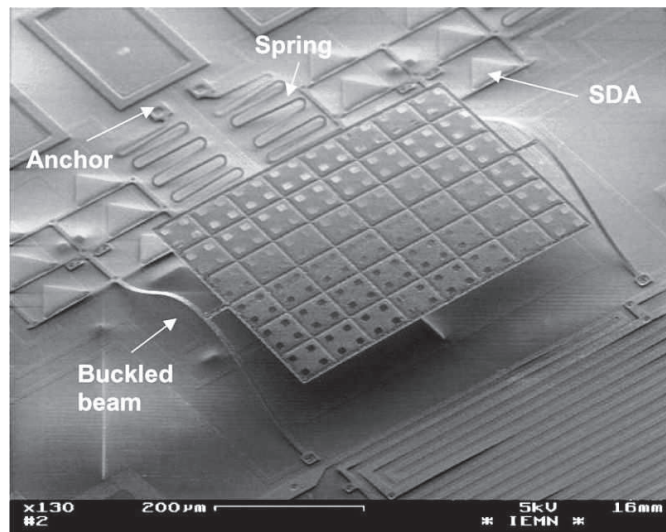


Figure 1.4: 3D self assembled microplate suspended in two buckled beams (reproduced from [115] with permission).

and can be electrostatically actuated using electrodes buried underneath the microplate. Before assembly, the structure is planar. Then, by using scratch drive actuators (SDA), the beams are forced to buckle and locked using a self locking mechanism to make the buckled state permanent. This forces the microplate to lift out of the substrate plane, creating enough space for large rotations of the microplate. The buckled beams do not only lift the microplate but also act as elastic torsional hinges. In this manner, actuation of the microplate can be achieved with rotations up to  $\pm 15$  degrees, while remaining in the elastic domain of the used material. During operation, the microplate is controlled to follow high speed prescribed motions, resulting in both torsional and transversal dynamic loading of thin buckled beams.

To obtain competitive designs for dynamically loaded thin-walled structures such as discussed above, it is vital to be able to understand, predict, and eventually optimize the dynamic stability behaviour of the structure. However, design strategies and fast (pre-)design tools for thin-walled structures under dynamic loading are still lacking. This can be partially explained by the involved computational complexity of the dynamic stability analysis, especially since in such analyses geometrical nonlinearities should be taken into account. Furthermore, in general time-dependent loads are described by multiple parameters (i.e. multi-parameter studies must be performed) and a wide



variety in possible time-dependent loading types can be considered, like for example shock/impact loading, step loading, periodic loading or stochastic loading. Furthermore, although already many theoretical studies have been performed regarding dynamically loaded thin-walled structures [15; 77; 121], experimental validation of these results is scarce. Based on these observations, the objectives of this thesis are formulated in the next subsection.

## 1.1 Objectives

The research objective of this thesis is to develop (fast) modelling and analysis tools which give insight in the behaviour of dynamically loaded thin-walled structures. To illustrate and to test the abilities of the developed tools, a number of case studies are examined. The tools are developed for structures with a relatively simple geometry. The geometric simplicity of the structures allows to derive models with a relatively low number of degrees of freedom which are, therefore, very suitable for extensive parameter studies (as essential during the design process of a thin-walled structure). These models are symbolically derived via an energy based approach, using analytical expressions for the undeformed and deformed structural geometry. This approach has been implemented in a generic manner in a symbolic manipulation software package, such that model variations can be easily performed. For the analyses, both nonlinear static and nonlinear dynamic responses will be computed using numerical techniques in combination with the derived nonlinear models. The combination of the symbolic derivation of the model and the numerical techniques to obtain the solutions, is called a semi-analytical approach. Using this semi-analytical approach, the buckling of four structures due to both quasi-static loads and time-dependent loads (i.e. shock loading and harmonic loading) are thoroughly studied. These studies will include investigation of the effect of several parameter variations and the effect of small deviations from the nominal geometry. For validation, the semi-analytical results will initially be compared with results obtained from computationally much more demanding FEM analyses. However, more important, for two cases the semi-analytical results will also be compared with experimentally obtained results. For this purpose, a dedicated experimental setup will be realized.

## 1.2 Outline of the thesis

The outline of this thesis is as follows. In the next chapter, firstly the semi-analytical approach to study dynamic buckling of structures will be discussed. Secondly, a brief overview of static and dynamic instability phenomena of structures will be presented. In the rest of the thesis, case studies will be performed to present the abilities of the adopted semi-analytical approach.

More specific, in Chapter 3, dynamic buckling of shock loaded arches will be considered. In Chapter 4, an initially buckled beam subjected to a harmonic forcing in transversal direction will be discussed. Chapter 5 considers a base-excited thin beam which carries a rigid top mass. For the latter case, semi-analytical results will be confronted with experimentally obtained results in Chapter 6. Chapter 7 will discuss a base-excited thin cylindrical shell which carries a rigid top mass. For this case, semi-analytical results will be confronted with experimentally obtained results in Chapter 8. Finally, in Chapter 9, the conclusions of the thesis will be presented and recommendations will be given for further research.

## *Preliminaries*

**T**his chapter will present in a general manner the adopted semi-analytical approach to study the dynamic buckling of structures (Section 2.1). Secondly, a brief overview of static and dynamic instability phenomena of structures will be presented in Section 2.2. Finally, in Section 2.3, computational tools will be discussed.

### *2.1 Semi-analytical approach*

The modelling of thin-walled structures like beams, plates and shells is a continuum mechanics problem, i.e. the response of the structure is described by Partial Differential Equations (PDEs) with continuous displacement fields as unknown variables. The displacement fields themselves are functions depending on the spatial coordinates and time. In general, PDEs are solved using numerical techniques, especially when nonlinearities must be taken into account. Hereto, the continuous variables of the PDEs are firstly discretized and subsequently the problem is restated as a set of Ordinary Differential Equations (ODEs) and solved. It should be noted that the solutions of the discretized problems are approximations of the original continuous problems. Probably the most generally used discretization technique used in structural engineering is the Finite Element Method (FEM). Indeed, the usage of FEM offers a very flexible way to deal with complex geometrical shapes and all kinds of geometrical and material nonlinearities. However, a drawback of the use of FEM is the fact that the resulting models possess in general many Degrees Of Freedom (DOFs). Even with the computational power of modern computers, solving a large set of coupled nonlinear equations of motion still remains a computationally heavy task, making the use of FEM for large parameter studies less feasible. Therefore, in this thesis a semi-analytical approach is adopted for fast modelling and analysis of dynamically loaded thin-walled structures. The approach is designated as semi-analytical, since analytical descriptions of the structural geometry and displacement fields in combination with symbolic manipulation tools are used for the derivation of the equations of motion while numerical tools are used to obtain solutions of these equations of motion. Note that for some specific cases, FEM will still be used for the numerical validation of the responses obtained by the semi-analytical approach. In this section, the derivation of the equations of motion will be discussed. As stated before, the

numerical tools will be introduced in Section 2.3.

### **2.1.1 Modelling steps**

The derivation of a model for a thin-walled structure via the semi-analytical approach, involves a number of steps. These steps will be described in this section.

#### ***Assumptions***

In order to derive a set of relations between the displacements and rotations and the strain measures (i.e. the strain-displacement relations) which can capture the dominant nonlinearities, kinematic assumptions must be adopted. Typically, for thin-walled beams, plates and shells these assumptions are the Euler-Bernoulli/Kirchhoff assumptions (i.e. the effect of transverse shear is neglected with respect to the effect of bending [17]) in combination with the assumption that deformations are dominated by out-of-plane displacements. Furthermore, depending on the problem, rotations can be considered to be small. Next to kinematic assumptions also assumptions regarding the type of material behaviour (i.e. linear or nonlinear and elastic or elasto-plastic) must be made. In general, thin-walled structures are able to operate at large (out-of-plane) displacements while staying in the linear elastic range of the material. Therefore, in this thesis only linearly elastic material responses are considered.

#### ***Reduction of displacement fields***

By adopting a set of strain-displacement relations, also the number of independent displacement fields is determined. For example, the modelling of a planar beam when neglecting the effect of transverse shear results in two independent displacement fields (one out-of-plane displacement field and one in-plane displacement field); the modelling of a three-dimensional plate or shell again without the effect of transverse shear results in three independent displacement fields (two in-plane displacement fields and one out-of-plane displacement field). These displacement fields are, in general, mutually coupled via the strain-displacement relations, especially if nonlinearities are taken into account. One approach to solve the problem in terms of the individual fields, is to discretize all fields independently (as usually is done in most FE packages). However, since it is desired to derive accurate models with a minimum number of DOFs, in the semi-analytical approach followed in this thesis, a reduction of the number of independent displacement fields is performed. The result of this reduction step is that only the most dominant displacement field needs to be discretized. In this thesis, two methods of reduction will be distinguished. In the first method (see Chapters 3 and 7), the effect of in-plane inertia will

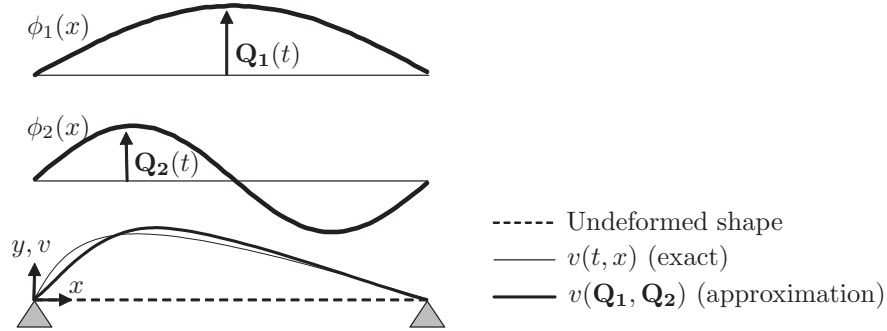


Figure 2.1: Global discretization.

be neglected with respect to the effect of out-of-plane inertia resulting in a combination of static PDEs (i.e. PDEs including only spatial derivatives and no time derivatives) and dynamic PDEs (i.e. PDEs including both time derivatives and spatial derivatives). The next step is to discretize the out-of-plane field and to solve analytically the static PDEs using the assumed expression for the out-of-plane field in combination with the in-plane boundary conditions. In the second method, which is only employed for beam structures (see Chapters 5 and 4), displacements are assumed to be completely determined by bending, i.e. the structure is assumed to be inextensible. This approach kinematically couples the axial displacement field to the transversal displacement field.

### Discretization

As discussed above, the reduction step of displacement fields and the discretization step are not decoupled, i.e. the actual computations involved for the reduction can only be performed after discretization of the remaining unknown fields. Nevertheless, due to its importance, the discretization is discussed separately from the reduction step. In the semi-analytical approach adopted in this thesis, only the out-of-plane displacement will be discretized. The in-plane (or axial) fields follow from this discretization and the assumptions made in the reduction step.

The discretization procedure used in most FE packages divides the structure into a number of smaller elements, which are interconnected at the nodes. The actual discretization is performed within the elements where the local displacements and/or rotations are determined from the nodal DOFs using interpolation functions. This approach is very suitable for analyses of localized

effects (e.g. stress concentrations), since elements can be arbitrarily divided over the structure. However, a drawback of the local discretization approach is that it results in models with relatively many DOFs.

For responses which are more evenly spread out over the structure, such as vibration and/or buckling modes (note that for some cases also buckling modes may have a localized nature [52; 95]), discretizations with much less DOFs can be obtained by adopting a global discretization approach. For the global discretization approach, the actual deflections are approximated using a linear combination of global shape functions with time varying amplitudes (i.e. separation of variables). The approach is illustrated for the discretization of the transversal deflection  $v(t, x)$  of a planar beam in Fig. 2.1 using two shape functions, i.e.

$$v(t, x) = \mathbf{Q}_1(t)\phi_1(x) + \mathbf{Q}_2(t)\phi_2(x), \quad (2.1)$$

where  $\mathbf{Q}_i(t)$  are the time dependent generalized DOFs and  $\phi_i(x)$  are the shape functions. Obviously, the number of modes used in the discretization is not limited to two, but can be extended to more DOFs if higher accuracy is desired. Furthermore, the approach can also be used for structures described by two spatial variables (i.e. plates and shells) by employing 2D shape functions. The global discretization approach in combination with an energy method to derive the equations of motion in terms of the DOFs  $\mathbf{Q}_i(t)$  is better known as the *assumed-modes* method [91; 131]. Note that the assumed-mode method is closely related to the *Rayleigh-Ritz* method [91; 131] and is often referred to as such. More comments on this matter will be discussed in the next step: "Derivation of equations of motion".

The key issue in the global discretization approach is the selection of the set of shape functions to be used for the discretization. A set of shape functions is admissible if

- the shape functions are linearly independent,
- each shape function is at least  $p$  times differentiable (with  $p$  the maximum order of partial differentials as present in the energy integrals),
- each shape function satisfies the geometric boundary conditions.

If the problem has natural boundary conditions (e.g. if the structure is connected to a discrete spring at one end), the use of admissible functions may give poor convergence [5; 91; 131], i.e. many DOFs must be used before accurate results are obtained. For such cases, it is better to select (if available) the shape functions from the set of *comparison functions* [91; 131]. Comparison functions are a subset of the admissible functions but satisfy, in addition, all the boundary conditions and are at least  $2p$  times differentiable (which corresponds

to the order of the governing PDEs).

A set of shape functions  $\phi_i(x)$  ( $i = 1, 2, \dots$ ) is said to be orthogonal in the domain of the structure ( $\mathfrak{D}$ ), if for any two distinct two functions  $\phi_i(x)$  and  $\phi_j(x)$  [91],

$$\int_{\mathfrak{D}} \phi_i(x)\phi_j(x)dx = 0, i \neq j. \quad (2.2)$$

Orthogonality of the set of shape functions is a favourable property since it simplifies the evaluation of the energy integrals in a later stage, but orthogonality of the set of shape functions is not a necessity. The eigenfunctions following from a linear vibrational and/or linear buckling eigenvalue problem are by definition comparison functions and are also orthogonal (and thus linearly independent [91]). Therefore, eigenfunctions are often utilized as shape functions for the discretization procedure. Also the eigenfunctions obtained for a simplification of the actual structure (e.g. obtained for a constant cross-section while the actual structure has a varying cross-section) may serve very well as shape functions [5; 91]. However, shape functions are not restricted to be eigenfunctions. More important, to keep the computational effort during for the derivation of the equations of motion to a minimum, the shape functions should have simple analytical expressions and their mutual products should be easy to evaluate by symbolic integration procedures. In this sense and based on experience, it can be stated that it is advisable to select shape functions from a single family of functions, e.g. use only polynomials or use only harmonic functions.

As a final note, the number of DOFs to be used in the model should be select with care. To minimize the computational time for the numerical analysis, the number of DOFs should be kept to a minimum. However, the number of DOFs should also not be selected too low, since this may result in a highly overestimated stiffness of the structure. For a careful selection of the number of DOFs to be used in the model, convergence studies (e.g. computations of eigenfrequencies, buckling loads or fully non-linear responses for increasing number DOFs) are essential.

### ***Derivation of equations of motion***

After the displacement fields are discretized, the equations of motion in terms of the DOFs  $\mathbf{Q}_i(t)$  (i.e. a set of ODEs) can be derived by either starting from energy expressions or from a set of PDEs. The first method is known as the energy or *Lagrangian* approach, the second method is known as the *Galerkin* approach.

For the energy approach, the discretized expressions for the displacement fields

are substituted in the kinetic energy  $\mathcal{T}$ , the strain energy  $\mathcal{U}$  and the potential energy of the conservative forces  $\mathcal{V}$  and the virtual work expression of the non-conservative external forces  $\mathcal{W}_{nc}$ , respectively. Damping of thin-walled structures is in general modelled as viscous damping. The non-conservative forces due to the viscous damping can be taken into account by using a so-called *Rayleigh dissipation function*  $\mathcal{R}$  [91]. After the energy integrals and the dissipation function are symbolically evaluated, the equations of motion are derived using *Lagrange's equations*

$$\frac{d}{dt}T_{,\dot{\mathbf{Q}}} - T_{,\mathbf{Q}} + \mathcal{U}_{,\mathbf{Q}} + \mathcal{V}_{,\mathbf{Q}} = -\mathcal{R}_{,\dot{\mathbf{Q}}} + F_{ex}(t), \quad (2.3)$$

where the column with non-conservative forces  $F_{ex}(t)$  follows from [91]

$$\delta\mathcal{W}_{nc} = F_{ex}(t)\delta\mathbf{Q}, \quad (2.4)$$

and  $\mathbf{Q} = [\mathbf{Q}_1(t), \mathbf{Q}_2(t), \dots, \mathbf{Q}_N(t)]^T$  with  $N$  the number of DOFs. As noted before, the global discretization approach in combination with the energy method to derive the final set of ODEs is known as the assumed-mode method. The Rayleigh-Ritz method is closely related to the assumed-mode method, but is strictly speaking concerned with the discretization of differential eigenvalue problems instead of with the formulation of a set of (nonlinear) ODEs [91].

The Galerkin approach has as starting point a set of PDEs, for example derived using first principles (Newton's equations) or from energy expressions using Hamilton's variational principle [91]. Since the shape functions in general do not satisfy the PDEs, a residual  $\psi(\mathbf{Q}, t, x)$  remains, after the discretized expressions for the displacement fields are substituted in the PDEs. To minimize this residual in some sense, the residual is multiplied by the shape functions (one by one) and the result, integrated over the domain of the structure ( $\mathfrak{D}$ ), is set to zero, i.e.

$$\int_{\mathfrak{D}} \psi(\mathbf{Q}, t, x) \phi_i(x) d\mathfrak{D} = 0, \quad i = 1, 2, \dots, N. \quad (2.5)$$

Equation (2.5) constitutes a set of ODEs in terms of the DOFs  $\mathbf{Q}_i(t)$ . It should be noted that if the adopted shape functions are not comparison functions (i.e. the shape functions only satisfy the geometrical boundary conditions), an integral over the boundaries of domain should be added to Eq. (2.5) such that deviations from the natural boundary conditions will be minimized as well [91].

When the PDEs used during the Galerkin approach are derived from the energy and work expressions, the energy and Galerkin approach result in exactly the same set of ODEs if the same set of shape functions is utilized. The energy method does not require to derive the PDEs (if they are not ready



available from literature), which may be an advantage for certain (complicated) cases. Furthermore, using the energy method, attachments like discrete springs and dash-pots can be included relatively simple by augmenting the energy expressions of the continuous structure with the energy expressions of the discrete elements. However, since in the end both methods result in the same set of equations, which method is adopted may depend also on personal preference and experience. In this thesis, the energy method is followed.

In a general form, the resulting set of  $N$  ODEs reads as follows

$$M(\mathbf{Q}) \ddot{\mathbf{Q}} + G(\mathbf{Q}, \dot{\mathbf{Q}}) + C\dot{\mathbf{Q}} + K[\mathbf{P}(t)] \mathbf{Q} + H[\mathbf{Q}, \mathbf{P}(t)] = B\mathbf{P}(t), \quad (2.6)$$

where  $M(\mathbf{Q})$  denotes the (nonlinear) mass matrix,  $G(\mathbf{Q}, \dot{\mathbf{Q}})$  denotes Coriolis, centrifugal and nonlinear damping loads,  $C$  denotes the linear viscous damping matrix,  $K[\mathbf{P}(t)]$  denotes the linear (possibly time dependent) stiffness matrix,  $H[\mathbf{Q}, \mathbf{P}(t)]$  denotes nonlinear elastic loads,  $B$  is a load input matrix and  $\mathbf{P}(t)$  denotes a column with time dependent loads. Column  $H[\mathbf{Q}, \mathbf{P}(t)]$  in Eq. (2.6) originates from the adopted nonlinear kinematic relations. The inertia nonlinearities in Eq. (2.6) are for example present for the case where the structure is considered inextensible and in-plane inertia effects are taken into account via a nonlinear kinematic coupling with the out-of-plane displacements. The time-dependent loads  $\mathbf{P}(t)$  may be introduced either directly as a time-dependent external force or indirectly via a prescribed motion (in terms of displacement or rotation). As can be noted, the loading  $\mathbf{P}(t)$  may appear both on the right-hand-side of Eq. (2.6) and on the left-hand-side of Eq. (2.6). This will be further discussed in Section 2.2.2.

## 2.2 Stability of structures

This section deals with the stability of structures. The stability problem will be divided in two parts. The first part will consider the stability of structures subjected to static conservative loads (i.e. loads which can be derived from an energy potential [12]). The second part will discuss the stability of structures subjected to time-varying loads.

### 2.2.1 Static buckling

The loss of stability of static equilibrium states of structures subjected to conservative loads  $\mathbf{P}$ , is in general known as static buckling of the structure. For conservative systems, the stability analyses can be solely based on properties of the sum of the strain energy  $\mathcal{U}$  and the potential energy of the conservative forces  $\mathcal{V}$

$$\Pi(\mathbf{Q}, \mathbf{P}) = \mathcal{U} + \mathcal{V}, \quad (2.7)$$

which is often denoted as total potential energy [44; 111]. The total potential energy of the structure depends on the DOFs  $\mathbf{Q}_i$ . Furthermore, without loss of generality, it will also be presumed to depend on a single scalar  $P$  which determines the magnitude (or distribution) of the external conservative loads  $\mathbf{P}$  working on the structure.

Static equilibria, denoted by  $\mathbf{Q} = \mathbf{Q}^*$  and  $P = P^*$ , are extrema of the total potential energy (2.7), i.e.

$$\Pi, \mathbf{Q} |_{\mathbf{Q}=\mathbf{Q}^*, P=P^*} = \mathcal{U}, \mathbf{Q} |_{\mathbf{Q}=\mathbf{Q}^*, P=P^*} + \mathcal{V}, \mathbf{Q} |_{\mathbf{Q}=\mathbf{Q}^*, P=P^*} = 0. \quad (2.8)$$

In general, Eq. (2.8) constitutes a set of  $N$  nonlinear algebraic equations with the DOFs  $\mathbf{Q}_i$  as the unknowns and the load  $P$  as variable. By computing a solution of Eq. (2.8) for a quasi-statically varying load  $P$ , a curve is obtained in the  $N + 1$  dimensional space spanned by  $\mathbf{Q}_i$  and  $P$ . This curve is called the *equilibrium path* or the *load-path*.

In what follows, the total potential energy Eq. (2.7) evaluated at some equilibrium state will be denoted by

$$\Pi^* = \Pi(\mathbf{Q}^*, P^*). \quad (2.9)$$

The Hessian of Eq. (2.9) with respect to the DOFs  $\mathbf{Q}_i$  is denoted as the tangent stiffness matrix  $K_0$  [111], i.e.

$$K_0 = \Pi^*, \mathbf{Q}\mathbf{Q}. \quad (2.10)$$

The (local) stability of equilibrium states of conservative systems can be assessed by looking at the eigenvalues of the tangent stiffness matrix  $K_0$ , which are all real, since  $K_0$  is a symmetric matrix. Let  $\mu_i$  denote the  $i^{\text{th}}$  eigenvalue of  $K_0$ . Based on theorems of *Lagrange-Dirichlet* and *Lyapunov* [12; 111], it can be concluded that an equilibrium state is stable if all  $\mu_i > 0$ , while an equilibrium state  $\mathbf{Q}^*$  is unstable if one or more  $\mu_i < 0$ . If along a load-path, at some equilibrium state one or more  $\mu_i = 0$ , this equilibrium state is denoted as a critical state. Static buckling refers in general to case where, starting from some stable state, a critical state is reached along the load-path. The critical state and corresponding load are denoted by  $\mathbf{Q}_c$  and  $P_c$ , respectively. At a critical state, it follows that

$$K_0 |_{\mathbf{Q}=\mathbf{Q}_c, P=P_c} \mathbf{z} = 0, \quad (2.11)$$

where the column  $\mathbf{z}$  denotes the buckling mode. In general, Eq. (2.11) constitutes a nonlinear eigenvalue problem, since  $K_0$  (in general) depends in a nonlinear fashion on the DOFs  $\mathbf{Q}_i$ , which in turn may depend in a nonlinear fashion on the load  $P$ , as defined by the equilibrium equations Eq. (2.8).

In general, Eq. (2.11) is solved by solving Eq. (2.8) for a varying load  $P$  with for example some sort of numerical path-following routine [105], while simultaneously tracking the eigenvalues of the tangent stiffness matrix Eq. (2.10). Buckling occurs where the matrix  $K_0$  becomes singular.

For some structures, such as axially loaded beams and in-plane loaded plates, the prebuckling response of the structure may be approximated using a linear load-displacement relation [17]. Consider some known (non-critical) equilibrium state  $\mathbf{Q}_0^*$  and  $P_0^*$  with the total potential energy denoted by  $\Pi_0^* = \Pi(\mathbf{Q}_0^*, P_0^*)$  and obeying

$$\Pi_{0,\mathbf{Q}}^* = 0. \quad (2.12)$$

Considering the first order Taylor series expansion of Eq. (2.12), i.e.

$$\Pi_{0,\mathbf{Q}}^*(\mathbf{Q}_0^* + \Delta\mathbf{Q}, P_0 + \Delta P) \approx \Pi_{0,\mathbf{Q}}^* + \Pi_{0,\mathbf{Q}\mathbf{Q}}^* \Delta\mathbf{Q} + \Pi_{0,\mathbf{Q}P}^* \Delta P = 0, \quad (2.13)$$

results in the following linear approximation for the prebuckling response

$$\Delta\mathbf{Q} = (\Pi_{0,\mathbf{Q}\mathbf{Q}}^*)^{-1} \Pi_{0,\mathbf{Q}P}^* \Delta P. \quad (2.14)$$

Similarly, for small displacements, the tangent stiffness matrix may be approximated using a first order expansion in terms of the increments  $\Delta\mathbf{Q}$  and  $\Delta P$

$$K_0 = \Pi_{0,\mathbf{Q}\mathbf{Q}}^* + \Pi_{0,\mathbf{Q}\mathbf{Q}\mathbf{Q}}^* \Delta\mathbf{Q} + \Pi_{0,\mathbf{Q}\mathbf{Q}P}^* \Delta P, \quad (2.15)$$

where (in index notation)

$$(\Pi_{0,\mathbf{Q}\mathbf{Q}\mathbf{Q}}^* \Delta\mathbf{Q})_{i,j} = \sum_{\mathbf{k}=1}^N \Pi_{0,\mathbf{Q}_i\mathbf{Q}_j\mathbf{Q}_\mathbf{k}}^* \Delta\mathbf{Q}_\mathbf{k}. \quad (2.16)$$

After substitution of Eq. (2.14) into Eq. (2.15), Eq. (2.11) may be rewritten to the linear buckling eigenvalue problem

$$[K_m + \Delta P K_g] \mathbf{z} = 0, \quad (2.17)$$

where  $K_m = \Pi_{0,\mathbf{Q}\mathbf{Q}}^*$  and  $K_g = \Pi_{0,\mathbf{Q}\mathbf{Q}\mathbf{Q}}^* (\Pi_{0,\mathbf{Q}\mathbf{Q}}^*)^{-1} \Pi_{0,\mathbf{Q}P}^* + \Pi_{0,\mathbf{Q}\mathbf{Q}P}^*$ . The matrix  $K_g$  is often designated as geometrical stiffness matrix and accounts for changes in stiffness of the structure during deformation. The linearized buckling analysis is available in many FE packages but should be used with great care, i.e. the obtained buckling load from the linearized buckling analysis may highly overestimate the actual buckling load [23].

At critical states, determined by either solving the nonlinear eigenvalue problem Eq. (2.11), or the (approximating) linear eigenvalue problem Eq. (2.17), the stability of the pre-buckling equilibrium state is lost and new stable and/or

unstable equilibrium states may appear instead. In other words, at critical states, the state-space of the underlying dynamical system of which the static equilibrium states are studied during the buckling analysis changes in a *qualitative* manner. In the theory of nonlinear dynamics of general systems [128; 129], such qualitative changes due the variation of one or more parameters are called *bifurcations*. The combination of states and parameters at which bifurcations occur are called *bifurcation points*. It should be noted that bifurcations of dynamical systems can occur both for static responses (as the case for static buckling) and for dynamic responses (e.g. the response of a dynamical system due to a time-varying force). Bifurcations of dynamic responses will be discussed in Section 2.2.2.

With respect to bifurcations of static equilibria in the context of buckling, two types of critical states can be distinguished, i.e. *limit-points* and *distinct bifurcation points* [127]. First limit-points will be discussed. Subsequently, distinct bifurcation points will be discussed.

A limit-point (also known as a saddle-node bifurcation [129]) corresponds to the situation where the slope of the initial load-path varies and the load-path reaches a maximum. This type of buckling is addressed as limit-point buckling. When the load is increased to just above the limit-point there is no adjacent equilibrium state anymore. Consequently, under an increasing load, at the limit-point the structure must jump to another (far) point on the load-path, a phenomenon known as *snap-through buckling* [127] or as *collapse* [23]. For illustration, a single DOF snap-through structure is depicted in Fig. 2.2-a. This structure consist of a vertical cart  $m$  (the mass of the cart is not of importance since gravity is not considered) which is suspended by an inclined linear spring  $k$ . The corresponding load-path in terms of the compressive load  $P$  and rotation  $\theta$  is depicted in Fig. 2.2-b. The part of the load-path which corresponds to stable equilibrium states is plotted with a solid line, while the part of the load-path which corresponds to unstable equilibrium states is plotted with a dashed line. When the structure is loaded above the maximum in the load-path (i.e. the limit-point  $P_c$ , see Fig. 2.2-b), the structure will jump towards a downward equilibrium state.

A *distinct* bifurcation point (or branching point) corresponds to a critical state where two or more load-paths coincide. This type of buckling is often addressed as bifurcation buckling and the corresponding buckling load as bifurcation load. To illustrate three types of distinct bifurcation points which are commonly encountered during the static buckling analysis [111; 127], three elementary discrete models with corresponding load-paths are depicted in Figs. 2.3 - 2.5, respectively. All models possess a single DOF  $\theta$  and consists of a linear (translational or torsional) spring  $k$ , a vertical rigid bar with length  $L$  and

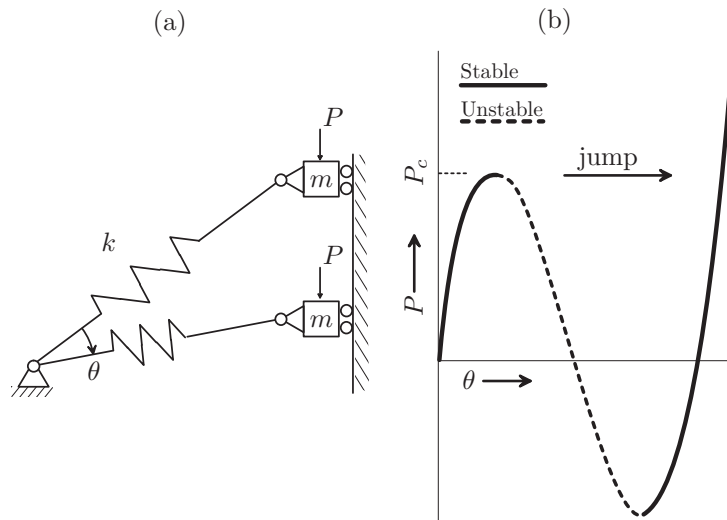


Figure 2.2: Single DOF snap-through structure (a) and corresponding static load-path (b).

are loaded by a compressive vertical force  $P$ . The load-path for each model is presented by plotting the load  $P$  against the rotation  $\theta$ . In contrast to limit-points, distinct bifurcation points may change in a qualitative manner when small imperfections are introduced in the structure. In the load-paths depicted Figs. 2.3 - 2.5, the effect of small deviations from the nominal (perfect) geometry and/or the effect of loading eccentricities (in other words the effect of geometric imperfections and/or load imperfections) on the associated 'perfect' load-path is illustrated with the thin lines.

The first load-path (Fig. 2.3-b) corresponds to probably the best known example of buckling in structures, i.e. buckling of an axially loaded elastic beam. A similar type of buckling occurs for the structure depicted in Fig. 2.3-a. The static equilibrium condition for this structure reads  $PL \sin \theta = k\theta$  [111]. As can be noted, the trivial solution  $\theta = 0$  is always a static equilibrium state of the structure. At the critical state  $P = P_c$  ( $P_c = k/L$  [111]), a secondary load-path corresponding to stable equilibrium states intersects with the fundamental equilibrium path  $\theta = 0$ , see Fig. 2.3-b. As stated before, such an intersection is called a distinct bifurcation point and more specifically for this case a *stable symmetric* point of bifurcation (or super-critical pitchfork bifurcation [129]), since the symmetric secondary path corresponds to stable equilibrium states. Introducing small imperfections (for example by considering the rigid bar to be initially not perfectly vertical), the response of the structure shifts from a

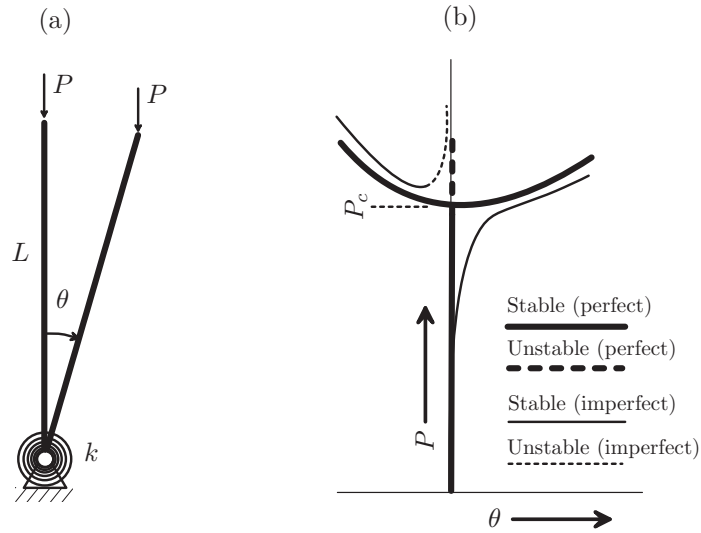


Figure 2.3: Vertically loaded rigid bar supported by a torsional spring at the bottom (a) and corresponding static load-path (b).

bifurcation type of load-path to a smooth nonlinear stable load-path without a distinct buckling phenomenon, see Fig. 2.3-b.

The static equilibrium condition for the structure depicted in Fig. 2.4-a reads  $L \sin \theta (kL \cos \theta - P) = 0$  [111]. Again, the trivial solution  $\theta = 0$  is always a static equilibrium state of the structure. However, now at the critical state  $P = P_c$  ( $P_c = kL$  [111]), a secondary (symmetric) load-path corresponding to *unstable* equilibrium states intersects with the fundamental equilibrium path  $\theta = 0$ , see Fig. 2.4-b. Such a bifurcation point is called an *unstable symmetric* point of bifurcation (or sub-critical pitchfork bifurcation [129]). For such a bifurcation point, small imperfections change the bifurcation type of response to a limit-point type of response, see Fig. 2.4-b. The critical load of the imperfect structure ( $P_{lp}$ ) is lower than the critical load of the perfect structure ( $P_c$ ) and will decrease further if a larger imperfection is considered. Structures with a critical load which decreases for an increasing level of imperfection are called *imperfection sensitive*.

Next to symmetric post-buckling behaviour (i.e. the stable or unstable secondary load-paths are symmetric with respect to the equilibrium state at which the bifurcation takes place), also asymmetrical post-buckling behaviour is possible. For illustration, consider the structure depicted in Fig. 2.5-a.

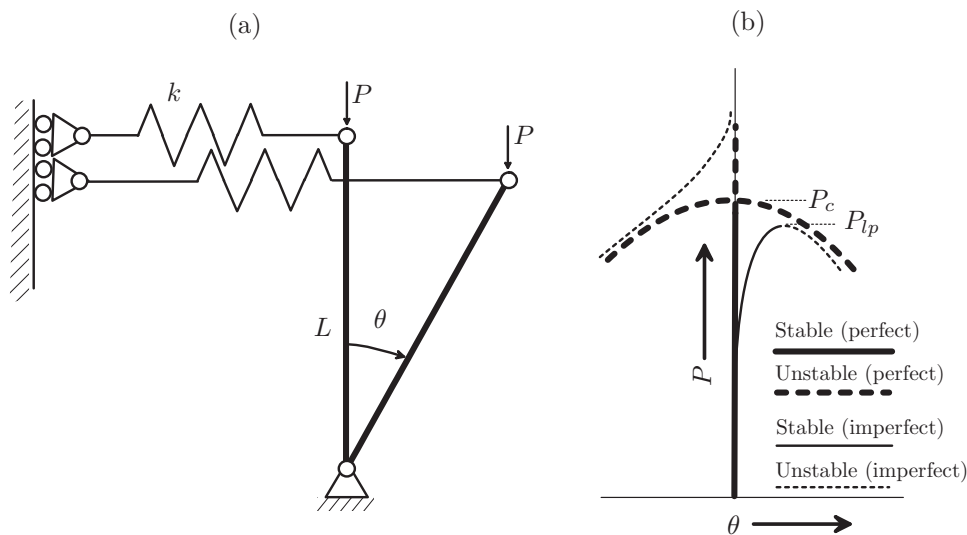


Figure 2.4: Vertically loaded rigid bar supported by a horizontal spring at the top (a) and corresponding static load-path (b).

For small  $\theta$ , the static equilibrium condition for this structure reads  $2\theta P = kL\theta(1 - 3\theta/4)$  [111]. As can be noted, at the critical state  $P = P_c$  ( $P_c = kL/2$  [111]), a secondary asymmetrical load-path intersects the fundamental equilibrium path  $\theta = 0$ , see Fig. 2.5-b. Such a bifurcation point is called an *asymmetric bifurcation point* (or *transcritical bifurcation* [129]), since the secondary load-path is stable in one direction but unstable in the other direction. For this case, the sign of the (dominant) imperfection will determine the qualitative behaviour of the structure. For example, consider the rigid bar initially to be not perfectly vertical. If the initial rotation of the bar is clockwise the structure will collapse via a limit-point load of critical state (as indicated for the imperfect case in Fig. 2.5-b). However, if the initial rotation of the bar is counter clockwise, the response of the structure will shift to a smooth nonlinear stable load-path without a distinct buckling phenomenon (not shown).

As shown, structures may exhibit various types of post-buckling behaviour and imperfection sensitivities. A complete general theory of the initial (linearized) post-buckling behaviour is derived by Koiter [66] (see also [20]). Koiter generally proved that if the initial post-critical load path is stable (as in Fig. 2.3-b), the structure is imperfection insensitive, while if the secondary post-critical load path is unstable (as in Fig. 2.4-b and Fig. 2.5-b) imperfections cause a decrease of the load at which the structure becomes unstable. For the

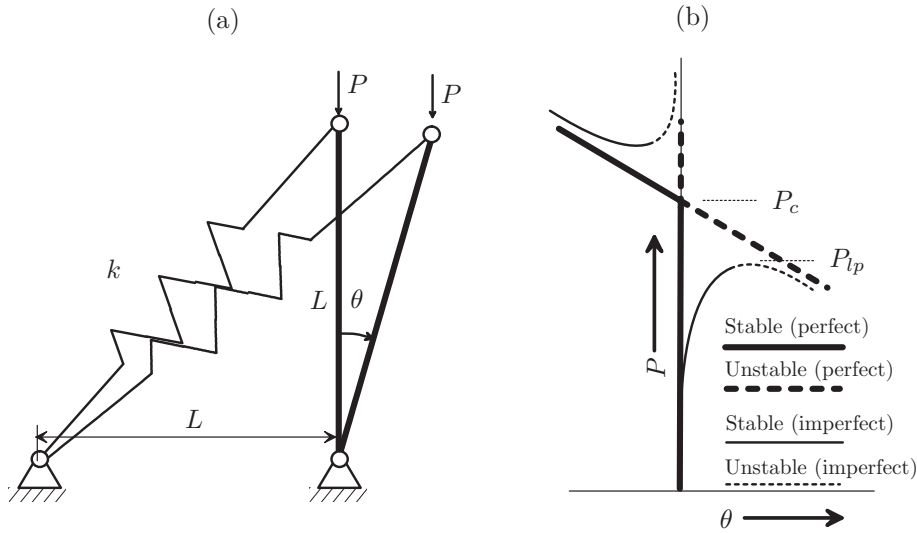


Figure 2.5: Vertically loaded rigid bar supported by an inclined spring at the top (a) and corresponding static load-path (b).

case where several buckling modes coincide at a single critical state or occur at very closely spaced critical states (e.g. occurring for axially compressed thin cylindrical shells), the effect of initial imperfections is typically far more severe than for the case of isolated critical states with an unique buckling mode [23].

### 2.2.2 Dynamic buckling

Structures subjected to an external load which varies in time (e.g. shock loading, harmonic loading, step loading and/or stochastic loading) will not be in static equilibrium but will experience some type of motion (transient or steady-state motion). Such time varying loading is called dynamic loading. In case the unloaded structure is in a stable equilibrium state (as defined in Section 2.2.1) and by assuming the presence of some damping (in reality this is always the case), a 'small' dynamic loading will result in motions which also will remain 'small'. However, there may exist regions in the dynamic loading parameter space, where the induced motions no longer remain 'small' and severe deformations may appear instead. If such critical regions exist, 'small' changes in the dynamic loading may induce sudden large increases in the dynamic responses (obviously the same can happen if the dynamic loading parameters are kept constant and instead the design parameters of the structure are varied). Such transitions are often addressed as dynamic buckling [15; 68; 121; 141]



and more specifically for the case of pulse loading as dynamic pulse buckling [77]. Furthermore, the resistance of structures liable to static buckling, to withstand dynamic loading is often addressed as the dynamic stability of these structures. It should be noted that dynamic stability of structures is a very broad subject that includes not only dynamic buckling due the transient or vibrational types of loading. It may also include problems like fluid/structure interaction [103; 104] and aeroelastic flutter [35]. The latter two types of problems are not considered in this thesis.

For the case of *non-periodic* dynamic loading of structures (e.g. due to shock loading, step loading and stochastic loading), the dynamic buckling analysis must deal with the transient response of the structure during loading and (in the case of shock loading) a certain finite time interval after the actual loading. For the case of shock loading and step loading, the dynamic stability problem may be studied by considering certain aspects of the total potential energy of the structure [53; 68; 121]. This energy based approach allows to determine a lower bound for the dynamic buckling load without the need to solve the nonlinear equations of motion. However, the established lower bound for the dynamic buckling load by the energy approach can be very conservative [63; 102]. Furthermore, the energy based approach does not allow to include the effect of damping rigorously, whereas little damping, as present in all real-life structures, can have a significant effect on the dynamic buckling load [50; 62; 79]. Due to these drawbacks, the energy based approach is not further considered in this thesis.

In general, for structural nonlinear dynamics analysis, one has to resort to numerical means. For the numerical dynamic stability analyses of structures subjected to non-periodic time-dependent loading, the most adopted dynamic buckling criterion is defined by Budiansky-Roth [19; 21; 22]. To apply this criterion, the equations of motion are (numerically) solved for various values of the load. The load at which there exists a sudden large increase in the response for small variation of the load parameter, is called the dynamic buckling load ( $P_{dyn}$ ). The use of the Budiansky-Roth criterion requires the specification of two additional (problem specific) items. Firstly, one must select a time-span to evaluate the response. The time-span should be selected not too short, since the actual buckling event may take some time to occur. Secondly, one must select a scalar measure (being a function of the DOFs present in the model) to characterize the response. Typically, the adopted measure reflects a transversal displacement for beam structures and an out-of-plane displacement for plate or shell structures. Favourably, both are measured at a point where the largest deflections are expected during buckling.

In Fig. 2.6, two examples of Budiansky-Roth criterion plots are depicted. From

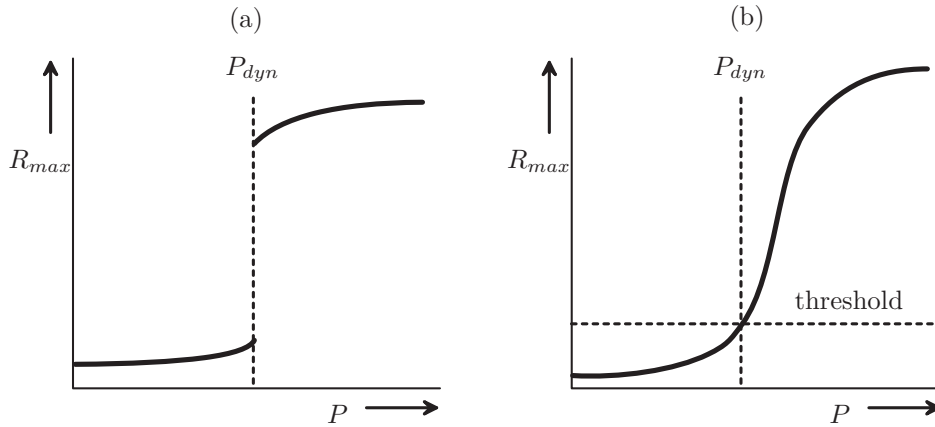


Figure 2.6: Two examples of Budiansky-Roth criterion plots ( $P_{dyn}$  denotes the dynamic buckling load,  $R_{max}$  denotes the maximum value during the considered time interval in terms of the chosen response quantity).

Fig. 2.6-a, the dynamic buckling load can be clearly identified by the sudden jump in the graph. Such sudden jumps are likely to occur for dynamically loaded structures which exhibit a limit-point type of instability under static loading (as in Fig. 2.2-b). In Fig. 2.6-b, an example of a Budiansky-Roth criterion plot is shown which does not exhibit a clear jump but instead a region where displacements rapidly start to increase. Such transitions occur for example for dynamically loaded structures which exhibit under static loading a stable post-buckling behaviour (as in Fig. 2.3-b). The Budiansky-Roth criterion is not explicit in the definition of the dynamic buckling load for the case shown in Fig. 2.6-b. For such cases, one should select (based on experience) a threshold value for the response quantity to be able to determine the dynamic buckling load. Obviously, in this manner the phenomenon of dynamic buckling is not uniquely defined.

Next, dynamic buckling of structures subjected to *periodic* loading  $P(t) = P(t+T)$  (with  $T$  the period time of the excitation) will be discussed. Assuming the presence of damping and assuming that the response remains bounded, the response of such structures will undergo two stages. In the first transient stage, the response will be irregular. After the transient response has damped out, a regular response will be reached representing the so-called *steady-state* behaviour. In contrast to the linear case, the nonlinear steady-state response of periodically forced structures does not need to be unique and it does not have to have the same period as the excitation force. It may even be not periodic

at all. Instead it may be quasi-periodic or chaotic [129].

For the case of a periodic nonlinear steady-state response, the response may be computed directly by solving periodic solutions of Eq. (2.6) defined by the two-point boundary value problem [40; 105; 120]

$$\begin{bmatrix} \mathbf{Q}(t) \\ \dot{\mathbf{Q}}(t) \end{bmatrix} = \begin{bmatrix} \mathbf{Q}(t + n_T T) \\ \dot{\mathbf{Q}}(t + n_T T) \end{bmatrix}, \quad (2.18)$$

where  $n_T \geq 1$  denotes a positive integer. For the case  $n_T = 1$ , the response is called harmonic while for the case  $n_T \geq 2$  the response is called subharmonic of order  $1/n_T$ . Next to a subharmonic *response*, periodically forced nonlinear systems may also exhibit superharmonic *resonances*. Superharmonic resonance is the phenomenon, in which one or more higher harmonics cause resonance in a (sub)harmonic response [40]. Various numerical algorithms exist to solve periodic solutions defined by Eqs. (2.6) and (2.18). Examples are the (multiple) shooting method [120], the finite difference method [40; 105] and the orthogonal collocation method [33]. The evolution of a periodic solution for a varying system parameter (e.g. the excitation frequency and/or the excitation amplitude), may be effectively studied using a numerical periodic solution solver combined with a numerical continuation (or path-following) routine [40; 105; 120].

Considering a structure (being prone to static buckling) subjected to a periodic forcing with a sufficiently small amplitude, the response of the structure may be expected to be harmonic with small displacements. However, for certain combinations of the excitation frequency and the excitation amplitude, the harmonic response may become unstable and severe large amplitude vibrations may appear instead. Such transitions may be studied using a transient analysis and the Budiansky-Roth dynamic buckling criterion. However, if the structure is slightly damped (as is common in practice), the equations of motion must be integrated over a long period before the transient is damped out and the steady-state behaviour is reached. Moreover, for every change of some system parameter, these computationally expensive calculations have to be repeated before the steady-state behaviour is reached again. Consequently, one can study the stability of periodically forced structures (much) more efficiently, by computing the steady-state response of the structure using numerical continuation of the periodic solutions defined by Eqs. (2.6) and (2.18).

During the numerical continuation of periodic solutions, the (local) stability of a periodic solution can be determined using techniques which are based on Floquet theory [120]. In a similar fashion as discussed for static equilibria (see Section 2.2.1), the (local) stability of a periodic solution may change at bifurcation points if one or more system parameters are varied [40; 120; 128]. To

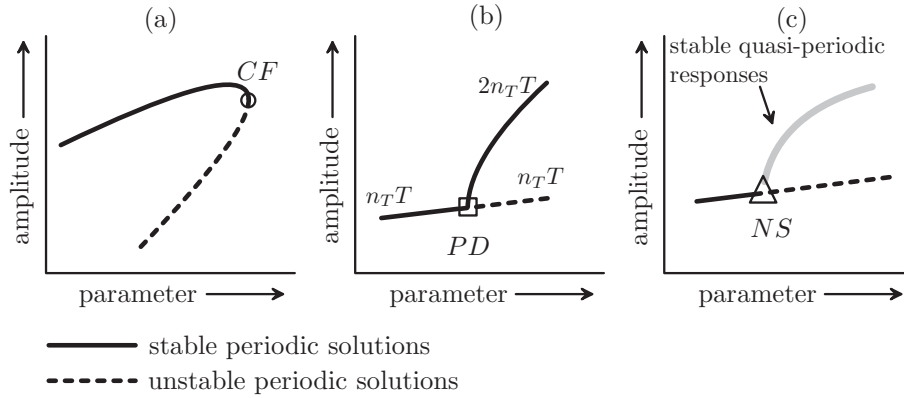


Figure 2.7: Typical bifurcation scenarios for periodic solutions (i.e. the cyclic fold bifurcation  $CF$ , (supercritical) period doubling bifurcation  $PD$  and the Neimark-Sacker bifurcation  $NS$ ).

illustrate three types of bifurcations of periodic solutions which are commonly encountered in this thesis, three bifurcation scenarios of period solutions are depicted in Fig. 2.7. The parts of the branches which correspond to stable periodic solutions are plotted with solid lines, while the parts of the branches which correspond to unstable periodic solutions are plotted with dashed lines. These three types of bifurcations of periodic solutions are so-called co-dimension 1 bifurcations as they are generically met under variation of one system parameter.

The first scenario (Fig. 2.7-a) illustrates the *cyclic fold* (or turning point) bifurcation. At the cyclic fold bifurcation (indicated by  $CF$ ), the stable and unstable periodic solution merge into each other. Just after the bifurcation point, locally no periodic solution exists anymore. Consequently, for an incrementally increasing parameter value, the steady-state response will jump to another attractor which may differ much from the response just before the cyclic fold bifurcation. The cyclic fold bifurcation of periodic solutions is in analogy with the limit-point bifurcation of equilibria (see Section 2.2.1).

The next scenario (Fig. 2.7-b) illustrates the *period doubling* (or flip) bifurcation. In analogy with distinct bifurcation points of static equilibria (see Section 2.2.1), at the period doubling bifurcation (indicated by  $PD$ ) a continuous branch of stable periodic solutions (with period  $n_T T$ ) loses its stability. In addition, at the period doubling bifurcation point, a new branch of stable periodic solutions emanates which correspond to periodic solutions with

period  $2n_T T$  (i.e. the period doubles). The period doubling bifurcation can be supercritical (i.e. the bifurcating branch is stable, as shown here) or subcritical (i.e. the bifurcating branch is unstable).

The last scenario (Fig. 2.7-c), illustrates the *Neimark-Sacker* (also known as Neimark or secondary Hopf) bifurcation. At the Neimark-Sacker bifurcation (indicated by  $NS$ ), the stability of the period solutions is lost and a branch of coexisting stable quasi-periodic solutions appears. Here the scenario is sketched for a supercritical Neimark-Sacker bifurcation but, just as for the period doubling bifurcation, there also exists a subcritical version of it. Quasi-periodic solutions of Eq. (2.6) do not obey Eq. (2.18) and can, therefore, not be studied with the numerical continuation tools used in this thesis (see Section 2.3). Continuation techniques for quasi-periodic responses are available (see [117] and cited therein) but will not be considered in this thesis. Instead standard numerical time integration will be used to study quasi-periodic (and chaotic) responses.

A large part of the research regarding the dynamic buckling of periodically forced structures deals with the phenomenon of parametric resonance [15; 97; 130]. Parametric resonance is a (dynamic instability) phenomenon in which a motion is excited through an excitation mechanism which effectively depends on both the external forcing and on one or more DOFs of the structure. For such excitation, known as *parametric excitation*, the excitation force will appear not at the right-hand-side of the equations of motion but as a parameter at the left-hand-side. Parametric excitation may excite modes, which are not forced in a direct manner, e.g. for a slender beam a periodic *axial* excitation may parametrically excite *transversal* bending modes (see also Chapter 5). In general, parametric resonance is possible for all structures which under static loading are prone to bifurcation buckling (see Section 2.2.1), regardless of the type of post-buckling behaviour (i.e. stable or unstable) [121].

For further illustration, consider again the vertical rigid bar depicted Fig. 2.3-a. The static load  $P$  at its free end now is replaced with a periodic vertical forcing  $P(t) = r_d \cos(\omega t)$  with amplitude  $r_d$  [N] and angular frequency  $\omega$  [rad/s]. Including viscous damping in the hinge and considering  $\theta$  to be small, the dynamics of the periodically forced rigid bar is described by a *Mathieu* differential equation [97; 130]

$$I\ddot{\theta} + b\dot{\theta} + [k + r_d/L \cos(\omega t)]\theta = 0, \quad (2.19)$$

where  $I$  denotes the mass-moment of inertia of the rigid bar with respect to the hinge and  $b$  is the viscous damping of the hinge. The effective torque at the hinge due to the external force  $P(t) = r_d \cos(\omega t)$  does not only depend on the external force itself, but also on the DOF  $\theta$ . Consequently,

the external excitation appears as a parameter at the left-hand-side of Eq. (2.19). In the parameter space spanned by the excitation amplitude  $r_d$  and the excitation angular frequency  $\omega$  regions exist where Eq. (2.19) exhibits unbounded solutions. Outside these regions, the solutions of Eq. (2.19) decays towards the trivial solution  $\theta(t) = 0$  and on the borders of these regions, Eq. (2.19) exhibits periodic solutions [97; 130]. The unbounded solutions occur in the regions where the excitation angular frequency ( $\omega$ ) equals

$$\omega = \frac{2\omega_0}{n}, \quad n = 1, 2, \dots, \quad (2.20)$$

where  $\omega_0 \approx \sqrt{k/m}$  (for small viscous damping  $b$ ) is the angular eigenfrequency. For increasing damping, the regions where unbounded solutions occur are lifted towards higher critical values for  $r_d$ . Below this critical value no parametric resonance occurs, whereas for values of  $r_d$  above this value, parametric resonance leads to an unbounded response. The critical value is determined by the instability region near twice the eigenfrequency ( $\omega = 2\omega_0$ ), since (in general) here the first instability occurs. It should be noted that for large amplitude responses, nonlinearities may no longer be neglected in Eq. (2.19). With additional damping and/or stiffness nonlinearities, responses of Eq. (2.19) may no longer grow unbounded but instead will saturate at a large amplitude (1/2 subharmonic) steady-state response [97].

Next to parametric resonance, also the dynamic stability of periodically forced structures which exhibit multiple coexisting stable static equilibrium states (e.g. shallow curved beams and shells) is an important topic. The total potential energy function of such a structure contains multiple wells, peaks, saddles and ridges. Each well corresponds to a stable static equilibrium state while peaks and saddles correspond to unstable static equilibrium states. For illustration, consider again the snap-through structure with single DOF  $\theta$  as depicted in Fig. 2.2-a. The shape of the potential energy of the structure is depicted in Fig. 2.8. As can be noted, the potential energy function has a so-called *double potential well* shape and shows two stable equilibrium states (the upwards configuration  $q_u^*$  and the downwards configuration  $q_d^*$ ) and one unstable equilibrium state ( $q_n^*$ ). In order to introduce a dynamic loading, the static force  $P$  (see Fig. 2.2-a) is replaced by a periodic external force  $P(t)$ . Starting at the stable equilibrium state  $q_u^*$  with a sufficiently small periodic forcing  $P(t)$ , the response of the structure will remain bounded to the well around  $q_u^*$ . However, for certain combinations of the amplitude and frequency of the periodic forcing  $P(t)$ , the solution may jump into the other well around  $q_d^*$  or may exhibit large cross-well (or snap-through) motions [48; 122; 123]. Such an *escape* from an initial potential well, may occur for any structure with multiple coexisting stable equilibrium states and may be initiated by a direct excitation force but also by a parametric excitation mechanism.

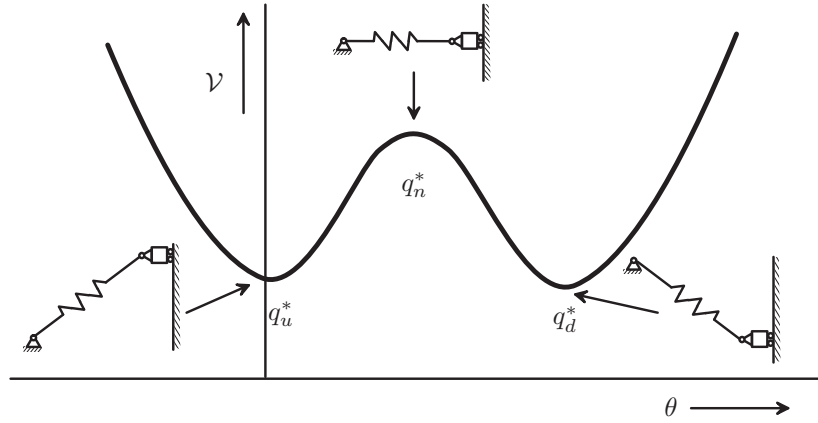


Figure 2.8: Potential energy of a single DOF snap-through structure.

The dynamic buckling concepts introduced in this section will be further elaborated in this thesis by considering four case studies. More specifically, in Chapter 3, the dynamic buckling of shock loaded shallow arches will be examined using a dynamic transient analysis. The Budiansky-Roth criterion will be used to define the dynamic buckling load. Next, in Chapter 4, the dynamic stability of an initially buckled beam subjected to a harmonic excitation in transversal direction will be investigated. The buckled beam possesses two coexisting stable equilibrium states and may, therefore, exhibit large amplitude snap-through motions. The regions where such snap-through motions occur are examined using numerical continuation of periodic solutions. In Chapter 5, a harmonically base-excited thin beam with top mass will be considered. The combination of the base-excitation and the weight of the top mass, results in a combination of static loading and harmonic excitation of the thin beam in axial direction. The most severe type of vibrations of the beam are due to parametric resonance. Using the semi-analytical approach and an experimental approach, the occurrence of parametric resonance will be examined in detail. In the last case study (Chapter 7), the dynamic stability of a base-excited cylindrical shell with top mass will be examined. Using numerical continuation of periodic solutions, standard numerical time integration and experiments, instationary (i.e. chaotic and/or quasi-periodic) types of responses with severe out-of-plane deformations are found.

## 2.3 Computational tools

The purpose of this section is to give an overview of the computational tools used for the adopted semi-analytical approach. As outlined in Section 2.1, the developed Lagrangian approach is used to derive low dimensional models of dynamically loaded thin-walled structures (i.e. equations of motion conform Eq. (2.6)). The approach involves a number of symbolic computations. Especially, the symbolic integration of energy expressions may require large computational times and memory resources. The steps needed to derive the equations of motion are implemented in the software package MAPLE [87] which is very suitable for the symbolic manipulation of large analytical expressions. Within MAPLE, dedicated routines are developed for the symbolic derivation of the equations of motions. Subsequently, the resulting equations are exported to MATLAB [89] code and Fortran code. The produced code is still in a symbolic form and is, therefore, very suitable for parameter variation studies.

MATLAB is a very flexible tool for the numerical analysis of low dimensional models. Using the symbolic code as derived in MAPLE, MATLAB routines are written such that the following analyses can be performed in a straight-forward manner

- Numerical path-following of static equilibrium points including the detection and localization of critical points.
- Linearized buckling eigenvalue analysis (linear buckling loads and modes).
- Linearized vibrational eigenvalue analysis (with or without damping) around any static equilibrium state, for example either in a pre-buckled state or in a post-buckled state.
- Numerical integration of the equations of motion using standard ODE solvers, for example used for a transient analysis, a steady-state analysis including a transient prefatory phase or for computing an initial guess for a periodic solution solver.

As outlined in Section 2.2.2, numerical continuation of periodic solutions can be very effective for the study of the dynamic stability of periodically forced structures. The continuation software package AUTO [33] is dedicated to these continuation calculations and is extensively used in this thesis. The Fortran model descriptions required by this package, can be generated automatically with the previously described MAPLE routines. AUTO offers the following analysis options



- Discretization of ODE boundary value problems (by which periodic solutions can be found) by the method of orthogonal collocation using piecewise polynomials. The mesh automatically adapts to the solution to equidistribute the local discretization error.
- One parameter continuation of periodic solutions with local stability analysis based on Floquet theory, including the detection, localization and classification of (local) bifurcation points. This option is frequently applied to generate frequency-amplitude plots which may show frequency ranges where (nonlinear, parametric) resonances occur or where snap-through motions occur.
- Automatic branch switching at detected local bifurcation points.
- Two parameter continuation of bifurcation points. This option is for example useful to study how the occurrence of certain bifurcations can be influenced and (possibly) can be avoided by parameter changes. Additionally, co-dimension 2 bifurcations can be detected.

For the standard numerical integration of initial value problems for models with a relative large number of DOFs (e.g. more than 10 DOFs), also a Fortran implementation of a Runge-Kutta integration scheme with adaptive step-sizing (NAG routine D02PDF [96]) is used to minimize the computational time for the numerical analysis. This commercially available integration routine is implemented in such a manner that it can call the same Fortran model descriptions as generated for the package AUTO.

As outlined in Section 2.1, the low dimensional models used in this thesis are derived based on a number of assumptions. Since it is desirable to examine the effects of these assumptions, the semi-analytical results must be verified with results obtained using an approach which is not based on the adopted assumptions. Favourably, experiments should be used for this purpose. However, for the case where experimental results are not available or for an initial *numerical* validation (i.e. to test the effect of only a specific subset of the adopted assumptions), results obtained using a FE package may serve for this purpose. In this thesis, the FE package MARC [94] will be used for the initial numerical validation of the semi-analytical results. For two cases, experiments will be performed and results will be compared with the semi-analytical results, see Chapters 6 and 8.



## *Dynamic buckling of a shallow arch under shock loading*

**S**hallowly curved thin-walled structures can for example be encountered in aerospace applications [125], in membrane pumps [45] and in MEMS structures [114]. If such structures are transversally loaded above some critical value, the structure may buckle so that its curvature suddenly reverses. This behaviour, also known as snap-through buckling (see Section 2.2.1), is often undesirable. Such snap-through responses may also be induced by shock (or pulse) loading. In this case, the failure mode is often addressed as dynamic pulse buckling [77].

In this chapter, dynamic pulse buckling of shallow arches is considered. More specifically, the objective is to examine the influence of the initial curvature of thin shallow arches on the dynamic pulse buckling load. The shock loading of the arch is modelled by a prescribed transversal acceleration of the end points of the arch. Using the semi-analytical approach (see Section 2.1), both quasi-static and nonlinear transient dynamical analyses will be performed. The influence of various parameters, such as the pulse duration, the damping and, especially, the arch shape will be illustrated. Moreover, the semi-analytical results will be compared with results obtained using FEA.

The dynamic stability of shallow arch structures can be studied by following an energy based approach [51; 53; 121], a numerical approach [50; 62; 79] or an experimental approach [26; 56; 80]. The energy based approach is capable of determining a lower bound for the dynamic buckling load without the need to solve the nonlinear equations of motion. However, the established lower bound for the dynamic buckling load by the energy approach can be very conservative [63; 102]. Furthermore, the energy based approach does not allow to rigorously include the effect of damping, whereas little damping, as present in all real-life structures, can have a significant effect on the dynamic buckling load [50; 62; 79]. Therefore, in this chapter a numerical approach will be followed. The Budiansky-Roth criterion will be used to define the dynamic buckling load (see Section 2.2.2).

---

Parts of this chapter are also presented in [85] and [86].

Dynamic buckling loads for arches with different shapes are earlier compared in [54; 102]. In [102], dynamic pulse buckling loads of a circularly shaped arch and a sinusoidally shaped arch are compared using an energy based approach and no major differences were found. In [54], the dynamic stability criterion based on energy considerations appeared to be sensitive to the amplitude of the second harmonic in the arch shape and insensitive to the amplitude of the third harmonic in the arch shape. In [112], it is found that for pinned-pinned shallow arches, a circular arch shape is almost optimal with respect to static buckling due to a transversally distributed load. The effects of shape variation on the static buckling of arches subjected to a sinusoidally distributed load are examined in [42] and for arches subjected to a concentrated point load at the center in [11; 42]. In [26], [27] and [76], dynamic snap-through of arches is considered due to an axial impact load, for a moving transversal point load and due to a prescribed axial motion, respectively. Shock loaded doubly-curved shells are considered in [149].

The outline for this chapter is as follows. The next section will deal with the derivation of the equations of motion. In Section 3.2, buckling of the arch under a quasi-static acceleration loading will be discussed. The influence of the arch shape and initial imperfections will be illustrated and results will be compared with FEM results. Dynamic buckling of the arch will be discussed in Section 3.3. The influence of the arch-shape, small geometric imperfections, the level of damping and the shock-pulse duration on the critical shock magnitudes will be examined. Furthermore, the sensitivities of the static buckling loads and dynamic pulse buckling loads with respect to the arch shape will be compared. Finally, in Section 3.4 conclusions will be presented.

### **3.1 Modelling of the arch**

The steel arch (see Fig. 3.1-*a*) has a thickness  $d$ , a width  $z$ , an initial height  $h$  at the center, a fixed span-width  $L$  and a rectangular cross-section with area  $A = zd$  and an area moment of inertia  $I = zd^3/12$ . The initial (undeformed) shape of the arch is indicated by  $w_0(x, t)$ , the shape after (elastic) deformation by  $w(x, t)$  and the axial displacement by  $v(x, t)$  (where  $x$  denotes the axial coordinate and  $t$  denotes time). All geometrical and material properties are considered to be constant over the arch length and are fixed to the values as shown in table 3.1. These dimensions correspond to the circular arch as experimentally examined in [30] (considering a concentrated load at the center). With respect to kinematic assumptions, two basic types of arches can be distinguished, i.e. high arches and shallow arches [12; 42]. High arches are those for which curvature changes are large while the axial strain is negligible (i.e. the center line of the arch may be considered as inextensible). For shallow (or flat) arches, the curvature changes remain small while the induced axial strain (caused by the fact that both end-

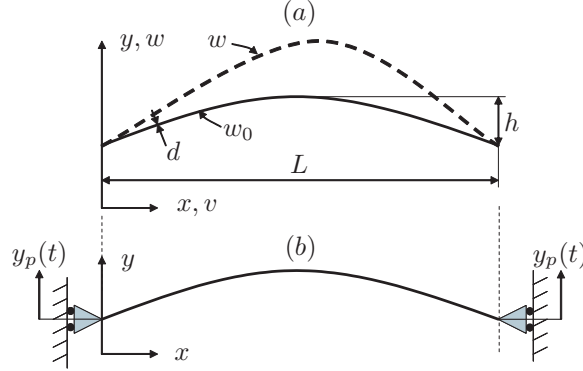


Figure 3.1: (a) : Arch geometry, (b) : pinned-pinned arch with prescribed transversal end-point motion.

points of the arch remain fixed during deformation) plays an important role in the elastic response. Here, a kinematic model based on the shallow arch assumptions is utilized. The internal normal force  $N$  and moment  $M$  in the arch are defined by  $N = EA\varepsilon$  and  $M = EI\kappa$ , with

$$\begin{aligned}\varepsilon &= v_{,x} + \frac{1}{2} \left( (w_{,x})^2 - (w_{0,x})^2 \right) [-], \\ \kappa &= - (w_{,xx} - w_{0,xx}) [\text{m}^{-1}].\end{aligned}\quad (3.1)$$

As stated, the nonlinear kinematic model Eq. (3.1) is valid for slightly curved, slender beams and moderate displacements [42]. In order to model the shock loading via a prescribed transversal acceleration, the arch is considered to be pinned-pinned to a movable frame (see Fig. 3.1-b). The boundary conditions for this load-case read as

$$\begin{aligned}v(0, t) &= v(L, t) = 0 [\text{m}], \\ M(0, t) &= M(L, t) = 0 [\text{Nm}], \\ w(0, t) &= w_0(0, t) = y_p(t) [\text{m}], \\ w(L, t) &= w_0(L, t) = y_p(t) [\text{m}].\end{aligned}\quad (3.2)$$

The prescribed transversal acceleration  $\ddot{y}_p(t)$  results in a loading equivalent to the uniformly distributed transversal loading as for example considered in [42; 112]. Damping in the arch is considered as a uniformly distributed viscous force in transversal direction only

$$F_d = -b(\dot{w} - \dot{w}_0) [\text{N/m}].\quad (3.3)$$

Table 3.1: Parameter values.

Property	Value	Unit
$EI$	0.232	[Nm <sup>2</sup> ]
$h$	$38.4 \cdot 10^{-3}$	[m]
$L$	0.8315	[m]
$d$	$0.803 \cdot 10^{-3}$	[m]
$A$	$2.056 \cdot 10^{-5}$	[m <sup>2</sup> ]
$\rho$	7850	[kg/m <sup>3</sup> ]

Under the assumption that rotary and axial inertia terms are negligible with respect to the transversal inertia, the kinetic energy of the arch equals

$$\mathcal{T} = \frac{1}{2} \rho A \int_0^L \dot{w}^2 dx. \quad (3.4)$$

Since no axial inertia or axial damping forces are considered, it follows that  $N_{,x} = 0$  [121]. Using this fact and  $v(0, t) = v(L, t)$ , the potential energy may be expressed in terms of  $w(x, t)$  solely [121]

$$\mathcal{V} = \frac{N^2 L}{2EA} + \frac{1}{2} \int_0^L (M\kappa) dx, \quad (3.5)$$

where

$$N = \frac{EA}{2L} \int_0^L [(w_{,x})^2 - (w_{0,x})^2] dx. \quad (3.6)$$

Note that gravity forces are not taken into account (the arch moves in the horizontal plane).

### 3.1.1 Initial shape

In order to be able to study the effect of shape-variations, the curvature of the initial (symmetrical) arch shape is parameterized with a single shape parameter  $a$ . Moreover, an imperfection in the form of a small asymmetry with amplitude  $e$  is incorporated. In order to trigger a wide range of harmonic asymmetrical modes with the single mode imperfection shape, a polynomial function is chosen to describe the asymmetry. The parameterization of the arch shape, including

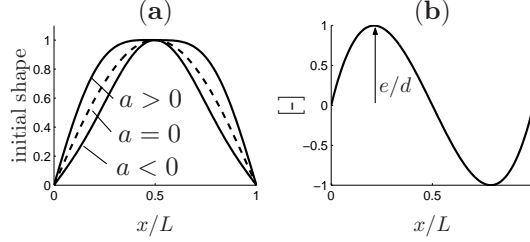


Figure 3.2: (a) : initial shape ( $= [w_0(x, t) - y_p(t)]/h$ ), (b) : imperfection shape.

the (prescribed) transversal movement  $y_p(t)$  of the end-points of the arch, reads

$$\begin{aligned}
 w_0(x, t) = & \underbrace{(h + a) \sin\left(\frac{\pi x}{L}\right) + a \sin\left(\frac{3\pi x}{L}\right)}_{\text{initial shape}} \\
 & + e \underbrace{\left[\frac{36}{L^3\sqrt{3}}x(x - L/2)(x - L)\right]}_{\text{imperfection shape}} + y_p(t). \quad (3.7)
 \end{aligned}$$

The shape parameter is restricted to  $a/h < 1/8$ , so the arch has maximum height at  $x = L/2$ . This leads to a fair comparison, because the shape parameterization leaves the initial height of the arch unchanged ( $w_0(L/2, t) - y_p(t) = h$ ). The initial shape and imperfection shape are illustrated in Fig. 3.2. As a reference, the shape factor  $a$  resembling the circular arch shape used in [30] the most (in a least squares sense), is computed to be  $a/h = 0.03649$ .

### 3.1.2 Discretization and equations of motion

In order to approximate the continuous problem with a discrete set of equations of motion, the field  $w(x, t)$  is discretized as

$$w(x, t) = w_0(x, t) + \sum_{i=1}^n \mathbf{Q}_i(t) \sin\left(\frac{i\pi x}{L}\right), \quad (3.8)$$

satisfying the boundary conditions Eq. (3.2) a priori. The equations of motion in terms of the generalized coordinates  $\mathbf{Q} = [\mathbf{Q}_1(t), \mathbf{Q}_2(t), \dots, \mathbf{Q}_n(t)]^T$  are derived by following the Lagrangian approach, see Section 2.1. Hereto, the energy integrals Eq. (3.4) and Eq. (3.5) are evaluated after substitution of Eq. (3.7) and Eq. (3.8). The non-conservative forces due to the viscous

damping force Eq. (3.3) are taken into account by using the following *Rayleigh* dissipation function [90]

$$\mathcal{R} = \frac{b}{2} \int_0^L (\dot{w} - \dot{w}_0)^2 dx, \quad (3.9)$$

which is evaluated after substitution of Eq. (3.7) and Eq. (3.8). Finally, the equations of motion are determined with *Lagrange's* equations

$$\frac{d}{dt} \mathcal{T}_{,\dot{\mathbf{Q}}} - \mathcal{T}_{,\mathbf{Q}} + \mathcal{V}_{,\mathbf{Q}} = -\mathcal{R}_{,\dot{\mathbf{Q}}}. \quad (3.10)$$

The equations corresponding to the 6-DOF ( $n = 6$  in Eq. (3.8)) approximation are given by

$$\mathbf{M}\ddot{\mathbf{Q}} + \mathbf{C}\dot{\mathbf{Q}} + \mathbf{K}(\mathbf{Q}) = -\mathbf{B}\ddot{y}_p(t), \quad (3.11)$$

where  $\mathbf{M} = \frac{\rho AL}{2}\mathbf{I}$ ,  $\mathbf{C} = \frac{bL}{2}\mathbf{I}$  with  $\mathbf{I}$  the identity matrix,

$$\mathbf{B} = \frac{2\rho AL}{\pi} \begin{bmatrix} 1 & 0 & \frac{1}{3} & 0 & \frac{1}{5} & 0 \end{bmatrix}^T,$$

and

$$\mathbf{K}(\mathbf{Q}) = \begin{bmatrix} \frac{\pi^2}{2L} N(\mathbf{Q})(a + h + \mathbf{Q}_1) + \frac{EI\pi^4}{2L^3} \mathbf{Q}_1 \\ \frac{2}{L\pi} N(\mathbf{Q})(18e\sqrt{3} + \pi^3 \mathbf{Q}_2) + \frac{8EI\pi^4}{L^3} \mathbf{Q}_2 \\ \frac{9\pi^2}{2L} N(\mathbf{Q})(\mathbf{Q}_3 + a) + \frac{81EI\pi^4}{2L^3} \mathbf{Q}_3 \\ \frac{2}{L\pi} N(\mathbf{Q})(9e\sqrt{3} + 4\pi^3 \mathbf{Q}_4) + \frac{128EI\pi^4}{L^3} \mathbf{Q}_4 \\ \frac{25\pi^2}{2L} N(\mathbf{Q})\mathbf{Q}_5 + \frac{625EI\pi^4}{2L^3} \mathbf{Q}_5 \\ \frac{6}{\pi L} N(\mathbf{Q})(2e\sqrt{3} + 3\pi^3 \mathbf{Q}_6) + \frac{648EI\pi^4}{L^3} \mathbf{Q}_6 \end{bmatrix},$$

where

$$\begin{aligned} N(\mathbf{Q}) = & \frac{EA\pi^2}{4L^2} [\mathbf{Q}_1(2a + 2h + \mathbf{Q}_1) + 18a\mathbf{Q}_3 \\ & + \frac{144\sqrt{3}}{\pi^3} e(\mathbf{Q}_2 + \frac{1}{2}\mathbf{Q}_4 + \frac{1}{3}\mathbf{Q}_6) \\ & + 4\mathbf{Q}_2^2 + 9\mathbf{Q}_3^2 + 16\mathbf{Q}_4^2 + 25\mathbf{Q}_5^2 + 36\mathbf{Q}_6^2]. \end{aligned}$$

With the adopted discretization Eq. (3.8),  $\mathbf{Q} = \mathbf{0}$  represents the (undeformed) initial shape. As can be noted, coupling of the individual modes is only attained via the non-linear stiffness terms. Moreover, the asymmetrical modes  $\mathbf{Q}_2, \mathbf{Q}_4, \dots$  are not excited directly by the loading and are only triggered if  $e/d \neq 0$  (assuming the initial conditions equal  $\mathbf{Q}(0) = \dot{\mathbf{Q}}(0) = \mathbf{0}$ ).



## 3.2 Static Buckling

First static buckling of the arch under a constant (time-invariant) acceleration  $\ddot{y}_p(t) = P$  [m/s<sup>2</sup>] is investigated. In order to follow the static buckling analysis presented in Section 2.2.1, the *constant* base-acceleration is included via the potential energy, resulting in the following *total* potential energy expression for the arch

$$\Pi = \mathcal{V} + \rho A \ddot{y}_p \int_0^L w \, dx, \quad (3.12)$$

with  $\mathcal{V}$  defined by Eq. (3.5). The static equilibrium equations follow from

$$\Pi_{,\mathbf{Q}} = \mathbf{K}(\mathbf{Q}) + \mathbf{B}P = 0, \quad (3.13)$$

Using a numerical path-following scheme, the evolution of static equilibrium points (obeying Eq. (3.13)) is studied for a varying quasi-static acceleration  $P$  (i.e. the load-path is computed). All presented load-paths are characterized by the following scalar measure

$$W_{\text{mid}}(t) = \frac{w(L/2, t) - w_0(L/2, t)}{\delta h}, \quad (3.14)$$

where  $\delta h$  is the distance between the unloaded upward stable equilibrium position and the unloaded downward stable equilibrium position measured at the mid-point (note that  $\delta h$  depends on  $a$ ). The time dependency of Eq. (3.14) is introduced since Eq. (3.14) will also be used for the dynamic analysis in the next section. Stability of the equilibrium states is assessed by evaluating the eigenvalues of the Hessian  $\Pi_{,\mathbf{Q}\mathbf{Q}} = \mathbf{K}(\mathbf{Q})_{,\mathbf{Q}}$  (see Section 2.2.1).

The load-path of the arch with  $a/h = e/d = 0$ , using the 6-DOF model Eq. (3.11), is depicted in Fig. 3.3-a. Starting at the unloaded initial state ( $W_{\text{mid}} = 0$ ), the slope of the obtained load-path for the quasi-static increasing load  $P$  varies and reaches a maximum at the limit-point [126]  $LP$  (the corresponding load is denoted with  $P_{LP}$ ). Due to the fact that all symmetric modes are directly forced by the loading (see Eq. (3.11)), the (symmetric) arch shape will change during loading, see Fig. 3.3-b. At a significantly lower load than the limit-point load  $P_{LP}$ , the initial load-path loses stability at the distinct bifurcation point  $B$  (the corresponding load is denoted with  $P_B$ ). In the secondary unstable load-path, which bifurcates from the initial load-path at point  $B$ , the first harmonic asymmetric arch shape becomes dominant. Three load-paths for the situation where  $e/d \neq 0$ , are depicted in Fig. 3.4-a. The deformed arch shapes for  $e/d = 0.5$  during loading are shown in Fig. 3.4-b. Clearly, the geometric imperfection initiates asymmetric deformations and introduces a new limit-point in the load-path. For  $e/d \rightarrow 0$ , the location of the limit-point for  $e/d \neq 0$  tends to the location of the bifurcation point  $B$  as

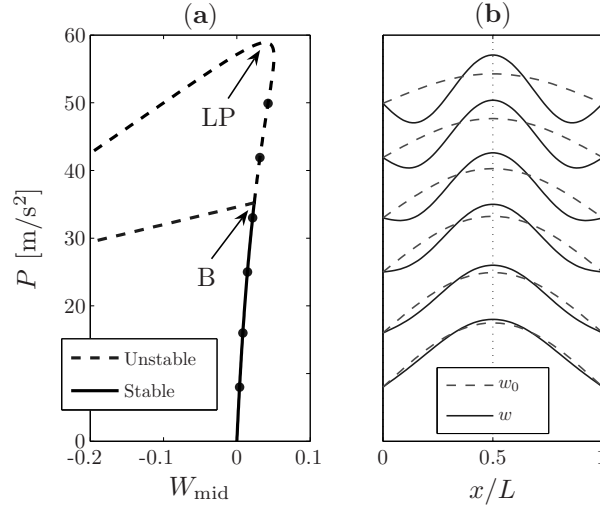


Figure 3.3: (Load-path for 6-DOF arch model with  $a/h = 0$  and  $e/d = 0$  (a), Shape of deformed arch (exaggerated) at indicated dots (b).

Table 3.2: Convergence bifurcation load ( $P_B$ ) and limit-point load ( $P_{LP}$ ) for  $a/h = e/d = 0$ .

$n$ (Eq. (3.8)):	2	3	6	12
$P_B$ [m/s <sup>2</sup> ]	35.323	35.219	35.219	35.219
$P_{LP}$ [m/s <sup>2</sup> ]	$2.3 \cdot 10^4$	58.913	58.908	58.907

found for  $e/d = 0$  (indicated in Fig. 3.4-a with the \*). In applications the arch will never be purely symmetric. Consequently, if in practise the arch would be quasi-statically loaded, the arch will exhibit snap-through buckling to a downward configuration ( $W_{\text{mid}} \approx -1$ ) at a load-level close to  $P_B$  (depending on the actual imperfection) and via an asymmetrical buckling mode.

The influence of the included number of DOFs in the semi-analytical model on the bifurcation load  $P_B$  and the limit-point load  $P_{LP}$  is shown in table 3.2. The results for the semi-analytical model do not change dramatically if more than 6 DOFs are used. As shown for the 6-DOF model in Fig. 3.3-b, the deformed arch shape shows clearly the presence of the third harmonic. The 2-DOF model does not include this mode, resulting in a highly overestimated  $P_{LP}$ , see table 3.2.

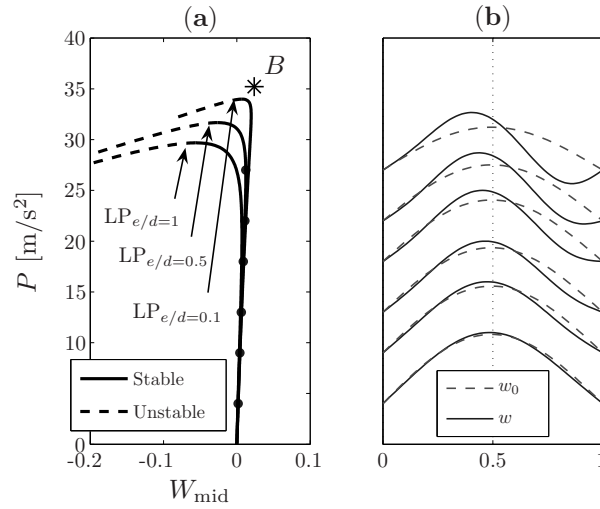


Figure 3.4: Load-path for 6-DOF arch model with  $a/h = 0$  and  $e/d \neq 0$  (a), Shape of deformed arch (exaggerated and only for  $e/d = 0.5$ ) at indicated dots (b).

The semi-analytical model is based on a number of assumptions. It does not include the effects of shear, axial and rotary inertia and some higher order terms are neglected in Eq. (3.1) due to the shallowness assumptions [42]. For validation of these assumptions, the results for the semi-analytical model with 6-DOF are compared with results obtained using a FE model which includes these effects, see Fig. 3.5. In this figure, the load-paths for two arches are compared; one for the perfect arch ( $e/d = 0$ ) to validate the limit-point load for the perfect arch ( $LP$  in Fig. 3.3-a) and one for an arch with a small geometric asymmetry ( $e/d = 0.1$ ) to validate the limit-point load for the imperfect arch ( $LP_{e/d=0.1}$  in Fig. 3.4-a). Both the FE model for the perfect arch and the FE model for the imperfect arch consist of twenty 3-node *Timoshenko* beam elements known as element type 45 [93]. In all FEM analyses kinematic relations are used which are valid for large displacements and moderate rotations.

The good agreement between the FEM results and the semi-analytical results supports the assumptions made for the semi-analytical model. It is noted that the negligible effect of shear also follows from the fact that FE analyses based on the less sophisticated *Euler/Bernoulli* beam theory (which corresponds closer to the adopted kinematics given by Eq. (3.1)), show practically the same results.

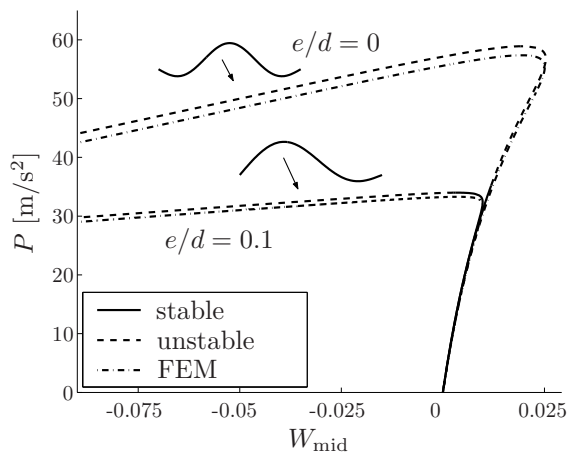


Figure 3.5: Comparison load-path FE model and 6-DOF arch model for  $a/h = 0$ .

As noted the bifurcation-buckling load  $P_B$  for  $e/d = 0$  dominates the static stability behaviour. Unfortunately, the bifurcation load  $P_B$  can hardly be influenced by varying the arch shape, as illustrated in Fig. 3.6. The bifurcation load can be increased by 6% (with respect to  $a/h = 0$ ) by setting the shape-factor to  $a/h = 0.097$ . For comparison with the results for dynamic pulse buckling in the next section, also the sensitivity of the secondary buckling load  $P_{LP}$  for  $e/d = 0$  with respect to the arch shape parameter  $a$  is examined. The limit-point load  $P_{LP}$  shows a distinct maximum at which the corresponding snap-through mode switches between the  $w$ -shape and the  $m$ -shape. With respect to the arch with  $a/h = 0$ ,  $P_{LP}$  can be increased by 40% by setting the shape-factor to  $a/h = 0.0384$  (a shape very close to the circular arch, see Section 3.1.1). However, observing the results of the quasi-static analysis, this secondary buckling load has no practical relevance.

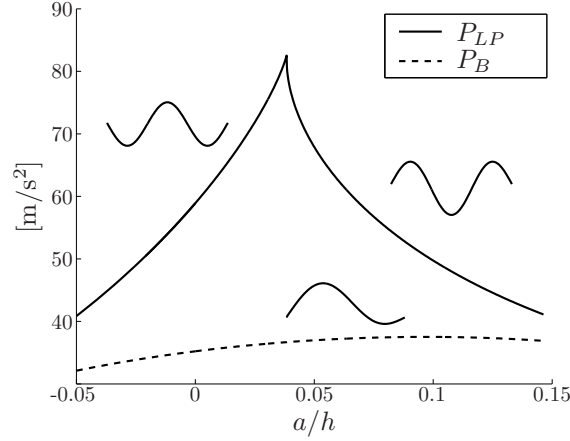


Figure 3.6: Influence of the arch shape on  $P_B$  and  $P_{LP}$  for  $e/d = 0$ .

### 3.3 Dynamic Pulse Buckling

In this section, dynamic buckling of the arch under shock loading is examined. First the loading and the approach used to analyze the dynamic buckling of the arch are discussed. Next the dynamic buckling of both the perfect arch and the imperfect arch are examined for various parameter variations. Finally, for generalization of the results, some arches with different dimensions are considered.

#### 3.3.1 Approach

The shock loading of the arch is modelled by a half-sine acceleration pulse, characterized by the pulse duration  $T_p$  and the maximum acceleration  $P$

$$\ddot{y}_p(t) = \begin{cases} P \sin\left(\frac{\pi t}{T_p}\right) & \text{if } 0 \leq t \leq T_p \\ 0 & \text{if } t > T_p \end{cases} . \quad (3.15)$$

After the arch is briefly loaded by the shock-load pulse, the arch is no longer subjected to external forces. Assuming that during the short interval  $0 \leq t \leq T_p$  no deformations occur ( $\mathbf{Q}(t) = \mathbf{0}$ ) and the effect of damping may be neglected, the only forces acting on the arch during this interval are the inertia forces due to the prescribed acceleration  $\ddot{y}_p(t)$ . Considering  $\dot{\mathbf{Q}}(0) = \mathbf{0}$ , the velocities just after the shock-pulse can be determined by using the impulse-momentum theorem, i.e.  $\dot{\mathbf{Q}}(T_p) = M^{-1} \int_0^{T_p} B \ddot{y}_p(t) dt = M^{-1} B \frac{2}{\pi} \lambda$  with only a single load

parameter

$$\lambda = PT_p \text{ [m/s]}. \quad (3.16)$$

Under the considered assumptions, the shock is imparted instantaneously into the structure as kinetic energy only. Relating this amount of kinetic energy to the level of potential energy at some saddle equilibrium point and neglecting the effect of damping, a lower bound for the dynamic pulse buckling load can be derived, see for example [53; 69; 121; 142]. However, application of the energy approach is not trivial for multi-DOF systems (such as considered in this chapter) and the established lower bound for the dynamic buckling load by the energy approach can be very conservative [63; 102]. Therefore, here the critical shock loads are determined by solving (numerically) the equations of motion for various values of the load. The Budiansky-Roth criterion [19; 21] will be used to define the dynamic buckling load, i.e. the load at which there exist a sudden jump in the response for small variation of the load parameter. In order to evaluate the time response, some scalar measure must be chosen. Here, the following measure is adopted

$$\widetilde{W}_{\text{mid}} = \max_{0 \leq t \leq T} |W_{\text{mid}}(t)|, \quad (3.17)$$

with  $W_{\text{mid}}(t)$  defined by Eq. (3.14) and  $T$  the total time-span considered. The parameter  $P$  is selected as load parameter to be varied. However, various (fixed) pulse durations  $T_p$  will be considered. The dynamic pulse buckling load is denoted with  $P_p$ . For the numerical integration of Eq. (3.11) in combination with Eq. (3.15), an integration routine based on an 8<sup>th</sup> order *Runge-Kutta* scheme with automatic step-size control [133] appeared to be very efficient. To absolutely assure that the shock-pulse energy is imparted correctly to the arch, the maximum step-size while  $0 \leq t \leq T_p$  is set to  $T_p/50$ . For all results a relative tolerance of  $TOL = 1 \cdot 10^{-8}$  is used.

Given the fact that little damping is taken into account, the energy in the structure imparted by the shock pulse decays for increasing time. Since a certain amount of energy is required for escape from the initial well, the time-span for dynamic buckling to occur is limited. Similar as in [63] and for the considered levels of damping, numerical simulations show that the occurrence of dynamic buckling of the pulse loaded arch (practically) always takes place in the time-span  $0 \leq t \leq 3T_1$ , where  $T_1$  is the period corresponding to the lowest eigenfrequency  $f_1$ . This time-span is, therefore, used for the numerical integration in all results, unless stated otherwise. Note that the time-span for dynamic buckling may become longer for lower levels of damping and that it can become considerably longer for step-loaded structures (also with small damping) [67; 70; 80].

The eigenfrequencies are determined by linearizing Eq. (3.11) around the unloaded upward configuration ( $\mathbf{Q} = 0$ ) and are in good correspondence with

Table 3.3: First two eigenfrequencies and modes for  $a/h = 0$  and  $e/d = 0$ .



mode shape		
$f_{1,2}$ 6-DOF [Hz]	10.88	24.51
$f_{1,2}$ FEM [Hz]	10.71	24.21

Table 3.4: Damping ratios of eigenmodes as listed in Table 3.3, for several values of  $b$ .

$b$ [Ns/m <sup>2</sup> ]	1	2	4
[Hz]	$\xi$ [-]	$\xi$ [-]	$\xi$ [-]
$f_1 = 10.88$	0.0453	0.0905	0.1810
$f_2 = 24.51$	0.0201	0.0402	0.0805

FEM results, see table 3.3. For the arch under consideration, the period corresponding to the lowest eigenfrequency for  $a/h = 0$  and  $e/d = 0$  appears to be  $T_1 \approx 0.1$  [s], see table 3.3. Note that the first eigenfrequency of the arch remains nearly constant for the considered range of the shape-factor  $a$ , see also [101; 112].

The damping ratios of the first two linear vibrational eigenmodes (see table 3.3) for the considered values of the viscous damping parameter  $b$ , are listed in table 3.4.

### 3.3.2 Perfect arch ( $e = 0$ )

As a reference first the results for perfect arches ( $e/d = 0$ ) are discussed. For this case, the asymmetrical modes ( $\mathbf{Q}_2, \mathbf{Q}_4, \mathbf{Q}_6$ ) are not triggered (see Section 3.1.2) and are therefore removed from Eq. (3.11). First the influence of damping is discussed for a pulse duration of  $T_p = 10$  [ms] and  $a/h = 0.04$ . As illustrated in Fig. 3.7, increasing the amount of damping results in an increasing dynamic pulse buckling load [50; 62; 79]. The dynamic pulse buckling loads ( $P_p$ ) can clearly be distinguished by the sudden jumps in the graphs. However, for the case with the lowest level of damping ( $b = 1$  [Ns/m<sup>2</sup>]), the boundary between the region where no dynamic buckling occurs and the region where dynamic buckling does occur, is not indicated by a single sudden jump in the response measure, but by a small transition region. In this region the

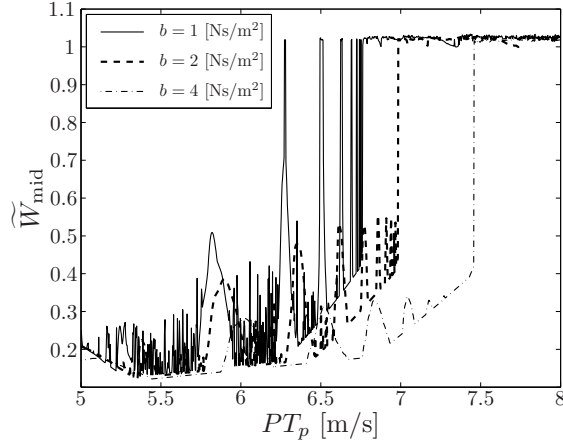


Figure 3.7: Influence of damping for  $T_p = 10$  [ms],  $e/d = 0$ ,  $a/h = 0.04$ .

occurrence of dynamic buckling is extremely sensitive to small variations in the load parameter as illustrated in Fig. 3.8. Note that the total time-span in Fig. 3.8 is extended from  $T = 0.3 (\approx 3T_1)$  [s] to  $T = 2.0$  [s] and the sensitivity is thus not due to a too short integration time. Furthermore, the complex transitions are also found using a model with 3 additional symmetrical modes ( $\mathbf{Q}_7 \sin(7\pi x/L)$ ,  $\mathbf{Q}_9 \sin(9\pi x/L)$  and  $\mathbf{Q}_{11} \sin(11\pi x/L)$ ), see Fig. 3.9. Indeed, the sudden jumps do not occur exactly at the same values of  $PT_p$ . However, the differences between the load values where the sudden jumps occur do not differ more than 3% and qualitatively the transitions are similar. It is noted that the complex transition only occurs in the region around  $a/h \approx 0.05$  (which will appear to be approximately the optimal shape of the arch with respect to dynamic pulse buckling) and only for a low level of damping (see also Fig. 3.7). Similar load-parameter sensitivities in transient analyses are reported in [59; 67; 128].

The influence of the arch shape on the dynamic buckling load is illustrated in Fig. 3.10 for various pulse durations and  $b = 2$  [Ns/m<sup>2</sup>]. Clearly, the shape of the arch has a distinct influence on the dynamic pulse buckling load for the perfect arch (the dynamic buckling load increases approximately 50% by changing the arch shape from  $a/h = 0$  to  $a/h = 0.04$ ). The arch shape during dynamic buckling is illustrated in Fig. 3.11. Similar as for the secondary static buckling mode (see  $P_{LP}$  in Fig. 3.6), the arch buckles for  $a/h = 0$  via a  $w$ -shape and for  $a/h = 0.08$  via a  $m$ -shape. Furthermore, in Fig. 3.10 the dynamic buckling loads are presented in terms of the product  $PT_p = \lambda$  (see Eq. (3.16)) allowing to examine the mutual relation between  $P$  and  $T_p$  with respect to



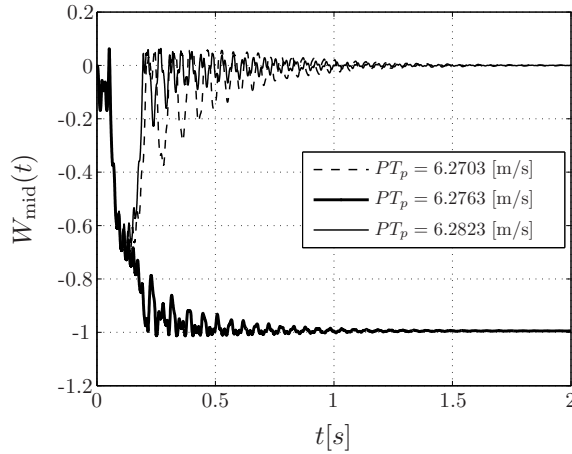


Figure 3.8: Load-parameter sensitivity of the occurrence of dynamic buckling for  $b = 1$  [Ns/m<sup>2</sup>],  $T_p = 10$  [ms],  $e/d = 0$ ,  $a/h = 0.04$ .

the dynamic pulse buckling load. As can be noted, the stability boundaries for the various pulse durations do not coincide perfectly and, therefore, if the parameters  $P$  and  $T_p$  are varied independently, the dynamic pulse buckling load does not scale exactly with the parameter  $\lambda$ . Still, the results for the various pulse durations match qualitatively, that is for each value of  $T_p$  the dynamic buckling load shows a comparable sensitivity to variations in the arch shape.

The optimal arch shape with respect to the secondary static buckling load  $P_{LP}$  ( $a/h \approx 0.04$ , see Fig. 3.6) and the optimal arch shape with respect to dynamic pulse buckling load  $P_p$  ( $a/h \approx 0.05$ , see Fig. 3.10) do not exactly match. Nevertheless, there seems to be a correspondence between the sensitivities of these two critical loads with respect to the arch shape parameter  $a$ . Although the (symmetric) buckling mode corresponding to the secondary static buckling  $P_{LP}$  and the (symmetric) deformations occurring during the dynamic pulse buckling for  $e/d = 0$  show similarities, the correspondence in sensitivity of these two critical loads with respect to  $a$  is not trivial. After all, in the case of dynamic pulse buckling, transient inertia and damping forces are taken into account which are absent in the quasi-static buckling case.

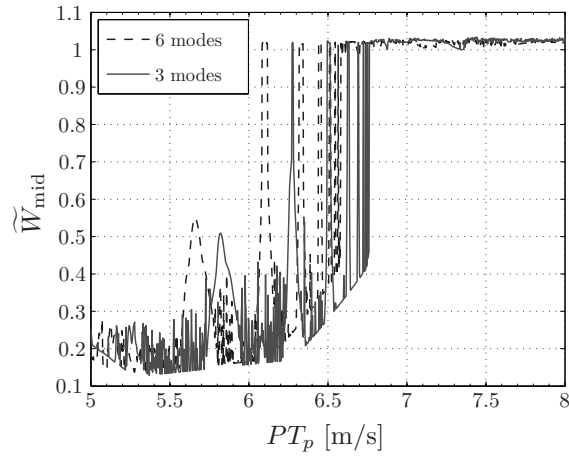


Figure 3.9: Influence of the number of (symmetrical) modes on the occurrence of dynamic buckling for  $T_p = 10$  [ms],  $b = 1$  [Ns/m<sup>2</sup>],  $e/d = 0$  and  $a/h = 0.04$ .

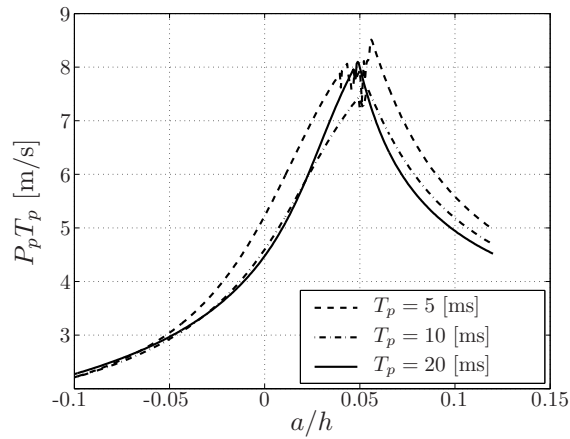


Figure 3.10: Dynamic stability boundary for various pulse durations,  $b = 2$  [Ns/m<sup>2</sup>] and  $e/d = 0$ .

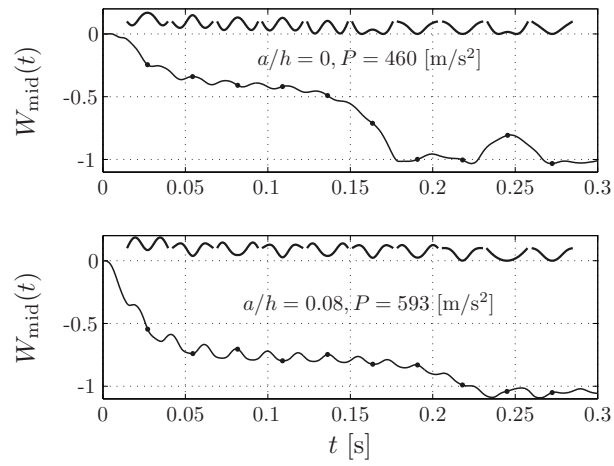


Figure 3.11: Arch-shape during dynamic buckling for  $T_p = 10$  [ms],  $b = 2$  [Ns/m<sup>2</sup>],  $e/d = 0$ .

### 3.3.3 Imperfect arch ( $e \neq 0$ )

Next, dynamic buckling of imperfect arches will be examined. For this analysis, the complete 6-DOF model Eq. (3.11) will be used, since asymmetrical deformations will occur for  $e/d \neq 0$ . In Fig. 3.12, the influence of a small imperfection on the dynamic buckling load is illustrated. The dynamic pulse buckling load shows a mild sensitivity to small geometric imperfections. The arch shape during dynamic buckling for  $P$  just exceeding  $P_p$  is illustrated in Fig. 3.13. Clearly, for  $e/d \neq 0$  the arch shape shows asymmetric deformations during dynamic buckling.

The influence of the arch shape on the dynamic pulse buckling load for  $e/d = 0$  and  $e/d = 1$  is compared in Fig. 3.14. For the depicted range of the shape-factor  $a$ , the dynamic buckling load decreases only with maximally 10% for the moderate imperfection of  $e/d = 1$  (compared to the case  $e/d = 0$ ). The distinct maximum in the dynamic buckling load as found around  $a/h \approx 0.05$  seems to be insensitive to the geometric imperfection. Similar stability boundaries, also with a maximum close to  $a/h \approx 0.05$ , are found at the lower level of damping  $b = 1$  [Ns/m<sup>2</sup>]. Consequently, also for the practical situation where  $e/d \neq 0$ , the arch shape has a distinct influence on the dynamic buckling load. Furthermore, since the dynamic stability boundaries do not change dramatically due the presence of imperfections they show again a clear qualitative correspondence with the secondary static buckling load for the perfect arch  $P_{LP}$  (see Fig. 3.6). For the imperfect arch this correspondence is even less expected as for the

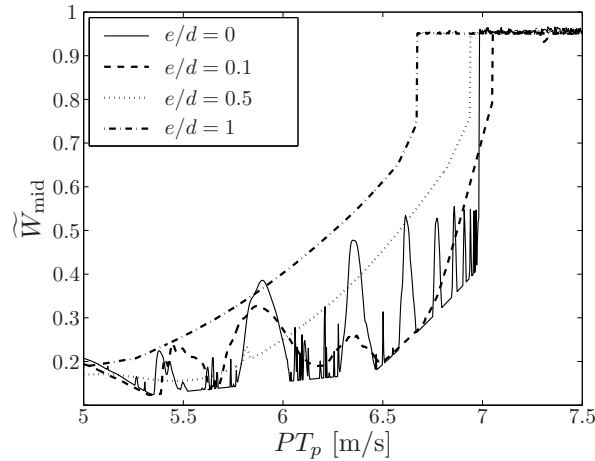


Figure 3.12: Influence of imperfections for  $a/h = 0.04$ ,  $b = 2$  [Ns/m<sup>2</sup>],  $T_p = 10$  [ms].

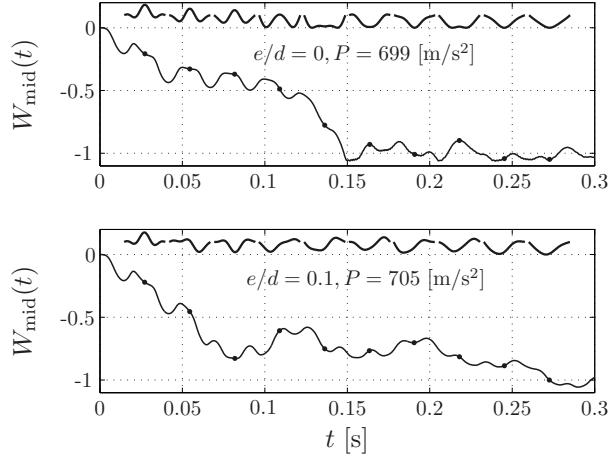


Figure 3.13: Arch-shape during dynamic buckling for  $T_p = 10$  [ms],  $b = 2$  [Ns/m<sup>2</sup>],  $a/h = 0.04$ .

perfect case, since now the arch buckles dynamically via an asymmetric mode whereas the secondary static buckling corresponds to a symmetrical buckling mode. This correspondence, however, could be very useful for shape parameter sensitivity studies based on quasi-static analyses. After all, compared to the nonlinear transient dynamic buckling analysis, the quasi-static analysis is computationally significantly less expensive. However, more research on the found correspondence will be necessary before it can be generalized.

For validation, dynamic pulse buckling results computed with the 6-DOF semi-analytical model (Eq. (3.11)) are compared with FEM results. For the nonlinear dynamical transient FE analyses, the same FE models are used as discussed in Section 3.2. However, now obviously also inertial and damping forces are taken into account. In the FE model, viscous damping is introduced via *Rayleigh* damping, i.e. the damping matrix is composed as  $C = \alpha K + \beta M$ , where  $K$  and  $M$  are the (linear) stiffness and consistent mass matrix of the FE model, respectively. Obviously, the Rayleigh damping model is different from the damping model (Eq. (3.3)) as incorporated in 6-DOF model (Eq. (3.11)). In order to obtain a comparable level of damping in the FE model,  $\alpha$  and  $\beta$  are tuned [29] so that  $\xi_{1,2}$  (the damping ratios of the first two vibrational eigenmodes) of the FE model are equal to  $\xi_{1,2}$  of the 6-DOF model for  $b = 1$  [Ns/m<sup>2</sup>] (see table 3.4) resulting in  $\alpha = 9.85 \cdot 10^{-7}$  [s] and  $\beta = 6.092$  [s<sup>-1</sup>]. Both models predict a slight increase in the dynamic pulse buckling load if

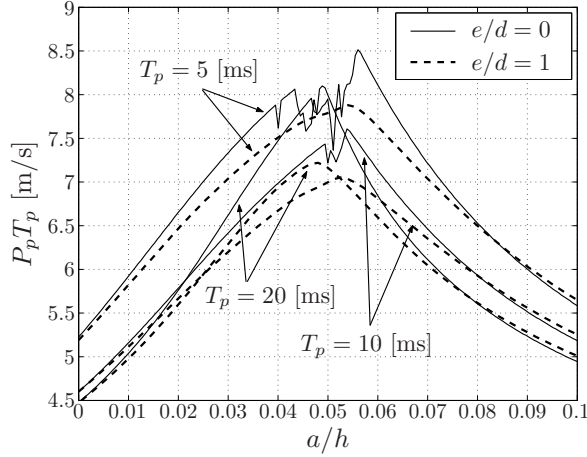


Figure 3.14: Influence of an imperfection on dynamic stability boundary for  $b = 2$  [Ns/m<sup>2</sup>] and various values for  $T_p$ .

Table 3.5: Dynamic buckling loads  $P_p$  as computed for 6-DOF model and FE model for  $a/h = 0$ ,  $b = 1$  [Ns/m<sup>2</sup>] and  $T_p = 20$  [ms].

$e/d$ [-]	0	0.1
6-DOF $P_p$ [m/s <sup>2</sup> ]	211.4	212.9
FEM $P_p$ [m/s <sup>2</sup> ]	206.9	208.8

a small imperfection ( $e/d = 0.1$ ) is incorporated in the arch shape, see table 3.5. Time histories or values of  $P$  near the dynamic pulse buckling load for  $e/d = 0.1$  are compared in Fig. 3.15. Note that in the FE model, next to shear also rotary and axial inertia are included which are not included in the 6-DOF model. Given the good agreement between the semi-analytical results and the FEM results, it is shown that these effects are indeed negligible.

### 3.3.4 Other arches

As a first step towards generalization of the results found so far, the influence of the arch shape on the dynamic pulse buckling load is examined for a number of variations in the arch dimensions. Only the initial height  $h$  and the thickness  $d$  will be varied while leaving the other parameters unchanged to the values as listed in table 3.1. For comparison, the height and thickness are scaled as  $\bar{h} = h/h^*$  and  $\bar{d} = d/d^*$ , where  $h^*$  and  $d^*$  are the height and thickness of the

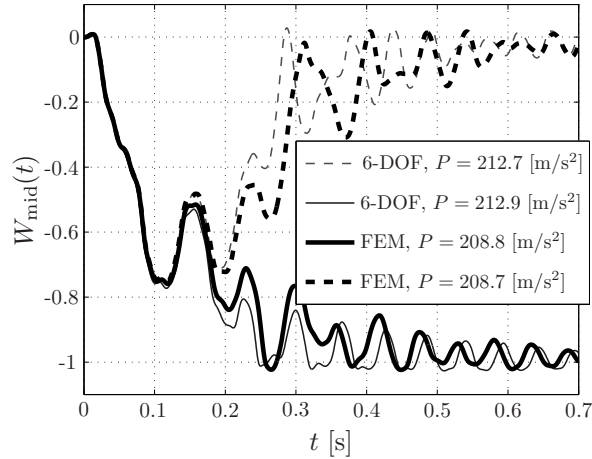


Figure 3.15: Comparison of time responses of 6-DOF model and FE model for  $a/h = 0$ ,  $b = 1$  [Ns/m<sup>2</sup>],  $e/d = 0.1$  and  $T_p = 20$  [ms].

original arch (see table 3.1) respectively. Furthermore, only one pulse duration is considered ( $T_p = 10$  [ms]) and the relative damping ratios  $\xi_i$  are set to the values for the original arch for  $b = 1$  [Ns/m<sup>2</sup>] (see table 3.4).

Considering  $e/d = 0$ , the sensitivities of the bifurcation buckling load  $P_B$  and the secondary limit-point load  $P_{LP}$  with respect to the arch shape parameter  $a$ , are compared in Fig. 3.16-a for the arch with double height ( $\bar{h} = 2$ ,  $\bar{d} = 1$ ), for the arch with double thickness ( $\bar{h} = 1$ ,  $\bar{d} = 2$ ) and for the original arch ( $\bar{h} = 1$ ,  $\bar{d} = 1$ ). The sensitivities of  $P_B$  and  $P_{LP}$  with respect to the shape parameter  $a$  are qualitatively similar. Quantitatively, for a double initial height, the critical loads (approximately) double, whereas for a double thickness, the critical loads (approximately) quadruplicate. Doubling the height of the arch does hardly affect the first two eigenfrequencies, whereas doubling the thickness of the arch doubles the first two eigenfrequencies. For both cases the corresponding eigenmodes are not affected. The dynamic stability boundaries for the three arches under consideration are compared in Fig. 3.16-b for  $e/d = 0.5$ . From these comparisons, the following observations can be made: 1) for all three (imperfect) arches, the arch shape has a distinct influence on the dynamic buckling load with a maximum around  $a/h = 0.05$  and 2) the dynamic pulse buckling loads for the arches with  $\bar{h} = 2, \bar{d} = 1$  and  $\bar{h} = 1, \bar{d} = 2$  are approximately the same, whereas their static buckling loads show a factor two in difference. This last observation may be explained by the fact that for the

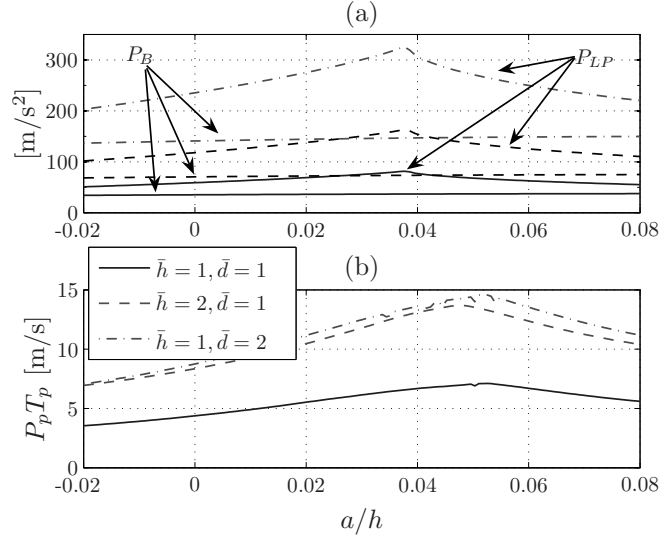


Figure 3.16: Influence of the arch shape on  $P_B$  and  $P_{LP}$  for  $e/d = 0$  (a) and on  $P_p$  for  $e/d = 0.5$  (b).

arch with  $\bar{h} = 2, \bar{d} = 1$ , the relative pulse duration  $T_p/T_1$  (with  $T_1$  the period of the lowest eigenfrequency) is not altered (with respect to the original arch), whereas for the arch with  $\bar{h} = 1, \bar{d} = 2$  this ratio doubles. As shown, the dynamic pulse buckling load approximately scales with the parameter  $\lambda$  (Eq. (3.16)), meaning that doubling the pulse duration, approximately halves the dynamic pulse buckling load  $P_p$ .

Snap-through buckling of perfect sinusoidal arches ( $a/h = 0$ ) due to shock loading is only possible for  $h/r > 4$  (where  $r^2 = I/A = d^2/12$ ) [51; 121]. After all, for heights  $h/d < 4/\sqrt{12} \approx 1.15$ , there is only one unloaded stable equilibrium state, making a sudden jump to the secondary stable equilibrium state at  $W_{\text{mid}} = -1$  impossible. By introducing an imperfection, the minimum height for which the second stable equilibrium state of the arch exists increases. For example, for  $e/d = 0.5$  and  $a/h = 0$ , the secondary stable equilibrium state of the unloaded arch ceases to exist at  $h/d = 3.6$  ( $\bar{h} \approx 0.075$ ). In Fig. 3.17,  $P_B$  and  $P_{LP}$  for  $e/d = 0$  and the dynamic stability boundaries for  $e/d = 0.5$  are compared for arches with thickness  $\bar{d} = 1$  and nine heights equidistantly distributed in the range  $0.08 \leq \bar{h} \leq 0.38$ . In this figure, the maxima for  $P_B$ ,  $P_{LP}$  and  $P_p$  are indicated with  $\diamond$ ,  $\times$  and  $\circ$ , respectively. In the considered region of heights, the first two eigenfrequencies and eigenmodes remain nearly the same as for the original arch. As can be noted, for decreasing  $\bar{h}$ , the



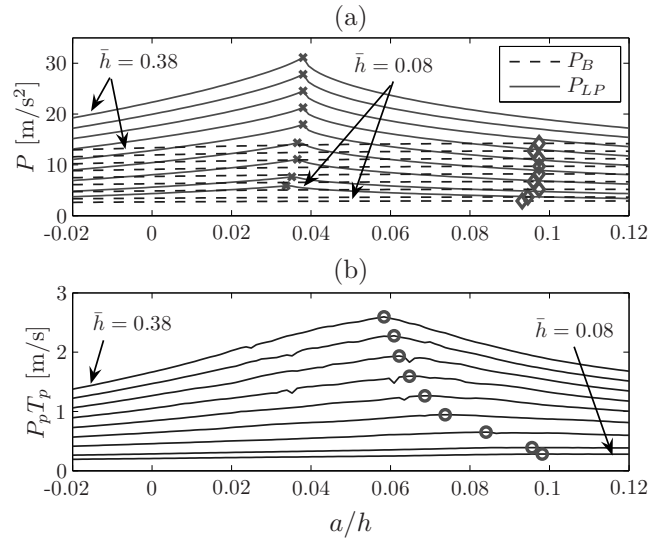


Figure 3.17: Influence of the arch shape on  $P_B$  and  $P_{LP}$  for  $e/d = 0$ ,  $\bar{d} = 1$  and  $0.08 \leq \bar{h} \leq 0.38$  (a) and on  $P_p$  for  $e/d = 0.5$  and  $T_p = 10$  [ms] (b).

optimal arch shape with respect to dynamic pulse buckling shifts from the optimal arch shape with respect to the secondary static buckling load  $P_{LP}$  towards the optimal arch shape with respect to the first static buckling load  $P_B$ . Consequently, for the considered dimensions and level of imperfection, the correspondence between the secondary static buckling load and the dynamic pulse buckling load seems to be restricted to arches with  $h/d > 20$  ( $\bar{h} > 0.4$ ). However, for generalization of this result more research is required.

### 3.4 Conclusions

The objective of this chapter is to study the influence of the arch shape on the dynamic pulse buckling load for thin shallow arches under shock loading and to compare parameter sensitivities of static and dynamic buckling loads. Based on an approximate nonlinear kinematic model, a multi-DOF model of the arch is derived. The model includes a shape-factor by which the arch shape (the initial curvature) can be varied while keeping the initial height of the arch unchanged and an imperfection parameter which controls the amplitude of an asymmetry in the arch shape. By comparing quasi-static responses, modal analysis results and nonlinear dynamical transient analysis results of this model with FEA results based on Timoshenko beam theory, the model is validated.

First static snap-through buckling of the arch under a quasi-static varying acceleration is considered. The primary static buckling load of the arch for this load-case corresponds to an asymmetrical buckling mode and can hardly be influenced by varying the arch shape. The arch shape has significant influence on the secondary buckling load corresponding to a limit-point in the load-path of the perfect arch.

The dynamic response of the arches under shock loading is studied by numerically solving the equations of motion. The dynamic buckling load is determined for various levels of damping, shock pulse durations, imperfection amplitudes, and a wide range of arch shapes. The shape of the arch (with or without an imperfection) has a significant influence of the dynamic pulse buckling load. Furthermore, the sensitivity of the dynamic buckling load with respect to the arch shape shows a clear maximum. Depending on the level of damping, the imperfection amplitude and the arch shape, the occurrence of dynamic buckling can be extremely sensitive to small variations in the load parameter. Small geometric imperfections have only a mild effect on the dynamic pulse buckling load and do not significantly change the sensitivity of the dynamic pulse buckling load with respect to the arch shape parameter.

Although the optimal arch shape with respect to the secondary static buckling load and the optimal arch shape with respect to dynamic pulse buckling load do not match exactly, there exists a quantitative correspondence between the arch shape sensitivities of these two critical loads. This correspondence is not trivial but could be very useful for shape parameter sensitivity studies of the dynamic pulse buckling load using quasi-static analyses. After all, compared to the nonlinear transient dynamic buckling analysis, the quasi-static analysis is computationally significantly less expensive. The correspondence between the secondary static load and the dynamic pulse buckling load is also found for arches with other dimensions. However, as shown, more research on the found correspondence will be necessary before it can be generalized.

## *Periodic Excitation of a Buckled Beam*

**B**uckled beam structures are frequently encountered in engineering practice, e.g. in MEMS [18; 25; 115] (see also Fig. 1.4), in vibration isolators [139] and in motion amplifiers [61]. Buckled beam structures may possess multiple coexisting stable equilibrium states. Consequently, when subjected to a periodic transversal excitation, buckled beam structures may exhibit severe vibrations which encircle two or more equilibrium states, i.e. snap-through motions.

In this chapter, the steady-state behaviour of a transversally excited, pinned-pinned buckled beam will be investigated using a semi-analytic approach. Compared to papers with similar research interest [36; 37; 60; 72; 73], this research will be focused on higher order approximations of the exact kinematics of the inextensible beam. Both single-mode as well as multi-mode models will be considered. Furthermore, not only phase space plots will be analyzed, but also frequency-amplitude plots and the effect of parameter variations will be investigated. Moreover, semi-analytic results are compared with results from FEM analyses.

The outline for this chapter is as follows. In the next section, the considered beam structure will be introduced, the equations of motion for three discretization cases will be derived and a FE model of the beam structure will be introduced. In Section 4.2, the convergence of the static postbuckling response and the lowest eigenfrequencies of the several discretized and higher order models will be investigated and results will be compared with FEM results. The steady-state nonlinear dynamical behaviour of the buckled beam structure will be investigated in Section 4.3. Frequency-amplitude plots will be calculated with a numerical continuation technique. Dynamically interesting areas (bifurcation points, routes to chaos, snap-through regions) will be analyzed using phase space plots and Poincaré plots. Also the influence of some parameters on the frequency-amplitude plots will be investigated. In Section 4.4, nonlinear dynamic responses obtained with the semi-analytic approach, will be compared with FEM results. Finally, in Section 4.5 conclusions will be given.

---

Parts of this chapter are also presented in [99] and [100].

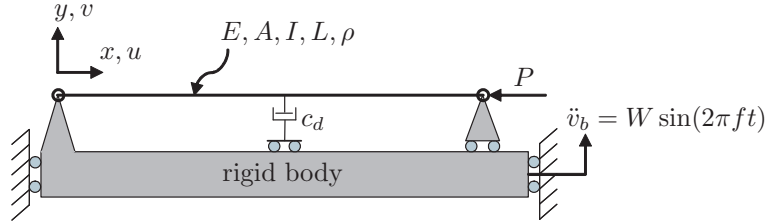


Figure 4.1: Transversally excited pinned-pinned prestressed beam.

### 4.1 Modelling of the beam structure

The axially pre-stressed pinned-pinned beam which is harmonically excited in transversal direction is depicted in Fig. 4.1. The beam has length  $L$ , cross-section  $A$ , modulus of elasticity  $E$ , area moment of inertia  $I$  and density  $\rho$ . The 2D in-plane case is considered. Gravity forces are neglected (vibrations are in the horizontal plane) and the supporting body is considered to be rigid. Since the beam is considered to be thin ( $h \ll L$ ), the effect of shear is neglected. Furthermore, since the end point of the beam at  $x = L$  is allowed to move freely in axial direction, the axial strain will be small and the displacements of the beam will be dominated by changes in curvature. These considerations allow to assume the beam to be inextensible. In this analysis no imperfections are taken into account, i.e. the beam is considered to be initially perfectly straight. In the next chapter (Section 5.1), more details will be given on how imperfections can be taken into account in the model of the inextensible beam. The beam is statically loaded by an axial force  $P$  at the right end, which is chosen to exceed the *Euler* buckling load

$$P_e = \frac{\pi^2 EI}{L^2}, \quad (4.1)$$

of the beam. Furthermore, the beam is harmonically excited in transversal direction by a prescribed acceleration  $\ddot{v}_b(t) = W \sin(2\pi ft)$ , where  $W$  [ $\text{m/s}^2$ ] is the amplitude and  $f$  [Hz] the excitation frequency. Finally, a linear dashpot with damping constant  $c_d$  in [ $\text{Ns/m}$ ] is connected between the middle of the beam and the rigid body.

The axial displacement field of the beam is indicated by  $u(t, x)$  and the transversal displacement field (measured relatively with respect to  $v_b(t)$ ) is indicated by  $v(t, x)$ . Due to the inextensibility assumption, the axial displacement field is coupled to the transversal displacement field by the following nonlinear relation [66]

$$u_{,x} = \sqrt{1 - (v_{,x})^2} - 1. \quad (4.2)$$

The exact curvature of the inextensible beam is defined by [66]

$$\kappa = -\frac{v_{,xx}}{\sqrt{1 - (v_{,x})^2}}. \quad (4.3)$$

Equations (4.2) and (4.3) can not be symbolically integrated. Therefore, these expressions are approximated by their Taylor series expansions in  $v_{,x}$  up to  $n^{\text{th}}$  order. For example, the 3<sup>rd</sup> order expansions of Eq. (4.2) and Eq. (4.3) yield

$$u_{,x} \approx -\frac{1}{2}(v_{,x})^2, \quad (4.4)$$

$$\kappa \approx -v_{,xx} \left(1 + \frac{1}{2}(v_{,x})^2\right). \quad (4.5)$$

The boundary conditions for the transversal displacement field of the pinned-pinned beam (see Fig. 4.1) are:  $v(t,0) = v(t,L) = 0$  and  $v(t,0)_{,xx} = v(t,L)_{,xx} = 0$  (reaction moments are zero). Each of the following modes

$$v_i(x) = \sin \frac{i\pi x}{L}, \quad i = 1, 2, \dots, \quad (4.6)$$

obeys a priori these conditions. The modes  $v_i(x)$  are the linear buckling modes of the pinned-pinned beam [66]. Based on Eq. (4.6), the transversal displacement field is discretized as

$$v(t,x) = \sum_{i=1}^N \mathbf{Q}_i(t) \cdot v_i(x). \quad (4.7)$$

The DOFs  $\mathbf{Q}_i$  [m] are collected in  $\mathbf{Q} = [\mathbf{Q}_1, \dots, \mathbf{Q}_N]^T$ . Taking into account the boundary condition  $u(t,0) = 0$ , the axial displacement field  $u(t,x)$ , corresponding to Eq. (4.7), can be computed by integrating the  $n^{\text{th}}$  order approximation of Eq. (4.2). Utilizing the resulting expression for  $u$  and the  $n^{\text{th}}$  order approximations of  $u_{,x}$  and  $\kappa$ , the kinetic energy  $\mathcal{T}$  and the potential energy  $\mathcal{V}$  are determined by

$$\mathcal{T}(\mathbf{Q}, \dot{\mathbf{Q}}) = \frac{1}{2}\rho A \int_0^L \left[ \alpha \dot{u}^2 + (\dot{v} + \dot{v}_b)^2 \right] dx, \quad (4.8)$$

$$\mathcal{V}(\mathbf{Q}) = \int_0^L \left[ \frac{1}{2}EI\kappa^2 + Pu_{,x} \right] dx. \quad (4.9)$$

Note that by setting  $\alpha = 0$  in Eq. (4.8), the effect of axial inertia is neglected whereas for  $\alpha = 1$ , the effect of axial inertia is included. Inclusion of the axial inertia leads to inertia nonlinearities in the final equations of motion. The

effect of including axial inertia on the dynamic steady-state response will be discussed in Section 4.4. The effect of rotatory inertia is neglected in the semi-analytical model.

The damping forces due to the discrete viscous dash-pot with damping constant  $c_d$  [Ns/m] are derived using the Rayleigh dissipation function [90]

$$\mathcal{R}(\mathbf{Q}, \dot{\mathbf{Q}}) = \frac{1}{2}c_d (\dot{v}(t, L/2))^2. \quad (4.10)$$

The equations of motion are derived via *Lagrange's* equations

$$\frac{d}{dt}\mathcal{T}_{,\dot{\mathbf{Q}}} - \mathcal{T}_{,\mathbf{Q}} + \mathcal{V}_{,\mathbf{Q}} = -\mathcal{R}_{,\dot{\mathbf{Q}}_i}. \quad (4.11)$$

For consistency, all terms in  $\mathbf{Q}_i$  higher than  $n^{\text{th}}$  order in Eq. (4.11) are omitted.

In general, the (set of) equation(s) of motion corresponding to an  $n^{\text{th}}$  order approximation of Eq. (4.2) and Eq. (4.3) are derived by the following steps

1. Discretize  $v(t, x)$  as in Eq. (4.7) with one or more modes.
2. Approximate  $u_{,x}$  and  $\kappa$  (Eq. (4.2) and Eq. (4.3)) with Taylor expansions including terms up to  $n^{\text{th}}$  order in  $v_{,x}$ .
3. Solve  $u(t, x)$  from the  $n^{\text{th}}$  order approximation of  $u_{,x}$  by symbolic integration (this step is only necessary if axial inertia is included, i.e.  $\alpha = 1$  in Eq. (4.8)).
4. Compute the energy expressions Eq. (4.8) and Eq. (4.9) by symbolic integration and evaluate Rayleigh dissipation function Eq. (4.10).
5. Derive the equations of motion using Lagrange equations Eq. (4.11) and omit all terms in  $\mathbf{Q}_i$  higher than  $n^{\text{th}}$  order.

#### 4.1.1 Three discretization cases

During the static and dynamical analyses, three discretization cases will be considered and compared. To illustrate some key features of the equation(s) of motion they will be shown for the case of third order expansions of  $u_{,x}$  and  $\kappa$  (see Eq. (4.4) and Eq. (4.5)) and no axial inertia ( $\alpha = 0$  in Eq. (4.8)).

In Case *I* only the first buckling mode will be considered (i.e.  $N = 1$  in Eq. (4.7)). This results in the following equation of motion

$$M\ddot{\mathbf{Q}}_1 + C\dot{\mathbf{Q}}_1 + K_{1,1}\mathbf{Q}_1 + K_{1,3}(\mathbf{Q}_1)^3 = -B \sin(2\pi ft). \quad (4.12)$$

Table 4.1: Coefficients of discrete equations of motion.

$K_{1,1}$	$= \frac{\pi^2}{2L^4} (P_e - P)$	$K_{2,1}$	$= \frac{2\pi^2}{L} (4P_e - P)$	$K_{3,1}$	$= \frac{9\pi^2}{2L} (9P_e - P)$
$K_{1,3}$	$= \frac{\pi^4}{4L^3} P_e$	$K_{2,3}$	$= \frac{16\pi^4}{L^3} P_e$	$K_{3,3}$	$= \frac{729\pi^4}{4L^3} P_e$
$M$	$= \frac{1}{2}\rho AL$	$K_{12,12}$	$= \frac{5\pi^4}{L^3} P_e$	$K_{13,12}$	$= \frac{45\pi^4}{2L^3} P_e$
$C$	$= c_d$	$K_{12,21}$	$= \frac{5\pi^4}{L^3} P_e$	$K_{13,21}$	$= \frac{9\pi^4}{4L^3} P_e$
$B$	$= 2\rho AW \frac{L}{\pi}$				

The coefficients in Eq. (4.12) are defined in Table 4.1. Note that the linear stiffness parameter  $K_{1,1}$ , depends on the axial load  $P$ . Equation (4.12) is also known as the damped forced Duffing equation [123; 128].

Case *II* will also take the second mode into account (i.e.  $N = 2$  in Eq. (4.7)). In Section 4.3, it will be shown that the influence of the second buckling mode is negligible. Therefore, in Case *III* the second buckling mode will be neglected and the first and third buckling mode will be considered (i.e.  $N = 3$  in Eq. (4.7) and setting  $\mathbf{Q}_2 = 0$ ). For the two-DOF Cases *II* and *III*, the equations of motion may be written in a more general form

$$\mathbf{M}\ddot{\mathbf{Q}} + \mathbf{C}\dot{\mathbf{Q}} + \mathbf{K}\mathbf{Q} + \mathbf{K}_{\text{nl}}(\mathbf{Q}) = \mathbf{B} \sin(2\pi ft), \quad (4.13)$$

where  $\mathbf{M}$  is the mass matrix,  $\mathbf{C}$  the damping matrix,  $\mathbf{K}$  the linear stiffness matrix,  $\mathbf{K}_{\text{nl}}$  the column with nonlinear restoring forces and  $\mathbf{B} \sin(2\pi ft)$  the external forces column. For these two cases, the following expressions hold:

Case *II* ( $\mathbf{Q} = [\mathbf{Q}_1, \mathbf{Q}_2]^T$ ):

$$\begin{aligned} \mathbf{M} &= \begin{bmatrix} M & 0 \\ 0 & M \end{bmatrix}, \quad \mathbf{C} = \begin{bmatrix} C & 0 \\ 0 & 0 \end{bmatrix}, \quad \mathbf{K} = \begin{bmatrix} K_{1,1} & 0 \\ 0 & K_{2,1} \end{bmatrix}, \\ \mathbf{K}_{\text{nl}} &= \begin{bmatrix} K_{1,3}(\mathbf{Q}_1)^3 + K_{12,12}\mathbf{Q}_1(\mathbf{Q}_2)^2 \\ K_{2,3}(\mathbf{Q}_2)^3 + K_{12,21}(\mathbf{Q}_1)^2\mathbf{Q}_2 \end{bmatrix}, \quad \mathbf{B} = \begin{bmatrix} -B \\ 0 \end{bmatrix}, \end{aligned} \quad (4.14)$$

Case *III* ( $\mathbf{Q} = [\mathbf{Q}_1, \mathbf{Q}_3]^T$ ):

$$\begin{aligned} \mathbf{M} &= \begin{bmatrix} M & 0 \\ 0 & M \end{bmatrix}, \quad \mathbf{C} = \begin{bmatrix} C & -C \\ \frac{1}{3}C & -\frac{1}{3}C \end{bmatrix}, \quad \mathbf{K} = \begin{bmatrix} K_{1,1} & 0 \\ 0 & K_{3,1} \end{bmatrix}, \\ \mathbf{K}_{\text{nl}} &= \begin{bmatrix} K_{1,3}(\mathbf{Q}_1)^3 + K_{13,12}\mathbf{Q}_1(\mathbf{Q}_3)^2 + K_{13,21}(\mathbf{Q}_1)^2\mathbf{Q}_3 \\ 3K_{1,3}(\mathbf{Q}_1)^3 + K_{3,3}(\mathbf{Q}_3)^3 + K_{13,12}\mathbf{Q}_3(\mathbf{Q}_1)^2 \end{bmatrix}, \\ \mathbf{B} &= \begin{bmatrix} -B \\ -\frac{1}{3}B \end{bmatrix}, \end{aligned} \quad (4.15)$$

with coefficients as defined in Table 4.1. The main differences between both models are obvious. The two ODEs for Case *II* are only coupled by the

Table 4.2: Simulation parameters (\* only used the FE model).

Parameter	Value	Unit
$\rho$	7850	$[kg/m^3]$
$E$	$2.1 \cdot 10^{11}$	$[N/m^2]$
$\nu^*$	0.3	$[-]$
$L$	1	$[m]$
$A$	$4 \cdot 10^{-4}$	$[m^2]$
$I$	$1.3 \cdot 10^{-8}$	$[m^4]$
$c_d$	8.3	$[Ns/m]$

nonlinear restoring forces  $\mathbf{K}_{nl}$  and only the first ODE is driven. The two ODEs for Case *III* are coupled by both the viscous damping terms  $\mathbf{BQ}$  and  $\mathbf{K}_{nl}$ , and both ODEs are driven.

#### 4.1.2 Finite element model

The numerical results for the analytic models will be compared with FEA carried out with MSC.Marc. The FE-model used consists of one-hundred, three-node linear elastic *Timoshenko* beam elements (element type 45, see [93]), which allow transverse shear as well as axial straining in addition to bending. During each analysis, an updated Lagrange procedure is used and kinematic relations are used which are valid for large displacements and large rotations. A discrete dashpot is added to the model, connected between the middle of the beam and the rigid body. The viscous damping constant of this dashpot is  $c_d$  [Ns/m].

Summarizing, if the FE model is compared with the semi-analytical model, next to the obvious differences in discretization, the following differences can be noted: the FE model includes the effects of axial deformation, axial inertia, rotatory inertia, and transverse shear, whereas these effects are absent in the semi-analytical model. However, as stated before, in Section 4.4 also results will be presented for the semi-analytical model including axial inertia.

## 4.2 Static and modal analysis

In this section, the convergence of the stable static initial postbuckling equilibrium points and the eigenfrequencies of the (linearized) discretized equations using approximations of Eq. (4.2) and Eq. (4.3) up to 11<sup>th</sup> order will be discussed. In all calculations the parameter values of Table 4.2 are used.



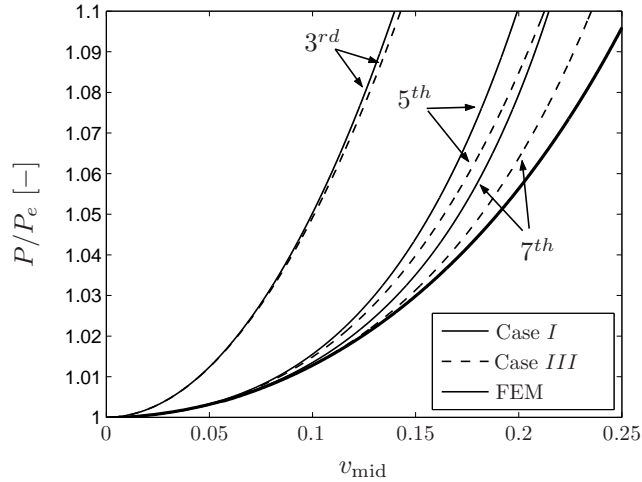


Figure 4.2: Load-paths for the single and two mode discretized models for  $3^{rd}$ ,  $5^{th}$ , and  $7^{th}$  order Taylor expansions of  $\kappa$  and  $u,x$  and FEM result.

#### 4.2.1 Static Equilibrium

The static initial post-buckling equilibrium points of the one and two mode discretizations for increasing axial load  $P$  are obtained using a path-following routine while setting  $\mathbf{f}_{\text{ex}}$  and the time derivatives of  $\mathbf{Q}_i$  equal to zero. The load-paths are presented in terms of the dimensionless transversal displacement of the middle of the beam

$$v_{\text{mid}} = v(t, L/2)/L, \quad (4.16)$$

and the axial load  $P$  (normalized on the Euler buckling load Eq. (4.1)). The positive post-buckling paths of the discrete models up to  $7^{th}$  order and the FE-model are shown in Fig. 4.2. Due to symmetry the negative post-buckling paths can be found by reflecting the positive ones around  $v_{\text{mid}} = 0$ . Figure 4.2 shows that a higher order approximation results in a less stiff post-buckling path approaching the FEM post-buckling path. In Table 4.3 it is shown that the value of the equilibrium points for  $P = 1.01P_e$  has converged to a constant value for the  $7^{th}$  order models and higher. Furthermore, it is also clear that addition of the third buckling mode further improves the accuracy of the static post-buckling path. For small excursions beyond the Euler load ( $P \leq 1.01P_e$ ), the error of the seventh order approximation for the one mode discretization with respect to the FEA result is very small (order of 1 %). For the  $7^{th}$  order model with two mode discretization (Case III) the error is even smaller (order of 0.1 %).

Table 4.3: Stable static equilibrium points (in terms of  $v_{\text{mid}}$ , see Eq. (4.16)) of discrete models and FE-model for  $P = 1.01P_e$ .

Order	3	5	7	9	11
Case I,II	0.045	0.083	0.087	0.087	0.087
Case III	0.045	0.084	0.089	0.089	0.089
FEM			0.089		

### 4.2.2 Modal Analysis

The undamped eigenfrequencies of the discretized models are calculated by eigenvalue analysis of the system linearized about the stable static equilibrium point for  $P = 1.01P_e$ . For this, again the parameters of Table 4.2 are used. The resulting eigenfrequencies are shown in Table 4.4. The eigenfrequencies of the discretized equations for the 7<sup>th</sup>-order approximation are within 1 % of the converged value of the 11<sup>th</sup>-order model. The first three undamped vibrational eigenmodes of the preloaded beam ( $P = 1.01P_e$ ) found by FEM analysis are depicted in Fig. 4.3 together with the buckled shape for  $P = 1.01P_e$ . Note, that with respect to the scaling of the eigenmodes, the same scale factor is used for the axial and transversal direction. This scale factor is chosen so, that the eigenmodes have the same maximum transversal displacement as the buckled equilibrium shape. It can be seen that the first eigenmode shows a distinct axial component. The inertia corresponding to these axial displacements is not taken into account in the semi-analytical model. The second and third vibrational eigenmodes show a much smaller axial component (relative to the transversal component). The first eigenfrequency fairly resembles the FEM result (7 % difference). The difference is most likely caused by the absence of the axial inertia in combination with the relatively large axial component of the first eigenmode of the FE-model. Another reason may be found in the small differences in static equilibrium states at  $P = 1.01P_e$  (see Table 4.3), resulting

Table 4.4: Vibrational eigenfrequencies of discrete models and FE-model for  $P = 1.01P_e$ .

	Order	3	5	7	9	11
$f_1$ [Hz]	Case I/II	6.634	7.188	6.970	6.936	6.933
	Case III	6.621	7.110	6.866	6.827	6.824
	FEM			6.512		
$f_2$ [Hz]	Case II	$1.63 \cdot 10^2$	$1.66 \cdot 10^2$	$1.66 \cdot 10^2$	$1.66 \cdot 10^2$	$1.66 \cdot 10^2$
	FEM			$1.59 \cdot 10^2$		
$f_3$ [Hz]	Case III	$4.00 \cdot 10^2$	$4.06 \cdot 10^2$	$4.06 \cdot 10^2$	$4.07 \cdot 10^2$	$4.07 \cdot 10^2$
	FEM			$3.93 \cdot 10^2$		

in different linearized stiffness terms. The second and third eigenfrequencies are reasonably close to the FEM eigenfrequencies (4 % difference).

It may be concluded that the static equilibrium points and the linearized undamped eigenfrequencies of the 7<sup>th</sup>-order approximation are more or less converged to a constant value. The prediction of the converged eigenfrequencies with respect to the FEM results is reasonably accurate. Therefore, unless stated otherwise, 7<sup>th</sup>-order approximations of Eq. (4.2) and Eq. (4.3) are used for the dynamic analyses in the remainder of this chapter.

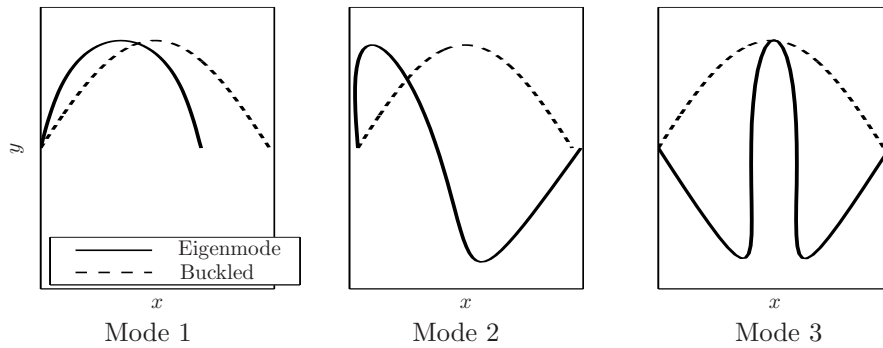


Figure 4.3: The lowest vibrational eigenmodes obtained by FEA.

### 4.3 Nonlinear Dynamic Analysis

In this section, the nonlinear steady-state behaviour for the three semi-analytic cases is evaluated by using numerical continuation of periodic solutions for varying excitation frequency [33]. The local stability of the periodic solutions is determined using Floquet theory [120]. Unless stated otherwise, the parameters of Table 4.2,  $P = 1.01P_e$  [N] and  $W = 15$  [m/s<sup>2</sup>] are used during simulations. This results in damping ratios of  $\xi_1 = 6.2$  [%],  $\xi_2 = 0.0$  [%] (undamped) and  $\xi_3 = 0.1$  [%] with respect to the first, second and third eigenfrequency of the linearized system for  $P = 1.01P_e$ , respectively. As stated before, 7<sup>th</sup>-order approximations of Eq. (4.3) and Eq. (4.2) are used for the dynamic analyses. It should be noted, that the order of expansion which should be used to obtain accurate dynamic responses, depends next to the preload  $P$  also on the harmonic excitation amplitude  $W$ . The accuracy of the dynamic responses based on the 7<sup>th</sup> order model for the considered values of  $P$  and  $W$  is illustrated at the end of Section 4.3.1. The axial inertia is not taken into account. The effect of including axial inertia on the results will be discussed in Section 4.4.

### 4.3.1 Steady-State Behaviour

In all presented phase diagrams the two stable static equilibrium points of (4.12) ( $|v_{\text{mid}}| = 0.087$ , see Table 4.3) are denoted by +, and the unstable equilibrium point  $v_{\text{mid}} = 0$  by \*. The iterates of the Poincaré mappings are shown by  $\square$ . In some regions solutions are found which encircle both the negative and the positive stable equilibrium point. The latter phenomenon is called a snap-through motion [36].

#### Case I

The frequency-amplitude plot for Case I is shown in Fig. 4.4. Note that the steady-state solutions are characterized by the following dimensionless measure

$$v_{\text{per}} = \max_T v_{\text{mid}} - \min_T v_{\text{mid}}, \quad (4.17)$$

with  $v_{\text{mid}}$  defined by Eq. (4.16) and  $T$  the period of the periodic solution. Figure 4.4 shows a harmonic resonance at about 6.4 [Hz]. Note that the

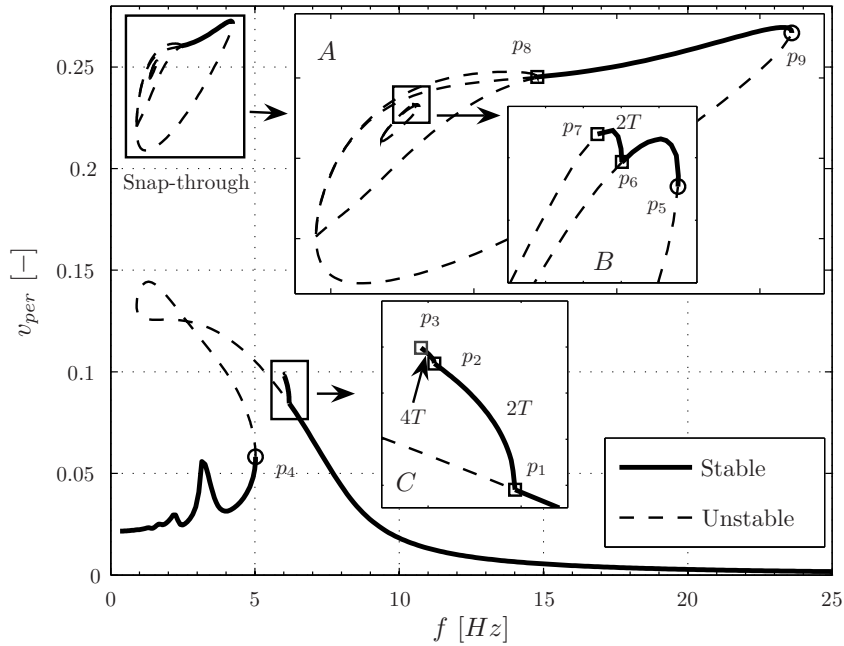


Figure 4.4: Frequency-amplitude plot for Case I.

harmonic solutions are unstable near the resonance peak. Because the resonance peak bends to the left, there exist coexisting periodic solutions.

Next, the frequency-amplitude plot of Eq. (4.12) shown in Fig. 4.4 will be discussed by following the periodic solutions branches in the direction of increasing frequency. At low frequencies the amplitude of the periodic solutions is very small; for  $f = 0.1$  [Hz] a harmonic solution exists that vibrates around the positive static equilibrium point. Such a harmonic solution is also present around the negative static equilibrium point (Fig. 4.5 a). The system is skew-symmetric since  $\mathbf{K}_{nl}(-\mathbf{Q}) = -\mathbf{K}_{nl}(\mathbf{Q})$ : the negative solution thus can be obtained by reflecting the positive solution over the origin. Note, that the skew-symmetry in the system would be lost if geometric imperfections would be present (see Chapter 5). In fact, in all presented phase plots skew-symmetric solutions pairs are present but only one solution will be shown.

Between  $f = 0.9$  [Hz] and  $f = 4.2$  [Hz], two separate islands of branches containing snap-through solutions are present (see enlargement A). The local stability of the snap-through solutions changes after period doubling bifurcations (some of the period doubling bifurcations are indicated by  $p_6$ ,  $p_7$  and  $p_8$ ). The period doubling sequences are more clearly visualized in Fig. 4.6. These bifurcation diagrams are obtained by performing numerically a decreasing stepped frequency sweep (starting at the stable snap-through solution). For each value of  $f$ , many times the Poincaré mapping of the steady-state value of  $v_{per}$  is plotted. Just after the period doubling sequences, first small regions are found where the responses seem to be chaotic. Subsequently, the response jumps back to the stable small-amplitude solution. For increasing frequencies, the stable snap-through solutions disappear again by cyclic fold bifurcations at points  $p_5$  and  $p_9$ . An example of the chaotic response just after the period doubling sequence ( $f = 1.56$  [Hz]) is shown in Fig. 4.5 b (also one coexisting stable low-amplitude harmonic solution is shown). In Fig. 4.5 c an example of a stable snap-through solution (solid curve, large amplitude) is shown at  $f = 3.2$  [Hz]. In addition for  $f = 3.2$  [Hz], Fig. 4.5 c also shows a stable second super-harmonic resonance solution (solid curve, small amplitude) and three unstable periodic solutions. One of these solutions shows snap-through motion.

Next, just above 5.02 [Hz], a cyclic fold bifurcation point is reached indicated by point  $p_4$ . The two stable harmonic solutions vanish and a chaotic snap-through motion appears. Figure 4.7 a shows that at 5.02 [Hz] a small difference in initial conditions results in completely different transient behaviour until the periodic solution is reached. Furthermore, nearly periodic windows can be recognized during the transient behaviour at 5.02 [Hz]. This indicates that the transients settling to the periodic solution are of a chaotic nature. According to [123; 128]

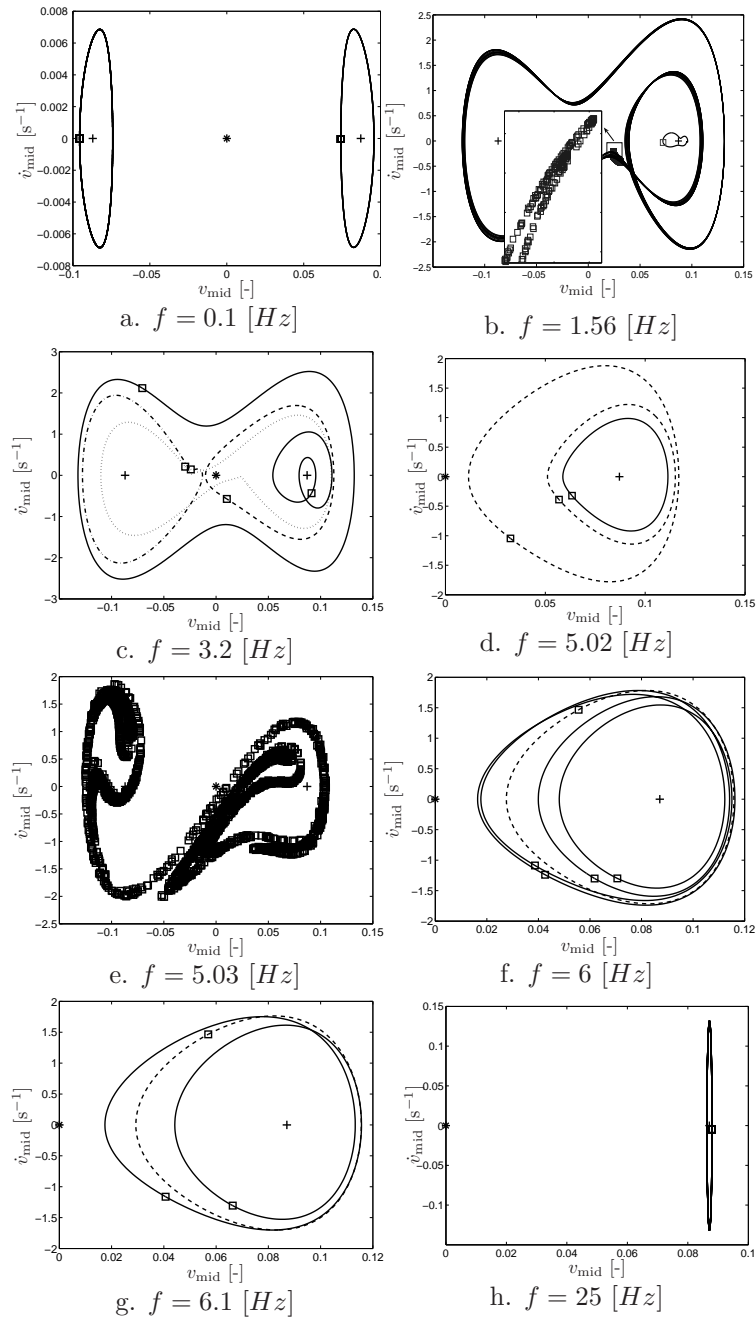


Figure 4.5: Periodic solutions in the phase plane and iterates of their Poincaré mapping ( $\square$ ) (+ stable static equilibrium point, \* unstable static equilibrium point).

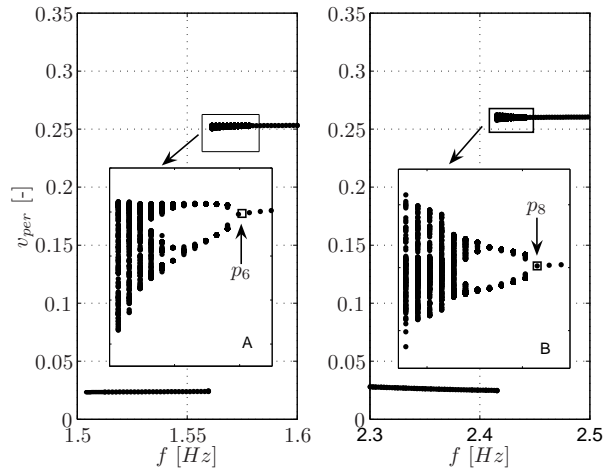


Figure 4.6: Bifurcation diagrams for varying excitation frequency.

this means that the periodic solutions are destroyed by a catastrophic local cyclic fold bifurcation. The local fold bifurcation by itself does not guarantee a transition to chaos; but if the global structure of phase space is such that transients settling to the periodic solution were chaotic, then a chaotic attractor can be expected after the periodic solution vanishes. This phenomenon is called an intermittency transition to chaos by a cyclic fold catastrophe. At  $f = 5.03$  [Hz] (Fig. 4.7 b) the solution indeed seems to be chaotic. The phase plots of the foregoing transition are illustrated in Fig. 4.5 d and e (e only showing the Poincaré mapping). Figure 4.5 d also contains the two coexisting unstable harmonic solutions.

In the frequency region that follows a great variety of chaotic behaviour is present. The chaotic regions and transitions to these regions are more clearly visualized in Fig. 4.8. This bifurcation diagram is obtained by performing numerically an increasing stepped frequency sweep, starting at the stable harmonic solution at  $f = 4.7$ . From this diagram it can be concluded that the chaotic snap-through solutions end at approximately 6 [Hz] (close to the period-doubling bifurcation  $p_3$ , see enlargement *C* in Fig. 4.4). Furthermore, Fig. 4.8 shows that the snap-through response locks to non-chaotic response in small regions.

At point  $p_3$  (6.0 [Hz]), see inset *C*, a period doubling bifurcation occurs. After this point, one stable  $1/4$  subharmonic solution, an unstable  $1/2$  subharmonic

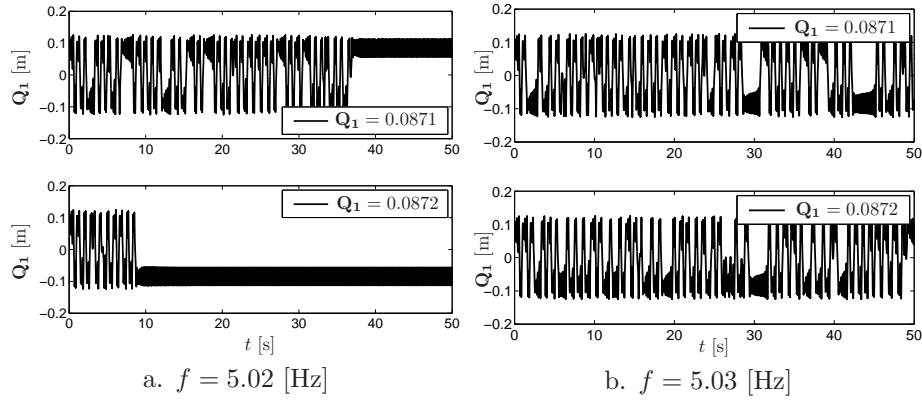


Figure 4.7: Transient behaviour near intermittency transition to chaos.

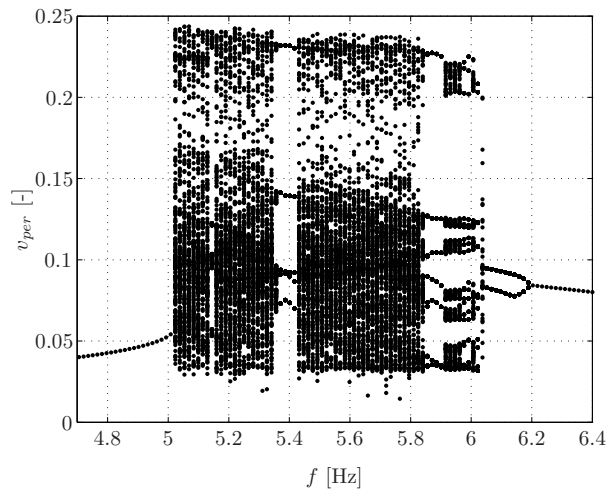


Figure 4.8: Bifurcation diagram for varying excitation frequency.

solution (not visible) and one unstable harmonic solution are present (Fig. 4.5 f). Next, at point  $p_2$ , again a period doubling is found, which transforms the stable  $1/4$  subharmonic resonance into a stable  $1/2$  subharmonic resonance as shown in figure 4.5 g. Finally, at point  $p_1$  at about  $6.18$  [Hz] another period doubling bifurcation changes the  $1/2$  subharmonic solution into a stable harmonic periodic solution which persists over a wide frequency range (see for example Fig. 4.5 h).

The accuracy of the dynamic responses based on the  $7^{th}$  order model for the



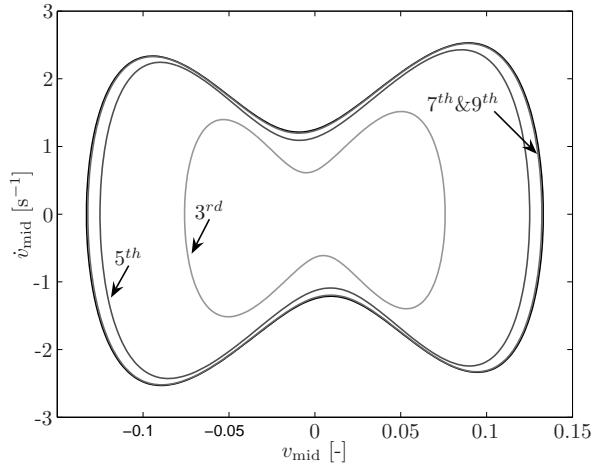


Figure 4.9: Snap-through solutions at  $f = 3.2$  [Hz] for 3<sup>rd</sup>, 5<sup>th</sup>, 7<sup>th</sup> and 9<sup>th</sup> order Taylor expansions of  $\kappa$  and  $u_{,x}$ .

considered value of  $W$  is illustrated for the (stable) snap-through response at  $f = 3.2$  [Hz] (see Fig. 4.9). It can be noted that expansions higher than 7<sup>th</sup> order do not significantly improve the accuracy of the (stable) snap-through response at  $f = 3.2$  [Hz], which has a relatively large amplitude. Similar observations are made for the dynamic responses with lower amplitudes.

### Case II

The frequency-response of the linearly undamped one-degree-of-freedom system  $m\ddot{x} + kx = 0$  contains only one non-zero solution; the resonance peak to infinity at  $f = \sqrt{k/m}/(2\pi)$ . Addition of the slightest amount of damping to such a system without excitation immediately results in the disappearance of this resonance peak. The second ODE of Case II (see Eq. (4.14)) behaves in a similar manner. The second mode, which is skew-symmetric with respect to the midpoint of the beam, is not excited since the excitation is symmetric. Because the second ODE is undamped, since the second mode has zero transversal displacement at the position of the damper, the resonance peak near the second harmonic resonance frequency of 166 [Hz] in principle exists. However, the slightest amount of damping would have the same effect as for the linear system: the second resonance peak ceases to exist. From this it can be concluded that the second generalized coordinate will have no effect on the steady-state behaviour of the system. So the frequency-amplitude plot for Case II is equal to that of Fig. 4.4 for Case I.

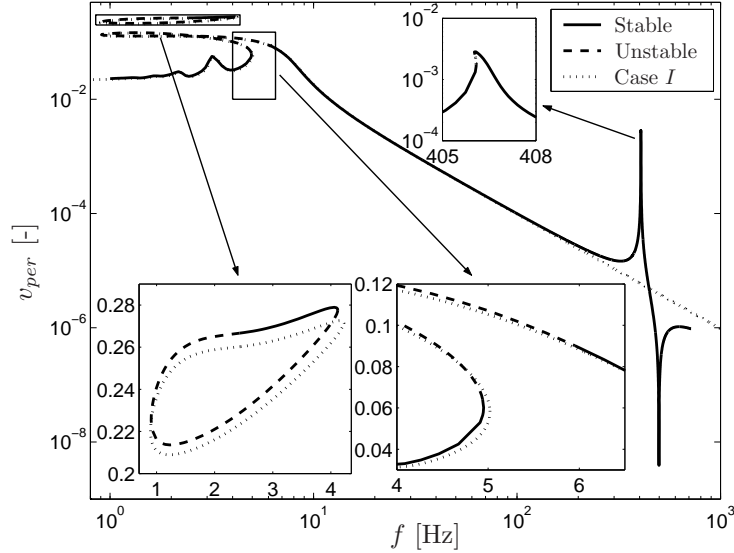


Figure 4.10: Frequency-amplitude plot for Case III compared to Case I.

### Case III

In the set of ODEs of Case III the two coupled equations of motion Eq. (4.15) both have a driving term on the right-hand side in contrast to Case II (Eq. (4.14)). Figure 4.10 shows that, due to the lower first vibrational eigenfrequency of Case III (6.87 [Hz]) with respect to Case I (6.97 [Hz]), the first harmonic resonance peak for Case III has shifted a little to lower frequencies compared to Case I. Hence, also all bifurcation points lie at a lower frequency and, therefore, now chaotic solutions are present from approximately 4.95 [Hz] to 5.95 [Hz]. Also, the extra DOF instigates an extra harmonic resonance peak at 406 [Hz]. This peak bends to the left, which makes it possible that in a very small frequency range two stable solutions and one unstable solution coexist. Furthermore, an anti-resonance peak is introduced at about  $f = 500$  [Hz].

### 4.3.2 Influence of Parameters

In this subsection the influence of some parameter changes on the frequency-amplitude plots is investigated. Simulations are solely performed for Case I-7<sup>th</sup> order model. Only harmonic solutions are plotted in the frequency-amplitude plots. First, the influence of the damping  $c_d$  is examined. Then the axial preload  $P$  is varied and finally the influence of the excitation amplitude  $W$

is considered. Only one parameter is varied at a time, the remaining parameter values are defined according to Table 4.2.

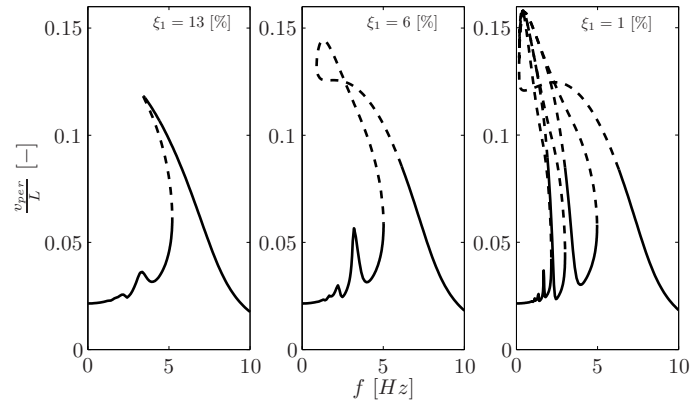


Figure 4.11: Frequency-amplitude plots for 13% damping ( $c_d = 17$  [Ns/m]), 6% damping ( $c_d = 8.3$  [Ns/m]), and 1% damping ( $c_d = 1.7$  [Ns/m]).

Figure 4.11 shows the frequency-amplitude plots for three values of the damping parameter. It is obvious that if the damping is decreased the 'height' of the (super) harmonic resonance peaks increases. Consequently, the peaks bend over to larger frequency ranges. Moreover, for 1% damping, even parts of the second and third superharmonic resonances have become unstable.

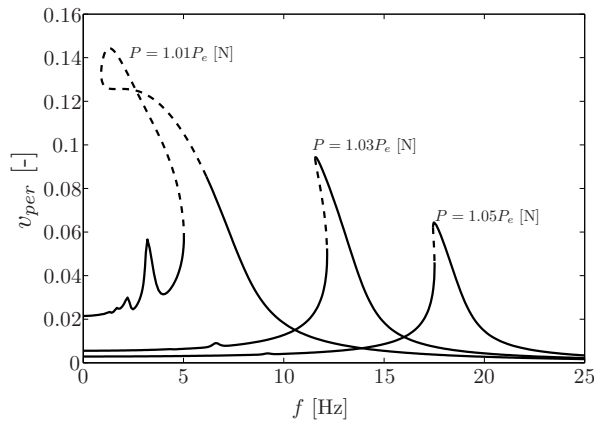


Figure 4.12: Frequency-amplitude plots for different axial preloads.

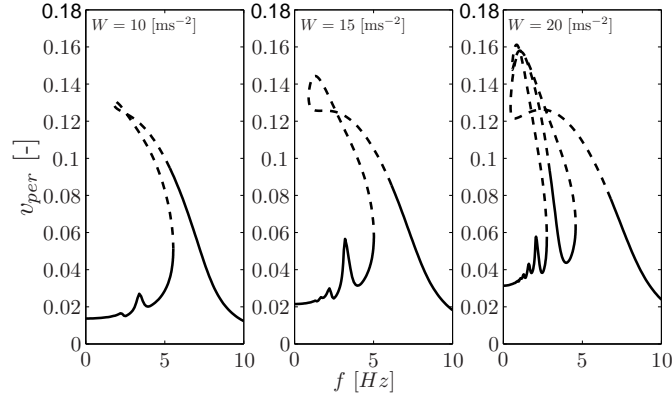


Figure 4.13: Frequency-amplitude plots for different excitation amplitudes.

It is clear, that if the axial preload  $P$  is increased, the linearized stiffness about the stable static equilibrium point (i.e. in this case the tangent of the load-path depicted in Fig. 4.2 for Case  $I$ -7<sup>th</sup> order model) increases. Figure 4.12 shows that increasing the preload and, thus, increasing stiffness leads to steeper and lower peaks and higher resonance frequencies. The unstable regions become smaller and eventually, if the preload is large enough, snap-through is made impossible for this level of  $W$ . Finally, the excitation amplitude  $W$  is considered. Increasing this parameter results in higher values for  $\frac{v_{per}}{L}$  as shown in Fig. 4.13. The harmonic and super-harmonic resonance peaks become higher and regions of instability become larger.

#### 4.4 Comparison with Transient FEA

In Section 4.3, frequency-amplitude plots for several semi-analytic models of the buckled beam structure have been presented. The construction of such plots using FEA is very elaborate (practically impossible) and time-consuming. In order to compare some results of Subsection 4.3.1 with FEM results, transient FEM analyses are performed for several excitation frequencies using the parameter values of Table 4.2. In each analysis, the integration time was taken long enough to reach the steady-state solution.

Figure 4.14 compares some steady-state results of FEM analyses with the steady-state solutions of the semi-analytic approach of Case  $I$  (7<sup>th</sup> order approximation). All steady-state results are obtained with the static buckled beam configuration for  $P = 1.01P_e$  [N] as initial condition. The Poincaré section of the FEM results is denoted by ■, whereas the Poincaré sections of

the semi-analytic results are still denoted by the  $\square$ . Symbols  $\blacksquare$  and  $\square$  may be separated due to a phase difference in the excitation term. The stable static equilibrium points for the FEM results are denoted by  $\times$  and for the semi-analytic approach by  $+$ .

At an excitation frequency of  $0.1 [Hz]$  (Fig. 4.14 a) both periodic solutions are period one and vibrate around their respective equilibrium points. The amplitude of the Case *I*-solution ( $v_{per} = 0.0215$ ) is approximately the same as for the FEA solution ( $v_{per} = 0.0227$ ).

At  $3.2 [Hz]$  (Fig. 4.14 b) the FEM analysis results is qualitatively comparable to the Case *I* result. Both phase diagrams show an extra loop, which indicates that a second superharmonic resonance is present (see also Fig. 4.5 c). However, the amplitude of the FEA solution  $v_{per} = 0.045$  is clearly smaller than the amplitude of the semi-analytic solution of Case *I*:  $v_{per} = 0.057$ . On the other hand, later on in Fig. 4.15 it will be shown that the amplitude is very sensitive for small excitation frequency changes in this frequency range.

The FEA results indicate that between  $f = 4.6 [Hz]$  (Fig. 4.14 c) and  $f = 4.7 [Hz]$  (Fig. 4.14 d) a transition from the harmonic solution to a solution of a chaotic nature is present. In the semi-analytic case, this transition appears between  $f = 5.02 [Hz]$  and  $f = 5.03 [Hz]$  (see Section 4.3.1). The amplitudes of the solutions before and after the transition are  $v_{per} = 0.050$  and  $v_{per} = 0.258$  for FEM and  $v_{per} = 0.053$  and  $v_{per} = 0.252$  for the semi-analytic approach. In conclusion, the transition frequency differs somewhat, but the amplitudes and (Poincaré) shapes are comparable.

The next transition from a chaotic solution to a harmonic solution is found near  $f = 5.8 [Hz]$  (Fig. 4.14 e) in the FEA, whereas this is found near  $f = 6 [Hz]$  by the semi-analytic approach. Again, a small difference between the transition frequency is detected. However, the amplitudes ( $\frac{v_{per,FEM}}{L} = 0.092$  versus  $\frac{v_{per,semi}}{L} = 0.084$ ) and shapes of the solutions after the transition are comparable.

From the foregoing, it is clear that the chaotic region of the FE-model starts and ends at a slightly lower frequency than it does for Case *I* (and Case *III*). This is in correspondence with a lower first eigenfrequency for the FE-model compared to Case *I*, see Table 4.4.

At  $f = 25 [Hz]$  (Fig. 4.14 f) both solutions are period-one solutions and vibrate around their respective equilibrium points. The amplitude of the FEA solution is slightly smaller ( $v_{per} = 0.0016$ ) compared to the amplitude of the semi-analytic solution ( $v_{per} = 0.0017$ ).

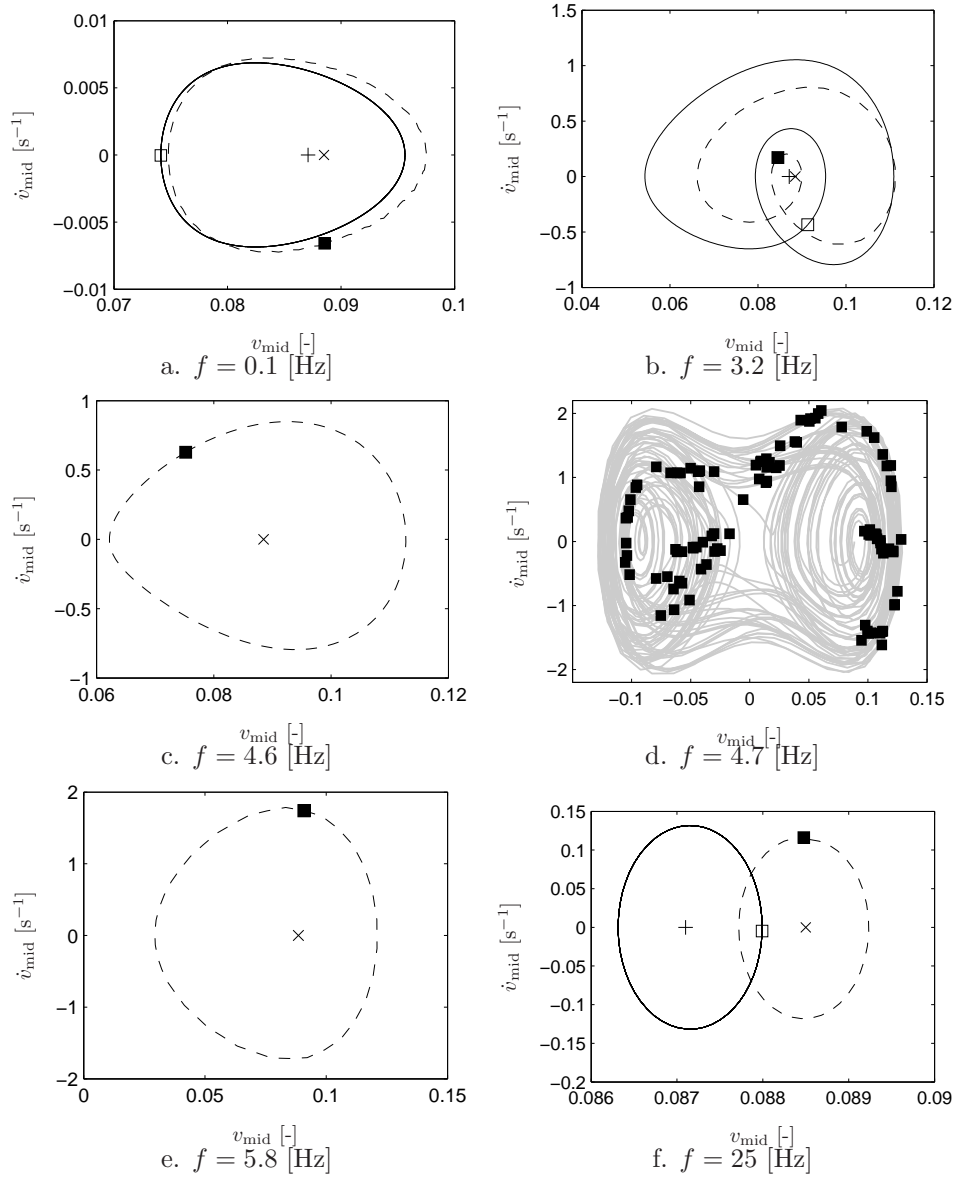


Figure 4.14: Steady-state results for FEM (dashed) and semi-analytic (solid) approach.

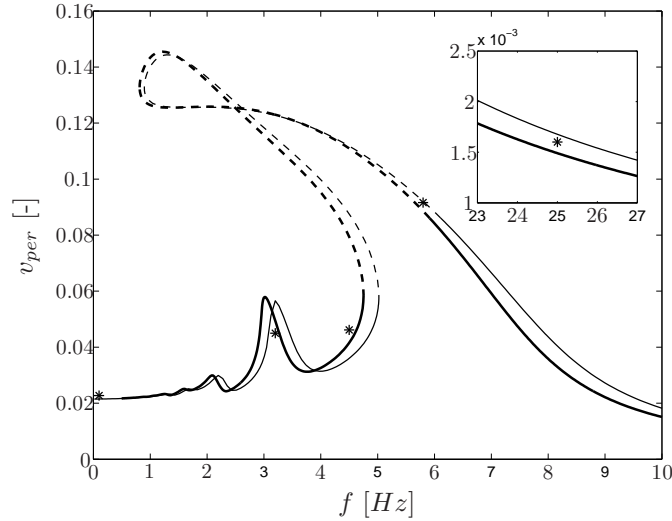


Figure 4.15: FEM solutions ( \* ) in the frequency-amplitude plot of Case I without axial inertia (thin lines) and of Case I with axial inertia (thick lines).

Figure 4.15 summarizes the foregoing by plotting the FEM solutions in the frequency-amplitude plot of Fig. 4.4. In terms of amplitude it may be concluded that a reasonably good match exists between the semi-analytic results without axial inertia and the FEM results.

Clearly, the semi-analytic approach offers more insight in the global nonlinear dynamic behaviour (e.g. detection of bifurcation points) than the FEM approach. Moreover, the semi-analytic method is much less time-consuming than the FEM approach. For example, the calculation of the harmonic solutions branch of Fig. 4.15 and the calculation of the corresponding Floquet multipliers takes about half the time of the calculation of only one FEM solution (including static preloading).

Several reasons may be given to explain the small differences between the semi-analytic and FEM results. The load-paths of Subsection 4.2.1 already show that due to slight differences in stiffness between the semi-analytic and FEM results, the static equilibrium points differ a little. Therefore, the difference in stiffness may explain that the periodic solutions encircle slightly different static equilibrium points. This, together with the fact that in the semi-analytic approach the axial inertia is neglected with respect to the transversal inertia, may explain the differences in the vibrational eigenfrequencies (see Table 4.4)

and in the amplitudes of the periodic solutions.

In order to investigate if the results will improve, axial inertia is taken into account in the 7<sup>th</sup> order model as used in Case *I* (i.e. by setting  $\alpha = 1$  in 4.8). Indeed, inclusion of the axial inertia decreases the difference between the first eigenfrequency of the semi-analytical model (without axial inertia:  $f_1 = 6.97$  [Hz], with axial inertia:  $f_1 = 6.60$  [Hz]) and the first eigenfrequency of the FE model ( $f_1 = 6.51$  [Hz]). Furthermore, as illustrated in Fig. 4.15, also the periodic solutions and the bifurcation points shift towards the FEM solutions. Therefore, it is recommended to take the axial inertia of the beam into account. Summarizing, the differences between the semi-analytical results and the FEM results become very small by considering higher order approximations for  $\kappa$  and  $u_{,x}$  and by including axial inertia. Apparently, the remaining differences between the FE model and the semi-analytical model (i.e. rotatory inertia, axial strain and transverse shear) are not important for dynamic responses of the system considered. Therefore, the semi-analytical model enables a detailed analysis of the global nonlinear dynamic behaviour of the buckled beam in a much more efficient manner than by using FEA.

## 4.5 Conclusions

In this chapter, the steady-state nonlinear dynamics of a transversally excited, buckled beam have been discussed. Based on Taylor series expansions of the inextensibility constraint and the exact curvature of the beam, and by using one or more basis functions, a semi-analytical modelling approach is presented.

Three sets of ODEs have been considered, in which the transversal displacement field has been approximated by one and two-mode discretizations based on the linear buckling modes of the simply supported beam. A conclusion from the static analyses is that a higher order approximation of the inextensibility constraint and the exact curvature of the beam using a single mode model leads to a more accurate initial post-buckling path than a lower order approximation using a two-mode model. The influence of 9<sup>th</sup>-order terms and higher on the initial post-buckling equilibrium points and eigenfrequencies of the discretized equations is limited. Therefore, in the steady-state dynamic analyses, a 7<sup>th</sup> order approximation of the inextensibility constraint and the exact curvature of the beam has been used. It has been shown that this 7<sup>th</sup> order approximation also is capable to accurately predict high amplitude snap-through solutions.

Frequency-amplitude plots have been created, using continuation of periodic solutions for varying excitation frequency. Periodic, chaotic and snap-through behaviour has been found. For the two-mode discretization approaches considered, inclusion of the second (skew-symmetric) linear buckling mode



appeared to have no effect whereas inclusion of the third linear buckling mode only affected the response significantly near the harmonic resonance at 406 [Hz]. Therefore, for the buckled beam considered in this chapter, the model based on the single mode discretization appeared to be sufficiently accurate to predict the nonlinear responses (including softening, transitions to chaos and snap-through solutions) for a wide frequency band around the first harmonic resonance (near 6.4 [Hz]).

It is concluded that the difference in the dynamic response of the FE model and the semi-analytical model with higher order approximations for the inextensibility constraint and the exact curvature of the beam and by including axial inertia becomes very small. The verification of results obtained from a semi-analytic approach with FEM results is a first step in obtaining insight in the accuracy of the semi-analytic models. However, for a full validation semi-analytical results should be compared with experimental results. This will be done (although for an initially unbuckled beam and for a different type of dynamic loading) in Chapter 6.

Finally, it can be concluded that using a semi-analytic approach in combination with modern nonlinear dynamics tools, the steady-state behaviour of the transversally excited buckled beam has been investigated and understood to a large extent in a very efficient way.



## *Dynamic stability of a base-excited thin beam with top mass*

**T**hin-walled structures are often employed as support for components with a relatively large weight and stiffness. In this case, the supported component may be considered as a rigid top mass. The inertia of this top mass may introduce severe dynamic loads on the structure if the base on which the structure is resting exhibits shocks or vibrations (e.g. due to earthquakes in civil engineering structures and due to propulsion systems in aerospace launch vehicles). Furthermore, as will be shown, the inertia of the top mass may also have significant influence on the qualitative nonlinear dynamics of the structure.

In this chapter, the dynamic stability problem of a base-excited thin beam with top mass is considered, see Fig. 5.1. The vertical beam will be subjected to a static pre-load due to the presence of gravity plus a dynamic load due to a base motion. The beam is considered to be thin, inextensible, without shear and initially not perfectly straight. By employing one or more basis functions, the continuous problem of the beam is approximated by a discrete set of equations of motion. In this approach, the inertia of the top mass is taken into account via the inextensibility constraint. The resulting equations of motion contain both nonlinear stiffness terms and nonlinear inertia terms. The forcing terms appear both in a parametric manner and in a direct manner (due to the imperfection of the beam). For the theoretical case where the beam is initially perfectly straight and when all nonlinearities are neglected, the dynamic stability problem of the beam is described by a *Mathieu* differential equation (see Eq. (2.19)).

Inclusion of axial inertia, for example of the beam itself or of an additional discrete mass added to the (top of the) beam results in nonlinear inertia terms, due to the nonlinear inextensibility constraint. Depending on the mode considered and/or the relative weight of the added discrete mass, these inertia nonlinearities can change the response of the beam from a hardening type of response to a softening type of response [7; 10; 144]. With respect to the damping of thin beams, addition of quadratic damping improves the agreement between theoretical and experimental results in many studies [7; 144; 145].

---

Parts of this chapter are also presented in [81].

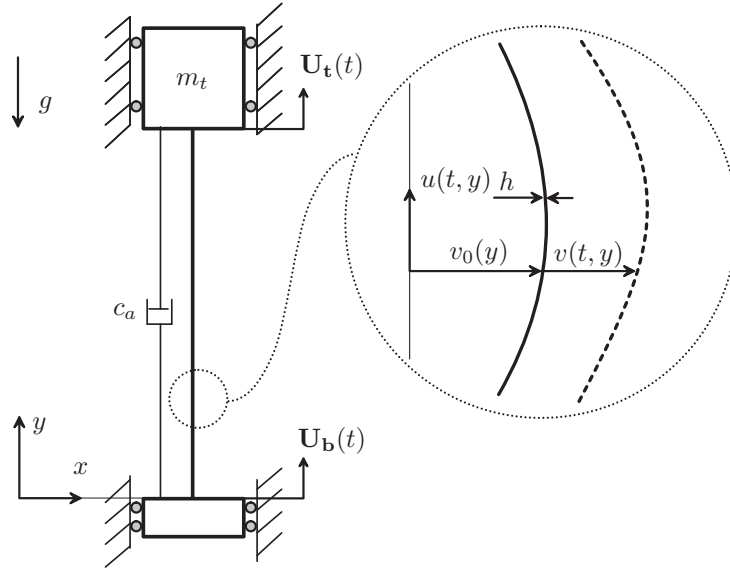


Figure 5.1: Base-excited thin beam with top mass.

The work presented in this chapter is different from other studies concerning parametrically excited beams with a top mass [144; 148], since here the top mass is considered to be transversally and rotationally restrained (instead of completely free). Furthermore, the effect of an imperfection is included and parameter studies and convergence studies are performed using advanced numerical tools. In addition, the results obtained using the semi-analytical approach will be confronted with FEM results.

The outline for the chapter is as follows. In the next section the beam structure will be introduced and the equations of motion will be derived. In Section 5.2, a quasi-static analysis and a modal analysis will be performed. The results of these analyses will be compared with results obtained from FEM analyses. In Section 5.3, the steady-state response of the base-excited beam will be considered using numerical continuation of both periodic solutions and bifurcations. In Section 5.4, the validity of the third-order single-mode semi-analytical model will be studied by performing a convergence study. Finally, conclusions will be drawn in Section 5.5.

## 5.1 Equation(s) of motion

In this section, the equation(s) of motion for the base-excited thin beam with top mass (see Fig. 5.1) will be derived. The initial shape of the thin beam with length  $L$ , thickness  $h$  and width  $b$  is denoted by  $v_0(y)$ . The axial displacement field relative to  $\mathbf{U}_b(t)$  is indicated by  $u(t, y)$  and the transversal displacement field relative to  $v_0(y)$  by  $v(t, y)$ . Since the beam is considered to be thin ( $h \ll L$ ), the displacements of the beam will be dominated by changes in curvature allowing to assume the beam to be inextensible. The length of an infinitesimally small piece of the beam in the initial state satisfies [92]

$$ds^2 = dy^2 + (v_{0,y} dy)^2. \quad (5.1)$$

Due to the inextensibility assumption, the length of  $ds$  stays constant. In the deformed state this length satisfies [92]

$$ds^2 = (dy + u_{,y} dy)^2 + ([v_{0,y} + v_{,y}] dy)^2. \quad (5.2)$$

Setting Eq. (5.1) equal to Eq. (5.2) results in the following inextensibility constraint

$$u_{,y} = \sqrt{1 - 2v_{0,y} v_{,y} - v_{,y}^2} - 1. \quad (5.3)$$

In the adopted Cartesian coordinate system  $[x, y]$ , the centerline of the deformed imperfect beam is described by the curve  $[X(t, y), Y(t, y)]$ , where  $X(t, y) = v_0(y) + v(t, y)$  and  $Y(t, y) = y + \mathbf{U}_b(t) + u(t, y)$ . The exact curvature of this curve follows from [43]

$$\kappa = \frac{X(t, y)_{,y} Y(t, y)_{,yy} - X(t, y)_{,yy} Y(t, y)_{,y}}{(X(t, y)_{,y} + Y(t, y)_{,y})^{\frac{3}{2}}}, \quad (5.4)$$

and can be evaluated in terms of  $v_0(y)$  and  $v(t, y)$  solely, after substitution of Eq. (5.3). Note that for the perfect beam ( $v_0(y) = 0$  [m]), Eq. (5.3) and Eq. (5.4) are exactly equivalent to the inextensibility constraint and the curvature expression used in the previous chapter (see Eqs. (4.4) and (4.5)). Depending on the maximum deflection, the constraint Eq. (5.3) and the curvature Eq. (5.4) may be approximated by their Taylor series expansions in  $v_{,y}$  and  $v_{0,y}$  up to  $n^{\text{th}}$  order. For example the 3<sup>rd</sup> order expansions of Eq. (5.3) and Eq. (5.4) yield

$$u_{,y} = -v_{0,y} v_{,y} - \frac{1}{2} v_{,y}^2, \quad (5.5)$$

$$\kappa = \kappa_0 + v_{,yy} + \frac{1}{2} (v_{0,yy} + v_{,yy}) v_{,y}^2 + v_{,yy} v_{0,y} v_{,y} - \frac{1}{2} v_{,yy} v_{0,y}^2, \quad (5.6)$$

where  $\kappa_0 = v_{0,yy} - \frac{3}{2} v_{0,yy} v_{0,y}^2$  is (in this case) the 3<sup>rd</sup> order approximation of the initial curvature. Higher order approximations include higher order terms

in  $v_{,y}$  and  $v_{0,y}$ .

The boundary conditions for the transversal displacement field of the clamped-clamped beam (see Fig. 5.1) are

$$v(t, 0) = v(t, L) = 0 \text{ and } v(t, 0)_{,y} = v(t, L)_{,y} = 0. \quad (5.7)$$

Each of the following modes a priori obeys these conditions

$$v_i(y) = \cos[(i-1)\pi y/L] - \cos[(i+1)\pi y/L], \quad i = 1, 2, \dots \quad (5.8)$$

Using these modes, the transversal displacement field is discretized as

$$v(t, y) = \sum_{i=1}^N \mathbf{Q}_i(t) \cdot v_i(y). \quad (5.9)$$

where  $\mathbf{Q}_i$  [m] are generalized degrees of freedom. In a similar fashion, the initial shape of the beam (i.e. the imperfection) is discretized as

$$v_0(y) = \sum_{i=1}^{N_e} \frac{1}{2} e_i \cdot h \cdot v_i(y), \quad (5.10)$$

where  $e_i$  are *dimensionless* imperfection parameters and  $N_e \leq N$ . After discretization of  $v_0(y)$  and  $v(t, y)$ , the corresponding axial displacement field  $u(t, y)$  can be computed by integrating an  $n^{\text{th}}$  order expansion of Eq. (5.3). Subsequently, the absolute displacement of the top mass (see Fig. 5.1) follows to be

$$\mathbf{U}_t = \mathbf{U}_b + u(t, L). \quad (5.11)$$

Note that (in general)  $\mathbf{U}_t$  depends in a nonlinear fashion on the DOF  $\mathbf{Q}_i$ .

The kinetic energy  $\mathcal{T}$  and the potential energy  $\mathcal{V}$  are determined by

$$\mathcal{T} = \frac{1}{2} \rho A \int_0^L \dot{v}^2 dy + \frac{1}{2} m_t \dot{\mathbf{U}}_t^2, \quad (5.12)$$

$$\mathcal{V} = \frac{1}{2} EI \int_0^L (\kappa - \kappa_0)^2 dy + m_t g \mathbf{U}_t, \quad (5.13)$$

where  $A = b \cdot h$  and  $I = b \cdot h^3/12$ . Note that the axial and rotatory inertia of the beam are neglected, i.e. the case  $m_{beam} \ll m_t$  and  $h/L \ll 1$  (as stated before) is considered. Damping of the thin beam is modelled by including for each DOF  $\mathbf{Q}_i$ , a linear and a quadratic viscous damping term of the form  $F_d = -c_i \dot{\mathbf{Q}}_i - c_{q,i} |\dot{\mathbf{Q}}_i| \mathbf{Q}_i$  and by modelling a discrete viscous dash-pot  $c_a$  (see Fig.

5.1). The generalized damping forces are derived using the Rayleigh dissipation function

$$\mathcal{R} = \frac{1}{2}c_a \dot{\mathbf{U}}_t^2 + \sum_{i=1}^N \left( \frac{1}{2}c_i \dot{\mathbf{Q}}_i^2 + \frac{1}{3}c_{q,i} \text{sign}(\dot{\mathbf{Q}}_i) \dot{\mathbf{Q}}_i^3 \right). \quad (5.14)$$

The equations of motion are derived via *Lagrange's* equations

$$\frac{d}{dt} \mathcal{T}_{,\dot{\mathbf{Q}}} - \mathcal{T}_{,\mathbf{Q}} + \mathcal{V}_{,\mathbf{Q}} = \mathbf{Q}_{nc}, \quad (5.15)$$

where

$$\mathbf{Q} = [\mathbf{Q}_1, \dots, \mathbf{Q}_N]^T \text{ and } \mathbf{Q}_{nc} = -\mathcal{R}_{,\dot{\mathbf{Q}}}. \quad (5.16)$$

To illustrate some of the key features of the model, the equation of motion of the thin beam structure for single-mode expansions of  $v(t, y)$  and  $v_0(y)$  ( $N = N_e = 1$  in Eqs. (5.9)-(5.10)) and the third-order approximation is given. This results in a single equation of motion of the form

$$\begin{aligned} M(\mathbf{Q}_1) \ddot{\mathbf{Q}}_1 + G(\mathbf{Q}_1, \dot{\mathbf{Q}}_1) + C(\mathbf{Q}_1, \dot{\mathbf{Q}}_1) + \\ p_1 \left( 1 - r_0 - p_2 e_1^2 - \ddot{\mathbf{U}}_b \right) \mathbf{Q}_1 + K(\mathbf{Q}_1) = p_3 e_1 \left( r_0 + \ddot{\mathbf{U}}_b \right), \end{aligned} \quad (5.17)$$

where

$$r_0 = \frac{m_t g}{P_c}, \quad (5.18)$$

is the ratio between the static load due the weight of the top mass and the first static buckling load of the beam ( $P_c = 4\pi^2 EI/L^2$ ). Furthermore,  $\ddot{\mathbf{U}}_b$  is the base-acceleration which will be directly prescribed (as a harmonic function in time).

In Eq. (5.17), the following abbreviations are used

$$\begin{aligned} p_1 &= \frac{8\pi^4 EI}{L^3}, \quad p_2 = \frac{\pi^2 h^2}{4L^2}, \quad p_3 = \frac{h}{2} p_1, \\ M(\mathbf{Q}_1) &= \left[ \frac{3}{2} \rho AL + \frac{m_t \pi^4}{L^2} (h^2 e_1^2 + 4h e_1 \mathbf{Q}_1 + 4\mathbf{Q}_1^2) \right], \\ C(\mathbf{Q}_1, \dot{\mathbf{Q}}_1) &= c_1 \dot{\mathbf{Q}}_1 + c_{q,1} |\dot{\mathbf{Q}}_1| \dot{\mathbf{Q}}_1 + \frac{c_a \pi^4}{L^2} \dot{\mathbf{Q}}_1 (e_1 h + 2\mathbf{Q}_1)^2, \\ G(\mathbf{Q}_1, \dot{\mathbf{Q}}_1) &= \frac{2m_t \pi^4}{L^2} \dot{\mathbf{Q}}_1^2 (h e_1 + 2\mathbf{Q}_1), \\ K(\mathbf{Q}_1) &= \frac{2\pi^6 EI}{L^5} (8\mathbf{Q}_1^3 + 9h e_1 \mathbf{Q}_1^2). \end{aligned} \quad (5.19)$$

As can be noted, Eq. (5.17) contains inertia nonlinearities due to the top mass ( $m_t$ ), and stiffness nonlinearities due to the adopted nonlinear kinematic relation Eq. (5.6). For  $e_1 = 0$ , the inertia nonlinearities are of the softening type (mass increases for increasing  $|\mathbf{Q}_1|$ ), whereas the stiffness nonlinearities are of the hardening type (stiffness increases for increasing  $|\mathbf{Q}_1|$ ). Furthermore,  $\mathbf{Q}_1$  is excited by  $\ddot{\mathbf{U}}_b$  in a parametric manner and for  $e_1 \neq 0$  also in a direct manner. The dash-pot  $c_a$  results in a position dependent viscous damping force, see expression  $C(\mathbf{Q}_1, \dot{\mathbf{Q}}_1)$  Eq. (5.19).

In general, the (set of) equation(s) of motion corresponding to an  $n^{\text{th}}$  order approximation of Eq. (5.5) and Eq. (5.6) are derived by the following steps

1. Discretize  $v(t, y)$  as in Eq. (5.9).
2. Approximate  $\kappa$  and  $u, y$  (Eq. (5.3) and Eq. (5.4)) with Taylor series expansions including terms up to  $n^{\text{th}}$  order in  $v, y$  and  $v_{0, y}$ .
3. Solve  $u(t, y)$  from the  $n^{\text{th}}$  order approximation of  $u, y$  by symbolic integration.
4. Compute the energy and work expressions Eq. (5.12), Eq. (5.13) and Eq. (5.14) by symbolic integration.
5. Derive the equations of motion using Lagrange equations Eq. (5.15) and omit all terms in  $\mathbf{Q}$  higher than  $n^{\text{th}}$  order.

This procedure is implemented in Maple routines [87], allowing to derive the equations of motions in an automatic manner. Higher order approximations of Eq. (5.5) and Eq. (5.6) result in higher order terms in  $\mathbf{Q}_i$  in the resulting equation(s) of motion.

## **5.2 Static and modal analysis**

In this section, the static response of the beam is examined for various orders of expansion of Eq. (5.3) and Eq. (5.4). Subsequently, a modal analysis is performed on the linearized equations of motion in order to study the eigenfrequencies of the initially pre-stressed beam. The results are numerically validated via a comparison with results obtained using FEM analyses.

For the static analysis, all the time-derivatives in the equation(s) of motion are set to zero and the case  $\ddot{\mathbf{U}}_b = 0$  [m/s<sup>2</sup>] is considered. By solving the resulting algebraic equation(s) for this case for a varying  $r_0$  [-] (the only present load-parameter for this case), static buckling of the thin beam is examined. Note that a numerical continuation scheme is used for this purpose. In all



Table 5.1: Parameter values.

$E$	$2.1 \cdot 10^{11}$	[N/m <sup>2</sup> ]
$\rho$	7850	[kg/m <sup>3</sup> ]
$L$	0.2	[m]
$b$	$15 \cdot 10^{-3}$	[m]
$h$	$0.5 \cdot 10^{-3}$	[m]
$g$	9.81	[m/s <sup>2</sup> ]

computations, the parameter values are used as listed in Table 5.1.

The static responses of the beam, using single-mode expansions of  $v(t, y)$  and  $v_0(y)$  ( $N = N_e = 1$  in Eqs. (5.9)-(5.10)) and various orders of expansion of Eq. (5.3) and Eq. (5.4), are depicted in Fig. 5.2. Note that the responses are characterized by plotting both the scaled transversal deflection of the middle of the beam ( $v(L/2)/h$ ) and the scaled axial deflection of the top of the beam ( $u(L)/L$ ) (for the quasi-static analysis the dependency on  $t$  of  $v(t, y)$  and  $u(t, y)$  is omitted). In the graphs also results from FE analysis are shown. The FE model of the beam consists of fifty 3-node *Timoshenko* beam elements known as element type 45, see [93]. In all FEM analyses kinematic relations are used which are valid for large displacements and large rotations and an updated Lagrange formulation is used. Note that the Timoshenko beam theory includes the effect of axial strain and transversal shear which are absent in the semi-analytical model derived in the previous section.

Since the beam is considered to be initially not perfectly straight ( $e_1 = 1$ ), the beam does not show a distinct buckling at  $r_0 = 1$  but a transition near  $r_0 \approx 0.95$  where the displacements rapidly increase. For low load levels (see enlargement **A** in Fig. 5.2), the FE model is axially less stiff than the semi-analytical model, irrespective of the order used for the expansions of Eq. (5.3) and Eq. (5.4). A plausible cause for this difference is the effect of axial strain which is present in the FE model and absent in the semi-analytical model. In the region  $r_0 \geq 0.9$ , the order of expansion of Eq. (5.4) and Eq. (5.3) has significant influence on the response. Note that in this region, higher order expansions converge to the FEM results. For the depicted range of displacements and orders of expansion, inclusion of the second mode and third mode ( $N = 3$  in Eq. (5.9), not shown) appeared to have no significant influence.

Next, the undamped eigenfrequencies of the beam with top mass are determined. Hereto, first the static equilibrium state for a given top mass  $r_0$  and imperfection  $e_1$  is determined. Subsequently, the equation(s) of motion are

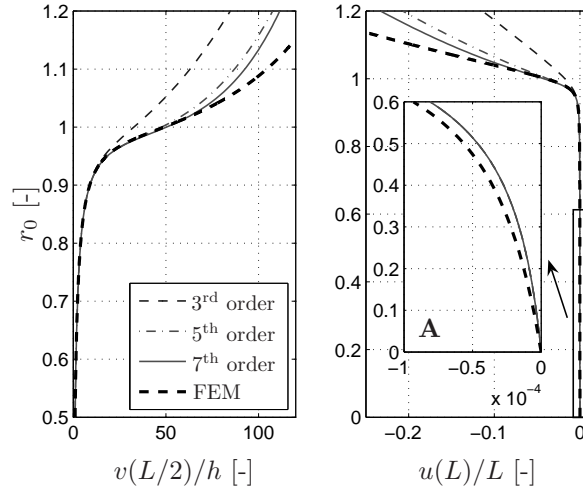


Figure 5.2: Static response (1-mode,  $e_1 = 1$ ).

linearized around this equilibrium state to determine the eigenfrequencies. The results are shown in Table 5.2 for various discretization approaches in combination with the third order expansions (Eq. (5.5) and Eq. (5.6)). Inclusion of the second mode and third mode in the discretization ( $N = 3$  in Eq. (5.9)) decreases the first eigenfrequency slightly. Especially for the first two eigenfrequencies, the semi-analytical results are in good agreement with the FEM results. For the considered values of  $r_0$ , higher order expansions of Eq. (5.3) and Eq. (5.4) do not show significant improvements.

Table 5.2: First three eigenfrequencies ( $f_i$ ) for  $e_1 = 1$ .

$r_0$	model	$f_1$ [Hz]	$f_2$ [Hz]	$f_3$ [Hz]
0.05	1-DOF	65.78	-	-
0.05	3-DOF	64.90	185.4	365.0
0.05	FEM	64.65	181.0	355.4
0.5	1-DOF	43.21	-	-
0.5	3-DOF	42.98	163.2	318.9
0.5	FEM	42.95	159.8	283.0
mode shape				

### 5.3 Steady-state analysis

In this section, the nonlinear dynamic response of the base-excited beam with top mass is considered for the case of a prescribed base acceleration of the form

$$\ddot{\mathbf{U}}_{\mathbf{b}} = r_d g \sin(2\pi ft). \quad (5.20)$$

The prescribed base-acceleration (Eq. (5.20)) has two parameters, i.e. the amplitude  $r_d$  [-] and the excitation frequency  $f$  [Hz] ( $g$  denotes the gravitation constant). Numerical continuation [33] of periodic solutions with the excitation frequency as continuation parameter is adopted to study the steady-state behaviour of the beam. Furthermore, also loci of bifurcations of the computed periodic solutions in a two parameter space are computed using two parameter numerical continuation [33]. The goal of the performed parameter study is to find out which instabilities (i.e. harmonic resonances and/or parametric resonances) are most severe and how they depend on the various parameters of the structure and/or the loading. Special attention is paid to the influence of the damping parameters, since it is known that the (nonlinear) damping characteristics are of great importance for the agreement between simulation results and experiments [7; 144; 145].

All results in this section are based on a model using the 3<sup>rd</sup> order expansions (Eq. (5.5) and Eq. (5.6)) and single-mode expansions of  $v(t, y)$  and  $v_0(y)$  ( $N = N_e = 1$  in Eqs. (5.9)-(5.10)). The validity of this model will be illustrated in the next section. Note that in all presented graphs, the periodic solutions are characterized by plotting the maximum dimensionless transversal displacement of the middle of the beam ( $\max[v(t, L/2)/h]$ ). The local stability of the periodic solutions is determined using Floquet theory [120]. Stable periodic solutions are plotted with solid lines whereas unstable periodic solutions are plotted with dashed lines.

First the response of the beam with a relatively small top mass ( $r_0 = 0.05$ ,  $m_t/m_{beam} = 14$ ) is considered. The frequency-amplitude plot for this case with a base excitation amplitude of  $r_d = 1.55$  and an initial imperfection of  $e_1 = 1$  is shown in Fig. 5.3. The linear viscous damping parameter  $c_1$  is set such that the linear vibration mode has a relative damping ratio of  $\xi = 0.02$ . The other damping parameter values are given by  $c_{q,1} = 0$  [kg/m] and  $c_a = 0.1$  [kg/s]. The response shows a 2<sup>nd</sup> superharmonic resonance at  $f \approx f_1/2$  (with  $f_1$  the undamped eigenfrequency, see Table 5.2), a harmonic resonance at  $f \approx f_1$  and a very strong 1/2 subharmonic resonance (period  $2T$  with  $T = 1/f$ ). The latter resonance is initiated at two period doubling bifurcations ( $PD$ , indicated by '◇') near  $f \approx 2f_1$  and ending at a cyclic fold bifurcation ( $CF$ , indicated by 'o') at  $f \approx 17$  [Hz]. The (small) harmonic resonance is due to direct excitation which only is present for  $e_1 \neq 0$ . The harmonic solutions decay in amplitude for  $|e| \rightarrow$

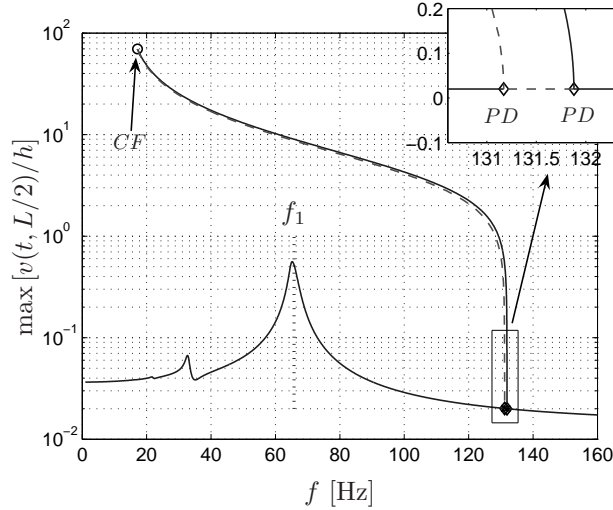


Figure 5.3: Frequency-amplitude plot ( $3^{\text{rd}}$ -order, 1-mode,  $e_1 = 1.0$ ,  $r_0 = 0.05$ ,  $r_d = 1.55$ ,  $c_a = 0.1$  [kg/s],  $c_{q,1} = 0$  [kg/m]).

0 and transform into the static equilibrium point  $\mathbf{Q}(t) = 0$  for the limit case  $e_1 = 0$ . The  $1/2$  subharmonic resonance is caused by the parametric excitation and shows softening behaviour. For  $e_1 = 0$  (not shown), the  $1/2$  subharmonic resonance also show softening. The inertia nonlinearities, therefore, clearly outweigh the stiffness nonlinearities in this case.

First the influence of the damping parameters  $c_{q,1}$  and  $c_a$  is examined. The influence of quadratic damping is studied first. In Fig. 5.4 the frequency-amplitude plot for  $c_{q,1} = 0.02$  (model and other parameters similar as used for Fig. 5.3) is shown. As can be noted, the additional quadratic damping force splits up the  $1/2$  subharmonic resonance peak into a smaller peak and a separate peak (island). For a higher quadratic damping constant ( $c_{q,1} = 0.05$ , see Fig. 5.5), the separate branch has disappeared and the small  $1/2$  subharmonic peak initiated around  $f \approx 2f_1$  no longer exhibits cyclic fold bifurcations. The harmonic response branches, depicted in the Figs. 5.3, 5.4 and 5.5, are hardly influenced by the quadratic damping (for the parameter values considered).

The evolution of the  $1/2$  subharmonic resonance peak for a varying quadratic damping parameter is further examined by computing the loci of the cyclic fold bifurcation(s)  $CF$  and the two period doubling bifurcations  $PD$  in the parameter space spanned by  $c_{q,1}$  and  $f$ , see Fig. 5.6. For clarification, the locations of the cyclic fold bifurcations  $CF_i$  as indicated in Fig. 5.4 for

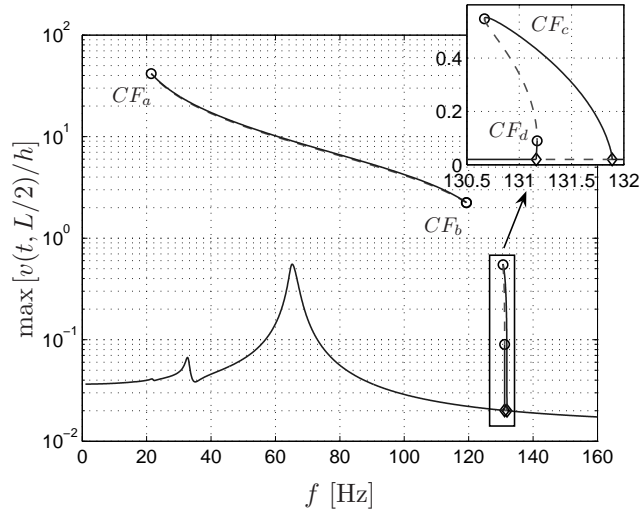


Figure 5.4: Frequency-amplitude plot ( $3^{\text{rd}}$ -order, 1-mode,  $e_1 = 1.0$ ,  $r_0 = 0.05$ ,  $r_d = 1.55$ ,  $c_a = 0.1$  [kg/s],  $c_{q,1} = 0.02$  [kg/m]).

$c_{q,1} = 0.02$  and the two period doubling bifurcations  $PD_i$  as indicated in Fig. 5.5 for  $c_{q,1} = 0.05$  are shown in Fig. 5.6. In the region  $0.017 \leq c_{q,1} \leq 0.034$  [kg/m], multiple cyclic fold bifurcations exist for one value of  $c_{q,1}$ . This indicates the existence of a separate branch (as shown in Fig. 5.4). For  $c_{q,1} \geq 0.032$  [kg/m], the small  $1/2$  subharmonic branch near  $f \approx 2f_1$  no longer exhibits cyclic fold bifurcations (see enlargement **A**), and for  $c_{q,1} \geq 0.034$  [kg/m] the separate branch between  $CF_a$  and  $CF_b$  has disappeared. At  $c_{q,1} \approx 0.385$  (see enlargement **B**), the two period doubling bifurcations merge and cease to exist, meaning that the harmonic response no longer exhibits a small region of instability around  $f \approx 2f_1$ . In general, this does not guarantee that the subharmonic response has disappeared. However, the two parameter bifurcation diagram (Fig. 5.6) gives a strong indication that this is the case here.

Using the same two parameter continuation approach, but now with continuation parameters  $c_a$  and  $f$ , the influence of the discrete dash-pot  $c_a$  is studied for  $c_{q,1} = 0$  [kg/m], see Fig. 5.7. For an increasing value of  $c_a$ , the locus of  $CF$  approaches the locus of  $PD$  in a monotonically increasing manner, meaning that the  $1/2$  subharmonic branch does not break up (no separate island(s)). At  $c_a \approx 4.34$  [kg/s], the locus of  $CF$  merges with the locus of  $PD$  in a codimension 2 bifurcation point (see enlargement **A**) and at  $c_a \approx 4.45$  [kg/s], the two period doubling bifurcations merge and cease to exist. Between these two parameter values, a small  $1/2$  subharmonic branch exists, see e.g. Fig. 5.8. The harmonic

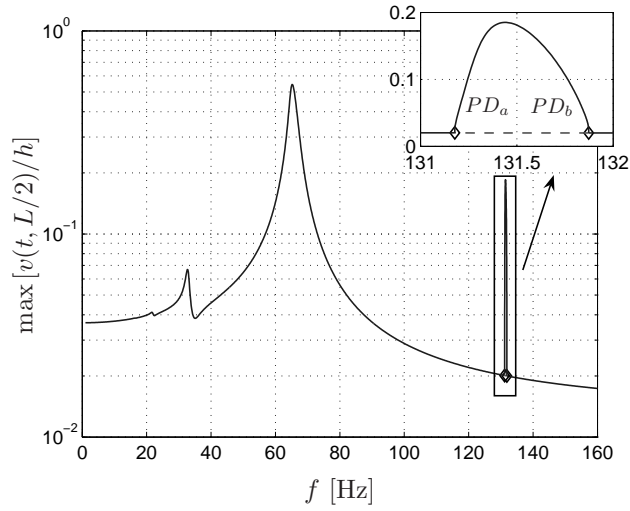


Figure 5.5: Frequency-amplitude plot ( $3^{\text{rd}}$ -order, 1-mode,  $e_1 = 1.0$ ,  $r_0 = 0.05$ ,  $r_d = 1.55$ ,  $c_a = 0.1$  [kg/s],  $c_{q,1} = 0.05$  [kg/m]).

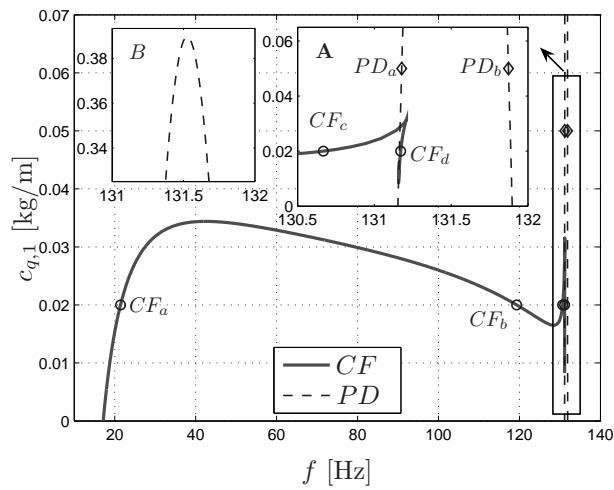


Figure 5.6: Two parameter continuation results ( $3^{\text{rd}}$ -order, 1-mode,  $e_1 = 1.0$ ,  $r_0 = 0.05$ ,  $r_d = 1.55$ ,  $c_a = 0.1$  [kg/s]).

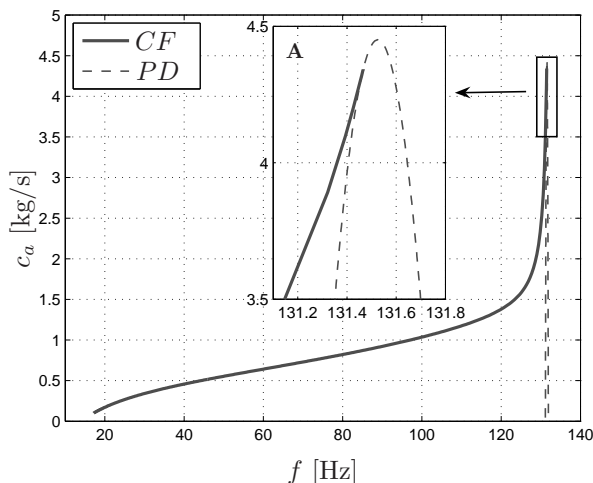


Figure 5.7: Two parameter continuation results ( $3^{\text{rd}}$ -order, 1-mode,  $e_1 = 1.0$ ,  $r_0 = 0.05$ ,  $r_d = 1.55$ ,  $c_{q,1} = 0.0$  [kg/m]).

branches, depicted in Figs. 5.3 and 5.8, are hardly influenced by the damping due to the discrete dash-pot (for the considered values of  $c_a$ ).

Depending on the values of the damping parameters, the  $1/2$  subharmonic resonance due to the parametric excitation can be very severe. Using again the two-parameter continuation approach of the cyclic fold bifurcation(s) and the period doubling bifurcations, now with continuation parameters  $r_d$  and  $f$ , a threshold value for  $r_d$  is determined with respect to the existence of this  $1/2$  subharmonic resonance. For the case considered in Fig. 5.9 ( $c_a = 0.1$  [kg/s] and  $c_{q,1} = 0$  [kg/m]), the small region of instability around  $f \approx 2f_1$  in the harmonic response branch disappears at  $r_d \approx 1.53$  for  $e_1 = 1$  and at  $r_d \approx 1.52$  for  $e_1 = 0$  (see enlargement A). However, for lower values of  $r_d$ , the  $1/2$  subharmonic resonance still exists as a separate branch (island). This island shrinks for decreasing values of  $r_d$  and disappears at  $r_d \approx 1.02$  (see Fig. 5.9). Inclusion of quadratic damping can significantly change the scenario, see Fig. 5.10. For  $c_{q,1} = 0.02$  [kg/m], the scenario is still similar as shown in Fig. 5.9, i.e. for a decreasing  $r_d$  the  $1/2$  subharmonic resonance branch becomes first detached from the harmonic resonance branch, shrinks further and finally disappears (now at  $r_d \approx 1.35$ ). However, for  $c_{q,1} = 0.05$  [kg/m], the threshold for  $r_d$  corresponds to the event where the two period doubling bifurcations merge at  $r_d \approx 1.53$ . So, only in the latter case, the existence of the  $1/2$  subharmonic resonance branch may be determined by considering the stability of harmonic

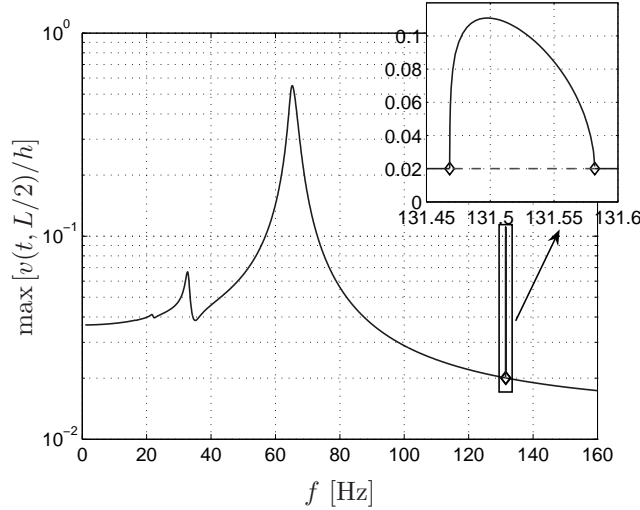


Figure 5.8: Frequency-amplitude plot (3<sup>rd</sup>-order, 1-mode,  $e_1 = 1.0$ ,  $r_0 = 0.05$ ,  $r_d = 1.55$ ,  $c_a = 4.35$  [kg/s],  $c_{q,1} = 0.0$  [kg/m]).

responses in the neighbourhood of  $f \approx 2f_1$ .

Until now the linear damping parameter  $c_1$  is set such that the linear vibration mode has a relative damping ratio of  $\xi = 0.02$ . The frequency-amplitude plot for a much lower linear damping ratio ( $\xi = 0.001$ , model and other parameters similar as used for Fig. 5.3) is depicted in Fig. 5.11. As can be noted, for the lower value of  $\xi$ , also the harmonic resonance at  $f \approx f_1$  and the 2<sup>nd</sup> super harmonic resonance at  $f \approx f_1/2$  show softening behaviour. Nevertheless, the parametric resonance remains the most severe type of resonance. The influence of the linear damping ratio  $\xi$  on the determined threshold value for  $r_d$  with respect to the existence of this 1/2 subharmonic resonance is depicted in Fig. 5.12 for the same nonlinear damping parameters as depicted in Fig. 5.9 and  $e_1 = 1$ . As can be noted, the value of  $\xi$  has a significant influence on the threshold value for  $r_d$ . Furthermore, for  $\xi = 0.001$ , the threshold for  $r_d$  corresponds to the event where the two period doubling bifurcations merge at  $f \approx 2f_1$ , while for the higher values of  $\xi$  the threshold for  $r_d$  corresponds to the minimum in loci of cyclic fold bifurcations.



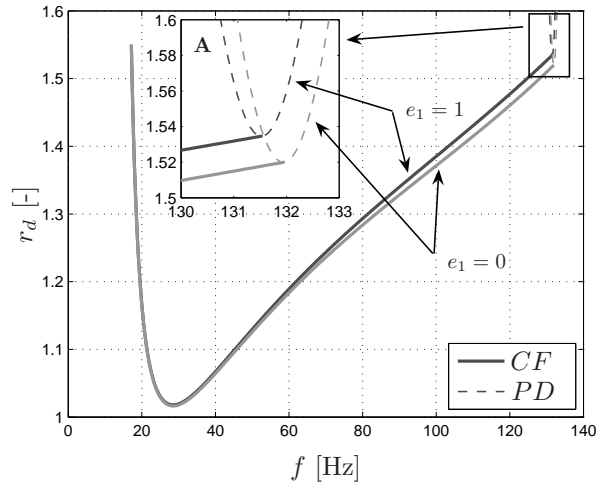


Figure 5.9: Two parameter continuation results ( $3^{\text{rd}}$ -order, 1-mode,  $r_0 = 0.05$ ,  $c_a = 0.1$  [kg/s],  $c_{q,1} = 0.0$  [kg/m]).

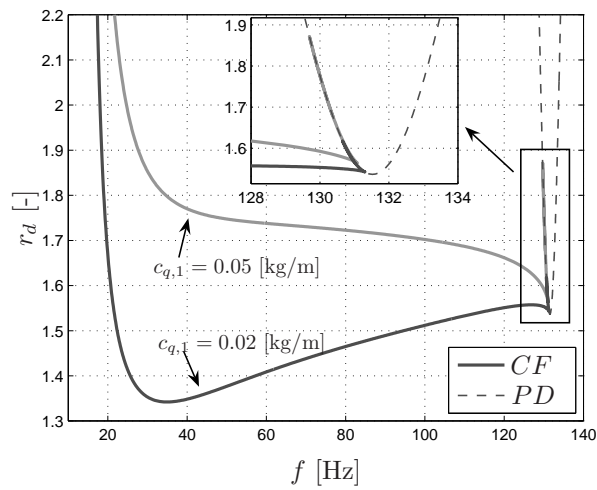


Figure 5.10: Two parameter continuation results ( $3^{\text{rd}}$ -order, 1-mode,  $e_1 = 1.0$ ,  $r_0 = 0.05$ ,  $c_a = 0.1$  [kg/s]).

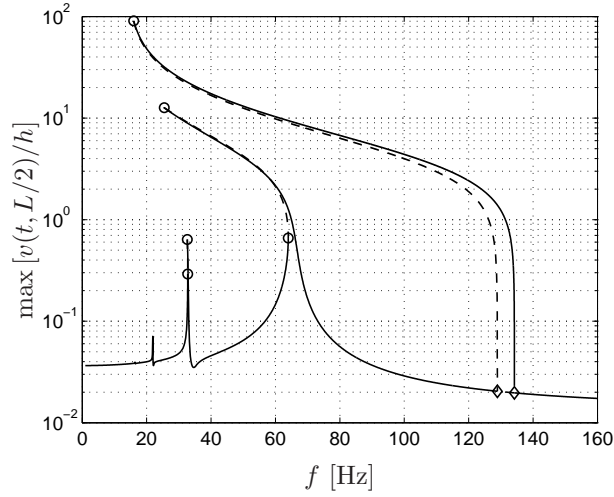


Figure 5.11: Frequency-amplitude plot ( $3^{\text{rd}}$ -order, 1-mode,  $e_1 = 1.0$ ,  $r_0 = 0.05$ ,  $c_{q,1} = 0.0$  [kg/m],  $c_a = 0.1$  [kg/s],  $\xi = 0.001$ ).

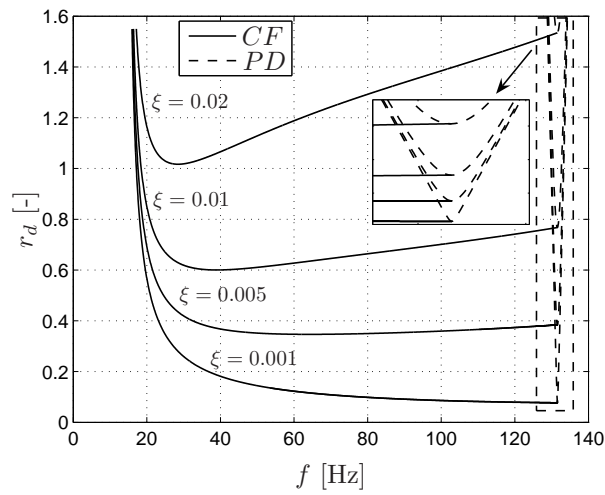


Figure 5.12: Two parameter continuation results ( $3^{\text{rd}}$ -order, 1-mode,  $e_1 = 1.0$ ,  $r_0 = 0.05$ ,  $c_{q,1} = 0.0$  [kg/m],  $c_a = 0.1$  [kg/s]).

Next, the steady-state response of the same beam is considered for a ten times larger top mass ( $r_0 = 0.5$  so the static load is half the static buckling load and  $m_t/m_{beam} = 140$ ). The frequency-amplitude plot for this case with a base excitation amplitude of  $r_d = 0.12$ , an initial imperfection of  $e_1 = 1$  and damping parameters  $\xi = 0.02$ ,  $c_{q,1} = 0$  [kg/m] and  $c_a = 0.5$  [kg/s] is shown in Fig. 5.13. Apart from the fact that for the larger top mass also the harmonic resonance at  $f \approx f_1$  (for  $f_1$ , see Tab. 5.2) shows softening, the global picture is similar as found for the small top mass, see Fig. 5.3.

In a similar manner as shown in Figs. 5.6 and 5.7 for  $r_0 = 0.05$ , the influence of the damping parameters  $c_a$  and  $c_{q,1}$  on the  $1/2$  subharmonic response is shown in Fig. 5.14 for  $r_d = 0.5$ . Figure 5.14 (top) shows the influence of  $c_a$  for  $c_{q,1} = 0$  [kg/m] and Fig. 5.14 (bottom) shows the influence of  $c_{q,1}$  for  $c_a = 0.5$  [kg/s]. The two-parameter bifurcation diagram for  $c_a$  and  $f$  shows in the region  $4.0 \leq c_a \leq 9.5$  [kg/s], multiple coexisting cyclic fold bifurcations, whereas at  $c_a \approx 4.25$  [kg/s] the two period doubling bifurcations merge and cease to exist. This means that in the region  $4.25 \leq c_a \leq 9.5$  [kg/s], a separate  $1/2$  subharmonic branch exists while the harmonic branch does not exhibit a small region of instability near  $f \approx 2f_1$ . The two-parameter bifurcation diagram for  $c_{q,1}$  and  $f$  for  $r_0 = 0.5$  and  $c_a = 0.5$ , depicted in Fig. 5.14 (bottom), is qualitatively similar as found for  $r_0 = 0.05$  and  $c_a = 0.1$ , see Fig. 5.6.

Similar as for the case  $r_0 = 0.05$  and  $c_a = 0.1$  (see Fig. 5.10), also for the case  $r_0 = 0.5$  and  $c_a = 0.5$  a threshold value for the existence of the  $1/2$  subharmonic response can be determined for  $r_d$ , see Fig. 5.15. The diagram is qualitatively similar to the diagram found for  $r_0 = 0.05$  and  $c_a = 0.1$  (see Fig. 5.10). However, for the larger top mass, the two period doubling bifurcations merge for  $e_1 = 0$  at a (relatively) much lower value for  $r_d$  than for the case  $e_1 = 1$ . Therefore, it seems that the considered geometric imperfection tends to *increase* the threshold for instability of the harmonic response at  $f \approx 2f_1$ . Note that the imperfect beam is forced in both a direct manner and in a parametric manner. The amplitude of the direct forcing depends on the initial imperfection and on the initial static deflection and apparently has a stabilizing effect on the harmonic response around  $f/f_1 = 2$ , as was also reported in [132].

Based on the results computed using the third-order single-mode model, it can be concluded that for both cases considered ( $r_0 = 0.05$  and  $r_0 = 0.5$ ), the  $1/2$  subharmonic responses show a strong dependence on the damping parameters. For example, without knowledge of the damping parameters, the question whether or not (for the considered level of imperfection) the  $1/2$  subharmonic resonance is more severe than the harmonic resonance (compare for example the cases depicted in Fig. 5.3 and Fig. 5.5) can not be answered. Experimental identification of the damping characteristics is, therefore, essential before any

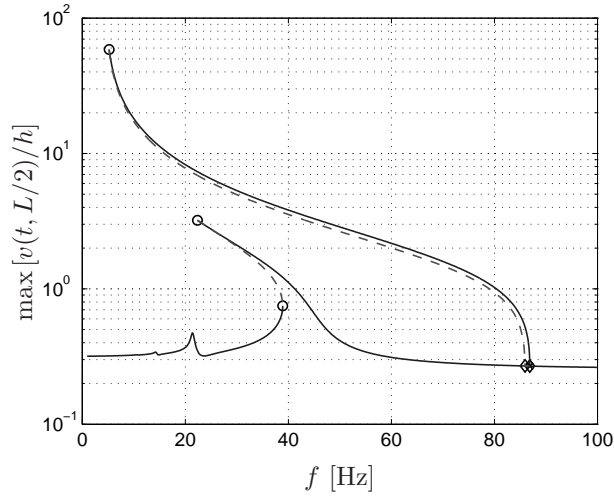


Figure 5.13: Frequency-amplitude plot ( $3^{\text{rd}}$ -order, 1-mode,  $e_1 = 1.0$ ,  $r_0 = 0.5$ ,  $r_d = 0.12$ ,  $c_a = 0.5$  [kg/s],  $c_{q,1} = 0.0$  [kg/m]).

conclusions can be drawn on the dynamic stability limits of the base-excited beam with top mass. Experimental results will be discussed in Chapter 6. In the next section, first the influence of the order of the expansions of Eq. (5.3) and Eq. (5.4) and the influence of the number of modes used in the discretization of the transversal displacement field will be discussed.

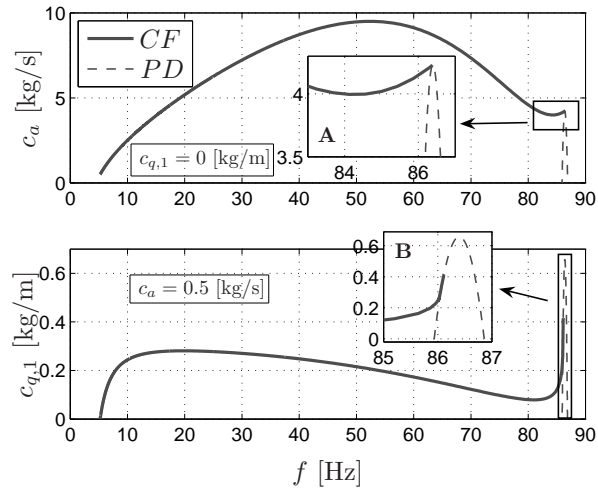


Figure 5.14: Two parameter continuation results ( $3^{\text{rd}}$ -order, 1-mode,  $e_1 = 1.0$ ,  $r_0 = 0.5$ ,  $r_d = 0.12$ ).

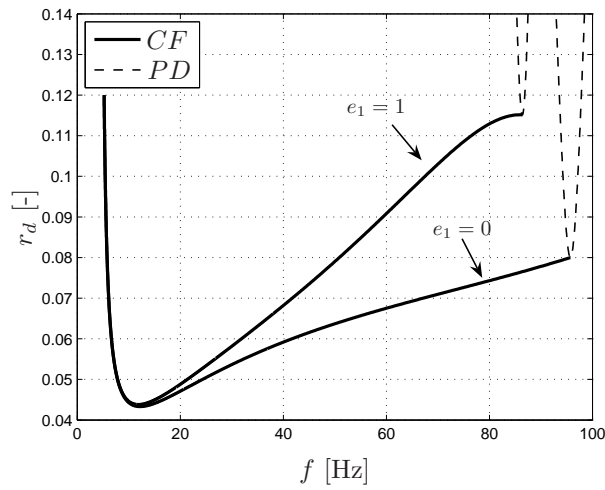


Figure 5.15: Two parameter continuation results ( $3^{\text{rd}}$ -order, 1-mode,  $r_0 = 0.5$ ,  $c_a = 0.5$  [kg/s],  $c_{q,1} = 0.0$  [kg/m]).

## 5.4 Convergence of steady-state results

In the previous section, large amplitude vibrations are predicted with the third-order single-mode approach. The accuracy of the results predicted by the third-order single-mode model is studied in this section. First, the influence of higher-order expansions of Eq. (5.3) and Eq. (5.4) for the single-mode model is illustrated in Fig. 5.16 by considering the stable 1/2 subharmonic response, which was already shown in Fig. 5.3 for the third-order single-mode model. Clearly, the order of expansion has some influence on the response with deflections  $\max[v(t, L/2)/h] > 20$ . The response, however, does not change qualitatively.

The difference in the harmonic response of the beam, modelled using one mode ( $N = 1$  in Eq. (5.9)) or using three modes ( $N = 3$  in Eq. (5.9)) is shown in Fig. 5.17 (both models are based on 3<sup>rd</sup> order expansions of Eq. (5.3) and Eq. (5.4)). For both models, the linear viscous damping parameter(s)  $c_i$  are set so that the linear vibration mode(s) have the same relative damping coefficient(s): for the single-mode model  $\xi_1 = 0.02$ , for the three mode model  $\xi_1 = \xi_2 = \xi_3 = 0.02$ . The small shift in frequency (see enlargement **A** in Fig. 5.17) of the first harmonic resonance is in agreement with the difference between the first eigenfrequency of the single-mode model and the first eigenfrequency of the three-mode model (see Table 5.2). Also, the third mode instigates an extra

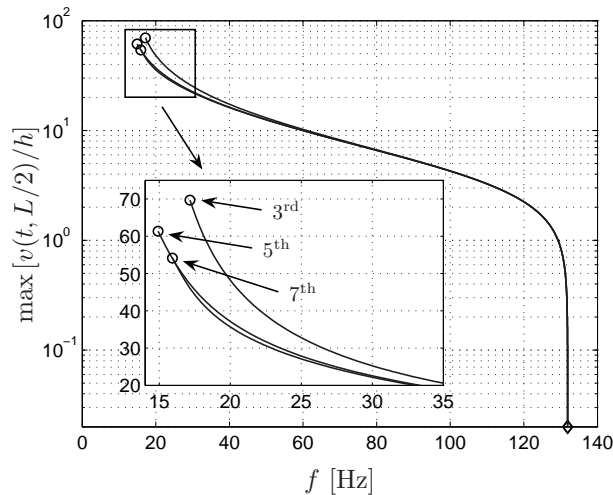


Figure 5.16: Stable 1/2 subharmonic response for various orders of expansion (1-mode,  $e_1 = 1.0$ ,  $r_0 = 0.05$ ,  $r_d = 1.55$ ,  $c_a = 0.1$  [kg/s],  $c_{q,1} = 0.0$  [kg/m]).

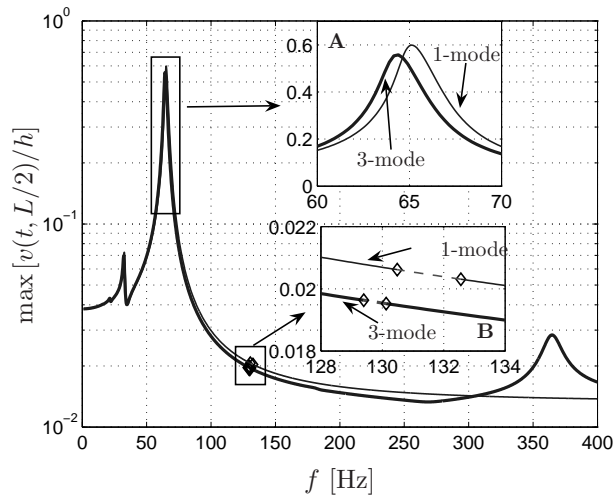


Figure 5.17: Influence of additional modes on the harmonic response (3<sup>rd</sup> order,  $e_1 = 1.0$ ,  $r_0 = 0.05$ ,  $r_d = 1.65$ ,  $c_a = 0.1$  [kg/s],  $c_{q,1} = c_{q,2} = c_{q,3} = 0$  [kg/m]).

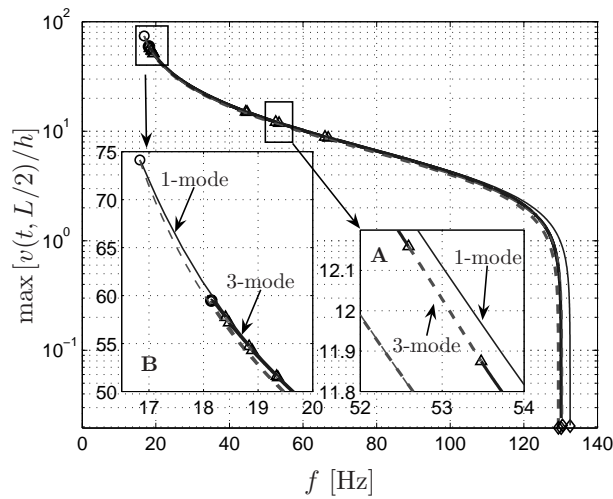


Figure 5.18: Influence of additional modes on 1/2 subharmonic response (3<sup>rd</sup> order,  $e_1 = 1.0$ ,  $r_0 = 0.05$ ,  $r_d = 1.65$ ,  $c_a = 0.1$  [kg/s],  $c_{q,1} = c_{q,2} = c_{q,3} = 0$  [kg/m]).

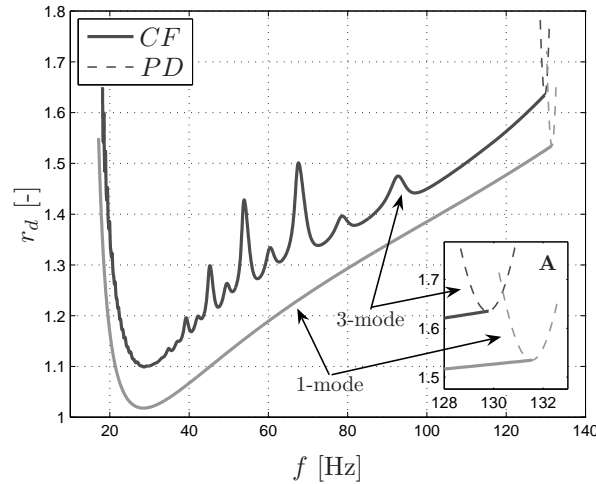


Figure 5.19: Two parameter continuation results ( $3^{\text{rd}}$  order,  $e_1 = 1.0$ ,  $r_0 = 0.05$ ,  $c_a = 0.1$  [kg/s],  $c_{q,1} = c_{q,2} = c_{q,3} = 0$  [kg/m]).

harmonic resonance peak around the third eigenfrequency ( $f \approx 365$  [Hz]). Since the considered geometric imperfection is symmetric with respect to  $y/L = 1/2$  and the second mode is skew symmetric, the second generalized coordinate  $\mathbf{Q}_2$  is not directly excited. Therefore, no harmonic resonance peak appears around  $f \approx f_2$ . Note, however, that the second mode can be parametrically excited near  $f \approx 2f_2$ . However, this is only possible for significantly higher values of  $r_d$ .

The influence of the extra modes on the  $1/2$  subharmonic response, initiated at the two period doubling bifurcations near  $f \approx 2f_1$  (see Fig. 5.17, enlargement **B**), is shown in Fig. 5.18. In the stable  $1/2$  subharmonic response branch of the 3-mode model, six regions of instability appear. One of such regions is shown in enlargement **A** in Fig. 5.18. At the borders of these small regions, centered around  $f = 18.44$ ,  $f = 18.86$ ,  $f = 19.85$ ,  $f = 44.62$ ,  $f = 53.03$  and  $f = 66.41$  [Hz], quasi-periodic responses are initiated via secondary Hopf bifurcations (indicated by ' $\Delta$ '). Furthermore, the  $1/2$  subharmonic response of the single-mode model ends at a slightly lower frequency than the  $1/2$  subharmonic branch of the three-mode model, see enlargement **B** in Fig. 5.18.

The loci of the cyclic fold bifurcations and the two period doubling bifurcations corresponding to the  $1/2$  subharmonic branches of the 1-mode and the 3-mode model in the space spanned by  $f$  and  $r_d$ , are compared in Fig. 5.19. The locus of the cyclic fold for the three-mode model is clearly less smooth than



the locus of the cyclic fold for the single-mode model. This indicates that for  $1.10 \leq r_d \leq 1.51$ , the  $1/2$  subharmonic branch of the three-mode model splits into a number of small separate branches. Furthermore, an important observation is that the threshold value for  $r_d$  for parametric resonance to occur appears to be somewhat higher for the three-mode model ( $r_d = 1.10$ ) than for the single-mode model ( $r_d = 1.02$ ). Although more research is required before this result can be generalized, this observation may be beneficial since it allows to compute a lower bound for the threshold value for  $r_d$  using the (computationally less expensive) single-mode model.

## 5.5 Conclusions

In this chapter, the steady-state nonlinear dynamics of a base-excited clamped-clamped thin beam with top mass has been discussed. Based on Taylor series expansions of the inextensibility constraint and the exact curvature, and by using one or more basis functions, a semi-analytical model has been derived. The semi-analytical model has been numerically validated by a comparison with quasi-static and modal analysis results obtained from FEM analyses. The steady-state response of the base-excited beam has been investigated for varying excitation frequency using numerical continuation of periodic solutions. Furthermore, also loci of bifurcations are computed in a two parameter space. The validity of steady-state results, computed using the third-order single-mode model is shown. Hereto, the influence of higher-order expansions of the inextensibility constraint and the exact curvature and the influence of the number of modes used in the discretization is examined.

Since the beam is considered to be not perfectly straight, the beam is excited both in a direct manner and in a parametric manner. The response of the beam, therefore, shows both harmonic and  $1/2$  subharmonic resonances. Depending on the values of the damping parameters, the  $1/2$  subharmonic resonance due to the parametric excitation can be very severe and must be avoided.

The  $1/2$  subharmonic resonance may appear as a resonance peak emerging from the harmonic response branch, as a separate branch (island) or as a combination of both. Despite this complicated appearance of the parametric resonance, the threshold value of the dynamic excitation parameter for the existence of parametric resonance can still be determined in a straightforward manner using the two-parameter continuation approach. The results indicate a strong dependence of the  $1/2$  subharmonic response on the damping parameters. Experimental identification of the damping characteristics is, therefore, essential before any conclusions can be drawn on the dynamic stability limits of the base-excited thin beam with top mass. For this purpose, in the next chapter experiments will be performed and experimental results

will be confronted with semi-analytical results.

## *Experiments with a base-excited thin beam with top mass*

**I**n the previous chapter, the dynamic stability of a base-excited thin beam with top mass is examined using a semi-analytical approach. In this study, it is shown that the third-order single-mode semi-analytical model is able to capture to a large extent, the first harmonic resonance and the first (large amplitude)  $1/2$  subharmonic resonance of the base-excited (initially unbuckled) thin beam. Furthermore, it is shown that nonlinear damping effects can strongly affect the  $1/2$  subharmonic resonance. The objective of this chapter is to validate the (nonlinear) semi-analytical model and to identify experimentally the damping characteristics and geometric imperfections of the thin beam.

In the numerical analysis as presented in Chapter 5, a base-excitation in the form of a prescribed harmonic base-acceleration is considered. However, at the experimental setup the base-excitation is realized by supplying a harmonic input voltage to an electrodynamic shaker system. For the latter case, the resulting base acceleration will not be purely harmonic, will not have a constant amplitude but will be determined by the dynamics of the shaker system carrying the thin beam with top mass. Results for voltage excitation can thus not directly be compared with results for a prescribed harmonic base-acceleration as considered in Chapter 5. To be able to compare the experimental results with the semi-analytical results, the equations of motion for the base-excited thin beam with top mass (as derived in Chapter 5) will be coupled with a model of the shaker.

The outline for this chapter is as follows. In the next section, the experimental setup of the base-excited thin beam with top mass will be introduced. In Section 6.2, the semi-analytical coupled shaker-structure model will be discussed. The steady-state dynamical responses predicted by the semi-analytical approach and obtained experimentally will be compared in Section 6.3. Finally, in Section 6.4 conclusions will be presented.

---

Preliminary results for this chapter are presented in [83].

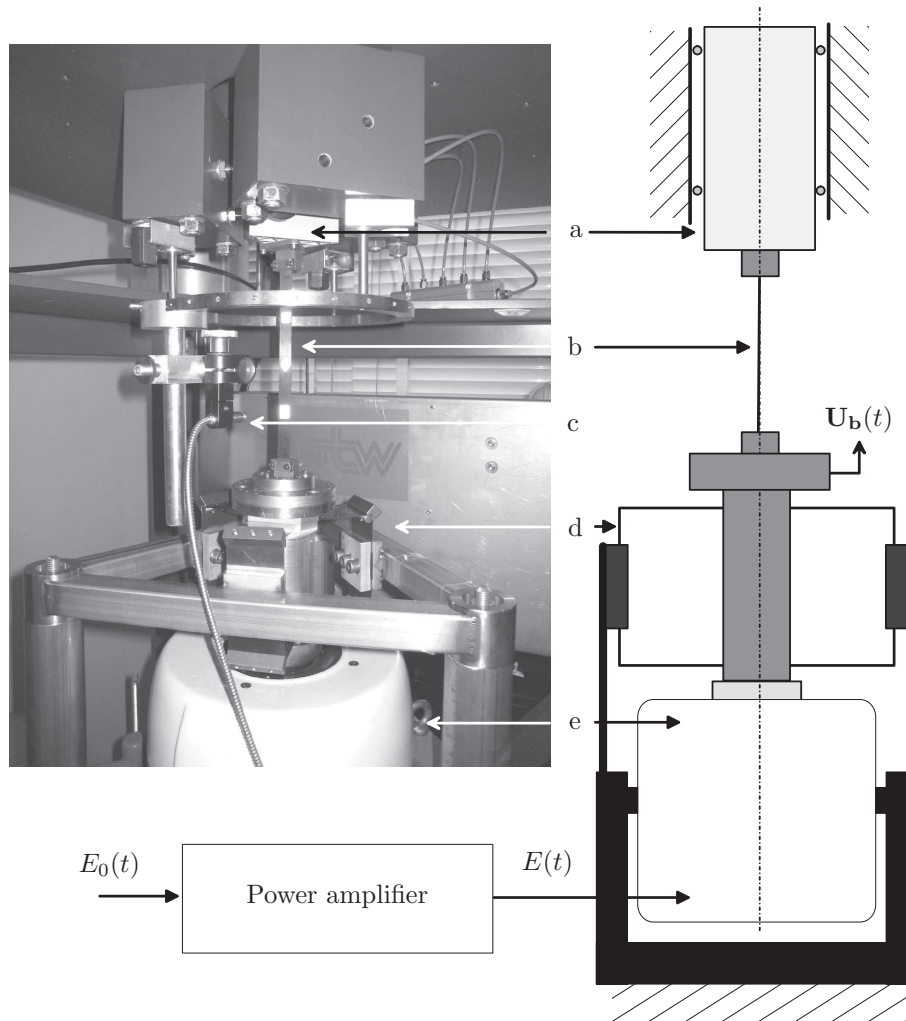


Figure 6.1: Picture and schematic overview of the experimental setup (a: top linear sledge (top mass) based on air bearings, b: thin beam, c: laser vibrometer, d: bottom elastic support mechanism, e: electrodynamic shaker).

## 6.1 Experimental setup

A picture and a schematic overview of the experimental setup are depicted in Fig. 6.1. The base excitation of the thin beam is realized by using an electrodynamic shaker system. The thin beam is clamped between two linear sledges with very low friction in axial direction. The linear sledge at the top side is based on air bearings and at the bottom side the linear sledge is realized by an elastic support mechanism based on folded leaf springs. The bottom linear sledge is mounted rigidly on top of the shaker. Note that the elastic support mechanism at the bottom side of the beam is included since the shaker armature suspension has a very low rotational stiffness. The upper linear sledge with clamping block also acts as the rigid top mass ( $m_t$ ). The top mass can be increased by mounting additional masses on top of the upper linear sledge. The moving mass of the lower linear sledge, including the mass of the bottom clamping block and the mass of the shaker armature, equals  $m_o = 3.2$  [kg]. The beam used for the experiments is made from spring steel. The material and geometric properties of the beam are listed in Table 6.1. Here it is noted that the value for the Young's modulus  $E$  later will be used as a parameter to be identified to account for, for example, (small) errors in the discretization of the displacement field and (small) errors in the assumed (clamped-clamped) boundary conditions for the beam. The identified Young's modulus should not differ too much from its well-known value given in Table 6.1.

Table 6.1: Geometrical properties of the thin beam (\* this parameter will be further refined during the identification procedure with the experimental results).

$E^*$	$2.0 \cdot 10^{11}$	[N/m <sup>2</sup> ]
$\rho$	7850	[kg/m <sup>3</sup> ]
$L$	180	[mm]
$b$	15	[mm]
$h$	0.5	[mm]

At the experimental setup, the base-excitation is introduced by supplying a harmonically varying input voltage

$$E_0(t) = v_d \sin(2\pi ft) \text{ [V]}, \quad (6.1)$$

to the power amplifier which output voltage ( $E(t)$ , see Fig. 6.1) is supplied to the shaker. Due to this voltage, a current will run through the shaker coil generating a force in axial direction of the assembly on top of the shaker. The amplifier works in a voltage mode of operation (i.e. the output voltage of the

amplifier is kept proportional to its input voltage) and no active feedback is used to control the acceleration of the shaker armature ( $\ddot{\mathbf{U}}_{\mathbf{b}}$ ). Consequently, the resulting acceleration of the shaker (and thus the effective axial force on the thin beam with top mass) will not be proportional to the input voltage  $E_0(t)$  as given by Eq. (6.1), but will be determined by the dynamics of the shaker system carrying the thin beam with top mass. More details about the shaker are provided in Appendix A.

A laser vibrometer (Ono Sokki LV 1500) is used to measure the transversal velocity ( $\dot{v}$ ) at one point of the beam. In the static equilibrium state obtained for zero input voltage ( $E_0 = 0$  [V]), the vibrometer is located at beam height  $y = L/4$  (see Fig. 5.1). Note that  $y$  is measured with respect to the base motion  $\mathbf{U}_{\mathbf{b}}$  (see Chapter 5) and  $\mathbf{U}_{\mathbf{b}}$  itself is measured with respect to its static equilibrium state. The vibrometer thus measures the transversal velocity of the beam at *absolute* height  $L/4 - \mathbf{U}_{\mathbf{b}}$  (note that in general  $\mathbf{U}_{\mathbf{b}} \ll L/4$ ). The signal of the laser vibrometer is numerically integrated to obtain measurements in terms of transversal displacements  $v$ . To avoid drift during the numerical integration, the measurement signal is filtered using the high pass filter

$$H_{hp}(s) = \frac{s^2}{s^2 + 14.14s + 100}, \quad (6.2)$$

where  $s = j\omega$  (with  $j^2 = -1$ ). The filter (Eq. (6.2)) has a cut-off frequency of  $f = 1.6$  [Hz]. The data-acquisition and input signal generation is performed using a Laptop with Matlab/Simulink in combination with a TUE-DACS AQI [55] (sample frequency 4 [kHz]).

## 6.2 Semi-analytical model

In the numerical analysis as presented in Chapter 5, the axial forcing of the thin beam with top mass is realized by prescribing a harmonically varying base-acceleration with constant amplitude. However, as noted before, at the experimental setup the axial forcing of the thin beam is realized by supplying a harmonic input voltage with constant amplitude to the shaker system. Dynamic response results for this type of excitation can not directly be compared with results for a prescribed harmonic base-acceleration.

To be able to compare the experimental results with the semi-analytical results, the equations of motion for the base-excited thin beam structure as derived in Chapter 5, must be coupled with a model of the electrodynamic shaker. The dynamics of the shaker are captured by two coupled linear ODEs (one describing the mechanical part of the shaker and one describing the

electrical part of the shaker). The derivation of the shaker model and the approach to obtain the total set of equations of motion describing the coupled shaker/structure dynamics is outlined in Section A.1 of Appendix A.

For the comparison with the experimental results, a semi-analytical model based on a single mode discretization of  $v$  and  $v_0$  ( $N = N_e = 1$ , see Eq. (5.9) and Eq. (5.10)) and a semi-analytical model based on a two mode discretization of  $v$  and  $v_0$  ( $N = N_e = 2$ , see Eq. (5.9) and Eq. (5.10)), will be considered. These models are designated as the 1-MODE model (with the shaker model the model has total 3-DOF) and the 2-MODE model (coupled model has 4 DOF), respectively. All models considered in this chapter are based on third-order Taylor series expansions of the inextensibility constraint Eq. (5.3) and the curvature Eq. (5.4). Note that the equations of motion for the 1-MODE model are illustrated in Appendix A.

The semi-analytical models have a number of parameters, i.e. imperfection and damping parameters, which must be identified to be able to make a comparison with the experimental results. As stated before, to be able to cope with small model mismatches, the Young's modulus  $E$  is also considered as a parameter to be identified. The effect of the discrete dash-pot with damping constant  $c_a$  (see Chapter 5) is not taken here. Consequently, the 1-MODE model has four unknown parameters (i.e.  $e_1$ ,  $c_1$ ,  $c_{q,1}$  and  $E$ ) and the 2-MODE model has seven unknown parameters (i.e.  $e_1$ ,  $c_1$ ,  $c_{q,1}$ ,  $e_2$ ,  $c_2$ ,  $c_{q,2}$  and  $E$ ). The numerical values for these parameters are identified by fitting experimental steady-state responses to periodic solutions of the semi-analytical model using a weighted least squares method. For the weighted least squares fitting procedure only harmonic responses are used, obtained for eight excitation frequencies equally distributed over the frequency range of interest. Further details on the applied weighted least squares procedure can be found in [71].

### 6.3 Results

In this section, experimental results for the base-excited thin beam will be compared with semi-analytical results obtained for the 1-MODE model and the 2-MODE model (see Section 6.2). The experimental steady-state results are obtained for a varying excitation frequency using the stepped sine frequency sweep procedure as outlined in Appendix B. For each case, a sweep-up (the excitation frequency is incrementally increased) and a sweep-down (the excitation frequency is incrementally decreased) is performed using a step size of  $\Delta f = 0.5$  [Hz]. For the frequency sweep analysis, the parameters  $N_e = 100$  [-] and  $N_t = 50$  [-] are used, see Appendix B.

The dynamic steady-state response of the beam is characterized using the laser

Table 6.2: Identified parameter values based on experimental results obtained for  $v_d = 0.03$  [V] and  $m_t = 0.51$  [kg].

Parameters	beam 1, 1-MODE	beam 2, 1-MODE	beam 2, 2-MODE
$e_1$ [-]	1.24	1.36	1.36
$c_1$ [Ns/m]	0.04	0.0	0.0
$c_{q,1}$ [kg/m]	0.20	0.20	0.2
$e_2$ [-]	-	-	0.04
$c_2$ [Ns/m]	-	-	0.04
$c_{q,2}$ [kg/m]	-	-	0.0
$E$ [N/m <sup>2</sup> ]	$1.92 \cdot 10^{11}$	$1.95 \cdot 10^{11}$	$1.95 \cdot 10^{11}$

vibrometer measurement signal  $m^1(t) = \dot{v}(t, L/4 - \mathbf{U}_b)$  and its filtered and numerically integrated version  $m^2(t) = v(t, L/4 - \mathbf{U}_b)$ . Based on these two signals, response measures are determined using the averaging procedure as explained in Appendix B. The measures obtained are denoted by  $\tilde{M}^1 = \tilde{V}_{L/4}$  [m/s] and  $\tilde{M}^2 = \tilde{V}_{L/4}$  [m]. Experimental results will be presented for two different beams (designated as **beam 1** and **beam 2**) which have the same dimensions and material properties (see Table 6.1) but have slightly different geometric imperfections and damping behaviour as will be illustrated. The semi-analytical results presented in this section are obtained using numerical continuation of periodic solutions [33]. Stable periodic solutions are plotted with solid lines whereas unstable periodic solutions are plotted with dashed lines. Furthermore, cyclic fold bifurcation are indicated by 'o' and period doubling bifurcations are indicated by '◇'.

In Fig. 6.2, the experimentally obtained frequency-amplitude plot (both in terms of dimensionless displacement  $\tilde{V}_{L/4}/h$  [-] and velocity  $\tilde{V}_{L/4}$  [m/s]) is depicted for **beam 1** with  $v_d = 0.03$  [V] and  $m_t = 0.51$  [kg]. In this figure also semi-analytical results are depicted based on the 1-MODE model. The identified parameter values for this case are listed in Table 6.2 (in this table also results are included for **beam 2**, these will be discussed at a later stage). As can be noted, the Young's modulus  $E$  is identified to be a little bit lower than the theoretical value. The semi-analytical 1-MODE model thus slightly overestimates the stiffness of the actual beam structure. This may be due to a combination of the following facts: 1) in the 1-MODE model axial inertia and axial strain of the beam are not included, 2) for the discretization of  $v$  (see Eq. (5.9)), not the exact the vibrational eigenmodes are used. As shown in Table 5.2, this may result in a small overestimation of the eigenfrequencies (in comparison with the eigenfrequencies predicted using FEA). Furthermore,



Table 6.3: Eigenfrequencies  $f_i$  and damping ratios  $\xi_i$  of linearized models with parameters according to Table 6.2 and  $m_t = 0.51$  [kg].

	beam 1, 1-MODE	beam 2, 1-MODE	beam 2, 2-MODE
$f_1$ [Hz]	18.1	18.1	18.1
$\xi_1$ [-]	0.489	0.489	0.489
$f_2$ [Hz]	72.7	73.1	73.1
$\xi_2$ [-]	0.0034	0.001	0.001
$f_3$ [Hz]	-	-	215.8
$\xi_3$ [-]	-	-	0.007

in the setup, the clamped-clamped boundary conditions will not be as ideal as considered in the model, which may also result in a small overestimation of the stiffness of the semi-analytical model.

The eigenfrequencies and damping ratios of the linearized version of the resulting 1-MODE model are listed in Table 6.3 (in this table also results are included for **beam 2**, these will be discussed at a later stage). The lowest eigenfrequency of the model ( $f_1$ ) corresponds to a suspension type of vibration mode of the shaker (i.e. the mode shape is dominated by  $\mathbf{U}_b$ ) and is highly damped. The second eigenfrequency of the model ( $f_2$ ) corresponds to the first bending mode of the beam (i.e. the mode shape is dominated by  $\mathbf{Q}_1$ ) and has very little damping.

Next the obtained dynamical steady-state response as depicted in Fig. 6.2 is discussed in more detail. The responses computed with the semi-analytical model show a second superharmonic resonance at  $f \approx f_2/2$ , a harmonic resonance at  $f \approx f_2$  and a 1/2 subharmonic resonance (period  $2T$ ) initiated at two period doubling bifurcations at  $f \approx 2f_2$  (indicated by ' $\diamond$ '). All three resonances show a softening type of behaviour due to the inertia nonlinearities and are qualitatively similar as found for the case of a prescribed base-acceleration, see Chapter 5. However, at the experimental setup, the harmonic resonance is not significantly smaller than the subharmonic resonance. This may be due to the fact that at the setup, the amplitude of the base-acceleration does not remain constant if the excitation frequency is varied. Especially around the suspension type of resonance ( $f = f_1$ ), the base-acceleration will show an increase in amplitude. Furthermore, the identified quadratic damping parameter ( $c_{q,1}$  see Table 6.2) is relative large with respect to the parameter values considered in Chapter 5. During the fit procedure it is found that inclusion of quadratic damping appeared to be essential to get good fit results, especially around the harmonic resonance and the subharmonic resonance.

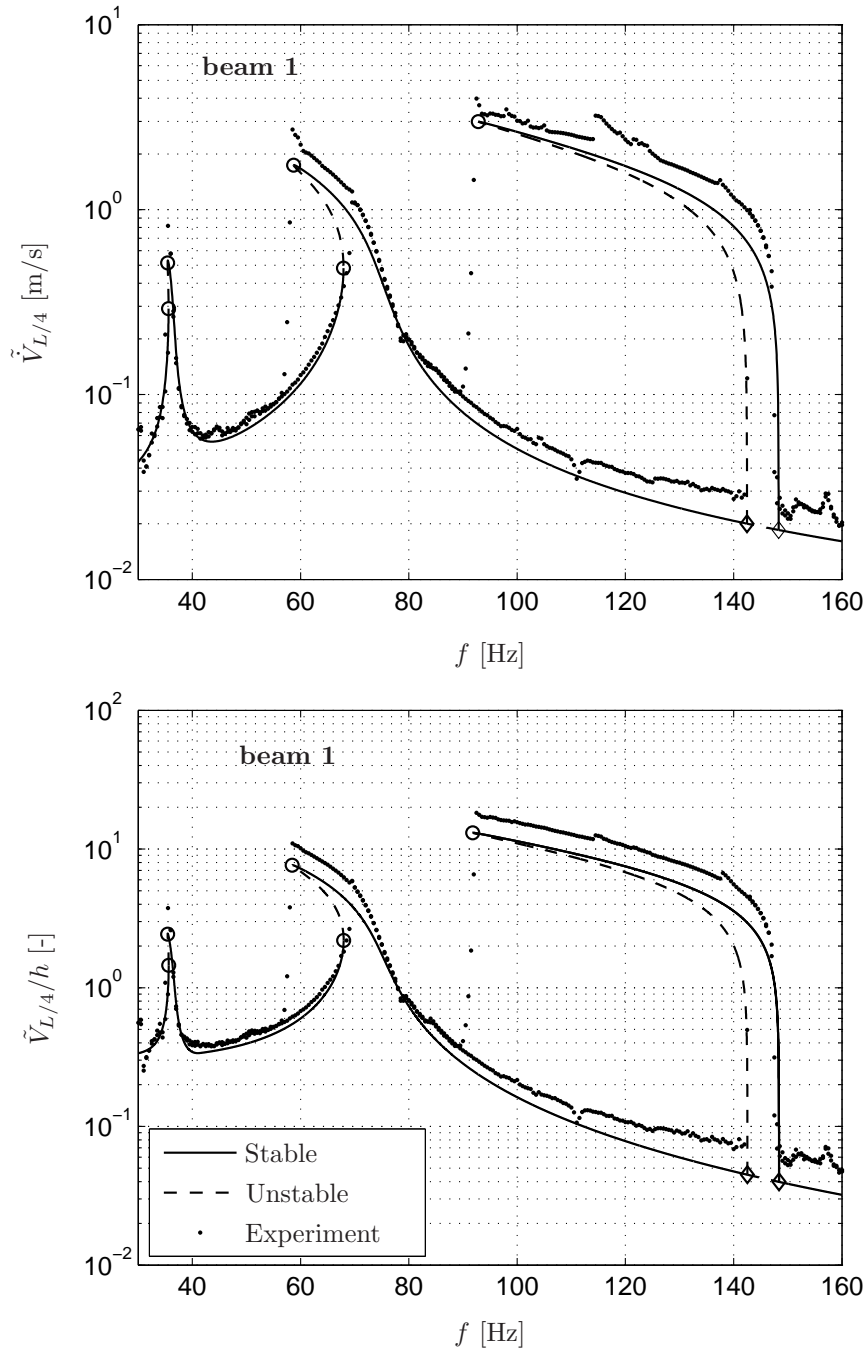


Figure 6.2: Frequency-amplitude plot in terms of displacement  $\tilde{V}_{L/4}/h$  (top) and in terms of velocity  $\tilde{V}_{L/4}$  (bottom) for **beam 1** with  $v_d = 0.03$  [V] and  $m_t = 0.51$  [kg] (experiments versus semi-analytical results based on 1-MODE model).

The importance of the quadratic damping on the quality of the fit between numerical results and experimental results is also observed in [7; 144] and for cubic damping in [147].

In general, the experimental results are in good correspondence with the semi-analytical results. However, some discrepancies can be noted. First of all, the experimental results show a somewhat larger amplitude, especially in the peaks of the harmonic and the subharmonic resonance (both in terms of  $\tilde{V}_{L/4}$  [m/s] and  $\tilde{V}_{L/4}/h$  [-]). Furthermore, the experimentally obtained frequency-amplitude plot shows at a number of frequency regions, small peaks and/or jumps which are not present in the semi-analytical results. These peaks can be most clearly observed in the frequency-amplitude plot in terms of  $\tilde{V}_{L/4}$  [m/s] (see Fig. 6.2-top), for example near the top of the harmonic resonance ( $f \approx 60$  [Hz]) and along the subharmonic resonance branch near  $f = 120$  [Hz]. More comments about these peaks will be given at the end of this section. From now on, the frequency-amplitude plots will only be presented in terms of  $\tilde{V}_{L/4}$  [m/s] since from these plots the most details can be distinguished.

The imperfection and damping parameters of the 1-MODE model for **beam 1** are identified using the experimental response obtained for  $v_d = 0.03$  [V] and  $m_t = 0.51$  [kg]. For further validation, the response predicted by this model is compared with experimental results for a higher excitation amplitude (i.e.  $v_d = 0.04$  [V], see Fig. 6.3-top) and a larger top mass (i.e.  $m_t = 1.01$  [kg], see Fig. 6.3-bottom). Except for the fact that for  $v_d = 0.04$  [V], the  $1/2$  subharmonic branch of the semi-analytical model continues to a lower excitation frequency, the semi-analytical results are in this case again in good correspondence with the experimental results. For  $m_t = 1.01$  [kg] (i.e. the top mass is twice as large as in Fig. 6.2), both the  $1/2$  subharmonic resonance and the harmonic resonance of the semi-analytical model continue to lower excitation frequencies than observed in the experimental results. Furthermore, the second eigenfrequency ( $f_2$ ) is slightly overestimated (approximately 3%) by the semi-analytical 1-MODE model. The larger overhang of the semi-analytical results is mainly influenced with the damping parameters. In this sense, the identified nonlinear damping characteristics based for one load case, show not to be able to predict exactly the damping characteristics for another load case. Nevertheless, for both cases shown in Fig. 6.3 the semi-analytical results based on the 1-MODE model are in satisfactory correspondence with the experimental results.

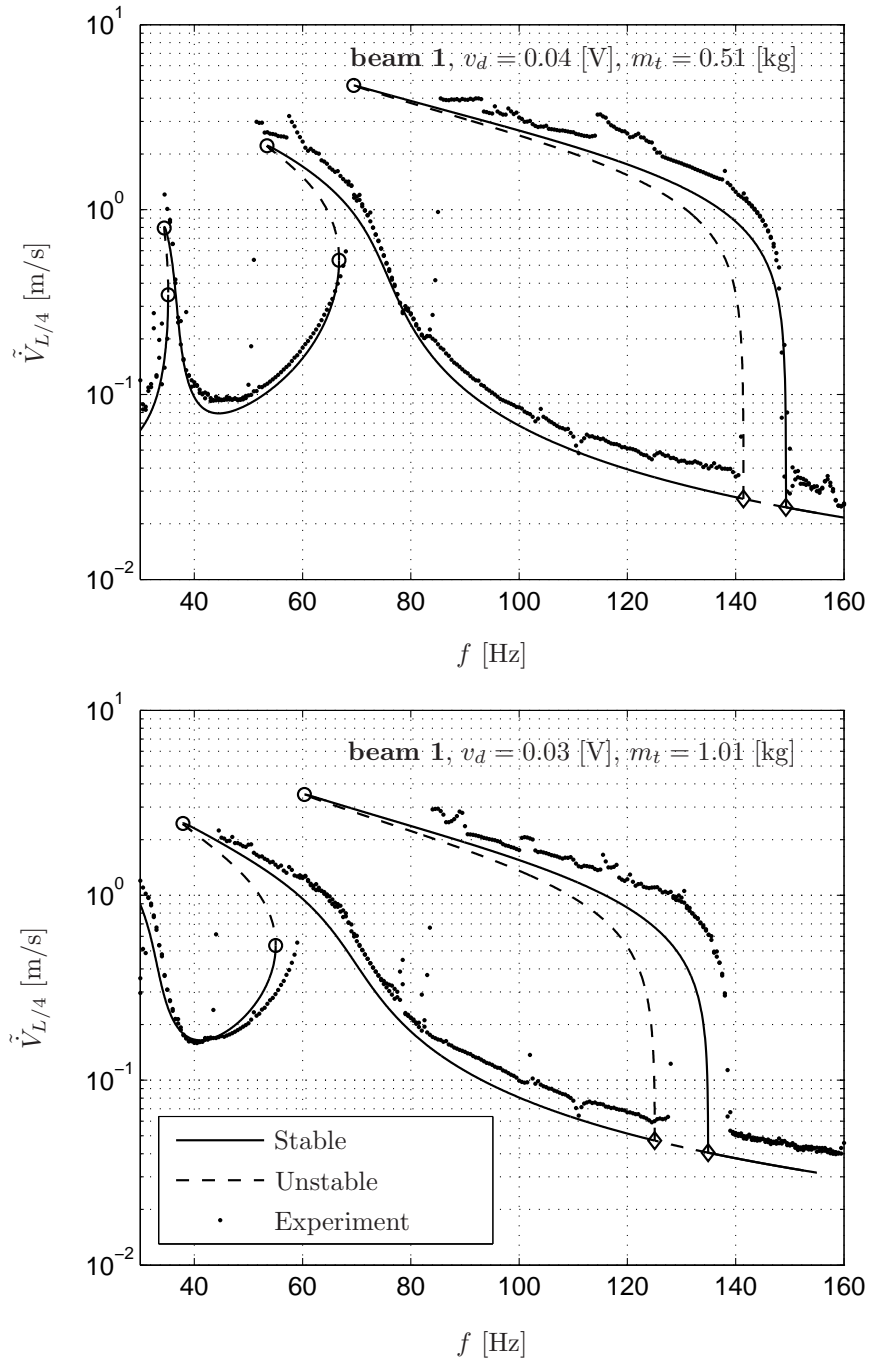


Figure 6.3: Frequency-amplitude plot for **beam 1** (experiments versus semi-analytical results based on 1-MODE model).

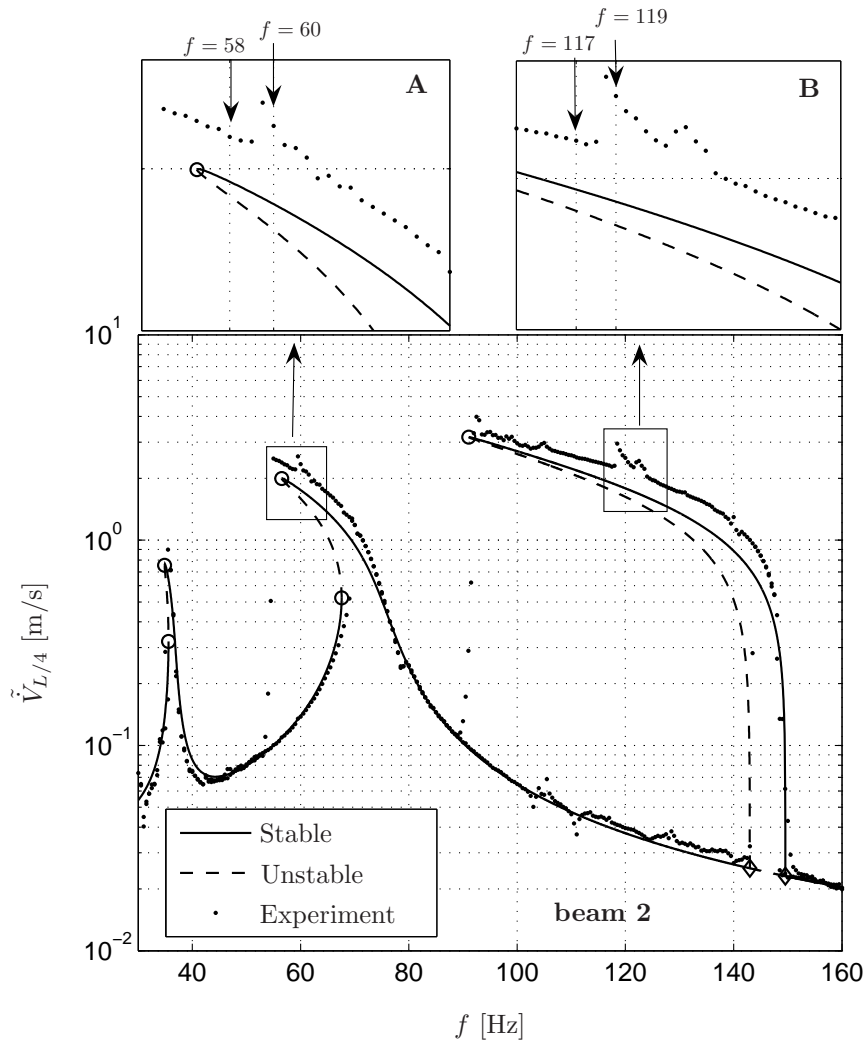


Figure 6.4: Frequency-amplitude plot for **beam 2** with  $v_d = 0.03$  [V] and  $m_t = 0.51$  [kg] (experiments versus semi-analytical results based on 1-MODE model).

Next, results for the second beam (**beam 2**) will be discussed. For this beam, experimental results will be compared with results for both the 1-MODE model and the 2-MODE model (see Section 6.2). In Fig. 6.4, the experimentally obtained frequency-amplitude plot and the corresponding 1-MODE fit is depicted for **beam 2** for the same loading conditions as considered in for **beam 1** in Fig. 6.2 ( $v_d = 0.03$  [V] and  $m_t = 0.51$  [kg]). The identified parameter values for this case are listed in Table 6.2 and the eigenfrequencies and damping ratios of the linearized version of the resulting 1-MODE model are listed in Table 6.3. The identified parameter values are for the largest part comparable to those obtained for **beam 1**. However, now the linear damping coefficient  $c_1$  is identified zero. Note that this does not result in a zero damping ratio for the first beam mode  $f_2$  (see Table 6.3), since this mode has some (linear) coupling with the heavily damped suspension mode of the shaker.

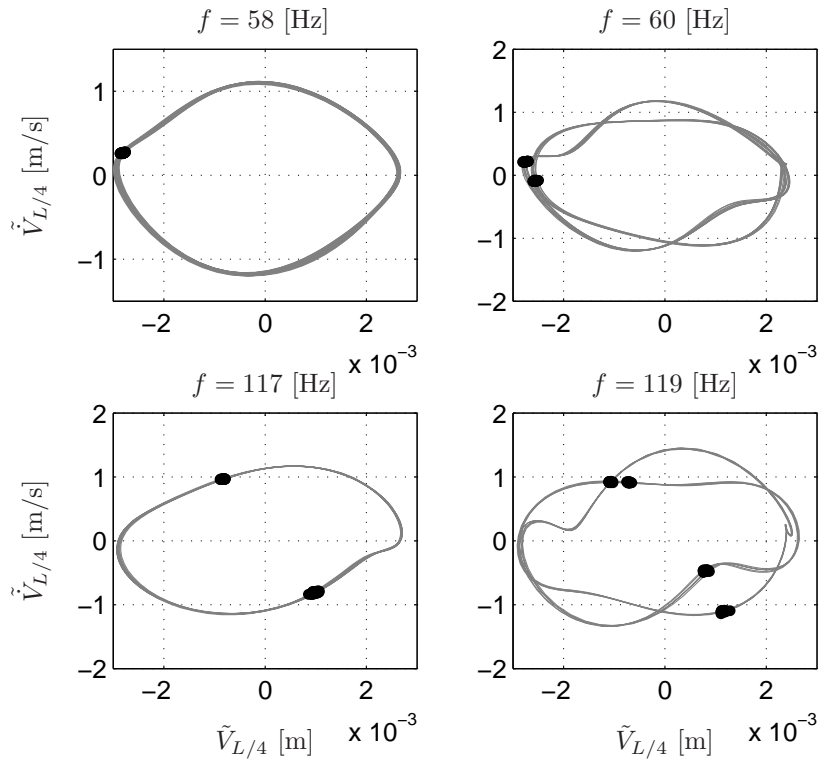


Figure 6.5: Phase-plane projections and Poincaré mappings for four experimentally obtained responses for **beam 2** with  $v_d = 0.03$  [V] and  $m_t = 0.51$  [kg].

Similar to Fig. 6.2, also in Fig. 6.4 the semi-analytical results based on the 1-MODE model are in good correspondence with the experimental results. Furthermore, also in this frequency-amplitude plot small peaks and/or jumps can be noted. Again a very clear jump occurs near the top of the harmonic resonance ( $f \approx 60$  [Hz]) and another one along the subharmonic resonance branch near  $f = 120$  [Hz], see enlargements **A** and **B** in Fig. 6.4. Projections of the experimental response on the phase plane spanned by  $V_{L/4}$  and  $\dot{V}_{L/4}$  and the corresponding Poincaré mappings (i.e. period  $T$  sampled values of  $V_{L/4}$  plotted against period  $T$  sampled values of  $\dot{V}_{L/4}$ ) close to these two jumps are depicted in Fig. 6.5. For  $f = 58$  [Hz] (just before the jump, see enlargement **A** in Fig. 6.4), the Poincaré map shows a single dot indicating that here the response is harmonic. However, for  $f = 60$  [Hz] (just after the jump, see enlargement **A** in Fig. 6.4), the Poincaré map shows two dots indicating that now the response is 1/2 subharmonic. Similarly for the scenario depicted in enlargement **B** in Fig. 6.4, for  $f = 117$  [Hz] the response is 1/2 subharmonic and for  $f = 119$  [Hz] the response has become 1/4 subharmonic.

These additional small branches with subharmonic responses are not captured by the 1-MODE model. In Section 5.4 of Chapter 5 it is shown using a multi-mode model, that higher beam modes may start to interact with the first beam mode in the large amplitude 1/2 subharmonic resonance. To examine if the experimentally observed period doubling behaviour is due to the interaction with the second beam mode, this mode is included in the semi-analytical model (i.e. the 2-MODE model is derived, see Section 6.2). In Fig. 6.6, the steady-state response predicted by the 2-MODE model is compared with experimental results obtained for **beam 2** and  $v_d = 0.03$  [V] and  $m_t = 0.51$  [kg] (similar as in Fig. 6.4). Also for this case, the identified parameter values are listed in Table 6.2 and the eigenfrequencies and damping ratios of the linearized version of the resulting 2-MODE model are listed in Table 6.3. As can be noted, a very small value for of the second bending mode is identified in the geometric imperfection of the beam (i.e.  $e_2 = 0.04$ , see Table 6.2). In the parameter identification for the second mode no quadratic damping is taken into account, i.e.  $c_{q,2} = 0$  [kg/m].

As can be noted in Fig. 6.6, inclusion of the second beam mode in the model instigates a second harmonic resonance with softening around  $f = 215$  [Hz]. This second harmonic resonance is observed at a slightly lower frequency in the experimental results (see Fig. 6.6). Furthermore and in correspondence with the experimental results shown in Fig. 6.4, in the semi-analytical results for the 2-MODE model at the 1/2 subharmonic branch near  $f = 123$  [Hz] two period doubling bifurcations to 1/4 subharmonic response are observed (see enlargement **B** in Fig. 6.6). Note that for clarity no experimental results are shown in the enlargements. The 1/4 subharmonic branch itself exhibits three

cyclic fold bifurcations resulting in two stable parts of the branch. Due to its complexity, this branch can not be easily compared with the experimental results in this region (see the experimental results depicted in enlargement **B** of Fig. 6.4, here only results for a downwards frequency sweep are shown). Nevertheless, it can be noted that for the semi-analytical results, the 1/4 subharmonic response continues to a lower excitation frequency as observed experimentally. This larger overhang is possibly due to the fact that in the semi-analytical model for the second mode no quadratic damping is taken into account.

A similar phenomenon occurs in the top of the first harmonic resonance. Again in correspondence with the experimental results, near  $f = 61$  [Hz] two period doubling bifurcations occur (very close to each other) from which (now) a complex 1/2 subharmonic branch bifurcates. Furthermore, in the semi-analytical results near  $f = 72$  [Hz] (see enlargement **A** in Fig. 6.6) a small 3<sup>rd</sup> superharmonic resonance can be distinguished related to the second beam mode ( $f_3$ ). This superharmonic resonance can not be seen in the experimental results but the corresponding frequency interval is so small that is possibly missed in the frequency sweep due to a too coarse frequency step. Finally, a very small 2<sup>nd</sup> superharmonic resonance related to the second beam mode ( $f_3$ ) can be observed near  $f = 108$  [Hz] both in the semi-analytical response and in the experimental response.

For further validation, power spectral densities (PSDs) of the experimentally and semi-analytically obtained velocity  $\dot{v}(t, L/4 - \mathbf{U}_b)$  are compared for  $f = 58$  [Hz] and  $f = 60$  [Hz] in Fig. 6.7 and for  $f = 117$  [Hz] and  $f = 119$  [Hz] in Fig. 6.8. In these PSD plots, the frequency axis of the PSD  $F$  is normalized by the excitation frequency  $f$  and for the semi-analytical results (which are based on the 2-MODE model) the locations of the eigenfrequencies corresponding to the first two beam bending modes (i.e.  $f_2$  and  $f_3$ , see Table 6.3) are indicated.

First consider the PSD of the harmonic response at  $f = 58$  [Hz] and the 1/2 subharmonic response at  $f = 60$  [Hz] (see also Fig. 6.5). As can be noted, for the 1/2 subharmonic response obtained for  $f = 60$  [Hz] in both the PSD of the semi-analytical response and the PSD of the experimental response a large peak occurs at  $F/f = 7/2$ . This peak occurs very close to the eigenfrequency of the second bending mode ( $f_3$ ) and is not present for  $f = 58$  [Hz]. In a similar fashion, for the 1/4 subharmonic response obtained for  $f = 119$  [Hz] again a large peak occurs at the eigenfrequency of the second bending mode (now occurring at  $F/f = 7/4$ ) which is not present for the 1/2 subharmonic response obtained at  $f = 117$  [Hz] (see Fig. 6.8). Consequently, it may be concluded that at  $f = 60$  [Hz], the second beam bending mode ( $f_3$ ) is excited due to a *two-to-seven* internal resonance with the first beam bending mode ( $f_2$ )



---

and at  $f = 119$  [Hz]  $f_3$  is excited due to a *four-to-seven* internal resonance with  $f_2$ . As illustrated, these interactions are also predicted by the semi-analytical 2-MODE model. It is of interest to note that a two-to-seven internal resonance between the first two beam bending modes is also observed experimentally in [116].

In conclusion, with the 2-MODE model the small extra peaks and associated jumps and the period doubling behaviour at the top of the first harmonic resonance and on the subharmonic branch as observed in the experiments can qualitatively be explained. For a better quantitative match of these details, the parameters of the model must be further refined and, possibly, also more modes must be included in the model. A detailed study of complex phenomena on such a small scale (experimentally or numerically with a multi-mode model) is very elaborating and out of the scope of this chapter. Nevertheless, it has been illustrated that with the semi-analytical approach even such small response details can be studied.

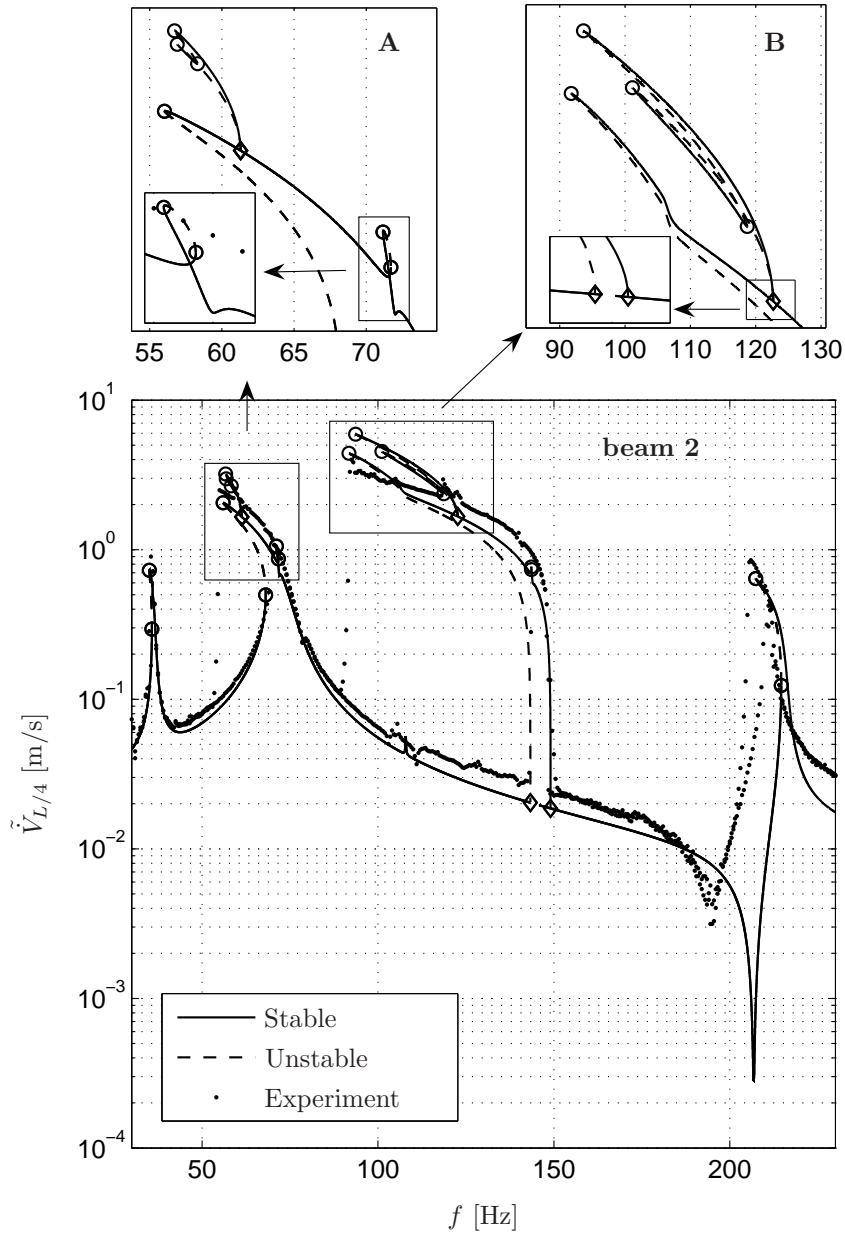


Figure 6.6: Frequency-amplitude plot for **beam 2** with  $v_d = 0.03$  [V] and  $m_t = 0.51$  [kg] (experiments versus semi-analytical results based on 2-MODE model).

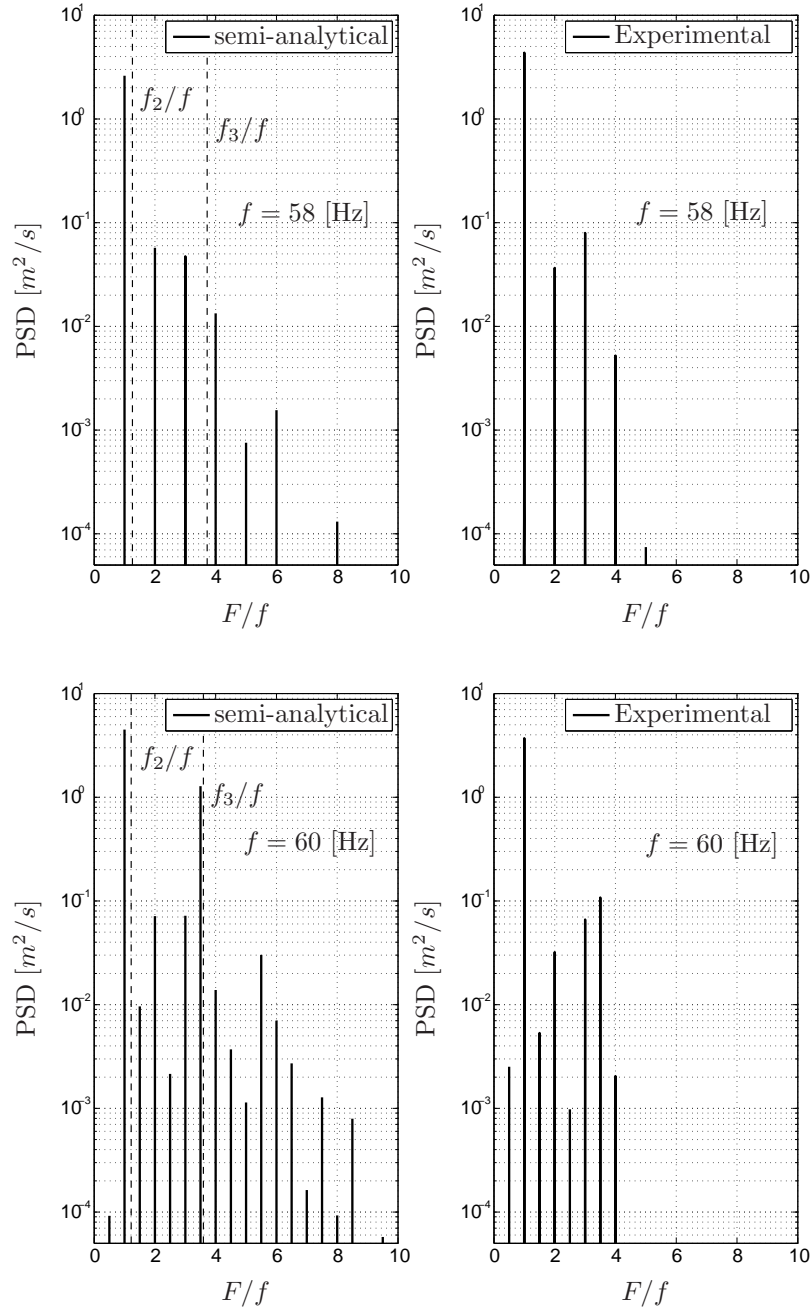


Figure 6.7: Power Spectral Density of the response (semi-analytical results based on 2-MODE model versus experiments) obtained for **beam 2** with  $v_d = 0.03$  [V],  $m_t = 0.51$  [kg],  $f = 58$  [Hz] (top) and  $f = 60$  [Hz] (bottom).

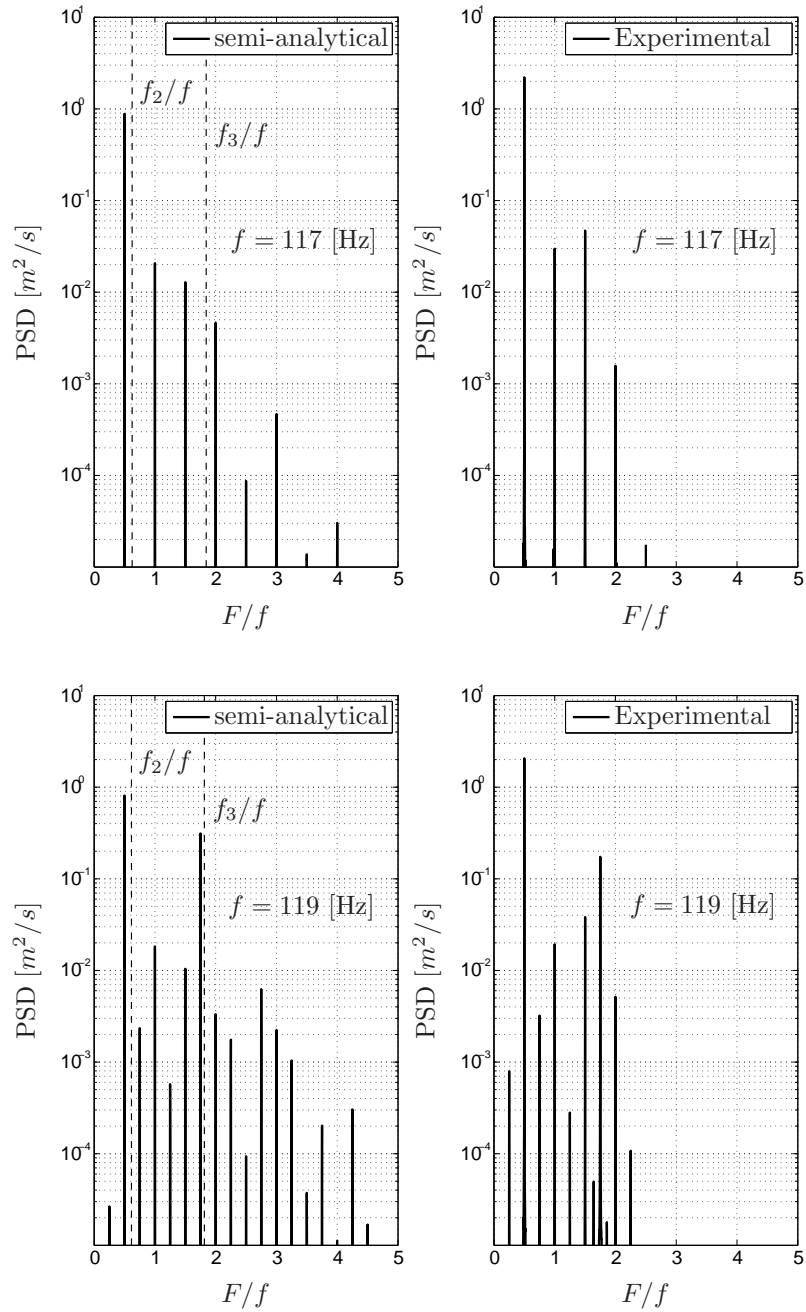


Figure 6.8: Power Spectral Density of the response (semi-analytical results based on 2-MODE model versus experiments) obtained for **beam 2** with  $v_d = 0.03$  [V],  $m_t = 0.51$  [kg],  $f = 117$  [Hz] (top) and  $f = 119$  [Hz] (bottom).

## 6.4 Conclusions

The objective of this chapter is to experimentally validate the semi-analytical model of the base-excited thin beam with top mass as derived in Chapter 5. At the experimental setup, base excitation is realized via a harmonic input voltage which is offered to an electrodynamic shaker. For this case, the resulting acceleration of the base is determined by the interactions between the dynamics of the electromechanical shaker system and the dynamics of the thin beam with top mass which is placed on top of the shaker. To be able to compare the experimental steady-state responses with the semi-analytical steady-state responses, a coupled shaker/structure model is derived. By the way, the responses obtained for the coupled shaker-beam system are qualitatively similar to the responses found for the case of a prescribed base-acceleration which has been considered in Chapter 5.

At the experimental setup, the steady-state response is examined using stepped sine frequency sweeps. The experimental results are compared with results obtained using the semi-analytical approach based on single mode and two mode discretizations of the transversal displacement field of the beam. The unknown geometric imperfection and damping parameters of these models are identified based on experimental steady-state results.

The semi-analytical steady-state responses based on the single (beam) mode model are globally in good correspondence with the experimental results. However, the experimental results show additional period doubling behaviour on the harmonic resonance peak of the first beam mode and its corresponding  $1/2$  subharmonic resonance. These phenomena are not present in the steady-state response predicted by the single mode model. It is shown that these discrepancies can be explained by considering a two mode model. Indeed, due to nonlinear interactions between the first and the second bending mode of the beam, the two mode model shows qualitatively similar period doubling behaviour as observed experimentally.

In conclusion, the semi-analytical results are in good correspondence with experimental results. Consequently, the semi-analytical approach turns out to be very suitable for fast and accurate prediction of the dynamic response of the beam structure with top mass.



## *Dynamic stability of a base-excited thin cylindrical shell with top mass*

**D**ynamically loaded thin cylindrical shells can be encountered in a wide variety of applications, for example in civil engineering structures [136] and in aerospace structures [1]. Thin cylindrical shells subjected to static compressive loading are very susceptible for buckling. The classical static buckling analyses of axially compressed perfect cylindrical shells (based on linearized small deflection theory, see [17; 146]) predict many closely spaced buckling loads with buckling modes being sinusoidal both in axial direction and in circumferential direction. Experiments on the static buckling of axially compressed cylindrical shells reveal a large scatter in the obtained buckling loads and notorious discrepancies with the results obtained from the classical static buckling analyses [8; 17]. Both the inevitable small deviations from the nominal cylindrical shape (geometric imperfections) and the boundary conditions have been widely accepted as contributing to the poor correlation between the experimental results and the classical static buckling results.

In this chapter, dynamic buckling of thin cylindrical shells is considered. The dynamic loading is introduced in a similar fashion as considered for the thin beam structure discussed in Chapter 5, i.e. the structure is placed on a vibrating base while it is supporting a rigid top mass, see Fig. 7.1. This is a load case with great practical relevance, since cylindrical shells are often employed as support construction for relatively heavy components. Nevertheless, the effect of the top mass on the dynamic stability limits of cylindrical shell structures is not yet considered in previous numerical studies.

Due to the harmonic base-excitation and the weight of the top mass, the cylindrical shell under consideration is loaded in axial direction by a combination of a static load and a time dependent load. Indeed, already in many papers the dynamic stability of harmonic axially loaded thin cylindrical shells has been considered [24; 38; 46; 59; 108; 109]. However, these studies consider parametric instabilities of cylindrical shells without a top mass, i.e. axisymmetrical vibration modes are excited through a *Mathieu* type of instability around excitation frequencies equal to two times the eigenfrequency of an axi-

---

Parts of this chapter are also presented in [82] and [84].

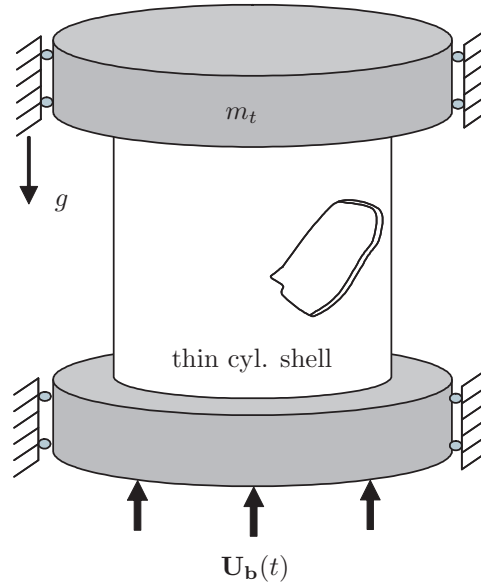


Figure 7.1: Base-excited cylindrical shell with top mass.

asymmetrical vibration mode. Due to the top mass, a relatively low frequent resonance corresponding to axi-symmetrical vibrations is introduced (far below the parametric instability regions). In this chapter, the dynamic stability of the shell around this resonance is studied using a semi-analytical approach.

The derived semi-analytical model of the shell is based on *Donnell's* nonlinear shell theory [34]. The effect of in-plane inertia is neglected, resulting in two static equilibrium equations for the in-plane fields and one dynamic equilibrium equation for the out-of-plane field. For the case of in-plane boundary conditions in terms of membrane forces, the equilibrium equations are usually written in terms of an in-plane stress function and the out-of-plane displacement field [24; 38; 46; 59; 108]. By solving the stress-function analytically for an assumed expression of the out-of-plane displacement field, the number of independent displacement fields is reduced from three to one, resulting in a model with a low number of DOF (i.e. a static condensation is performed). The stress-function approach is, however, less straightforward for the case when the boundary conditions involve the in-plane displacements (as considered here). Another approach which allows to include the effect of in-plane inertia and satisfying exactly the in-plane boundary conditions, is to discretize all three displacement fields using global shape functions [2; 3; 107; 109] or to use a FEA approach



[13; 14; 32; 140]. A drawback of these approaches, however, is that the resulting models have relatively many DOFs.

Since the in-plane boundary conditions have a significant influence on the thin shell behaviour [3; 65; 78; 146], an alternative static reduction approach will be developed in this chapter, which solves directly the in-plane displacement fields in terms of the out-of-plane displacement field. The obtained expressions for the in-plane displacement fields satisfy exactly the in-plane boundary conditions for the cylindrical shell with rigid end-disks. Note that a comparable approach, however only for one specific three mode expansion of the out-of-plane displacement field, is followed in [124]. The resulting nonlinear model is numerically validated through a comparison with static and modal analysis results obtained using FEA. The steady-state nonlinear dynamics of the base-excited cylindrical shell with top mass will be examined using numerical continuation of periodic solutions for a varying excitation frequency and by using standard numerical integration.

In the analysis, the influence of geometrical imperfections is taken into account. For the case of parametrically induced instabilities it is known that geometrical imperfections have a very mild influence on the dynamic critical loads [24; 81; 109]. Base-excited cylindrical shells carrying a top mass are previously studied for the case of shock loading in [124]. Experimental results considering a base-excited cylindrical shell with a free top mass (i.e. the top mass is only supported by the cylindrical shell), are presented in [106]. Around the resonance of the first axial symmetric vibration mode, a very severe unstationary response is found. The obtained results, however, could not be explained using numerical simulations (see also [110]). An extensive review of the research performed on the nonlinear vibrations of cylindrical shells until 2003 can be found in [6].

Summarizing, the contributions of this chapter are the derived static condensation approach of the in-plane fields and the dynamic stability results, including an imperfection sensitivity analysis, obtained for the (relatively) low frequent dynamic loading conditions. In addition, results obtained using the semi-analytical approach will be confronted with FEA results. Note that in the next chapter, semi-analytical results for a base-excited thin cylindrical shell with top mass will be confronted with experimental results.

The outline for this chapter is as follows. The next section will deal with the derivation of the equations of motion. In Section 7.2, buckling of the cylindrical shell under a static loading will be discussed and a modal analysis will be performed. The influence of initial imperfections will be illustrated and results will be compared with FEA results. Dynamic stability of the base-

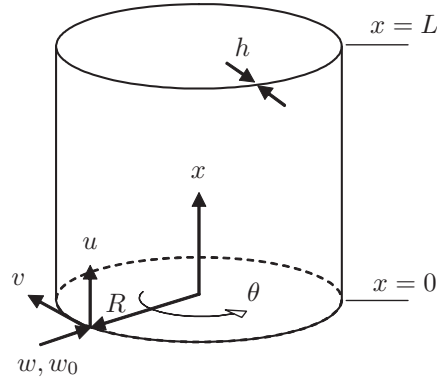


Figure 7.2: Cylindrical shell geometry.

excited cylindrical shell with top mass will be discussed in Section 7.3. Finally, in Section 7.4 conclusions will be presented.

## 7.1 Modelling approach

In this section, the equations of motion are derived for the thin cylindrical shell which carries a rigid top mass  $m_t$  and is loaded in axial direction by a base motion  $\mathbf{U}_b(t)$  and by gravity  $g$ , see Fig. 7.1. To be able to accurately capture the mechanical properties of the cylindrical shell which will be used in the experimental approach in the next chapter, orthotropic material behaviour (i.e. the directional dependent material properties are specified along two mutually orthogonal directions) is included during the derivation of the equations of motion. When appropriate, simplifications for isotropic material behaviour (i.e. the material properties are not directional dependent) are addressed.

The dimensions of the cylindrical shell are defined by the radius of the neutral plane  $R$ , thickness  $h$  and length  $L$ . Considering the cylindrical coordinate system  $[r = R, x, \theta]$  (see Fig. 7.2), the axial in-plane displacement field is denoted by  $u(t, x, \theta)$ , the circumferential in-plane displacement field by  $v(t, x, \theta)$ , the radial out-of-plane displacement field by  $w(t, x, \theta)$  and the radial imperfection shape by  $w_0(x, \theta)$ . For readability, the notations for the displacement fields and radial imperfection shape will be abbreviated to  $u$ ,  $v$ ,  $w$  and  $w_0$ , respectively. The axial coordinate  $x$  and axial displacement field  $u$  are measured relative with respect to the base-motion  $\mathbf{U}_b(t)$ . Donnell's shallow shell theory is adopted [34; 146] as kinematic model for the thin cylindrical shell. Note that using Donnell's theory, good agreement between simulation results

and experimental results is obtained for static (post) buckling in [146] and for (nonlinear) large amplitude vibrations of thin cylindrical shells in [4].

According to *Donnell's* assumptions, the nonlinear strain-displacement relations read [17; 34]

$$\begin{aligned} \varepsilon_x &= u_{,x} + \frac{1}{2}w_{,x}^2 + w_{,x} w_{0,x}, & \kappa_x &= -w_{,xx}, \\ \varepsilon_\theta &= \frac{1}{R}(v_{,\theta} + w) + \frac{1}{2R^2}w_{,\theta}^2 + \frac{1}{R^2}w_{,\theta} w_{0,\theta}, & \kappa_\theta &= -\frac{1}{R^2}w_{,\theta\theta}, \\ \gamma_{x\theta} &= \frac{1}{R}u_{,\theta} + v_{,x} + \frac{1}{R}(w_{,x} w_{,\theta} + w_{,x} w_{0,\theta} + w_{0,x} w_{,\theta}), & \kappa_{x\theta} &= -\frac{1}{R}w_{,x\theta}, \end{aligned} \quad (7.1)$$

where  $_{,x}$  means  $\frac{\partial}{\partial x}$  and  $_{,\theta}$  means  $\frac{\partial}{\partial \theta}$ . Note that in Eq. (7.1), the radial displacement field  $w$  and the radial imperfection shape  $w_0$  are measured positively inwards.

Considering orthotropic material properties for the cylindrical shell with principle axes which coincide with the cylindrical coordinate axes, the stress resultants and stress couples per unit length are defined by [74; 75]

$$\begin{bmatrix} N_x \\ N_\theta \\ N_{x\theta} \end{bmatrix} = h \begin{bmatrix} C_{11} & C_{12} & 0 \\ C_{21} & C_{22} & 0 \\ 0 & 0 & C_{33} \end{bmatrix} \begin{bmatrix} \varepsilon_x \\ \varepsilon_\theta \\ \gamma_{x\theta} \end{bmatrix}, \quad (7.2)$$

$$\begin{bmatrix} M_x \\ M_\theta \\ M_{x\theta} \end{bmatrix} = \frac{h^3}{12} \begin{bmatrix} C_{11} & C_{12} & 0 \\ C_{21} & C_{22} & 0 \\ 0 & 0 & C_{33} \end{bmatrix} \begin{bmatrix} \kappa_x \\ \kappa_\theta \\ \kappa_{x\theta} \end{bmatrix}, \quad (7.3)$$

where

$$\begin{aligned} C_{11} &= \frac{E_x}{1 - \nu_x \nu_\theta}, \quad C_{22} = \frac{E_\theta}{1 - \nu_x \nu_\theta}, \quad C_{33} = G_{x\theta}, \\ C_{12} = C_{21} &= \nu_\theta \frac{E_x}{1 - \nu_x \nu_\theta} = \nu_x \frac{E_\theta}{1 - \nu_x \nu_\theta}. \end{aligned} \quad (7.4)$$

Since it holds that  $\nu_\theta E_x = \nu_x E_\theta$ , the orthotropic shell material is described by four parameters, i.e. the Young's moduli in  $x$  and  $\theta$  direction ( $E_x$  and  $E_\theta$ ), the shear modulus  $G_{x\theta}$  and one Poisson ratio (either  $\nu_x$  or  $\nu_\theta$ ). Note that for isotropic material  $E_x = E_\theta = E$ ,  $\nu_x = \nu_\theta = \nu$  and  $G_{x\theta} = E/(2(1 + \nu))$ , resulting in two independent material parameters.

The following boundary conditions for the cylindrical shell with rigid end-disks are considered ('-' means not prescribed)

$$\begin{array}{c|ccccc} & u & u_{,\theta} & v & w & M_x \\ \hline x = 0 & 0 & 0 & 0 & 0 & 0 \\ x = L & - & 0 & 0 & 0 & 0 \end{array}. \quad (7.5)$$

Note that the base-motion does not appear in the boundary conditions, since  $u$  and  $x$  are measured relatively with respect to  $\mathbf{U}_b(t)$ . Indeed, for a thin cylindrical shell mounted between two rigid end-disks, the clamping condition (in practice) is probably closer to the case  $w_{,x} = 0$  (instead of  $M_x = 0$ ). Nevertheless, the clamping condition is assumed to be  $M_x = 0$  since this allows for a simple expansion of  $w$ . This assumption is supported by the fact that previous studies show that the rotational restraint ( $M_x = 0$  vs.  $w_{,x} = 0$ ) has only a mild influence on the static buckling load [146], eigenfrequencies [65; 78], parametric instabilities [98] and nonlinear vibrations [3; 78]. Furthermore, the boundary condition in terms of the membrane force  $N_x$  at  $x = L$  due to the inertia force of the top mass is not included. This force will be included via the kinetic energy.

The strain energy of the structure, corresponding to *Donnell's* assumptions, reads as

$$\begin{aligned} \mathcal{U}_s = & \frac{1}{2} \int_0^{2\pi} \int_0^L (N_x \varepsilon_x + N_\theta \varepsilon_\theta + N_{x\theta} \gamma_{x\theta}) dx R d\theta \\ & + \frac{1}{2} \int_0^{2\pi} \int_0^L (M_x \kappa_x + M_\theta \kappa_\theta + M_{x\theta} \kappa_{x\theta}) dx R d\theta. \end{aligned} \quad (7.6)$$

The case  $m_t \gg m_{shell}$ , where  $m_t$  is the top mass and  $m_{shell}$  the mass of the shell, is considered. Therefore, the effect of the mass of the shell is neglected in the potential energy of the structure

$$\mathcal{U}_g = m_t g (\mathbf{U}_b(t) + u(t, L, \theta)). \quad (7.7)$$

Furthermore, the influence of in-plane inertia of the shell is also neglected in the kinetic energy

$$\mathcal{T} = \frac{1}{2} \rho h \int_0^{2\pi} \int_0^L \dot{w}^2 dx R d\theta + \frac{1}{2} m_t \dot{u}_t^2, \quad (7.8)$$

where  $\dot{u}_t = \dot{\mathbf{U}}_b(t) + \dot{u}(t, L, \theta)$  (note that  $u_{, \theta} = 0$  for  $x = L$ ). Previous studies concerning nonlinear vibrations of cylindrical shells show that neglecting the in-plane inertia results in a moderately overestimated softening behaviour [2] and a moderately overestimated dynamic critical load (with respect to parametric instabilities) [59; 109]. These studies, however, consider cylindrical shells without a top mass.

Using *Hamilton's* variation principle on the basis of the sum of Eqs. (7.6), (7.7)

and (7.8), the resulting nonlinear equilibrium equations are

$$RN_{x,x} + N_{x\theta} = 0, \quad (7.9)$$

$$RN_{x\theta} + N_{\theta,\theta} = 0, \quad (7.10)$$

$$\begin{aligned} M_{x,xx} + \frac{2}{R}M_{x\theta,x\theta} + \frac{1}{R^2}M_{\theta,\theta\theta} + \frac{1}{R}N_{\theta} + N_x(w_{,xx} + w_{0,xx}) + \\ \frac{2}{R}N_{x\theta}(w_{,x\theta} + w_{0,x\theta}) + \frac{1}{R^2}N_{\theta}(w_{,\theta\theta} + w_{0,\theta\theta}) = \rho h\ddot{w}, \end{aligned} \quad (7.11)$$

Note that for isotropic cylindrical shells, Eq. (7.11) can be expressed in a more compact form:

$$\begin{aligned} -D\nabla^4 w + \frac{1}{R}N_{\theta} + N_x(w_{,xx} + w_{0,xx}) + \\ \frac{2}{R}N_{x\theta}(w_{,x\theta} + w_{0,x\theta}) + \frac{1}{R^2}N_{\theta}(w_{,\theta\theta} + w_{0,\theta\theta}) = \rho h\ddot{w}, \end{aligned} \quad (7.12)$$

where  $D = Eh^3/(12(1 - \nu^2))$  and the biharmonic operator  $\nabla^4$  is defined by

$$\nabla^4 w = w_{,xxxx} + \frac{2}{R^2}w_{,xx\theta\theta} + \frac{1}{R^4}w_{,\theta\theta\theta\theta}. \quad (7.13)$$

Since the effects of in-plane inertia are neglected, Eqs. (7.9)-(7.11) constitute a set of two static (in-plane) equilibrium equations (Eqs. (7.9)-(7.10)) and one dynamic (out-of-plane) equilibrium equation (Eq. (7.11)).

The out-of-plane displacement field is expanded as

$$w(t, x, \theta) = \sum_{i=1}^N \sum_{j=0}^M [\mathbf{Q}_{ij}^s(t) \sin(jn\theta) + \mathbf{Q}_{ij}^c(t) \cos(jn\theta)] \sin(\lambda_i x), \quad (7.14)$$

where  $\lambda_i = i\pi/L$ ,  $i$  is the number of axial half-waves,  $n$  is the number of circumferential waves and  $\mathbf{Q}_{ij}^{s,c}(t)$  are  $N(2M + 1)$  generalized degrees of freedom (DOF). Note that Eq. (7.14) satisfies exactly the boundary conditions for  $w$ , see Eq. (7.5). The  $N$  DOF  $\mathbf{Q}_{i0}^s(t)$  correspond to axi-symmetrical radial displacements and the  $2NM$  DOF  $\mathbf{Q}_{ij}^{s,c}(t)$  ( $j \neq 0$ ) to axi-asymmetrical displacement fields. The presence of pairs of modes (with DOF  $\mathbf{Q}_{ij}^s$  and  $\mathbf{Q}_{ij}^c$  for  $j \neq 0$ ) with the same shape but with a different angular orientation is due to axi-symmetry of the (perfect) shell. Considering, for example, a radial imperfection with shape  $\sin(jn\theta) \sin(\lambda_i x)$ , the mode  $\mathbf{Q}_{ij}^s$  will be excited directly by the axial loading [24]. However, depending on the amplitude and frequency of the axial excitation, also the companion mode  $\mathbf{Q}_{ij}^c$  can appear in the response with a certain difference in phase with respect to the driven mode  $\mathbf{Q}_{ij}^s$ . The latter phenomenon may result in a travelling-wave vibration in circumferential direction [6; 58; 108].

As a final note regarding the discretization of  $w$ , the axi-asymmetrical deformations of the shell are *assumed* to be periodic in circumferential direction (similar as for the linear buckling modes and vibrational eigenmodes of perfect cylindrical shells). This assumption is also adopted by [2; 3; 24; 38; 46; 59; 107–109] and allows to use a relatively simple expansion of  $w$ . However, other studies show that the buckling of axially compressed cylindrical shells may (initially) occur via a circumferentially non-periodic deformation pattern [52; 119; 140]. Such deformations are not considered here since it would require a discretization of  $w$  with many DOFs.

The following (axi-asymmetrical) expansion of the radial imperfection  $w_0$  is considered

$$w_0(x, \theta) = h \sum_{i=1}^{N_e} e_i \sin(n\theta) \sin\left(\frac{i\pi x}{L}\right), \quad (7.15)$$

where  $N_e \leq N$  and  $e_i$  are dimensionless imperfection amplitudes. Note that preliminary simulations showed that axi-symmetrical imperfections are of less importance for the obtained results and are, therefore, not considered.

Using the above expressions for  $w$  and  $w_0$ , the in-plane equilibrium equations (Eqs. (7.9)-(7.10)) now consist of a set of linear inhomogeneous static partial differential equations in terms of only  $u$  and  $v$ . In order to perform a reduction of the three independent displacement fields to one independent displacement field  $w$ , these two PDEs are solved symbolically. The solution procedure for this purpose is outlined in Appendix C and results in expressions for  $u$  and  $v$  satisfying exactly the in-plane equilibrium equations (Eqs. (7.9)-(7.10)) and the in-plane boundary conditions (Eq. (7.5)). During this step, an extra DOF  $\mathbf{U}_t(t)$  is introduced which corresponds to the unknown axial displacement of the top mass.

### 7.1.1 Equations of motion

Now the displacement fields are known, the equations of motion in terms of the DOFs

$$\mathbf{Q}(t) = [\mathbf{Q}_{ij}^c(t), \mathbf{Q}_{ik}^s(t), \mathbf{U}_t(t)]^T, \quad i = 1, \dots, N, \quad j = 0, \dots, M, \quad k = 1, \dots, M, \quad (7.16)$$

are determined. Hereto, first the energy expressions (Eqs. (7.6)-(7.8)) are evaluated symbolically. Linear viscous damping in the structure is included via the following Rayleigh dissipation function

$$\mathcal{R} = \frac{1}{2} \sum_{i=1}^N \sum_{j=0}^M c_{ij} \left(\dot{\mathbf{Q}}_{ij}^c\right)^2 + \frac{1}{2} \sum_{i=1}^N \sum_{k=1}^M c_{ik} \left(\dot{\mathbf{Q}}_{ik}^s\right)^2 + \frac{1}{2} c_t \dot{\mathbf{U}}_t^2, \quad (7.17)$$

where  $c_{ij}$ ,  $c_{ik}$  and  $c_t$  are positive constants. Subsequently, the equations of motion are determined using *Lagrange's* equation

$$\frac{d}{dt}T_{,\dot{\mathbf{Q}}} - T_{,\mathbf{Q}} + \mathcal{V}_{,\mathbf{Q}} = \mathbf{Q}_{nc}, \quad (7.18)$$

where  $\mathcal{V} = \mathcal{U}_s + \mathcal{U}_g$  and

$$\mathbf{Q}_{nc} = -\mathcal{R}_{,\dot{\mathbf{Q}}}. \quad (7.19)$$

In summary, the equations of motion are derived by the following steps

1. Discretize the out-of-plane displacement field  $w$  as in Eq. (7.14) and the radial imperfection shape  $w_0$  as in Eq. (7.15).
2. Solve the corresponding in-plane fields  $u$  and  $v$ . During this step, an extra DOF  $\mathbf{U}_t(t)$  is introduced which corresponds to the unknown axial displacement of the top mass (see appendix C).
3. Substitute the resulting expressions for  $w$ ,  $w_0$ ,  $u$  and  $v$  in the energy and work expressions Eqs. (7.6)-(7.8), and evaluate the integrals symbolically.
4. Derive the equations of motion using Lagrange's equation Eq. (7.18) and add to each equation of motion a linear viscous damping term in the form  $c_{ij}\dot{\mathbf{Q}}_{ij}^{s,c}$  or  $c_t\dot{\mathbf{U}}_t$ , respectively.

This procedure is implemented in Maple routines [87], allowing to derive the equations of motions in an automatic manner after the expressions for  $w$  and  $w_0$  have been supplied. The equations of motions are exported from Maple [87] to both Fortran code and Matlab code [89] for further analysis.

To illustrate some key features of the model, the equations of motion of the perfect shell ( $w_0 = 0$  [m]) using an expansion of  $w$  with  $N = M = 1$  (see Eq.

(7.14)) are given

$$\begin{aligned}
 & m_1 \ddot{\mathbf{Q}}_{10}^c + c_{10} \dot{\mathbf{Q}}_{10}^c + \left[ k_1 + k_3 \mathbf{U}_t + k_2 (\mathbf{Q}_{11}^s)^2 + k_2 (\mathbf{Q}_{11}^c)^2 + \right. \\
 & \left. k_4 (\mathbf{Q}_{10}^c)^2 \right] \mathbf{Q}_{10}^c - k_5 (\mathbf{Q}_{10}^c)^2 - k_6 (\mathbf{Q}_{11}^c)^2 - k_6 (\mathbf{Q}_{11}^s)^2 - k_7 \mathbf{U}_t = 0 \\
 & m_2 \ddot{\mathbf{Q}}_{11}^s + c_{11} \dot{\mathbf{Q}}_{11}^s + \left[ k_8 + k_9 (\mathbf{Q}_{11}^c)^2 + k_{10} \mathbf{U}_t - k_{11} \mathbf{Q}_{10}^c + \right. \\
 & \left. k_{12} (\mathbf{Q}_{10}^c)^2 + k_{13} (\mathbf{Q}_{11}^s)^2 \right] \mathbf{Q}_{11}^s = 0 \\
 & m_2 \ddot{\mathbf{Q}}_{11}^c + c_{11} \dot{\mathbf{Q}}_{11}^c + \left[ k_8 + k_9 (\mathbf{Q}_{11}^s)^2 + k_{10} \mathbf{U}_t - k_{11} \mathbf{Q}_{10}^c + \right. \\
 & \left. k_{12} (\mathbf{Q}_{10}^c)^2 + k_{13} (\mathbf{Q}_{11}^c)^2 \right] \mathbf{Q}_{11}^c = 0 \tag{7.20} \\
 & m_t \ddot{\mathbf{U}}_t + c_t \dot{\mathbf{U}}_t + k_{14} \mathbf{U}_t - k_{15} \mathbf{Q}_{10}^c + k_{16} (\mathbf{Q}_{11}^c)^2 + \\
 & k_{17} (\mathbf{Q}_{10}^c)^2 + k_{18} (\mathbf{Q}_{11}^s)^2 = -m_t (\ddot{\mathbf{U}}_b + g),
 \end{aligned}$$

where  $k_i$  and  $m_i$  are positive constants. The DOF  $\mathbf{U}_t$ , which has both a linear coupling and a nonlinear coupling with the axi-symmetrical mode  $\mathbf{Q}_{10}^c$  (the linear coupling is due to the Poisson effect), is directly excited by the prescribed base-acceleration  $\ddot{\mathbf{U}}_b$ , see Eq. (7.20). The coupling with the axi-asymmetrical modes  $\mathbf{Q}_{11}^{s,c}$  is only attained via the non-linear stiffness terms (since in this case  $w_0 = 0$  [m]).

## 7.2 Static and modal analysis

In this section, first the static response of the cylindrical shell with top mass is examined. Subsequently, a modal analysis is performed for linearized models of the cylindrical shell with top mass. The goal of these two studies is to analyze the static buckling behaviour and the linear eigenfrequencies of the cylindrical shell including the influence of geometric imperfections and to test the convergence of the results for various expansions of the out-of-plane displacement field  $w$ . The results are numerically validated via a comparison with results obtained using the FEM package MSC.Marc. As a test case, a cylindrical shell is considered of which the static buckling behaviour due to compressive loading is experimentally studied in [146]. The material properties of the cylinder, which is made out of isotropic polyester film, are defined in Table 7.1.

During the experimental axial compression test of this shell [146], the shell buckles from the axi-symmetrical pre-buckling state to an axi-asymmetrical post-buckled state which is dominated by one full sine-wave in axial direction



Table 7.1: Material properties isotropic cylindrical shell.

$E$	5.56	[GPa]
$\nu$	0.3	[-]
$\rho$	1370	[kg/m <sup>3</sup> ]
$R$	100	[mm]
$L$	160.9	[mm]
$h$	0.247	[mm] ( $R/h = 405$ )

(i.e.  $i = 2$ , see Eq. (7.14)) and a circumferential wave number of  $n = 11$ . Therefore, detailed results will be presented for  $n = 11$ . In Subsection 7.3.4, the influence of the specific choice of the value for  $n$  on the obtained results will be further discussed.

### 7.2.1 FE model

Since a deformation pattern in circumferential direction with  $n$  periods is assumed, only one  $1/n^{\text{th}}$  segment is modelled in the FE package MSC.Marc. The resulting FE model consists of 3500 four-node thin shell elements (100 elements in axial direction and 35 elements in circumferential direction of type 139 [93], see Fig. 7.3. The (nonlinear) kinematic relations used in the FE model are based on the *Kirchhoff* assumptions and are valid for large displacements and moderate rotations. Furthermore, an updated Lagrange procedure is used. Note that Donnell's kinematic relations which are used for the semi-analytical model, are also based on the Kirchhoff assumptions [17]. However, in Donnell's theory, further approximations are introduced by assuming that the deformations are dominated by radial displacements and that the displacement components are rapidly varying functions of the circumferential coordinate, i.e.  $n > 4$ , see [17] and [34]. The latter approximations are not used in the FE model.

For the FE model, the same boundary conditions are considered as for the semi-analytical model (see Eq. (7.5)). To enforce periodicity in circumferential direction, the displacements and rotations of the nodes along the side edges of the FE model are linked and the displacements in circumferential direction are suppressed. The top mass is modelled as a point mass of  $m_t/n$  [kg], attached to a node placed at the top center. The axial displacement of this node is linked with the axial displacements of the nodes along the top edge of the FE model (enforcing the boundary condition  $u_{,\theta} = 0$  at  $x = L$ ). In the FE model, the initial imperfection is included by positioning the nodes radially according to

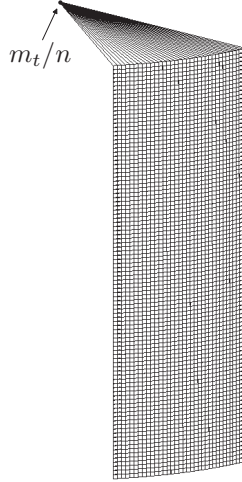


Figure 7.3: FE model of a  $1/n^{\text{th}}$  segment of the cylindrical shell with top mass ( $n = 11$ ).

the considered imperfection shape  $w_0$ .

### 7.2.2 Static analysis

For the static analysis, all time-derivatives in the equations of motion are set to zero and the case  $\mathbf{U}_b(t) = 0$  is considered. In the static case, the only force exerted on the cylindrical shell is due to the weight of the top mass

$$\int_0^{2\pi} N_x(x=L)Rd\theta = -m_t g = -P \cdot P_c \text{ [N]}, \quad (7.21)$$

where  $P$  is a newly introduced dimensionless load-parameter and

$$P_c = 2\pi E h^2 / \sqrt{3(1-\nu^2)} \text{ [N]}, \quad (7.22)$$

is the classical static buckling load of the axially compressed cylindrical shell [17] ( $P_c = 1289 \text{ [N]}$  for the parameters according to Table 7.1). By solving the resulting algebraic equations for a varying static load  $P$  (which can, for example, be considered as a variation in  $m_t$ ), using the continuation package AUTO [33], the static (post) buckling behaviour of the cylindrical shell is examined.

The considered expansion of the imperfection  $w_0$  (see Eq. (7.15)) will trigger the modes with DOFs  $\mathbf{Q}_{i1}^s$ . Consequently, for a discretization of  $w$  (see Eq.

(7.14)) with  $M = 2$ , only the modes with DOFs  $\mathbf{Q}_{i0}^c$ ,  $\mathbf{Q}_{i1}^s$  and due to internal couplings the modes with DOFs  $\mathbf{Q}_{i2}^c$  will appear in the static response. The modes with DOFs  $\mathbf{Q}_{i1}^c$  and  $\mathbf{Q}_{i2}^s$  do not contribute to the static response and are, therefore, removed from the model.

In Fig. 7.4, the static response of the axially loaded imperfect shell ( $e_1 = e_2 = 0.284$ , other  $e_i = 0$ ), based on a 31-DOF model ( $N = 10, M = 2$  with  $\mathbf{Q}_{i1}^c = \mathbf{Q}_{i2}^s = 0$  [m]) is depicted. The accuracy of this model will be discussed later on. Note that the load-path is presented in terms of the dimensionless load  $P$  (Eq. (7.21)) and the dimensionless axial displacement

$$u_L = u(t, L, \theta)/L. \quad (7.23)$$

Note that  $u_L = \mathbf{U}_t(\mathbf{t})/L$ , see Eq. (C.12). Furthermore,  $u_L < 0$  corresponds to axial shortening of the cylindrical shell, see Fig. 7.2. Starting at the initial unloaded state ( $P = 0$ ), buckling of the shell occurs at the limit-point at approximately  $P = P_b = 0.77$ , see enlargement *A* in Fig. 7.4. The post-critical behaviour shows many coexisting stable and unstable post-buckled states. The deformed shapes for six (stable) states (indicated in Fig. 7.4 with **a-f**) are shown in Fig. 7.5. As can be noted, along the complex load-path depicted in Fig. 7.4, successively the stability is lost and reattained again, resulting in a so-called 'cellular' buckling sequence [57].

The post-critical load-path exhibits a minimum at point **f** ( $P = 0.230$ ). This minimum is of practical importance since above this load, it is possible that due to some external disturbance, the shell may jump from the initial unbuckled state to a stable buckled state. At the local minimum at point **c** in Fig. 7.4 ( $P = 0.245$ ,  $u_L = -1.17 \cdot 10^{-3}$ ), the buckled shape is dominated by one full sine-wave in axial direction, see Fig. 7.5-**c**. In experiments performed with the same shell but with slightly different boundary conditions ( $w_{,x} = 0$  instead of  $M_x = 0$ ), a comparable (local) minimum post-buckling load with corresponding axial shortening and buckled shape is obtained ( $P \approx 0.24$  and  $u_L \approx -1.3 \cdot 10^{-3}$ , see Fig. 3.52 in [146]). Obviously, also the initial imperfection considered in the semi-analytical model and the imperfection in the actual shell in [146] will differ. Small imperfections have, however, only a mild influence on such (far) post-critical responses [24; 109; 146].

The post-buckled state dominated by three axial half sine-waves (see Fig. 7.5-**f**) is not found in the experiments of [146]. Instead, a buckling event to a state with another circumferential distribution ( $n = 10$ ) is found for further increasing axial shortening. This buckling event can, obviously, not be captured with the current semi-analytical model, since during the computations the circumferential wave number remains fixed to  $n = 11$ .

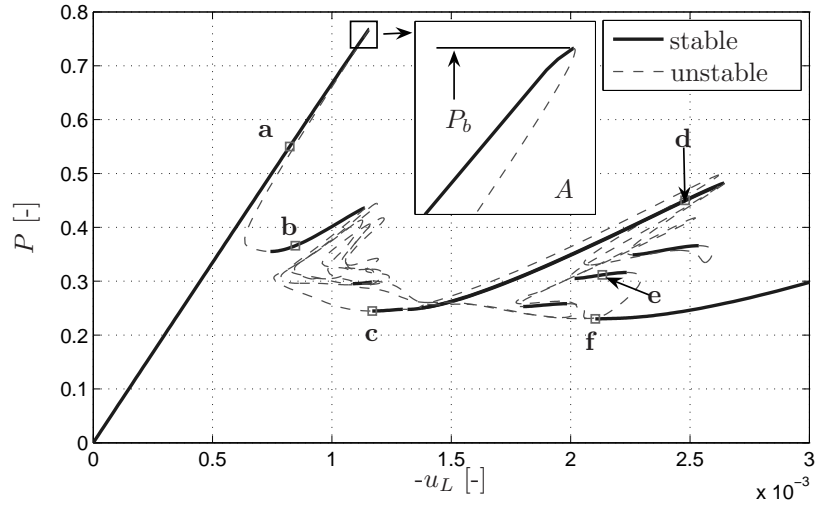


Figure 7.4: Static load-path imperfect cylindrical shell ( $e_1 = e_2 = 0.284$ ,  $n = 11$ ).

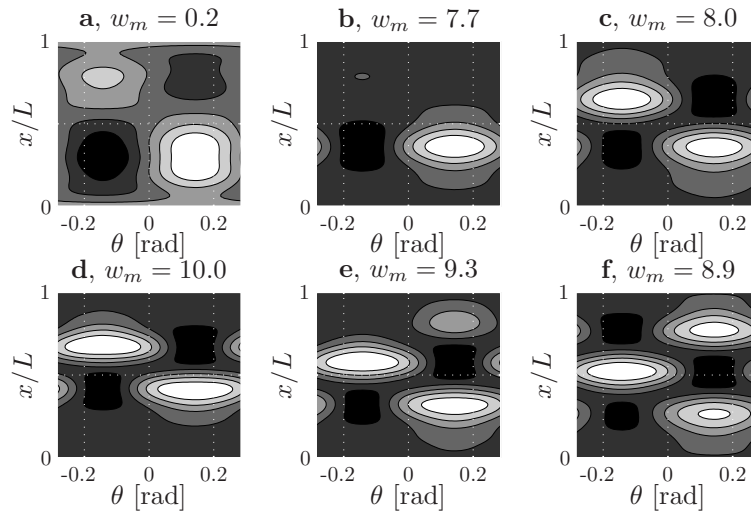


Figure 7.5: Contour plots of  $w$  (only  $1/n^{\text{th}}$  segment shown) for labelled states in Fig. 7.4 (max  $w$  = white, min  $w$  = black,  $w_m = \max |w|/h$ ).

In Fig. 7.6, the first part of the load-path depicted in Fig. 7.4 (computed using the 31-DOF semi-analytical model) is compared with results obtained using the FE model. Note that no stability information for the FE results is included, since this information is not provided by the FE package. Although the semi-analytical results do not exactly match the FEM results, there is a good qualitative correspondence. Compared with the FE results, the semi-analytical model predicts a 7.4 % higher primary buckling load (FEM :  $P_b = 0.714$ , 31-DOF :  $P_b = 0.767$ ) but a very well corresponding (local) minimum post-buckling load with corresponding axial shortening, see enlargement *A* in Fig. 7.4. Note that at two points, also the maximum out-of-plane displacement  $w_m$  is compared.

Primary static buckling loads ( $P_b$ ) for other imperfection shapes, all with only one nonzero  $e_i$  and  $\max|w_0|/h = 0.5$ , are compared in Table 7.2. Note that the buckling loads are obtained in a similar fashion as in Fig. 7.4, i.e. by determining the limit-point in the initial load-path. Next to results obtained using the 31-DOF model and the FE model, also results for other discretizations of  $w$  (Eq. (7.14)) are included. As can be noted, the imperfection shapes with the higher number of axial half wave numbers give the largest decrease in buckling load. For comparison of the semi-analytical results (for various discretizations of  $w$ ) with the FEA results, their mean relative differences  $\Delta$  are included in Table 7.2,  $\Delta$  being defined by

$$\Delta = \frac{1}{6} \sum_{i=1}^6 \left( \frac{P_b^i - P_b^{i,\text{FEM}}}{P_b^{i,\text{FEM}}} \right), \quad (7.24)$$

where  $P_b^i$  and  $P_b^{i,\text{FEM}}$  denote the primary static buckling load for  $e_i \neq 0$ , computed using the semi-analytical model (for a given discretization of  $w$ ) and the FE model, respectively. For the models considered, the 31-DOF model shows the best overall correspondence with the FE results. The necessity to include the modes with a double harmonic in circumferential direction ( $\mathbf{Q}_{12}^c$ ) is illustrated in Table 7.2 for  $N = 10$ , i.e. using  $M = 2$  (31-DOF) instead of  $M = 1$  (21-DOF) in Eq. (7.14) results in a large decrease in the primary buckling loads. Due to computational limitations, extension of the 31-DOF model with even more modes was not possible.

### 7.2.3 Modal Analysis

Next, the undamped eigenfrequencies of the perfect cylindrical shell with top mass are determined. Hereto, first the static equilibrium state for a given static preload is determined. Subsequently, the equations of motion are linearized around this equilibrium state and a modal analysis is performed. The top mass is fixed at  $m_t = 10$  [kg] and two levels of pre-load are considered, i.e.

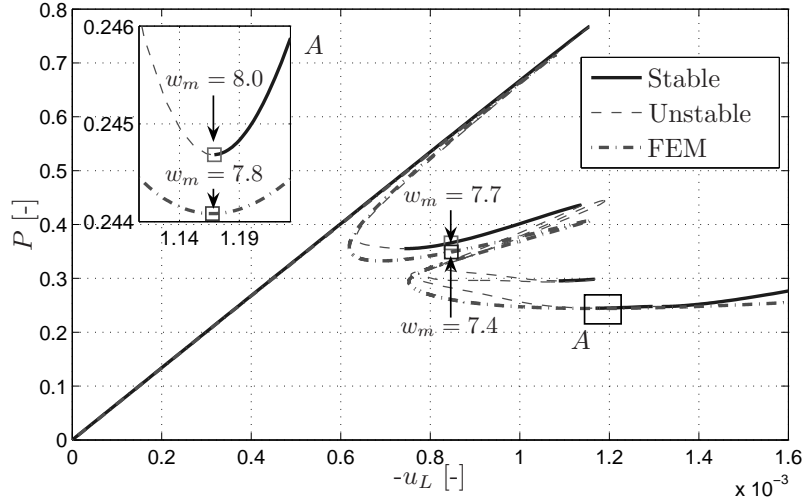


Figure 7.6: Static load-path of imperfect ( $e_1 = e_2 = 0.284$ ) cylindrical shell, FEM vs. 31-DOF semi-analytical model ( $w_m = \max |w|/h$ ).

Table 7.2: Primary static buckling loads of the imperfect cylindrical shell ( $\Delta$  defined by Eq. (7.24)).

Model			$P_b$ [-]						$\Delta$
N	M	DOF	$e_1 = 0.5$	$e_2 = 0.5$	$e_3 = 0.5$	$e_4 = 0.5$	$e_5 = 0.5$	$e_6 = 0.5$	
6	2	19	0.937	0.659	0.644	0.649	0.618	0.614	27.5%
8	2	25	0.868	0.655	0.531	0.546	0.557	0.526	13.0 %
10	1	21	0.930	0.718	0.596	0.597	0.656	0.621	27.2 %
10	2	31	0.861	0.669	0.541	0.495	0.519	0.463	7.8 %
FEM			0.800	0.642	0.512	0.482	0.456	0.412	-

$g = 0$  [m/s<sup>2</sup>] ( $P = 0$ ) and  $g = 9.81$  [m/s<sup>2</sup>] ( $P = 0.076$ ). The results are shown in Table 7.3, using the same models as used for the static analysis.

The lowest vibration mode is an axi-symmetrical suspension type of mode and the higher vibration modes correspond to axi-asymmetrical modes, see also Fig. 7.7. The pre-load ( $g = 9.81$  [m/s<sup>2</sup>]) results in a small decrease (2-3%) of the eigenfrequencies corresponding to axi-asymmetrical vibrational eigenmodes. The results are in good agreement with the FEM results, i.e. the maximum difference between the semi-analytical results and the FEM results

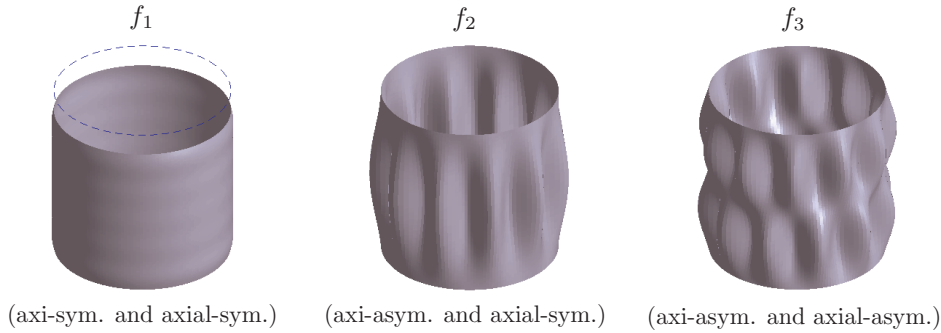


Figure 7.7: First three vibrational eigenmodes cylindrical shell ( $n = 11$ , top mass not shown).

is approximately 0.6%. All models predict approximately the same values for the first three eigenfrequencies. Apparently, for accurate calculation of the first three vibration modes, less modes are required than for an accurate static buckling analysis (see Table 7.2).

Including the same geometrical imperfections as considered in Table 7.2, the eigenfrequencies  $f_1$ ,  $f_2$  and  $f_3$  of the pre-loaded shell decrease maximally 1.4%, 2.9% and 4.5% (compared to the pre-loaded perfect case), respectively. Similar as for the buckling loads (see Table 7.2), the largest decreases occur for the imperfection with the largest number of axial half waves ( $e_6$ ). In conclusion, the imperfections have more influence on the primary static buckling loads than on the linearized eigenfrequencies.

Table 7.3: First three eigenfrequencies perfect cylindrical shell with top mass ( $n = 11$ ,  $m_t = 10$  [kg]).

N	M	DOF	$g = 0$ [m/s <sup>2</sup> ]			$g = 9.81$ [m/s <sup>2</sup> ]		
			$f_1$ [Hz]	$f_2$ [Hz]	$f_3$ [Hz]	$f_1$ [Hz]	$f_2$ [Hz]	$f_3$ [Hz]
6	2	19	116.9	357.6	567.9	116.9	350.6	551.5
8	2	25	116.8	357.5	567.9	116.8	350.5	551.2
10	1	21	116.8	357.5	567.9	116.7	350.5	551.2
10	2	31	116.8	357.5	567.9	116.7	350.5	551.2
FEM			116.6	355.7	568.9	116.6	348.5	552.0

### 7.3 Dynamic analysis

In this section, the nonlinear dynamic steady-state response of the cylindrical shell subjected to the combination of a static load (due to the weight of the top mass) and a harmonic prescribed base-acceleration

$$\ddot{\mathbf{U}}_{\mathbf{b}}(t) = r_d g \sin(2\pi ft), \quad (7.25)$$

will be studied. The top mass is fixed at  $m_t = 10$  [kg] and only the preloaded case  $g = 9.81$  [m/s<sup>2</sup>] is considered. Note that for this level of preload ( $P = 0.076$ , see Eq. (7.21)), the unbuckled configuration is still a unique stable equilibrium state of the cylindrical shell (see Fig. 7.4). For small amplitudes of the base-acceleration  $r_d$  [-] the response is expected to be harmonic with small (out-of-plane) displacements. However, for increasing values of  $r_d$  the harmonic response may become unstable and/or severe large (out-of-plane) amplitude vibrations may appear. The goal of the dynamic analysis is to determine where such instabilities will occur (i.e. for which combinations of frequency and amplitude of the base-acceleration) and how these results depend on possible geometric imperfections in the cylindrical shell. Special attention will be paid to the behaviour near the first resonance peak at about 117 [Hz], since here the first instabilities are found. In all simulations, a little amount of damping is taken into account by setting the linear viscous damping parameters  $c_{ij}$  and  $c_t$  such, that all the linear vibration modes have the same relative damping ratio, namely  $\xi = 0.01$ .

Numerical continuation of periodic solutions [33] with the excitation frequency  $f$  [Hz] as continuation parameter is adopted to study the steady-state behaviour of the cylindrical shell. The local stability of the periodic solutions is determined using Floquet theory [120]. Furthermore, for excitation frequencies where no stable periodic solutions are found, standard numerical integration of the equations of motion is performed using a Runge-Kutta integration scheme with adaptive step-sizing (NAG routine D02PDF [96]).

Among the semi-analytical models considered in the static and modal analyses (see Section 7.2), the 31-DOF model (expanding  $w$  with  $N = 10$ ,  $M = 2$ , see Eq. (7.14), excluding companion modes) showed to be the most accurate (especially for determining the primary static buckling load, see Table 7.2). This model will, therefore, also be used in the dynamic analysis. However, prior to the analysis based on this 31-DOF semi-analytical model, first analyses will be performed using two models with less DOF. These models are obtained by setting all DOF in the expansion of  $w$  with  $N = 10$  and  $M = 2$ , which correspond to axial-asymmetrical radial displacements (an example of an axial-asymmetrical deformed shell can be seen in the right plot of Fig. 7.7), to zero. This results in a 26-DOF model if companion modes are included (see also



Subsection 7.2.2) and in a 16-DOF model if companion modes are excluded. Note that the exclusion of the axial-asymmetrical modes may be justified by the fact that the lowest two vibrational eigenmodes are also axial-symmetrical, see Fig. 7.7. The models which will be considered for the dynamic analysis are summarized in Table 7.4.

Table 7.4: Models derived from the full expansion of  $w$  with  $N = 10$  and  $M = 2$ , see Eq. (7.14).

	16-DOF	26-DOF	31-DOF
axial asymmetrical modes (with DOFs $\mathbf{Q}_{ij}^{s,c}$ with $i = 2, 4, \dots$ )	excluded	excluded	included
companion modes (with DOFs $\mathbf{Q}_{i2}^s$ and $\mathbf{Q}_{i1}^c$ )	excluded	included	excluded

First the nonlinear dynamic steady-state results obtained with the three models will be discussed for one fixed value of  $n$  ( $n = 11$ ) in Subsections 7.3.1, 7.3.2, and 7.3.3, respectively. By comparing the results obtained for the three models, the effect of including the companion modes or the axial-symmetrical modes will be examined. Hereafter, in Section 7.3.4 the influence of the specific choice of the value for  $n$  on the obtained results will be examined.

### 7.3.1 Model without companion modes and without axially asymmetrical modes (16-DOF)

In this subsection, dynamic buckling of the cylindrical shell with top mass due to the prescribed harmonic base-acceleration Eq. (7.25) is studied in detail using the most simple model (i.e. the 16-DOF model, see Table 7.4). The accuracy of this model will be illustrated in the next two subsections. First the response of the perfect cylindrical shell is considered. Hereafter, the influence of geometrical imperfections on the found dynamic buckling results is examined. To obtain more insight in the found dynamic buckling response, the subsection concludes with an analysis of the exerted axial force on the cylindrical shell during the dynamic buckling.

The steady-state response of the perfect case ( $w_0 = 0$  [m]) for a varying excitation frequency  $f$  is depicted in Fig. 7.8 for  $r_d = 0.27$ . Note that the steady-state response is plotted in terms of the following measure

$$U_m = \max_T u_L - \min_T u_L \geq 0, \quad (7.26)$$

where  $u_L$  denotes the dimensionless axial displacement (see Eq. (7.23)) and  $T = 1/f$ . The response shows a harmonic resonance around the first linear

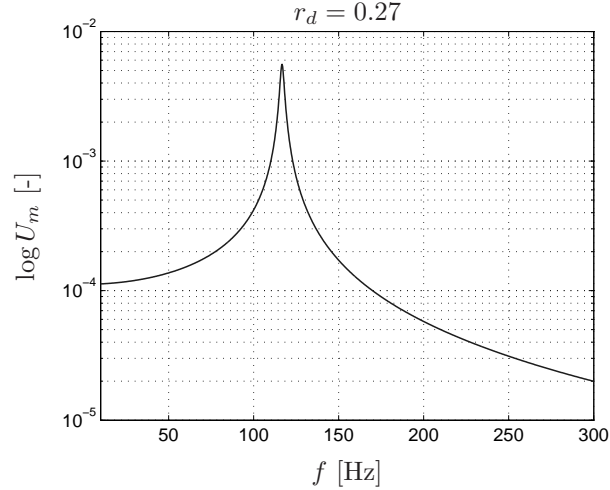


Figure 7.8: Frequency-amplitude plot of the perfect shell for  $r_d = 0.27$ .

eigenfrequency ( $f_1 = 116.7$ , see Table 7.3) and does not exhibit any regions of instability. However, for  $r_d > 0.279$ , a small region of instability appears in the top of the harmonic resonance, see Fig. 7.9. Note that the stability of the harmonic response is lost due the appearance of period doubling bifurcations at frequencies indicated in Fig. 7.9 with '□'. The response in the region of instability is further examined using numerical integration of the equations of motion. As initial condition, very small perturbations are given to the DOFs ( $\mathbf{Q}_{ij}^{s,c}/h = 1 \cdot 10^{-3}$ ) to initiate (possible) instabilities. Transient effects are excluded by only considering the response after  $t/T = 2000$  ( $T = 1/f$ ). Results of this approach for three values of  $r_d$  and  $f = f_1$  are depicted in Fig. 7.10 and Fig. 7.11. Note that the responses are depicted in terms of two measures, i.e. the dimensionless axial displacement  $u_L$  (see Eq. (7.23)) and the dimensionless out-of-plane displacement

$$w_{L/2} = w(t, L/2, \pi/(2n))/h. \quad (7.27)$$

Note that  $w_{L/2}$  is scaled using the shell thickness  $h$  while  $u_L$  is scaled using the shell length  $L$ .

For  $r_d = 0.27$ , i.e. just below the loss of stability of the harmonic response at  $f = f_1$  (see Fig. 7.9), the out-of-plane response is in phase with the axial shortening and only small out-of-plane displacements are initiated due to the Poisson effect, see Fig. 7.10.

For  $r_d = 0.3$  the harmonic solution is no longer stable at  $f = f_1$  and instead a  $1/2$  subharmonic response is found (period  $2T$ ), see Fig. 7.10 (this response is

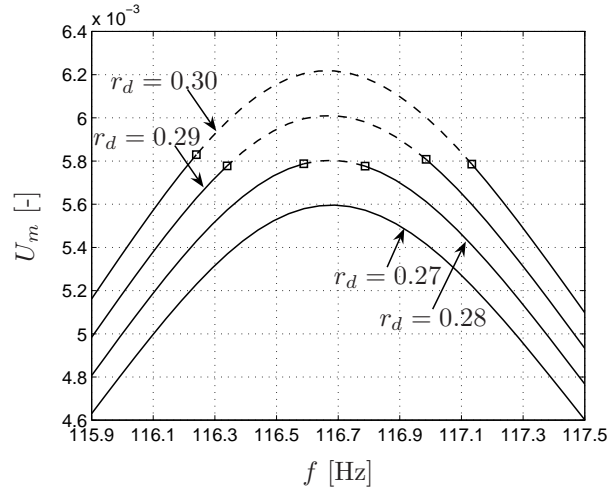


Figure 7.9: Frequency-amplitude plot of the perfect shell for four increasing values of  $r_d$  and  $f$  close to  $f_1$  ( $f_1 = 116.7$  [Hz]).

most clearly visible in the time response in terms of  $w_{L/2}$  for  $r_d = 0.30$ ). The Power Spectral Density (PSD) of this  $1/2$  subharmonic response in terms of the measure  $w_{L/2}$  and the normalized frequency  $F/f_1$  (the excitation frequency equals  $f = f_1$ ) is depicted in Fig. 7.12. The  $1/2$  subharmonic behaviour is clearly indicated by a peak at  $F = \frac{1}{2}f_1$ . Note that the PSD is determined from a data set obtained by sampling the response (obtained using numerical integration) with a fixed time step of  $\Delta t = 1/16000$  [s]. Furthermore, as a reference, the locations of the 16 damped linear eigenfrequencies of the 16-DOF model are also indicated in Fig. 7.12 (note that  $f_{12}$ ,  $f_{13}$  and  $f_{14}$  nearly coincide).

By increasing the amplitude of the base-excitation further to  $r_d = 0.33$ , a very severe beating response is found, see Fig. 7.11. This type of response exhibits short time intervals in which energy is transferred back and forward from the suspension mode at  $f = f_1$  (see Fig. 7.7), to severe axi-asymmetrical out-of-plane vibrations. The PSD of this beating response is depicted in Fig. 7.13 (in a similar fashion as in Fig. 7.12). The PSD of the beating response is broad-banded, suggesting that the beating response has a chaotic nature. The spikes in the PSD at  $f = 3f_1 = f_2$  and at  $f = 10f_1 = f_4$  indicate internal resonances with the modes present at these two frequencies (at  $f = 3f_1$  the second mode with  $\langle n, m \rangle = \langle 11, 1 \rangle$  occurs and at  $f = 10f_1$  the fourth mode with  $\langle n, m \rangle = \langle 22, 1 \rangle$  occurs, where  $m$  denotes the number of half sine waves in axial direction). For other values of  $n$ , these ratios becomes less favourable

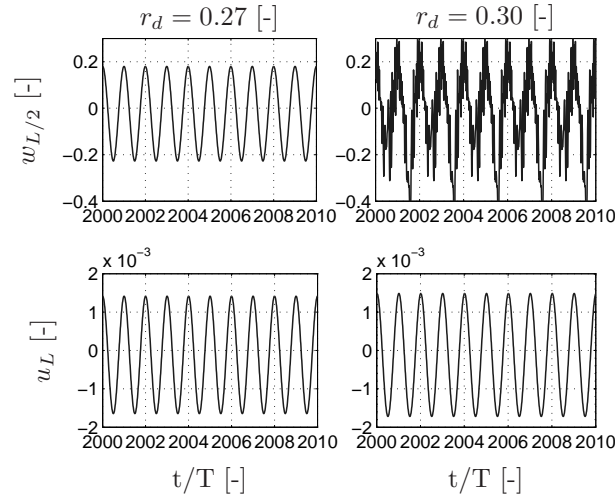


Figure 7.10: Harmonic (left) and 1/2 subharmonic response (right) ( $w_0 = 0$  [m],  $f = f_1$ ).

for internal resonance, but still similar beating types of response are found (see Section 7.3.4). For further illustration, an enlargement of  $w_{L/2}$  during the time interval  $A$  in Fig. 7.11 is shown in Fig. 7.14. The deformed shapes at six time instances during this interval of time are shown in Fig. 7.15. As can be observed from Fig. 7.15, also modes with a relatively short wave-length (i.e.  $n = 22$  and  $m > 1$ ) participate in the beating response.

As shown for the perfect cylindrical shell under consideration, there exists a threshold value  $r_d^c$  for the base-acceleration  $r_d$  [-] such that for  $r_d < r_d^c$  the harmonic solution is always stable and for  $r_d > r_d^c$  there exists a small region of instability in the top of the harmonic resonance. In this region the response is first subharmonic and for further increasing  $r_d$ , a response with short time intervals of very severe out-of-plane vibrations is obtained.

Next the influence of geometrical imperfections of the cylindrical shell on the dynamic buckling results is examined. The steady-state response of the imperfect ( $e_1 = 0.5$ ) cylindrical shell with top mass for a varying excitation frequency  $f$  is depicted in Fig. 7.16. Note that for  $e_i \neq 0$ , see Eq. (7.15), a direct coupling is present between the axi-symmetrical modes with DOF  $\mathbf{Q}_{i0}^c$  and the axi-asymmetrical modes with DOF  $\mathbf{Q}_{i1}^s$ . Similar as for the perfect case, the stability of the harmonic response is firstly lost at period doubling bifurcations (indicated in Fig. 7.16 with '□') in the top of the harmonic resonance around  $f = f_1$  for increasing values of  $r_d$ . Compared to the perfect case ( $r_d^c = 0.279$ ,

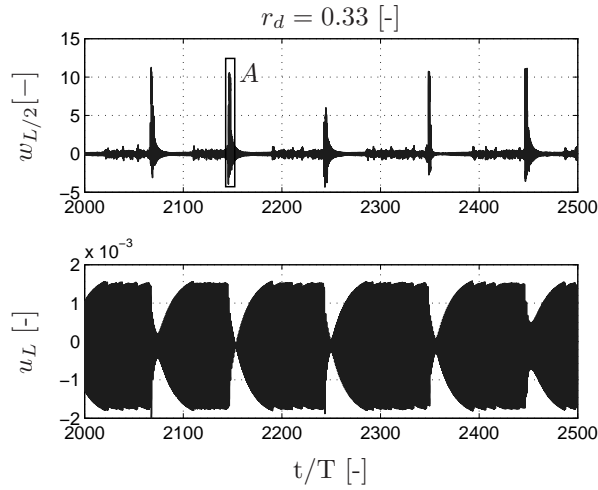


Figure 7.11: Beating response ( $w_0 = 0$  [m],  $f = f_1$ ).

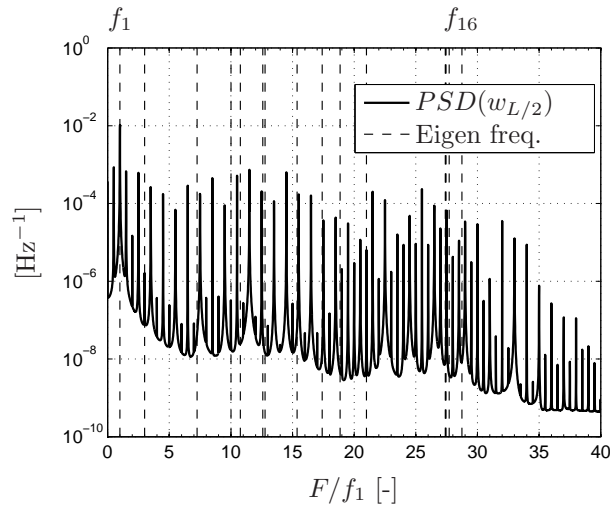


Figure 7.12: Power Spectral Density of 1/2 subharmonic response depicted in Fig. 7.10 (right:  $f = f_1$ ,  $r_d = 0.30$ ).

see Fig. 7.9), the value of  $r_d^c$  is (slightly) lower for  $e_1 = 0.5$  ( $r_d^c = 0.252$ ). The response for  $f = f_1$  and  $r_d = 0.25$  (i.e. just below  $r_d^c$ ), obtained using the numerical integration approach, is depicted in Fig. 7.17 and in a similar fashion for  $r_d = 0.255$  (just above  $r_d^c$ ) in Fig. 7.18. In contrast to the perfect case, for the imperfect case ( $e_1 = 0.5$ ) the response for values of  $r_d$  just above  $r_d^c$  is

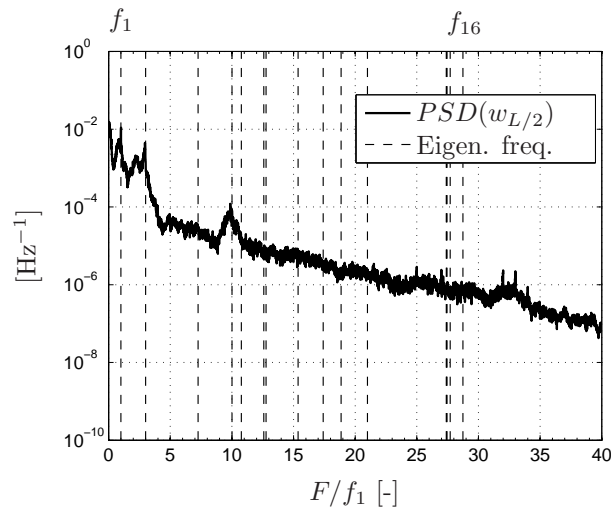


Figure 7.13: Power Spectral Density of beating response depicted in Fig. 7.11 ( $f = f_1$ ,  $r_d = 0.33$ ).

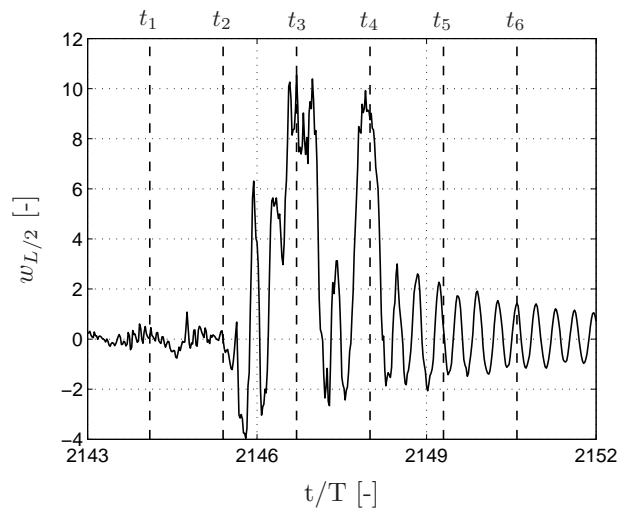


Figure 7.14: Enlargement of  $w_{L/2}$  during time interval A in Fig. 7.11.

directly the beating response (instead of first a subharmonic response, see Fig. 7.10). The sudden transition between the harmonic response and the beating response is more clearly visualized in Fig. 7.19. This bifurcation diagram is obtained by plotting 1000 times the  $T$ -sampled steady-state value of  $w_{L/2}$  for

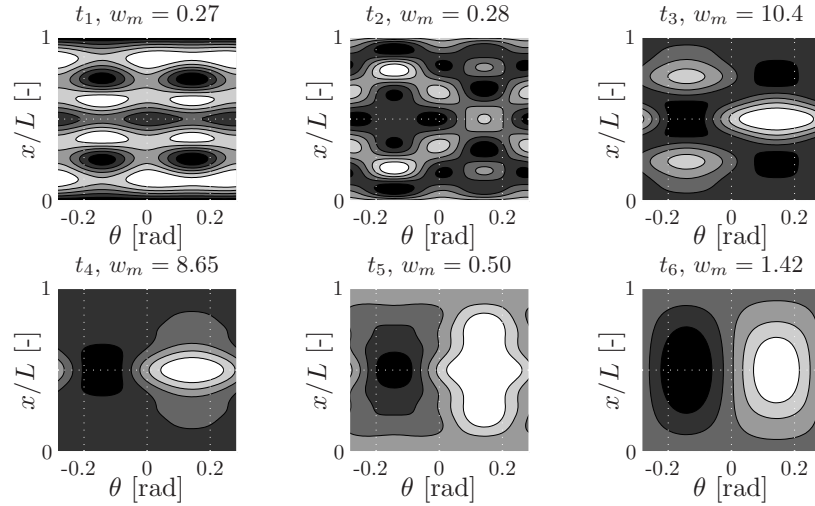


Figure 7.15: Contour plots of  $w$  (only  $1/n^{\text{th}}$  segment shown) at indicated time instances in Fig. 7.14 (max  $w$  = white, min  $w$  = black,  $w_m = \max |w|/h$ ).

each value of  $r_d$  ( $\Delta r_d = 0.001$ ).

In the dynamic case, a time-varying axial loading is exerted on the cylindrical shell with a magnitude of

$$\int_0^{2\pi} N_x(x=L) R d\theta = -m_t (\ddot{\mathbf{U}}_t + \ddot{\mathbf{U}}_b + g) - c_t \dot{\mathbf{U}}_t = -P_d(t) \cdot P_c \text{ [N]}, \quad (7.28)$$

where  $P_d(t)$  is a newly introduced dimensionless dynamic loading parameter and  $P_c$  is the classical static buckling load of the axially compressed cylindrical shell, see Eq. (7.22). For the imperfection under consideration ( $e_1 = 0.5$ ), the primary static buckling load of the cylindrical shell equals  $P_b = 0.8607$  (see Table 7.2). Obviously, the primary static buckling load  $P_b$  and the dynamic load  $P_d(t)$  can not be compared in a straightforward manner since for the dynamic case the load is varying in time and out-of-plane inertia and (small) damping effects of the shell are taken into account which are absent in the static case. Nevertheless, it is of interest to examine the level of the dynamic loading and to compare it with the static buckling load as a reference. In Fig. 7.20, the dynamic loading  $P_d(t)$  is shown for (parts of) the responses depicted in Fig. 7.17 and Fig. 7.18. For the case  $r_d = 0.25$  the dynamic loading moderately exceeds the static buckling load (i.e.  $\max(P_d(t))/P_b = 1.175$ ). Nevertheless, the response remains harmonic for this value of  $r_d$  (see Fig. 7.17). For the slightly higher value of the prescribed base-acceleration ( $r_d = 0.255$ ), initially

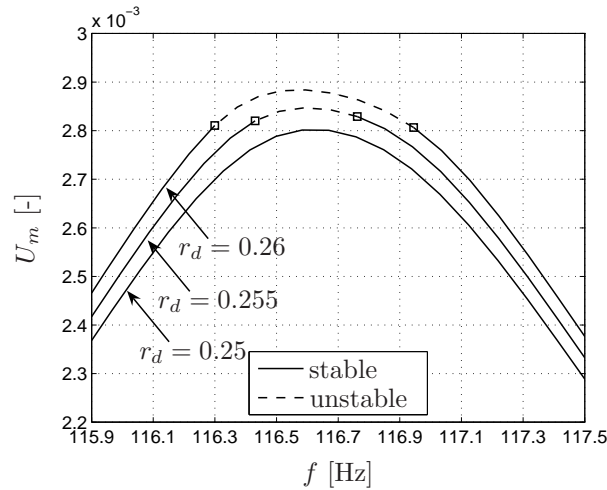


Figure 7.16: Frequency-amplitude plot imperfect shell ( $e_1 = 0.5$ ) for increasing values of  $r_d$  and  $f$  close to  $f_1$ .

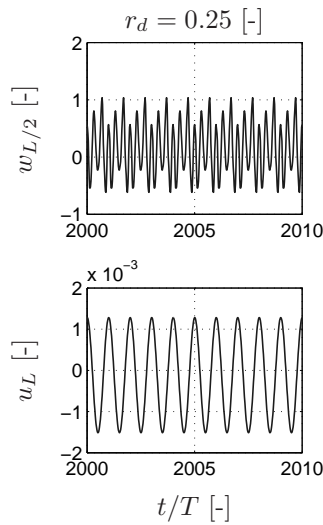


Figure 7.17: Harmonic response ( $e_1 = 0.5$  and  $f = f_1$ ).

the dynamic loading slowly increases to a maximum of  $\max(P_d(t))/P_b = 1.193$ , see enlargement *A* in Fig. 7.20). From this point, the large out-of-plane displacements occur for a short time interval (see also Fig. 7.18), in which the dynamic load drops to a level far below  $P_b$  (likely due to the fact that the axial rigidity of the cylindrical shell is lost for large out-of-plane displacements).



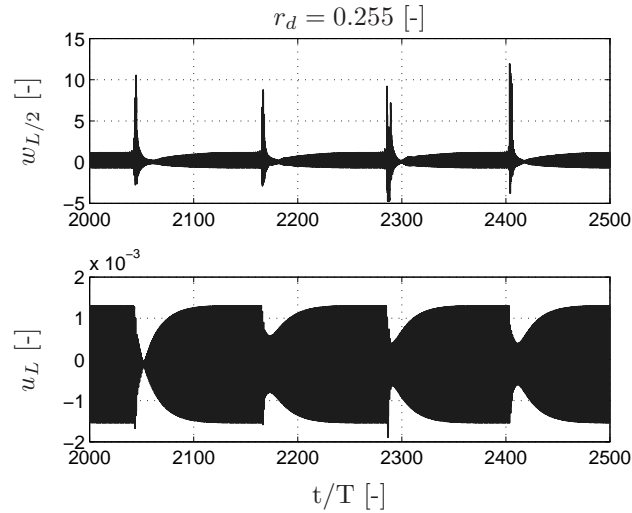


Figure 7.18: Beating response ( $e_1 = 0.5$  and  $f = f_1$ ).

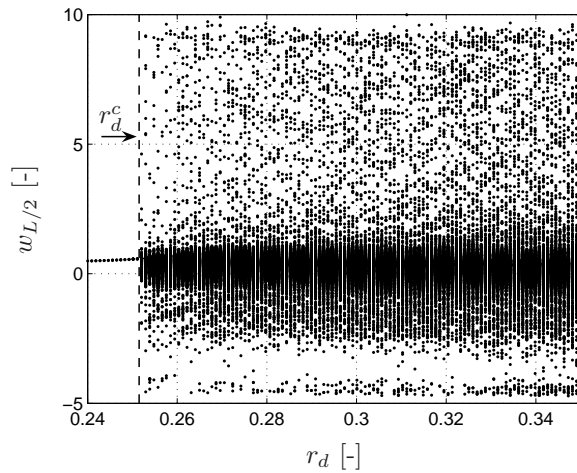


Figure 7.19: Bifurcation diagram ( $e_1 = 0.5$ ,  $f = f_1$ ).

After the severe out-of-plane displacements have disappeared, the dynamic loading starts to recover and after some time again a maximum is reached. Consequently, the beating response seems to be a cycle of 1. dynamic loading slowly building up, 2. a dynamic buckling event in which large out-of-plane vibrations occur, 3. a large drop in magnitude of the dynamic loading causing

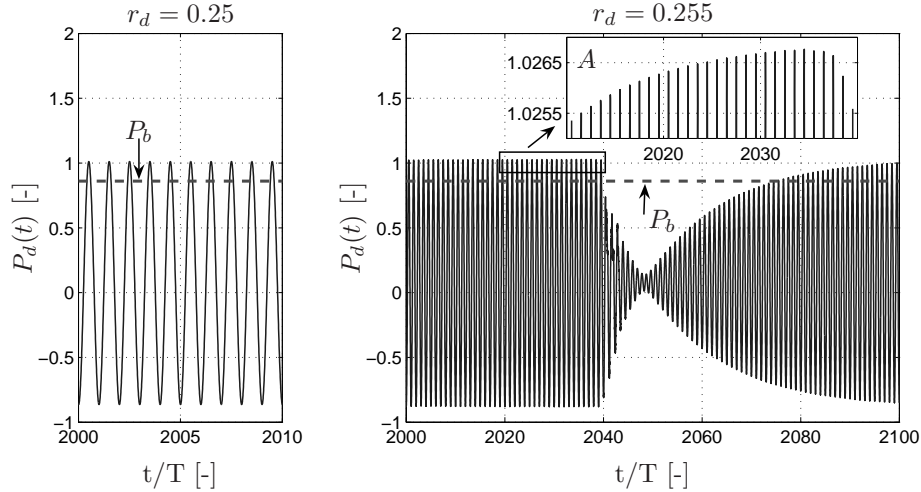


Figure 7.20: Dynamically exerted load for two values of  $r_d$  and  $e_1 = 0.5$ ,  $f = f_1$ .

the large out-of-plane vibrations to disappear after which the dynamic loading can be again slowly build up.

### 7.3.2 Model with companion modes but without axially asymmetrical modes (26-DOF)

Next, the effect of extending the semi-analytical model with the companion modes, on the obtained dynamic buckling results for the imperfect cylindrical shell is examined (i.e. the 26-DOF is used, see Table 7.4). Similarly as found in [109] for the onset to parametric instabilities of an imperfect cylindrical shell without a top mass, it appeared that inclusion of the companion modes does not affect the value of  $r_d^c$ . Furthermore, for values of  $r_d$  just above  $r_d^c$ , the companion modes also do not contribute to the beating response. Consequently, for determining the dynamic critical loads of the imperfect cylindrical shell with top mass (considering imperfections according to Eq. (7.15)), the companion modes do not have to be included in the semi-analytical model.

### 7.3.3 Model with axially asymmetrical modes but without companion modes (31-DOF)

Finally, the effect of including the axially asymmetrical modes is examined, i.e. the now 31-DOF model is used (see Table 7.4). Considering the response of the perfect shell obtained with this model, stability of the harmonic solution for

$f = f_1$  is lost at  $r_d^c = 0.274$  which is slightly lower than obtained for the model without the axially asymmetrical modes (16-DOF model :  $r_d^c = 0.279$ , see also Fig. 7.9). The transition from the harmonic solution to the beating type of solution via an intermediate subharmonic solution is not changed by including the axial-asymmetrical modes. However, now also axially asymmetrical modes participate in the response obtained for  $r_d > r_d^c$ .

The values of  $r_d^c$  obtained using the 31-DOF model for imperfection shapes with only one nonzero  $e_i$  and  $\max |w_0|/h = 0.5$  (similar as considered in Table 7.2), are shown in Table 7.5. For the axial symmetrical imperfections shapes ( $e_1$ ,  $e_3$  and  $e_5$ ), also the values of  $r_d^c$  obtained using the 16-DOF model are included. As can be noted, the values for  $r_d^c$  obtained using the 31-DOF model and the 16-DOF are the same or differ very little. Although for the 31-DOF model also axially asymmetrical modes participate in the response obtained for  $r_d > r_d^c$ , the post-critical responses obtained with the 31-DOF model are qualitatively similar to those obtained using the 16-DOF model, see for example Fig. 7.21. Similar as for the primary static buckling loads ( $P_b$ , see Table 7.5), the shape of the imperfection has a large influence on  $r_d^c$ . Consequently, for the load-case and cylindrical shell under consideration, the dynamic critical load exhibits a similar severe imperfection sensitivity as found for the primary static buckling load.

Table 7.5: Dynamic critical loads  $r_d^c$  of the imperfect cylindrical shell.

Model	$r_d^c$ [-]					
	$e_1 = 0.5$	$e_2 = 0.5$	$e_3 = 0.5$	$e_4 = 0.5$	$e_5 = 0.5$	$e_6 = 0.5$
16-DOF model	0.2518	-	0.1633	-	0.1347	-
31-DOF model	0.2518	0.16157	0.1633	0.12285	0.1318	0.11468

### 7.3.4 Influence circumferential wave number $n$

In the static, modal and dynamic analyses performed until now, only one circumferential wave number has been considered ( $n = 11$ ). The selection of this circumferential wave number is based on experimental static buckling results [146], where the shell under consideration (initially) buckles to a post-buckling state dominated by  $n = 11$ . Obviously, this does not guarantee that for the dynamic case  $n = 11$  will also prevail with respect to other values of  $n$ . It is, therefore, of interest to examine the influence of  $n$  on the obtained results. Note that for this analysis, the 16-DOF model will be used (see Table 7.4). Similar as in Subsections 7.3.1, 7.3.2, and 7.3.3, the top mass is fixed at  $m_t = 10$  [kg] and all damping ratios are set to  $\xi = 0.01$ .

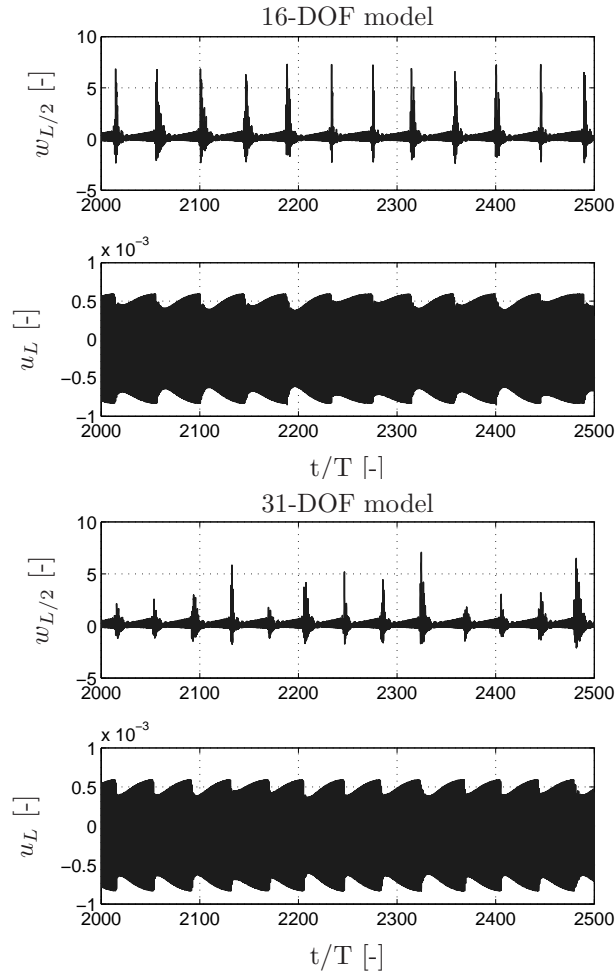


Figure 7.21: Beating response ( $e_5 = 0.5$ ,  $f = f_1$ ,  $r_d = 0.14$ ) computed using the 16-DOF model and the 31-DOF model (see Table 7.4).

In Fig. 7.22, the influence of  $n$  on the second eigenfrequency  $f_2$  (the first axisymmetrical vibration mode, see Fig. 7.7), the primary static buckling load  $P_b$  and the value of  $r_d^c$  is depicted. For  $f_2$  only the preloaded perfect case is considered, whereas for  $P_b$  and  $r_d^c$  three imperfection shapes are considered (all with only one nonzero  $e_i$  and  $\max |w_0|/h = 0.5$ ). Note that the lowest value for  $f_2$  is obtained for  $n = 10$ , the lowest value for  $P_b$  for  $n = 14$  and  $e_5 = 0.5$  and the lowest value for  $r_d^c$  for  $n = 13$  and  $e_5 = 0.5$ . For  $P_b$  the lowest values are

always obtained for the imperfection shape with the highest number of axial half waves ( $e_5 = 0.5$ ). This is not the case for  $r_d^c$ .

The dynamic responses for values of  $r_d$  just below  $r_d^c$  and just above  $r_d^c$  for the considered imperfection shapes in Fig. 7.22, are shown for  $n = 12$  in Fig. 7.23 and for  $n = 13$  in Fig. 7.24. For the case  $r_d > r_d^c$ , also Poincaré maps (i.e.  $T$  sampled values of  $u_L$  plotted against  $T$  sampled values of  $w_{L/2}$ ) are shown. Similar as in Fig. 7.12 and Fig. 7.13, the locations of the 16 damped linear eigenfrequencies of the 16-DOF model (for the considered value of  $n$ ) are again indicated.

Starting with  $n = 12$  and  $e_1 = 0.5$  (see Fig. 7.23), the response for  $r_d$  just above  $r_d^c$  ( $r_d^c = 0.194$ ) is the familiar beating response with very large out-of-plane displacements. The Poincaré map of this response (see Fig. 7.23 for  $e_1 = 0.5$  and  $r_d = 0.2$ ) is a bounded cloud of points, suggesting that the response has a chaotic nature [129]. Considering the same value of  $n$  but now for  $e_3 = 0.5$ , the Poincaré map of the response for  $r_d$  just above  $r_d^c$  ( $r_d^c = 0.108$ ) becomes a closed curve, suggesting that the response now has a quasi-periodic nature [129]. For  $n = 12$  and  $e_5 = 0.5$ , the Poincaré plot of the response for  $r_d$  just above  $r_d^c$  ( $r_d^c = 0.118$ ) shows only a single dot indicating a harmonic post-critical response.

For  $n = 13$  the responses for  $r_d$  just above  $r_d^c$  seem to be chaotic for the cases  $e_1 = 0.5$  and  $e_3 = 0.5$  and for  $e_5 = 0.5$ , a  $1/2$  subharmonic post-critical response is obtained (see Fig. 7.24). It should be noted that exact classification of the post-critical responses (for example by computing Lyapunov exponents [129]) is out of the scope of this chapter.

More important, for each value of  $n$ , the first instabilities are always found close to the resonance peak corresponding to the low frequent suspension type of vibration mode, see e.g. Fig. 7.7. Furthermore, for each value of  $n$ , the obtained post-critical responses show large increases in out-of-plane deflections which are undesirable in practice. Which type of post-critical response and which value of  $n$  will be critical in practice will depend on the actual imperfection in the shell. In addition to this observation, it should be noted that for the considered values of  $n$ , the lowest obtained values for  $r_d^c$  are closely grouped together. This may suggest that if one would include additional DOFs to the model corresponding to modes with different circumferential wave numbers (or perform an experiment on a real cylindrical shell), multiple modes with different values of  $n$  may start to interact for  $r_d > r_d^c$  leading to even more complicated dynamics as observed in this section. For the onset to parametric instabilities of a cylindrical shell without a top mass, this is for example observed in [47].

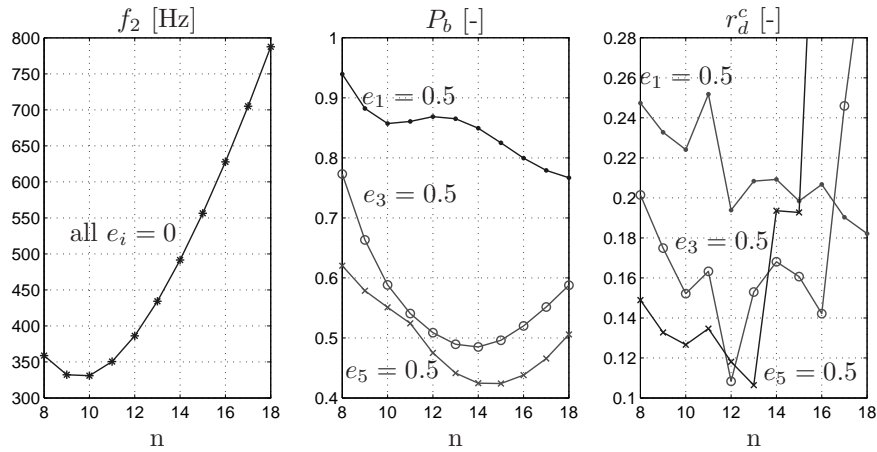


Figure 7.22: Influence of  $n$  on the second eigenfrequency  $f_2$ , the primary static buckling load  $P_b$  and the dynamic critical load  $r_d^c$ .

The results presented above suggest that the dynamic stability analysis of base-excited cylindrical shells structures with top mass and thus with a relatively low frequent axi-symmetrical vibration mode (Fig. 7.7-a) should be concentrated around the corresponding low frequent resonance peak. This observations is supported by the experimental results presented in [106] for a base-excited cylindrical shell with a free top mass (i.e. the top mass is only supported by the cylindrical shell). Indeed, in these experiments around the resonance of the first axial symmetric vibration mode, a very severe unstationary response is found. The obtained results of [106], however, could not be explained using numerical simulations.

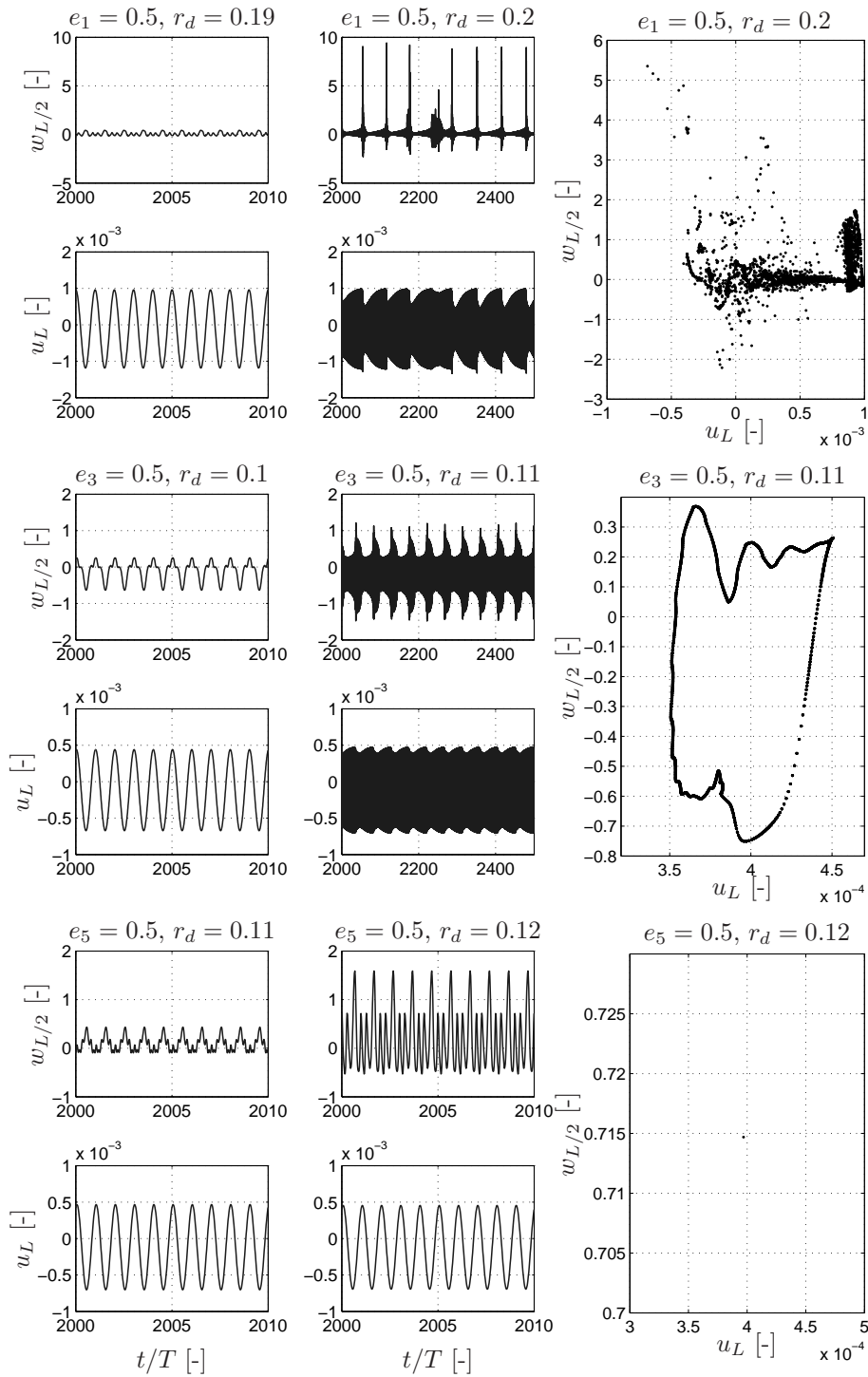


Figure 7.23: Responses for  $r_d < r_d^c$  and  $r_d > r_d^c$  for various imperfection shapes ( $f = f_1$ ,  $n = 12$ ).

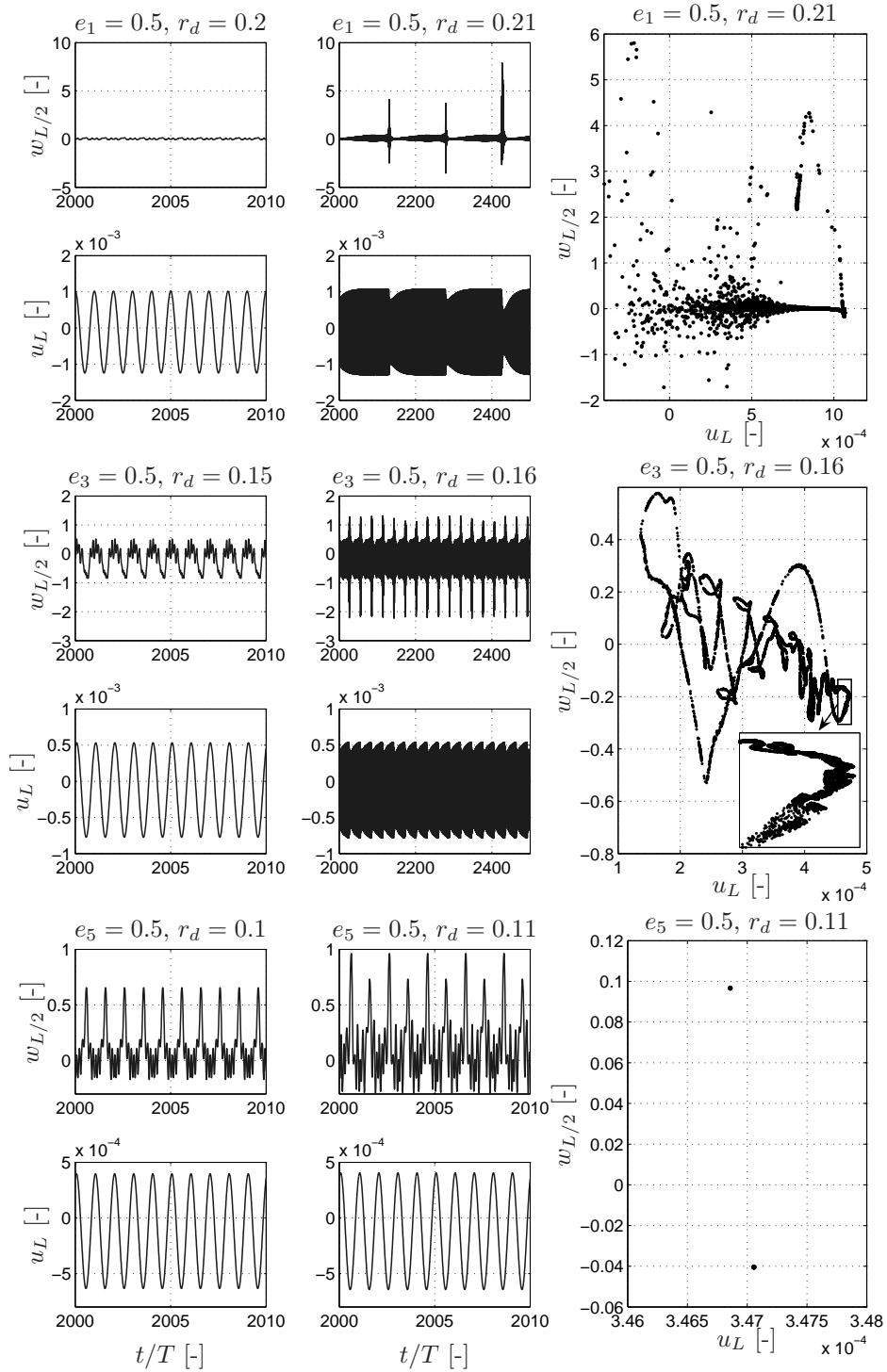


Figure 7.24: Responses for  $r_d < r_d^c$  and  $r_d > r_d^c$  for various imperfection shapes ( $f = f_1, n = 13$ ).



## 7.4 Conclusions

The objective of this chapter is to determine the dynamic stability limits of a base-excited thin cylindrical shell with top mass and how these results are affected by possible geometrical imperfections.

First a semi-analytical model is derived which satisfies exactly the in-plane boundary conditions. For this purpose, a static condensation procedure is derived in which the in-plane fields are directly solved in terms of the assumed expressions for the radial displacement field and the radial imperfection shape. The resulting model is numerically validated through a comparison with static buckling and modal analysis results obtained using FEA. Static buckling loads appear to be very sensitive for imperfections. The sensitivity of modal analysis results with respect to imperfections is much less. Although there are still some discrepancies, generally a good correspondence is obtained between the semi-analytical results and the FEA results.

The dynamic stability of the base-excited cylindrical shell is studied using numerical continuation of periodic solutions with the excitation frequency as continuation parameter. Due to the top mass, a relatively low frequent resonance is introduced, corresponding to an axi-symmetrical vibration mode. It is shown that for increasing excitation amplitude, the harmonic response may become unstable in the peak of this resonance and a beating response with severe out-of-plane deformations may appear instead. Depending on the considered imperfection and circumferential wave number, several types (periodic, quasi-periodic and chaotic) of (severe) post-critical behaviour are observed. Similar to the static buckling case, the critical value for the amplitude of the prescribed harmonic base-acceleration for which the harmonic response changes to the severe post-critical response, highly depends on the initial imperfections present in the shell. The semi-analytical models considered in this thesis include only modes with a single circumferentially wave number. By considering the dynamic stability limits of a base-excited thin cylindrical shell with top mass for several different circumferential wave numbers and for several imperfections, closely grouped critical values for the amplitude of the base-acceleration are obtained. Not only the presence but also the shape of an imperfection may strongly affects the critical values for the amplitude of the base-acceleration. This may suggested that there exists a worst-case imperfection shape, i.e. for this shape the lowest critical value for the amplitude of the base-acceleration occurs. Determination of the worst-case imperfection shape(s) is a topic for future research.

The presented semi-analytical results suggest that the dynamic stability analysis of base-excited cylindrical shells structures with substantial top mass

(and thus with a low frequent axi-symmetrical vibration mode) should be concentrated on the corresponding low frequent resonance peak. In practise, cylindrical shells are often employed as support construction of relatively heavy components. Thus in many cases, the cylindrical shell will exhibit such a low frequent axi-symmetrical vibration mode.

The dynamic stability results obtained for the (relatively) low frequent dynamic loaded cylindrical shell with top mass as presented in this chapter are not observed in previous numerical studies of dynamically axially loaded cylindrical shells, since these studies did not include the effect of a top mass. As a next important step towards validation of these results, in the next chapter experiments will be performed on a base-excited cylindrical shell with top mass and experimental results will be confronted with semi-analytical results.

## *Experiments with a base-excited thin cylindrical shell with top mass*

**I**n the previous chapter, a cylindrical shell with top mass being subjected to a prescribed harmonic base acceleration is examined. It is shown that due to the top mass, the cylindrical shell exhibits a relatively low frequent resonance corresponding to an axi-symmetric vibration mode dominated by axial displacements. Furthermore, it is shown that by increasing the amplitude of the prescribed base-acceleration, the harmonic response may become unstable in the peak of this resonance and a beating type of response with severe (undesired) out-of-plane deformations may appear instead.

In this chapter, experimental results for a base-excited thin cylindrical shell with top mass will be presented and a comparison with semi-analytical results will be made. For this purpose, the same experimental setup will be used as considered for the experimental analysis of the base-excited thin beam with top mass (see Chapter 6). However, now the thin beam is replaced with a thin cylindrical shell. Recall that at the experimental setup, the base-excitation is realized by supplying a harmonic input voltage to an electrodynamic shaker system. As stated before, for this case the resulting base acceleration will not be purely harmonic, will not have a constant amplitude but will be determined by the dynamics of the shaker system carrying (in this case) the thin cylindrical shell with top mass. Results for voltage excitation can thus not directly be compared with results for a prescribed harmonic base-acceleration as considered in Chapter 7. In analogy with Chapter 6 and to be able to compare the experimental results with the semi-analytical results, the equations of motion for the base-excited cylindrical shell with top mass (as derived in Chapter 7) will be coupled with a model of the shaker.

At the experimental setup, the cylindrical shell with top mass is supported by the shaker which has a relatively low support stiffness in axial direction. Nevertheless, also for this case a low frequent resonance dominated by axi-symmetrical shell vibrations occurs (i.e. far below the parametric instability regions, similar as in Chapter 7). In analogy with the results presented in Chapter 7, in the top of this peak the stability of the harmonic response may be lost and (possibly) severe responses may appear instead if the excitation

amplitude is increased above some threshold. This will be confirmed in a preliminary numerical dynamic steady-state analysis based on the derived semi-analytical coupled shaker/structure model.

Next a brief literature survey regarding experiments conducted on dynamically loaded cylindrical shells is presented. Experimental results regarding parametric instabilities of an axial excited cylindrical shell with a free top edge (i.e. no top mass) are reported in [16]. Cylindrical shells loaded in transversal direction by a point load are studied experimentally in [49] and [4]. Thin cylindrical shells immersed in a fluid and subjected to a horizontal base excitation are experimentally investigated in [41] and the effect of an internal fluid flow on the dynamic stability of a cylindrical shell is examined experimentally in [64]. Experimental results considering a base-excited cylindrical shell with a free top mass (i.e. the top mass is only supported by the cylindrical shell), are presented in [106]. Around the resonance of the first axi-symmetric vibration mode, a very severe unstationary response is found. In this region, the base-acceleration due to the shaker could not be controlled to remain purely harmonic. Furthermore, the obtained results could not be explained using numerical simulations. Consequently, a combined numerical and experimental analysis of a base-excited cylindrical shell carrying a top mass, as will be presented in this chapter, is not previously presented.

The outline for this chapter is as follows. In the next section, the experimental setup of the cylindrical shell with top mass will be introduced and the material properties of the cylindrical shell will be determined. In Section 8.2, the coupled shaker-structure model will be discussed. In Section 8.3, a modal analysis and static buckling analysis will be performed and results will be compared with FEA results. The theoretical modal analysis results will be compared with experimental results. Dynamic stability of the cylindrical shell with top mass excited by the shaker will be studied numerically in Section 8.4 and experimentally in Section 8.5. Finally, in Section 8.6 conclusions will be presented.

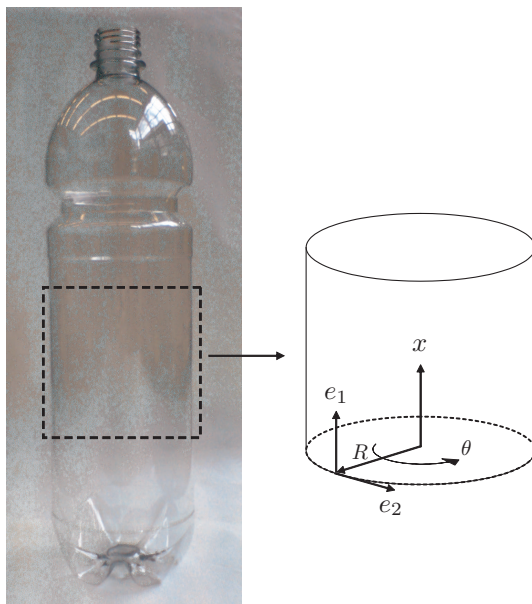


Figure 8.1: Cylindrical shell from PET beverage bottle.

---

## 8.1 Experimental setup

The (seamless) cylindrical shells which are used for the experiments are cut out from unused beverage bottles made of Poly Ethylene Terephthalate (PET), see Fig. 8.1. The obtained cylindrical shells have radius  $R = 44$  [mm] and (average) thickness  $h = 0.23$  [mm] (the shell thickness varies in axial direction by approximately 2%). The PET bottles are produced by using a blow moulding technique. During this process, the material is first stretched in the axial direction of the bottle and subsequently in the circumferential direction of the bottle. Since this biaxial stretching is performed with different stretch ratios in the two (perpendicular) directions, a directional dependency of the elasticity properties is introduced [28]. In [150], it is found that the elasticity properties of a biaxially stretched thin PET film may fairly well be approximated using an orthotropic symmetric material description with principle directions aligned with the two stretch directions. This approximation is also used to characterize the elasticity properties of the PET cylindrical shell. More specifically, the shell is assumed to be made of orthotropic material with principle directions  $e_1$  and  $e_2$  coinciding with respectively the axial coordinate  $x$  and the circumferential coordinate  $\theta$  (i.e. the two stretch directions), see Fig. 8.1.

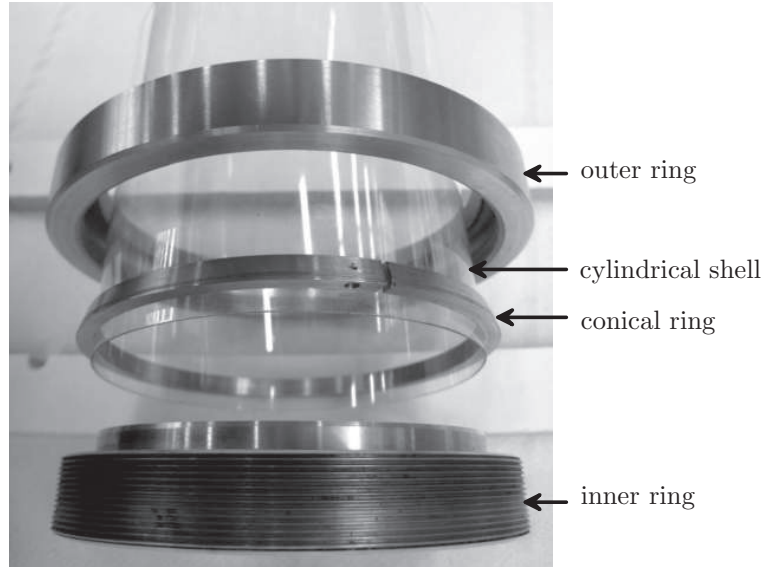


Figure 8.2: Exploded view of one clamping ring for cylindrical shell.

The elastic properties of orthotropic shells are described by four parameters, see Eq. (7.2)-Eq. (7.4). For an orthotropic material, the in-plane Young's modulus at an angle  $\phi$  with respect to the principle axis  $e_1$  (i.e. in this case the  $x$ -axis) is determined by [39]

$$\frac{1}{E_\phi} = \frac{\cos^4 \phi}{E_x} + \frac{\sin^4 \phi}{E_\theta} + \frac{1}{4} \left[ \frac{1}{G_{x\theta}} - \frac{2\nu_x}{E_x} \right] \sin^2 2\phi. \quad (8.1)$$

By performing tensile tests on samples which are cut-out from the shell in the axial direction ( $\phi = 0$ ) and the circumferential direction ( $\phi = \pi/2$ ), the Young's moduli  $E_x$  and  $E_\theta$  are estimated. The Poisson ratios are estimated based on values from literature [39; 150]. Additional tensile tests are performed using samples which are cut-out from the PET bottle under an angle  $\phi = \pi/4$ . Based on the estimated Young's modulus for these samples ( $E_{\pi/4}$ ) and the estimated values for  $E_x$ ,  $E_\theta$  and  $\nu_x$ , the shear modulus  $G_{x\theta}$  can be obtained from Eq. (8.1). The mass density  $\rho$  is determined by weighting a number of test samples. The resulting shell parameters are listed in Table 8.1.

An exploded view of the construction used to clamp the bottom edge and the top edge of the cylindrical shell is depicted in Fig. 8.2. The thin cylindrical shell edge is fixed between an inner ring which fits exactly to the inner diameter of the shell and a conical ring, see Fig. 8.2. The outer diameter of the conical

Table 8.1: Material and geometrical properties of the orthotropic cylindrical shell.

$E_x$	3.85	[GPa]
$E_\theta$	6.00	[GPa]
$G_{x\theta}$	1.94	[GPa]
$\nu_x$	0.25	[-] ( $\nu_\theta = 0.39$ )
$\rho$	1350	[kg/m <sup>3</sup> ]
$R$	44	[mm]
$L$	85	[mm]
$h$	0.23	[mm] ( $R/h = 191$ )

ring has a conical shape. The outer ring, which has internally also a conical shape, is screwed over the conical ring on the inner ring. In this manner, the conical ring is compressed radially on the cylindrical shell surface resulting in a stiff circle line contact between the clamping rings and the thin shell.

A picture and a schematic overview of the experimental setup are depicted in Fig. 8.3. The thin cylindrical shell, on its top and bottom fixed between clamping rings, is mounted between two linear sledges with very low friction in axial direction, see Fig. 8.3. At the top side, the linear sledge is based on air bearings and at the bottom side the linear sledge is realized as a elastic mechanism based on folded leaf springs. The purpose of these support mechanisms is to minimize transversal movements and rotations of the bottom and top edges of the cylindrical shell (corresponding to the boundary conditions of the semi-analytical model, see Eq. (7.5)). The upper linear sledge and upper clamping ring (total mass = 4.7 [kg]) also act as the rigid top mass (i.e.  $m_t = 4.7$  [kg]). The moving mass of the lower linear sledge, including the mass of the bottom clamping ring and the mass of the shaker armature, equals  $m_o = 4.1$  [kg].

The axial excitation of the cylindrical shell is realized using an electrodynamic shaker system, see Fig. 8.3. A periodic excitation is introduced by supplying a harmonically varying input voltage

$$E_0(t) = v_d \sin(2\pi ft) \text{ [V]}, \quad (8.2)$$

to the power amplifier which output voltage is supplied to the shaker. Due this voltage, a current will run through the shaker coil generating a force in axial direction on the assembly on top of the shaker. The amplifier works in a voltage mode of operation (e.g. the output voltage of the amplifier is kept proportional to its input voltage) and no active feedback is used to control the acceleration

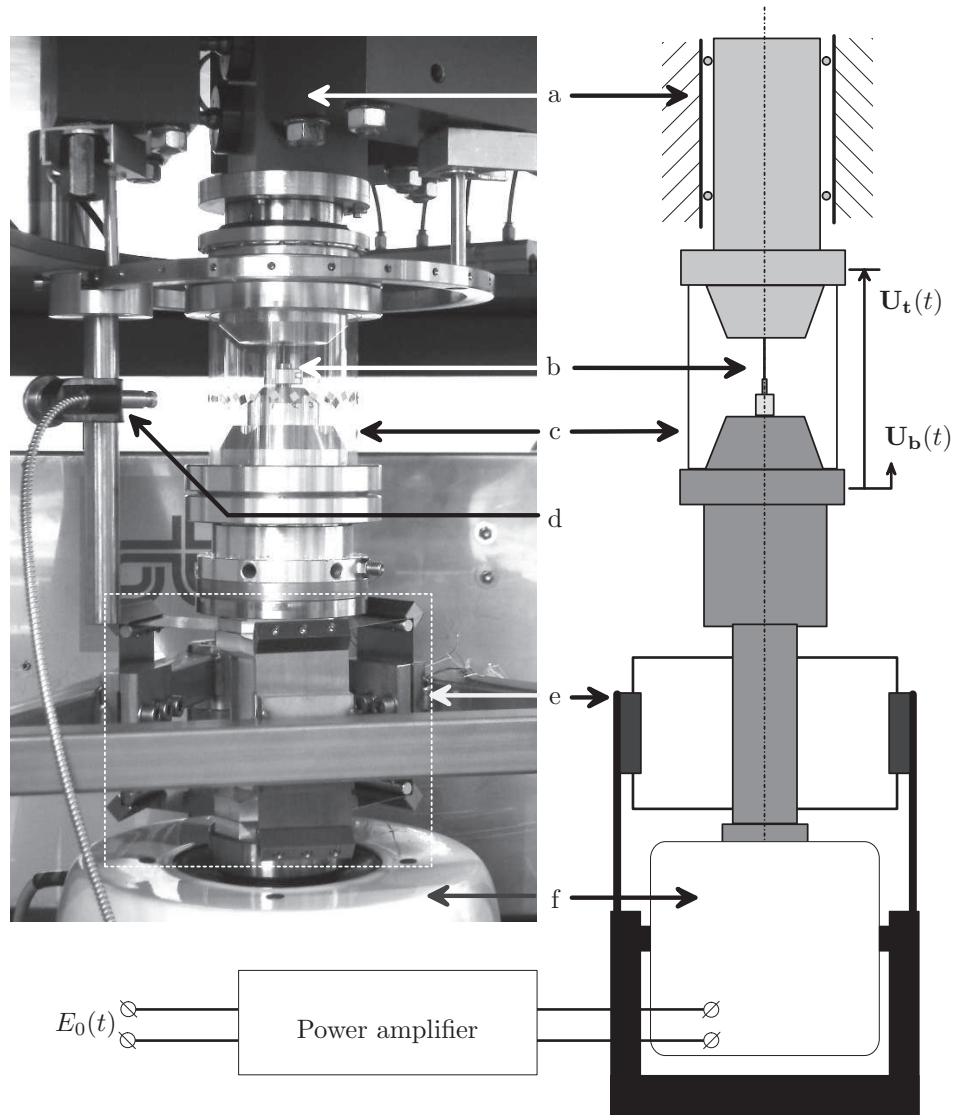


Figure 8.3: Picture and schematic overview of the experimental setup (a: top linear sledge based on air bearings, b: LVDT, c: cylindrical shell, d: laser vibrometer, e: bottom elastic support mechanism, f: electrodynamic shaker).



of the shaker armature ( $\ddot{\mathbf{U}}_{\mathbf{b}}$ ). Consequently, the resulting acceleration of the shaker (and thus the effective axial force on the cylindrical shell with top mass) will not be proportional to Eq. (8.2), but will be determined by the dynamics of the electro/mechanical shaker system with on top the cylindrical shell with top mass. More details about the shaker are provided in Appendix A.

For measuring the deformation of the shell, two sensors are used. Firstly, the relative axial displacement of the top mass ( $\mathbf{U}_{\mathbf{t}}(t)$ , see Fig. 8.3) is measured using an LVDT (Shaevitz 100 MHR). Furthermore, a laser vibrometer (Ono Sokki LV 1500) is used to measure the transversal velocity ( $\dot{w}$ ) at one point of the cylindrical shell. The signal of the laser vibrometer is numerically integrated to obtain measurements in terms of transversal displacements  $w$ . To avoid drift during the numerical integration, the measurement signal is filtered using a high pass filter with a cutoff frequency of  $f = 1.6$  [Hz] (see Eq. (6.2)). The data-acquisition and input signal generation is performed using a Laptop with Matlab/Simulink in combination with a TUEDACs AQI [55] (sample frequency 4 [kHz]).

## 8.2 *Semi-analytical model*

In the numerical analysis as presented in Section 7.3, the axial forcing of the cylindrical shell is realized by prescribing a harmonically varying base-acceleration. However, as noted before, at the experimental setup the axial forcing of the cylindrical shell is realized by supplying a harmonic input voltage to the shaker system. For this case, the resulting acceleration of the shaker is determined by the dynamics of the electro/mechanical shaker system with on top the cylindrical shell with top mass. Results for this type of excitation can thus not be compared with results for a directly prescribed harmonic base-acceleration (as considered in Chapter 7).

To be able to compare the experimental results with the semi-analytical results, the equations of motion for the base-excited cylindrical shell must be coupled with a model of the electrodynamic shaker. The dynamics of the shaker are captured using a set of two coupled linear ODEs (one describing the mechanical part of the shaker and one describing the electrical part of the shaker). The derivation of the shaker model and the approach to obtain the total set of equations of motion describing the coupled shaker/structure dynamics is outlined in Section A.1 of Appendix A.

All semi-analytical results presented in this section are based on the same 16-DOF expansion of  $w$  as considered in Section 7.3 of Chapter 7 (i.e. axial asymmetric modes and companion modes are not included) in combination

with the geometrical and (orthotropic) material properties as listed in Table 8.1. This expansion of  $w$  showed to be sufficient for predicting the onset to the severe beating response as found for the case of prescribed base-acceleration. Coupled with the model for the shaker (see Appendix A), the resulting semi-analytical model possesses in total 18-DOF. Similar to the approach in Section 7.3 of Chapter 7, wherever the influence of imperfections is addressed, only single mode imperfection shapes (i.e. only one  $e_i \neq 0$ ) will be considered.

### 8.3 Modal and buckling analysis

To obtain insight in the eigenfrequencies and damping ratios of the experimental setup, experimental modal analyses are performed. Results will be compared with semi-analytical results (using the 18-DOF model with  $w_0 = 0$  [m], see Section 8.2) and for some cases also with FEM results. For the FEA, the same type of elements and kinematic relations are used as discussed in Subsection 7.2.1. However, now orthotropic material parameters are used and the full cylindrical shell is modelled (using 100 elements in axial direction and 300 elements in circumferential direction).

First, the eigenfrequencies corresponding to axial symmetric modes (see also Fig. 7.7) are determined. For this purpose, FRFs are measured by exciting the system with a randomly varying input voltage  $E_0$  while measuring the relative axial displacement of the top mass  $\mathbf{U}_t$  (with the LVDT, see Fig. 8.3). The resulting FRF (see Fig. 8.4) shows a heavily damped ( $\xi_1 = 0.30$ ) resonance at  $f = f_1 \approx 12$  [Hz] and moderately damped ( $\xi_2 = 0.05$ ) resonance at  $f = f_2 \approx 182$  [Hz]. The first resonance corresponds to a suspension type of vibration mode of the shaker (dominated by  $\mathbf{U}_b$ ). The second resonance corresponds to a vibration mode dominated by  $\mathbf{U}_t$ . Based on the experimentally determined damping ratios, the damping parameter of semi-analytical model  $c_t$  ( $c_{ij}$  are kept zero, see Eq. (7.17)) is tuned to fit these ratios. In Fig. 8.4, also the FRF obtained using the 18-DOF semi-analytical model is depicted. As can be noted, until  $f = 300$  [Hz] the semi-analytical results are in very good agreement with the experimental results. The measured FRF shows small resonances around  $f = 350$  [Hz] which are not present in the semi-analytical results. These resonances are likely due to the finite stiffness of the shaker support construction.

The eigenfrequencies and damping ratios of the lowest axi-asymmetric vibrational eigenmodes of the cylindrical shell (which are also axial-symmetric, see Fig. 7.7) are determined while the cylindrical shell with the clamping rings was not mounted between the two linear sledges. Instead, the cylindrical shell with clamping rings and top mass is attached at the bottom side to a

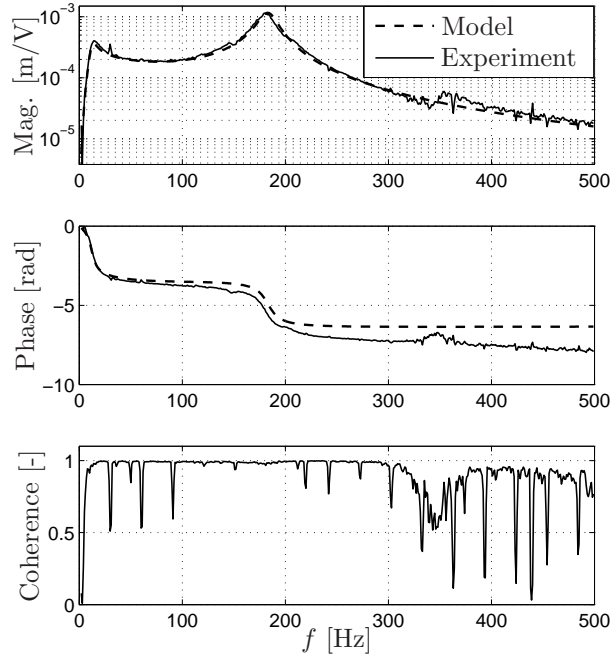


Figure 8.4: FRF from input voltage  $E_0(t)$  to relative axial top mass displacement  $U_t(t)$ .

heavy rotatable table. The top mass was left unsupported for this case. Next, FRFs are determined by exciting the cylindrical shell at the top mass using an impulse hammer while measuring the out-of-plane velocity at 40 equidistantly distributed points along the circumference of the shell at height  $x = L/2$  (using the same laser vibrometer applied at the setup, see Fig. 8.3). Based on these FRFs, the eigenfrequencies with corresponding eigenmodes and damping ratios are determined, see [31] for more details. The experimental results are shown in Table 8.2. For  $n = 7$  no results are included since for this value of  $n$ , experimentally no mode could be identified. In Table 8.2, also *undamped* eigenfrequencies of the *perfect* cylindrical shell structure, determined using the semi-analytical approach (using the 18-DOF model) and the FEA, are shown. As can be noted, the semi-analytical results are in good correspondence with the FEA results (maximum difference 2% for  $n = 4$ ). The semi-analytical results show an average difference of 8% with the experimental results. Differences may

Table 8.2: Eigenfrequencies of lowest axi-asymmetric modes (18-DOF and FE model consider the undamped case for  $w_0 = 0$  [m],  $\xi_{n1}$  denotes the experimentally estimated damping ratio).

$n$	18-DOF [Hz]	FEM [Hz]	Experiment [Hz]	$\xi_{n1}$ [-]
4	1415	1387	1293	0.005
5	1070	1063	1030	0.007
6	896	896	886	0.010
7	858	858	-	-
8	929	926	997	0.020
9	1076	1070	1165	0.010
10	1276	1268	1496	0.007
11	1514	1506	1683	0.020

be due to various reasons, e.g. due to imperfections (which are not accounted for in the semi-analytical and FE model), due to inaccuracies in the identified material properties and/or measurement inaccuracies.

For the orthotropic cylindrical shell subjected to a static axial compressive force, an analytical expression is not available for the theoretical static buckling load (i.e. similar to Eq. (7.22) for isotropic cylindrical shells). Therefore, as a reference, the static buckling of the orthotropic (perfect) shell is determined using a linearized buckling eigenvalue analysis based on the 18-DOF semi-analytical model and by using FEA (using the same model as used for the modal analysis). The 18-DOF semi-analytical model predicts the first buckling of the perfect cylindrical shell to be  $P_c = 990$  [N] while the FEA predicts  $P_c = 975$  [N] (2% lower). Based on the buckling load predicted by the FEA, the weight of the top mass as considered during the experiments equals 5% of the static buckling load, i.e.  $m_t \cdot g / P_c = 0.05$ .

## 8.4 Numerical steady-state analysis

In this section, a numerical steady-state analysis will be performed for the cylindrical shell with top mass excited by the shaker. All results obtained are based on the 18-DOF semi-analytical model as discussed in Section 8.2. Similar to Section 7.3 of Chapter 7, the objective of the dynamic analysis is here to determine where instabilities will occur (i.e. for which combinations of excitation frequency  $f$  and amplitude  $v_d$  of the input voltage, see Eq. (8.2)) and how these results depend on possible geometric imperfections in the cylindrical shell. The amount of damping taken into account during the simulations is

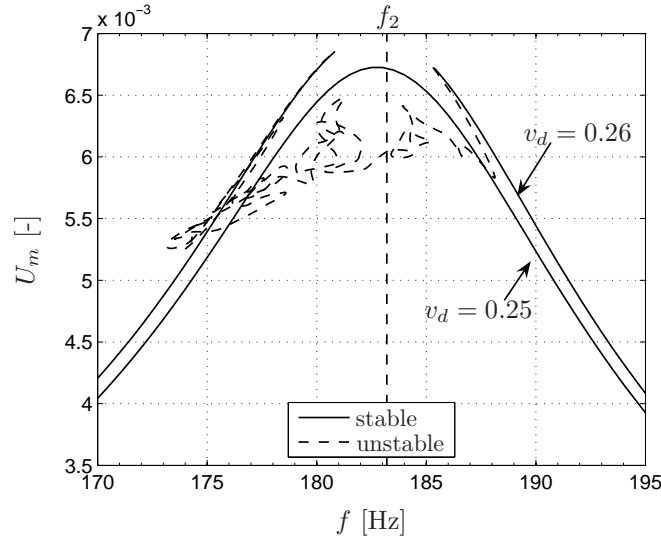


Figure 8.5: Frequency-amplitude plot of the imperfect shell ( $e_1 = 0.5$ ).

based on the modal analysis results as discussed in the previous section, i.e. the damping ratios of the first two (axi-symmetric) modes are set to  $\xi_1 = 0.3$  and  $\xi_2 = 0.05$  (related to  $c_t$ ). To all other vibration modes (related to  $c_{ij}$ ),  $\xi = 0.01$  is assigned which corresponds (more or less) to the average of the experimentally determined damping ratios of the lowest axi-asymmetric modes (see Table 8.2).

For the analysis, numerical continuation of periodic solutions [33] will be used to determine the region(s) where the stability of the harmonic response is lost. In the frequency regions where the harmonic response is no longer stable, the response is further examined using standard numerical integration and a numerical implementation of a stepped frequency sweep procedure. Detailed results are presented for a circumferential wave number  $n = 9$  and various imperfection shapes while considering three (single mode) imperfection shapes, i.e.  $e_1 = 0.5$ ,  $e_3 = 0.5$  and  $e_5 = 0.5$ . The influence of the selected value for  $n$  will be addressed at the end of this section.

Using numerical continuation of periodic solutions with the frequency  $f$  [Hz] of the input voltage as continuation parameter (see Eq. (8.2)), it is found that for sufficient large excitation amplitude  $v_d$ , the harmonic response loses stability firstly in the top of the resonance peak around  $f_2 = 182$  [Hz]. Recall that the resonance around  $f = f_2$ , corresponds to vibrations dominated by axial displacements of the shell (i.e. by  $\mathbf{U}_t$ ). Similar to the case of prescribed

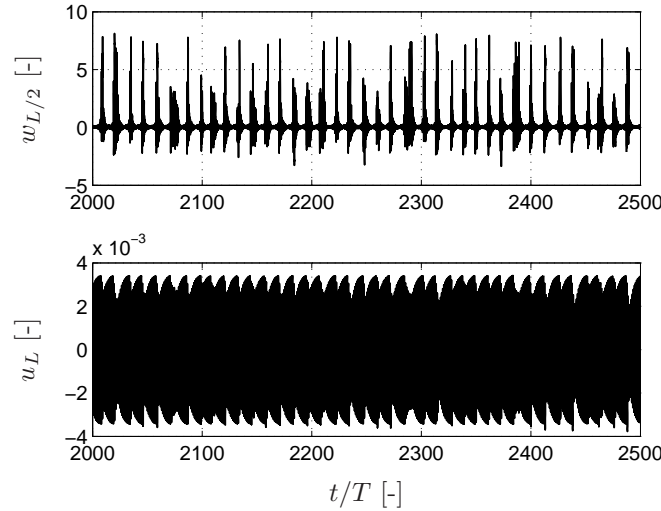


Figure 8.6: Response for  $v_d = 0.26$  [V],  $f = f_2$  and  $e_1 = 0.5$  [-].

base-acceleration, responses with large out-of-plane deflections appear, when the stability of the harmonic solution is lost. The value of  $v_d$  for which the harmonic solution loses stability for  $f = f_2$  is called  $v_d^c$ .

For the perfect cylindrical shell ( $w_0 = 0$  [m]), the harmonic solution loses stability in the peak of the resonance near  $f = f_2$  for  $v_d = v_d^c = 0.298$  [V]. By introducing an imperfection of the form  $e_1 = 0.5$  (see Eq. (7.15)), this critical value decreases 15% to  $v_d^c = 0.253$  [V]. For this case, the frequency-amplitude plots around  $f = f_2$  for  $v_d$  just below and just above  $v_d^c$  are depicted in Fig. 8.5. Note that in this section the same response measures are used as in Section 7.3, see Eq. (7.26) and Eq. (7.27). As can be noted, for  $v_d > v_d^c$ , a very complicated branch of unstable periodic solutions appears in the resonance peak around  $f = f_2$ . Using the same procedure as outlined in Section 7.3, the response in this region of instability is further examined using standard numerical integration of the equations of motion, see Fig. 8.6. Similar to the case of a prescribed base-acceleration, a very severe beating response appears in the region of instability. The PSD of this beating response is broad-banded (see Fig. 8.7), suggesting that this response has a chaotic nature.

During the experiments, the response of the cylindrical shell with top mass excited by the shaker will be examined using the stepped sine frequency sweep procedure as outlined in Appendix B. The obtained frequency-amplitude plots from these frequency sweep experiments can not fully be compared

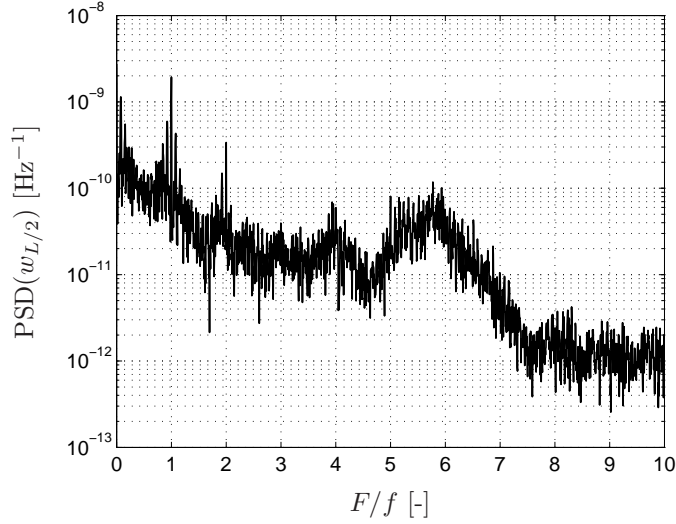


Figure 8.7: Power Spectral Density of time history of  $w_{L/2}$  depicted in the upper plot of Fig. 8.6.

with the frequency-amplitude plots computed using the continuation approach since the latter ones do not include nonstationary responses (as obtained numerically for  $v_d > v_d^c$ ). Therefore, the numerical response is also examined using an implementation of the stepped sine procedure based on numerical integration of the equations of motion. During the stepped sine frequency sweep, the excitation frequency is incrementally increased (in case of sweep-up) or decreased (in case of sweep-down) using a step size  $\Delta f = 0.5$  [Hz]. For each discrete value of  $f$ , the measurement signals are saved during  $N_e = 150$  excitation periods. Response measures are determined based on  $m^1(t) = u_L(t)$  (see Eq. (7.23)) and  $m^2(t) = w_{L/2}$  (see Eq. (7.27)) using the averaging procedure explained in Appendix B. Here, the measurement data during the first  $N_t = 50$  periods is not used, to minimize transient effects. The measures obtained are denoted by  $\tilde{M}^1 = \tilde{U}_m$  and  $\tilde{M}^2 = \tilde{W}_m$ .

Results for the numerical frequency sweep for  $e_1 = 0.5$  and  $v_d = 0.26 > v_d^c$  are shown in Fig. 8.8. As can be noted, very severe responses (note that  $\tilde{W}_m$  is plotted on a logarithmic scale) are found in the region where no stable harmonic solutions are found with the continuation approach (i.e.  $182 \leq f \leq 185$ , see Fig. 8.5). Furthermore, the transitions between the low amplitude (harmonic) responses and the high amplitude (nonstationary) responses occur suddenly (i.e. the response in terms of  $\tilde{W}_m$  shows large jumps at the borders of the frequency region where the high amplitude responses are found).

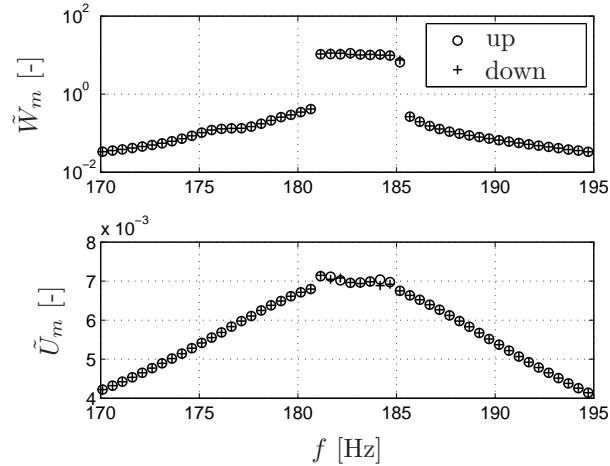


Figure 8.8: Frequency-amplitude plot based on frequency sweep analysis for  $e_1 = 0.5$  and  $v_d = 0.26$  [V] (simulation).

Next, an imperfection of the form  $e_3 = 0.5$  is considered. Using continuation of periodic solutions for this case, a somewhat different scenario is found in the top of the resonance around  $f = f_2$ , see Fig. 8.9. First of all, the harmonic response loses stability for a much lower value of  $v_d$  (i.e.  $v_d^c = 0.145$  [V]). Furthermore, for  $v_d > v_d^c$  two regions of instability appear. Between these two regions, a small branch with stable harmonic solutions is found (see enlargement A, Fig. 8.9). An example of the response in the right region of instability at  $f = 183$  [Hz] is depicted in Fig. 8.10. The PSD of this response (see Fig. 8.11.) shows many discrete peaks at frequencies  $F$  being incommensurate with the excitation frequency (i.e. components for which  $F/f$  is irrational number) suggesting that this beating response has a quasi-periodic nature. In the left region of instability a different response occurs at  $f = 179$  [Hz], see Fig. 8.12. The PSD of this response (see Fig. 8.13) is broad-banded suggesting that the response now has a chaotic nature. A numerical frequency sweep analysis for  $v_d = 0.15 > v_d^c$  [V] reveals that in both regions where no stable harmonic solutions are obtained, again severe responses appear instead, see Fig. 8.14.



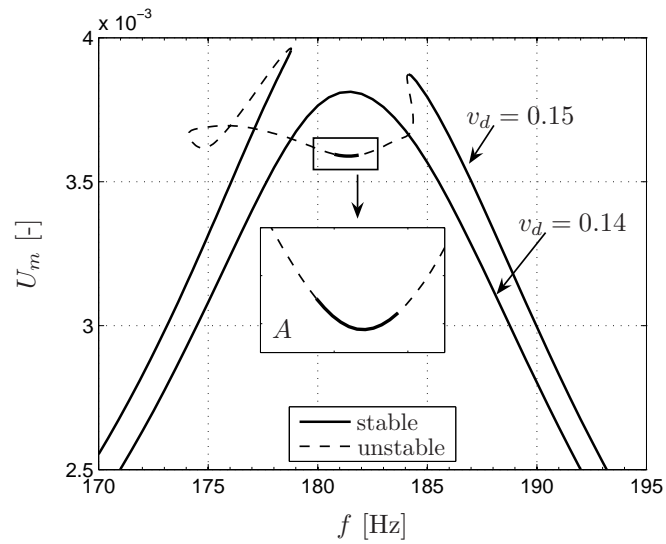


Figure 8.9: Frequency-amplitude plot of the imperfect shell ( $e_3 = 0.5$ ).

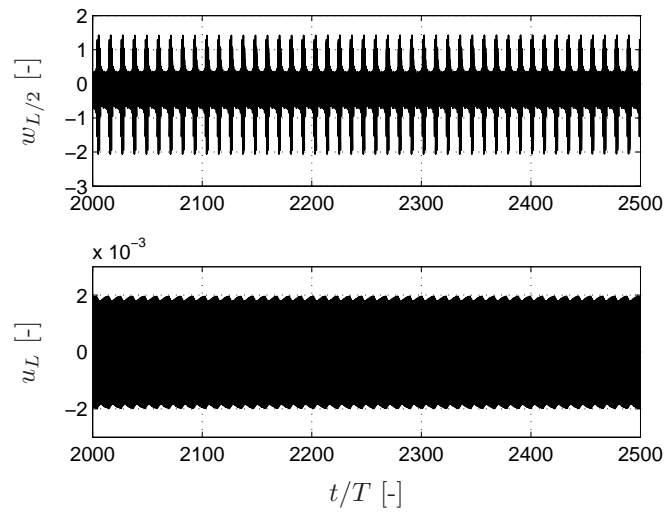


Figure 8.10: Response for  $v_d = 0.15$  [V],  $e_3 = 0.5$  and  $f = 183$  [Hz].

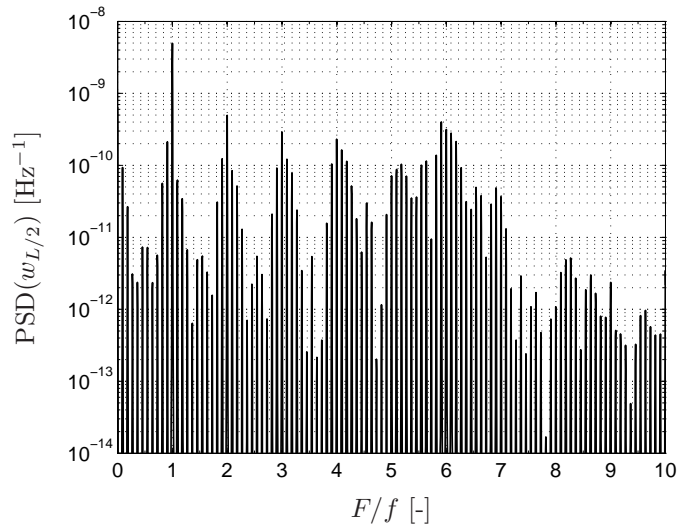


Figure 8.11: Power Spectral Density of the time history of  $w_{L/2}$  depicted in the upper plot of Fig. 8.10.

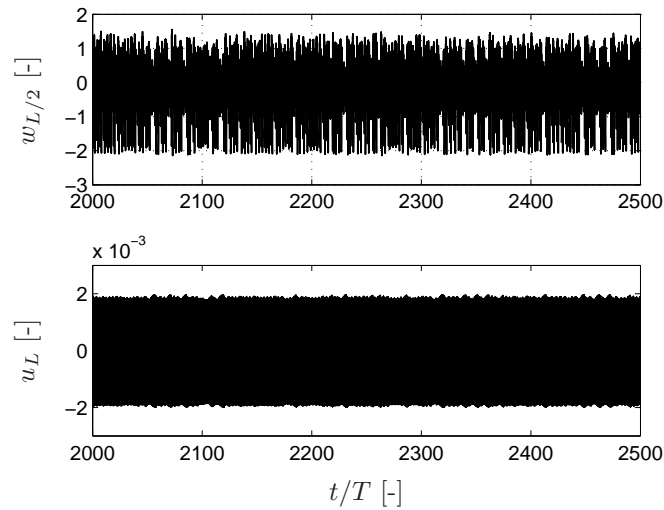


Figure 8.12: Response for  $v_d = 0.15$  [V],  $e_3 = 0.5$  and  $f = 179$  [Hz].

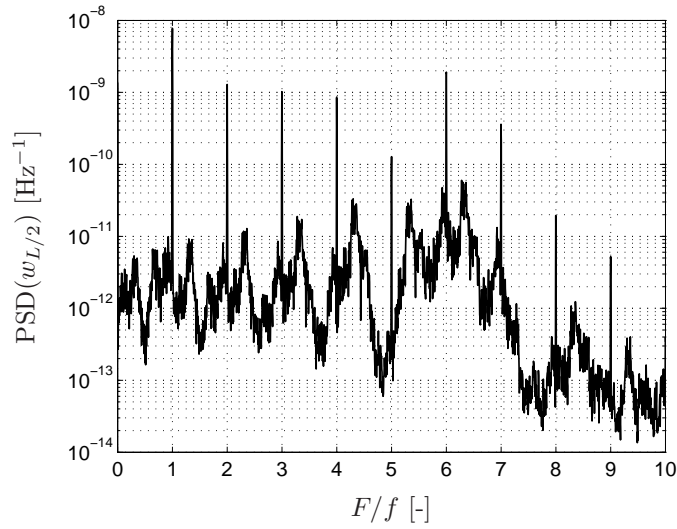


Figure 8.13: Power Spectral Density of the time history of  $w_{L/2}$  depicted in the upper plot of Fig. 8.12.

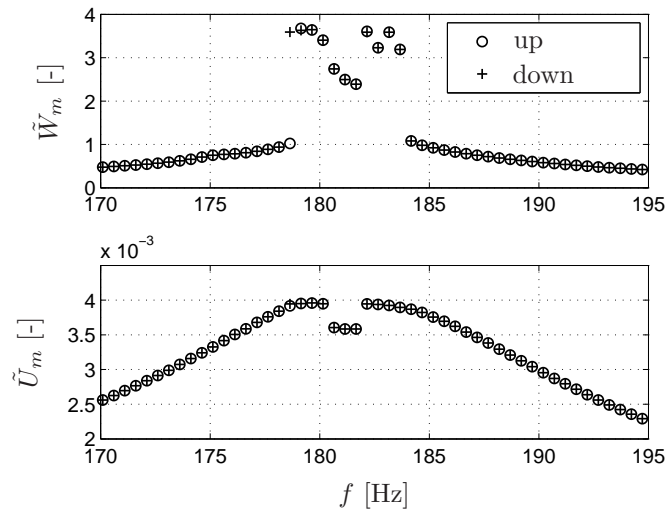


Figure 8.14: Frequency-amplitude plot based on frequency sweep analysis for  $e_3 = 0.5$  and  $v_d = 0.15$  [V] (simulation).

Next the frequency-amplitude plot for an imperfection of the form  $e_5 = 0.5$  is discussed, see Fig. 8.15. For this case, the critical amplitude for the input voltage is even lower, i.e.  $v_d^c = 0.135$  [V]. For  $v_d > v_d^c$ , a region appears at the left from  $f = f_2$  where two stable harmonic solutions coexist. The frequency sweep analysis results for this case in terms of  $\tilde{W}_m$  (see Fig. 8.16), shows that here a softening response appears. Near  $f = 183$  [Hz] also a sudden jump can be seen in the stepped sine results in terms of  $\tilde{W}_m$ . This jump occurs in the small frequency region where no stable harmonic solutions exist (see enlargement *A* in Fig. 8.16). In this small region, beating responses are found comparable to the response as shown in Fig. 8.12.

Finally, the influence of the considered circumferential wave number  $n$  on the critical amplitude of the input voltage ( $v_d^c$ ) is examined. In Fig. 8.17, the influence of  $n$  on the value of  $v_d^c$  is depicted for three imperfection shapes. For the considered range of  $n$ , the lowest value of  $v_d^c$  is obtained for  $n = 9$  and  $e_5 = 0.5$ , while  $v_d^c$  is more than a factor two higher for  $n = 5$  and  $e_1 = 0.5$ . This indicates that, similar to the case of prescribed base-acceleration (see Fig. 7.22 in Chapter 7), the obtained critical value highly depends on the imperfection shape. Furthermore, also in analogy with the results obtained for the case of prescribed base-acceleration, the lowest obtained critical amplitudes of the input voltage are closely grouped together. As stated before, this may suggest that if one would include additional DOFs to the model corresponding to modes with different circumferential wave numbers (or perform an experiment on a real cylindrical shell), multiple modes may start to interact for  $v_d > v_d^c$ , leading to even more complicated dynamics than observed in this section.

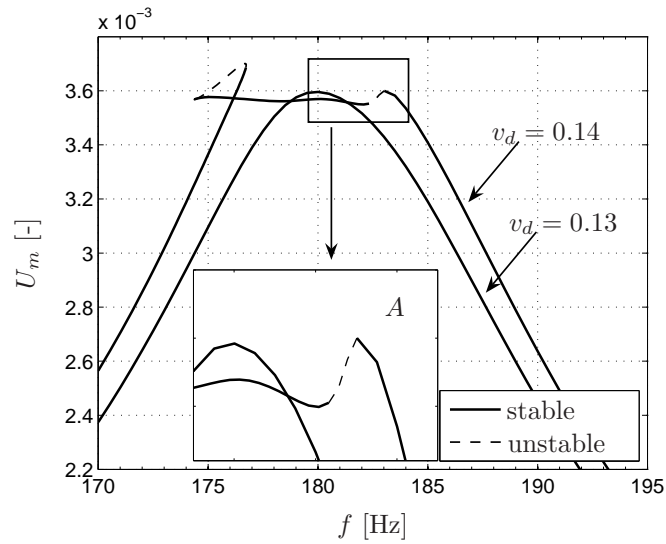


Figure 8.15: Frequency-amplitude plot of the imperfect shell ( $e_5 = 0.5$ ).

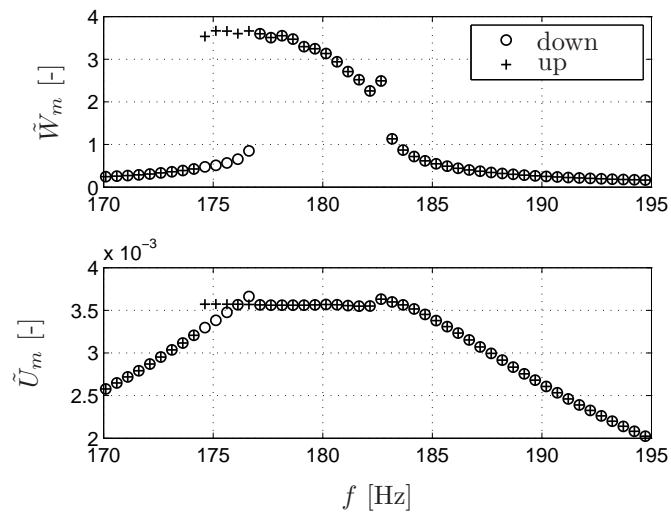


Figure 8.16: Frequency-amplitude plot based on frequency sweep analysis for  $e_5 = 0.5$  and  $v_d = 0.14$  [V] (simulation).

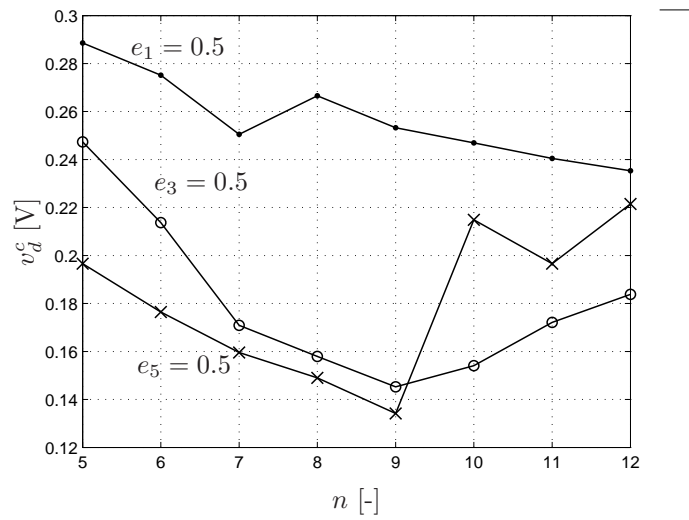


Figure 8.17: Influence of circumferential wave number  $n$  and imperfection  $e_i$  on  $v_d^c$ .

## 8.5 Experimental steady-state analysis

In this section, experimental results obtained for the shaker excited cylindrical shell with top mass will be discussed. The experimental steady-state results are obtained for a varying excitation frequency and a varying excitation amplitude using the stepped sine procedure as outlined in Appendix B. For the experimental stepped sine analysis, the same parameters ( $N_e = 150$ ,  $N_t = 50$ , see Appendix B) and response measures ( $\tilde{U}_m$  and  $\tilde{W}_m$ ) are used as discussed for the numerical stepped sine analysis, see Subsection 8.4. Note that for the experimental analysis, the angular location for measuring the transversal velocity of the shell with the laser vibrometer is chosen by testing initially a number of angular positions along the circumference of the cylindrical shell at height  $x = L/2$ , see Fig. 8.3. The location where the largest velocities are measured is used during the actual experiments. As stated before, the obtained velocity measurements are numerically integrated to obtain measurements in terms of transversal displacement  $w_{L/2}$  (from which eventually the measure  $\tilde{W}_m$  is determined). The measure  $\tilde{U}_m$  is computed using the LVDT measurements, see Fig. 8.3.

In Fig. 8.18, stepped frequency sweep results for various values of  $v_d$  and  $\Delta f = 0.5$  [Hz] are depicted. As can be noted, for the smallest considered amplitude of the input voltage ( $v_d = 0.02$  [V]), a single resonance peak appears near  $f = 177$  [Hz] (close to  $f = f_2 = 182$  [Hz]). However, by increasing the value of  $v_d$ , additional peaks appear close to this peak. Furthermore, by increasing the value of  $v_d$ , the largest resonance peak shifts a little to the left. Time histories of the steady-state response for  $f = 170$  [Hz] in terms of  $w_{L/2}$  and their PSDs are depicted in Fig. 8.19 and Fig. 8.20. To minimize the effect of measurement noise, each PSD is averaged over 8 sets of 2048 data points, measured using a sample frequency of 4 [kHz] and an anti-aliasing filter. For  $v_d = 0.06$  [V] (see Fig. 8.19), the PSD is dominated by peaks at integer multiples of the excitation frequency ( $F/f = 1, 2, 3..$ ) indicating a harmonic response. However, for a slightly higher value of  $v_d$  (i.e.  $v_d = 0.08$  [V], see Fig. 8.20), additional peaks appear in the PSD at frequencies being incommensurate with the excitation frequency (i.e. there are components  $F/f$  which have an irrational value) meaning that the response has become non-stationary. The transition from the harmonic response to the non-stationary response occurred without a (noticeable) sudden increase in out-of-plane vibrations, i.e. the frequency-amplitude plot does not exhibit jumps for this value of  $v_d$  (see Fig. 8.18). Note that in the semi-analytical analysis the appearance of additional peaks around  $f = f_2$  also occurred, see for example Fig. 8.14. However, there the additional peaks correspond directly to very severe nonstationary responses with high amplitude.

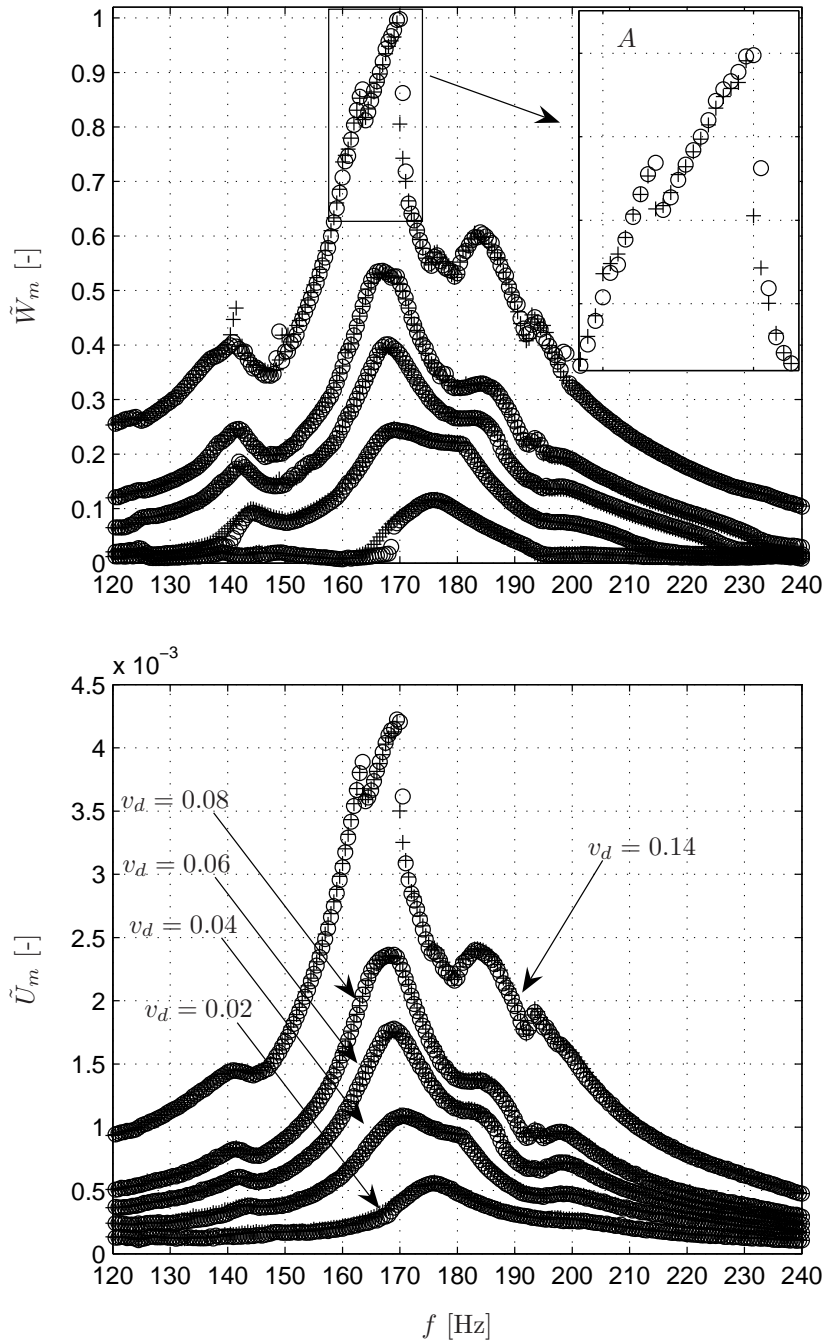


Figure 8.18: frequency sweep results ('+' sweep down, 'o' sweep up).



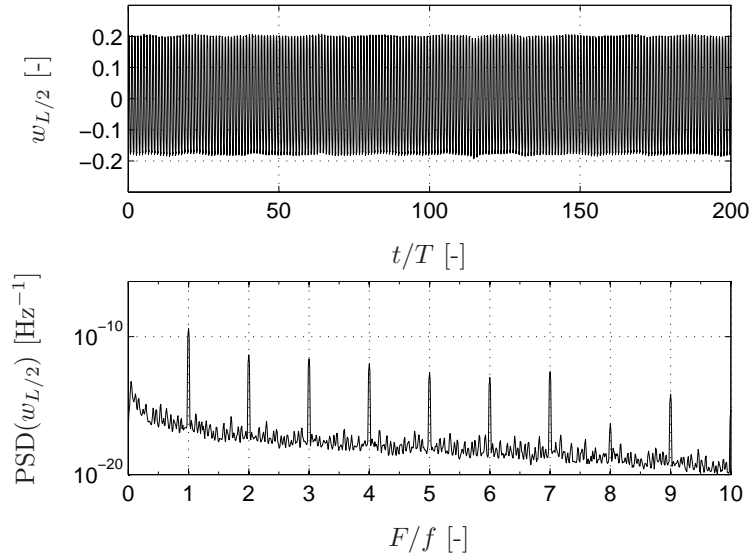


Figure 8.19: Measured dimensionless out-of-plane displacement ( $w_{L/2}$ , top) and corresponding PSD (bottom) for  $f = 170$  [Hz] and  $v_d = 0.06$  [V].

By increasing the value of  $v_d$  further to  $v_d = 0.14$ , the frequency-amplitude plot starts to exhibit jumps near  $f = 162$  [Hz] and near  $f = 170$  [Hz], see enlargement *A* in Fig. 8.18. Especially the jump near  $f = 170$  [Hz] rapidly increases if  $v_d$  is increased further, see the frequency-amplitude plot for  $v_d = 0.2$  [V] in Fig. 8.21. Furthermore, several small transition regions can be observed, see enlargements *A* and *B* in Fig. 8.21. For this level of  $v_d$ , the jump near  $f = 170$  [Hz] could also very clearly be noted audibly. More specifically, for the sweep down, the noise produced by the cylindrical shell significantly increased suddenly after passing the jump. By examining the time histories of the sweep-down response in terms of  $w_{L/2}$  just before the large jump ( $f = 170$  [Hz], see Fig. 8.5) and just after the large jump ( $f = 167.5$  [Hz], see Fig. 8.23), a significant change of the response can be noted. At  $f = 167.5$  [Hz], the response not only has a much larger amplitude but also has a much broader PSD compared to  $f = 170$  [Hz].

The transition from the harmonic response towards the nonstationary response is further examined by performing stepped sine *amplitude* sweeps ( $\Delta v_d = 0.0025$  [V]). Results of this investigation (now only in terms of out-of-plane displacements  $\tilde{W}_m$ ) are depicted in Fig. 8.24 for various excitation frequencies in the frequency region where the large jumps occurred during the

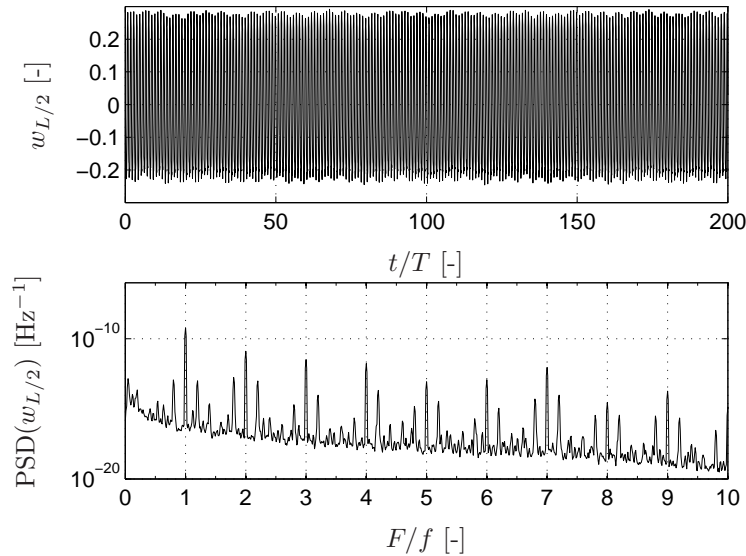


Figure 8.20: Measured dimensionless out-of-plane displacement  $w_{L/2}$  (top) and corresponding PSD (bottom) for  $f = 170$  [Hz] and  $v_d = 0.08$  [V].

stepped frequency sine sweeps. As can be noted, for all considered excitation frequencies, a transition in response amplitude can be observed in the low excitation amplitude region (i.e.  $v_d < 0.03$  [V]). These transitions can also be noted in the measurements in terms of  $u_L$  (not shown). Possibly, these transitions are due to the presence of little dry friction somewhere in the shaker, the LVDT sensor and/or the air bearing supported upper sledge (see Fig. 8.3). The transitions in the 'large' excitation amplitude region for  $f = 165$  and  $f = 167.5$  [Hz] are more important. At these transitions (around  $v_d = 0.19$  [V]), the response amplitude starts to increase rapidly. Similar as during the frequency sweeps, these sudden increases could also be heard very clearly. The responses with the largest amplitude are found for  $f = 167.5$  [Hz]. As already illustrated in Fig. 8.23, for this excitation frequency and  $v_d = 0.2$  [V], the corresponding 'large' amplitude response also exhibit a very broad PSD.

In conclusion, the experiments confirm that for increasing excitation amplitude, the harmonic response around the (relative low frequent) resonance at  $f = f_2$  [Hz] may switch to a nonstationary (large amplitude) response with a very broad PSD. However, in the experiments the transition is far less clear as observed during the semi-analytical analysis (see Section 8.4). In the experiments, already for relatively low values of the excitation amplitude  $v_d$ ,

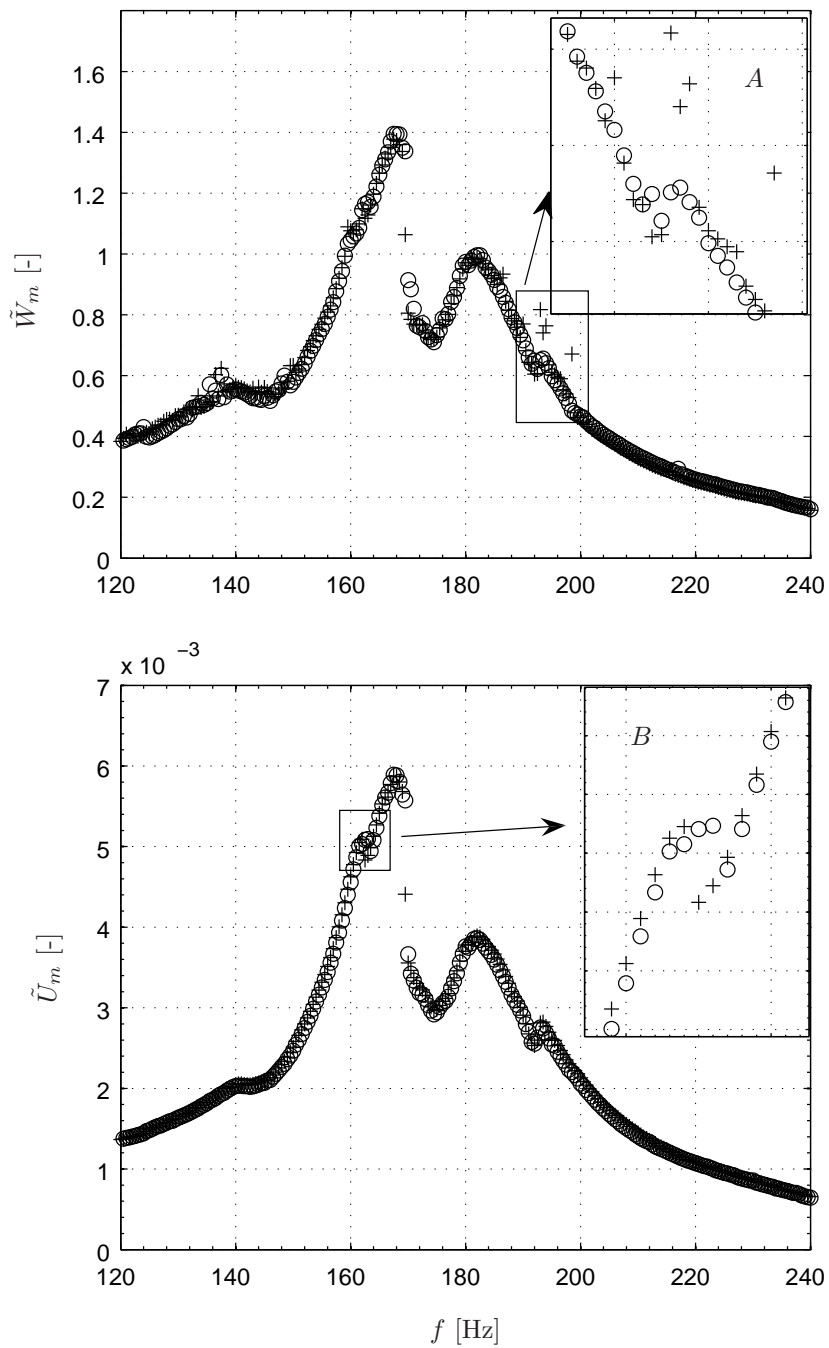


Figure 8.21: Frequency sweep results for  $v_d = 0.2$  [V] ('+' sweep down, 'o' sweep up).

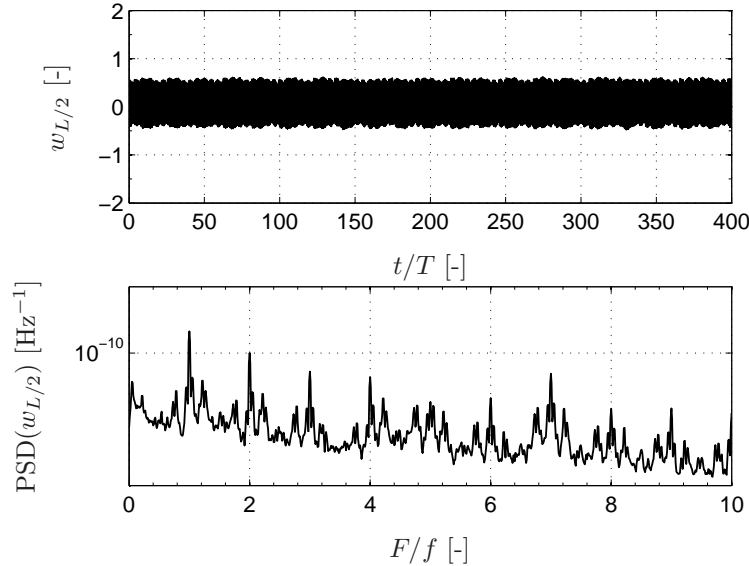


Figure 8.22: Measured dimensionless out-of-plane displacement  $w_{L/2}$  (top) and corresponding PSD (bottom) for  $f = 170$  [Hz] and  $v_d = 0.20$  [V].

additional peaks start to appear around the resonance at  $f = f_2$  (see Fig. 8.18). Furthermore, in this frequency region also transitions are found where the response switches from a harmonic response to a non-stationary response. In the experimental analysis these transitions occur, however, without (noticeable) sudden increases of the out-of-plane vibrations of the shell. This behaviour is not found in the numerical analysis. For larger amplitudes of the harmonic input voltage, the experimental frequency-amplitude plot indeed starts to exhibit jumps for  $v_d \geq 0.14$  [V] around  $f = 162$  [Hz] and  $f = 170$  [Hz]. By increasing  $v_d$  further to  $v_d \geq 0.19$  [V], large amplitude responses with a very broad PSD appear for excitation frequencies in the neighbourhood of  $f = 167.5$  [Hz].

Quantitatively, the semi-analytical results do not show a clear match with the experimental results. This can be explained by (a combination) of two main causes. Firstly, this mismatch can be explained by the imperfection sensitivity of the post-critical response as illustrated in the semi-analytical analysis (e.g. compare Fig. 8.8, Fig. 8.14 and Fig. 8.16). The cylindrical shell used in the experiments will obviously not be geometrically perfect and its actual (unknown) radial imperfection shape will be different from the imperfection shapes considered in the semi-analytical analysis. Furthermore,

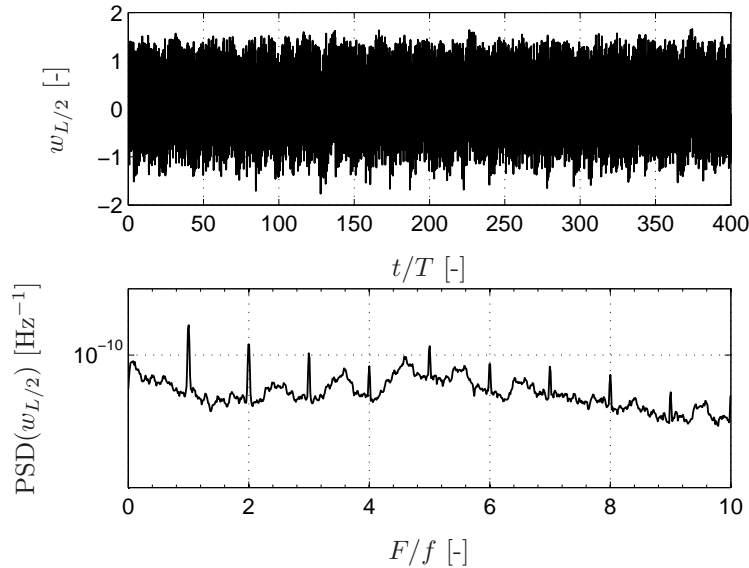


Figure 8.23: Measured dimensionless out-of-plane displacement  $w_{L/2}$  (top) and corresponding PSD (bottom) for  $f = 167.5$  [Hz] and  $v_d = 0.20$  [V].

at the experimental setup, also other types of imperfections will be present, for example small misalignments between the lower and the upper sledge (see Fig. 8.3), small thickness variations of the shell and non-perfect shell clamping conditions.

As a second cause, arbitrary imperfections in the shell and/or in its boundary conditions will simultaneously trigger multiple axi-asymmetrical modes with different circumferential wave numbers ( $n$ ). The effect of the participation of multiple modes with different circumferential wave numbers is not examined in the semi-analytical analysis. However, the effect of variation in the circumferential wave number  $n$  on the dynamic stability has been considered in the semi-analytical analysis for several imperfections, see Fig. 8.17. From these analysis follows that the lowest obtained critical amplitudes of the input voltage are closely grouped together for different values of  $n$ . This suggests that in case of arbitrary imperfections, multiple modes with different circumferential wave numbers may start to interact for  $v_d > v_d^c$ . To examine such responses using the semi-analytical approach, more DOFs (corresponding to modes with other circumferential wave numbers) should be included in the expansion of  $w$  and  $w_0$  (see Eq. (7.14) and Eq. (7.15)).

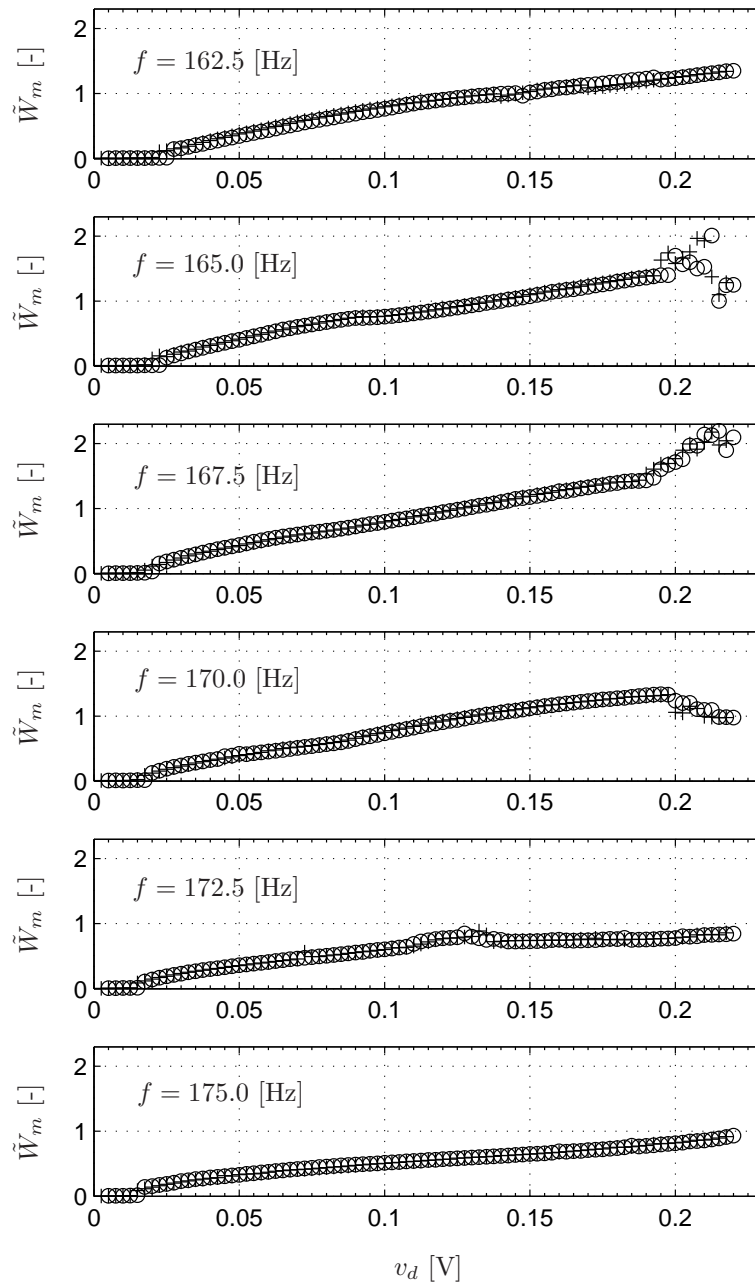


Figure 8.24: Amplitude sweep results ('+' sweep down, 'o' sweep up).

Nevertheless, the presented experimental results agree qualitatively with the semi-analytical results in the sense that for increasing excitation amplitude, the harmonic response around the (relative low frequent) resonance at  $f = f_2$  [Hz] may switch to a nonstationary (large amplitude) response with a very broad PSD. This confirms that the dynamic stability analysis of base-excited cylindrical shells structures with top mass and thus with a relatively low frequent axi-symmetrical vibration mode (Fig. 7.7-a) should be concentrated around the corresponding low frequent resonance peak.

With respect to a detailed analysis of the experimental response, much more sensors should be used. With the current two sensors (the LVDT and the laser vibrometer), it is not straightforward to obtain insight in which (axi-asymmetrical) modes substantially participate in the response. To be able to measure instantaneously the vibrations of the complete cylindrical shell surface, currently a measurement technique based on sound pressure measurements [118] using a cylindrically orientated array of microphones is under development.

In addition, in order to quantitatively verify semi-analytical models and in order to validate the observed imperfection sensitivity of the dynamic instability phenomena, it would be of interest to measure the actual (level of) imperfection of the cylindrical shell and to consider various shells with different imperfections shapes and amplitudes. These will be topics for further research.

## 8.6 Conclusions

The objective of this chapter is to determine numerically and experimentally, the dynamic stability limits of a thin cylindrical shell with top mass which is axially excited at the base using an electrodynamic shaker. For this case, the resulting acceleration of the base is determined by the interactions of the dynamics of the electro/mechanical shaker system carrying the cylindrical shell with top mass. To be able to compare the experimental results with the semi-analytical results, a coupled shaker/structure model is derived. The linearized model is validated by comparing numerical and experimental results for the FRF from input voltage to top mass acceleration and eigenfrequencies.

The coupled shaker/cylindrical shell/top mass structure exhibits two (relatively) low frequent resonances. The first resonance ( $f_1$ ) corresponds to a suspension type of vibration mode of the shaker and the second resonance ( $f_2$ ) corresponds to a vibration mode dominated by axial displacements of the cylindrical shell. Numerical analysis show that around the second resonance, the harmonic response may become unstable and a nonstationary response with severe out-of-plane deformations may appear instead. The critical value

for the input voltage for which the harmonic response changes to the severe post-critical response, highly depends on the initial imperfections present in the shell.

Experiments quantitatively confirm the dynamic response predicted by the semi-analytical model (including the shaker dynamics) showing that in the neighbourhood of the (relative low frequent) resonance at  $f = f_2$ , the harmonic response may switch to a severe nonstationary response by increasing the excitation amplitude. A quantitative match between the experimental and the semi-analytical results is not realized yet. In order to achieve this it is important to extend the semi-analytical model with modes corresponding to multiple circumferential wave numbers and to measure the actual imperfection of the shell under experimental investigation, so that these can be included in the semi-analytical model.

The presented experimental results confirm the observation from the semi-analytical analysis, that the dynamic stability analysis of base-excited cylindrical shells structures with top mass and thus with a relatively low frequent axisymmetrical vibration mode should be concentrated around the corresponding low frequent resonance peak.



## *Conclusions/Recommendations*

In this chapter the main conclusions regarding the work in this thesis will be presented and recommendations for future research will be given.

### *9.1 Conclusions*

The response of a dynamically loaded thin-walled structure may change abruptly due to a small change of one or more of the system and/or load parameters. Such sudden changes show a strong similarity to the phenomena of static buckling of structures and are, therefore, often denoted as dynamic buckling. The resistance of structures liable to buckling, to withstand dynamic (i.e. time-dependent) loading is often addressed as the dynamic stability of these structures. The dynamic stability analysis of thin-walled structures encompasses several challenges. Firstly, determining the time-response of dynamically loaded thin-walled structures is computationally complex, especially since in such analyses (at least) geometrical nonlinearities should be taken into account. Furthermore, in general time-dependent loads are described by multiple parameters (i.e. multi-parameter studies must be performed) and a wide variety in possible time-dependent loading types can be considered, like for example shock/impact loading, step loading, periodic loading or stochastic loading. Finally, the behaviour of thin-walled structures may be very sensitive to geometric imperfections (small deviations from the nominal shape) and loading imperfections.

To obtain competitive designs for dynamically loaded thin-walled structures such as discussed above, it is vital to be able to understand, predict, and eventually optimize the dynamic stability behaviour of the structure. However, design strategies and fast (pre-) design tools for thin-walled structures under dynamic loading are still lacking. In this thesis, a set of computational tools for modelling and analysis of dynamically loaded thin-walled structures is developed and/or combined. The tools are developed for structures with a relatively simple geometry. The geometric simplicity of the structures allows to derive approximate models with a relatively low number of degrees of freedom which are, therefore, very suitable for extensive parameter studies (as essential during the design process of a thin-walled structure). These models are derived via an energy based approach based on analytical expressions for

the undeformed and deformed structural geometry. This approach has been implemented in a symbolic manipulation software package in such a manner that model variations can be easily performed. In the analyses, both nonlinear static and nonlinear dynamic responses will be computed using numerical techniques in combination with the derived models (i.e. sets of coupled nonlinear ordinary differential equations). Hereto, a set of designated numerical tools is combined (e.g. continuation tools for equilibria, periodic solutions and bifurcations, and numerical integration routines) to solve the analytically derived models in a computationally efficient manner. The combination of the symbolic derivation of the model and the numerical techniques to obtain the solutions is called a semi-analytical approach. To illustrate and to test the abilities of the developed semi-analytical tools, four case studies are examined. For each of the case study, new research results have been found with respect to existing literature. Moreover, these results have been verified by FEM analysis and/or experiments.

In the first case study (Chapter 3), dynamic buckling of shallow arches due to shock loading in transversal direction is studied. For this structure and loading, dynamic buckling corresponds to a sudden reverse of the curvature of the shallow arch if the transversal shock load exceeds a critical value (i.e. the dynamic buckling load). In the case study, the semi-analytical tools are used to study the effect of the arch shape (i.e. the initial curvature of the arch) on the dynamic buckling load. It is shown that the dynamic buckling load, in contrast to the static buckling load, can be influenced significantly by varying the arch shape. Small asymmetries in the arch shape (i.e. geometric imperfections) have only a mild effect on the dynamic pulse buckling load and do not significantly change the sensitivity of the dynamic pulse buckling load with respect to the arch shape parameter. Quasi-static buckling results, modal analysis results and nonlinear dynamical transient analysis results obtained with the semi-analytical approach and obtained from FEM analysis are compared and a good correspondence is obtained.

The second test case (Chapter 4) considers dynamic buckling of a (statically) buckled beam subjected to harmonic excitation in transversal direction. The buckled beam structure possesses two coexisting stable static equilibrium states. Consequently, for sufficient large periodic transversal excitation, the buckled beam may exhibit severe vibrations which encircle both equilibrium states, referred to as snap-through motions. In the derived model, the beam is assumed to be inextensible. Based on Taylor series expansions of the inextensibility constraint and the exact curvature of the beam, and by using one or more displacement functions, a semi-analytical modelling approach is presented. The effect of using Taylor expansions of the inextensibility constraint and the exact curvature of the beam higher than third order is not

previously considered in literature. Nevertheless, in this case study it is shown that Taylor expansions of at least of seventh order or higher are necessary to obtain a good match with results obtained using accurate FEM analysis. Also inclusion of the effect of the axial inertia of the beam appeared to be important to get a good match with the FEM analysis results. With the developed semi-analytical approach such model variations (i.e. varying the order of the Taylor expansions and including or excluding the effect of axial inertia) can be studied very effectively.

The third case study (Chapters 5 and 6) considers a base-excited thin beam with top mass. The vertical beam is subjected to an axial static pre-load due to the presence of gravity plus an axial dynamic load due to the base motion. For this case, the same modelling assumptions as presented in the previous chapter are followed. However, now also geometric imperfections in the beam are incorporated. First, in a preliminary numerical analysis (Chapter 5), base-excitation in the form of prescribed harmonic base-acceleration is considered. The lowest vibration modes of the beam structure correspond to modes dominated by transversal displacements (i.e. beam bending modes). The bending modes of the imperfect beam are excited both in a direct manner and in a parametric manner. In general and for the considered level of imperfection, the (subharmonic) resonance due to the parametric excitation (i.e. parametric resonance) appears to be the most severe. For parametric resonance to occur, the excitation amplitude must exceed a certain critical value. It is shown that this critical value (mildly) depends on the level of geometric imperfection in the beam and (strongly) on possible nonlinear damping characteristics of the beam. The parametric resonance may appear as a resonance peak emerging from the harmonic response branch, as a separate branch (island) or as a combination of both. Such complex appearance of the parametric resonance peak complicates the computation of the critical value for the excitation amplitude. It is shown that the threshold value of the excitation amplitude for the existence of parametric resonance can be determined in a straightforward manner using a two-parameter continuation approach of bifurcations.

In the second part of the third case study (Chapter 6), semi-analytical results are compared with experimental results. For this purpose an experimental setup dedicated to test base-excited structures with top mass is realized. At the experimental setup the base-excitation is realized by supplying a harmonic input voltage to an electrodynamic shaker system. To be able to compare the experimental results with the semi-analytical results, the semi-analytical model of the thin beam structure is coupled with a model of the shaker system. In the semi-analytical approach, single mode and two mode discretizations of the transversal displacement field of the beam are considered. The unknown

geometric imperfection and damping parameters of the resulting model(s) are identified based on experimental steady-state results. The semi-analytical steady-state responses based on the single (beam) mode model are in good correspondence with the experimental results. However, still some qualitative discrepancies can be observed. It is shown that these discrepancies occur because of the nonlinear interactions between the first and the second bending mode of the beam. Obviously, such interactions can only be predicted correctly by a two mode model. The semi-analytical results based on the two mode model are in good agreement with the experimental results.

The last case study considers a base-excited thin cylindrical shell with top mass. The dynamics of thin cylindrical shells may depend strongly on the in-plane boundary conditions. However, a procedure to derive a (nonlinear) semi-analytical model with a low number of degrees of freedom and which satisfies exactly the in-plane boundary conditions is not readily available in literature. Therefore, such an approach is derived in this thesis. Initially, the resulting model is numerically validated through a comparison with static buckling and modal analysis results obtained using FEM analysis.

Similar as for the beam with top mass, first a preliminary numerical analysis is performed considering base-excitation in the form of a prescribed harmonic base-acceleration (Chapter 7). The lowest resonance frequency of the cylindrical shell with top mass corresponds to an axi-symmetrical vibration mode dominated by in-plane displacements in axial direction. It is shown that for increasing excitation amplitude, the harmonic response may become unstable in the peak of this resonance and that a beating response with severe out-of-plane deformations may appear instead. The critical value for the amplitude of the prescribed harmonic base-acceleration for which the harmonic response changes to the severe post-critical beating response highly depends on the initial imperfections present in the shell. As shown in many other studies in literature, for harmonically axially excited cylindrical shells without top mass, the dynamic stability limits are in general determined by parametric resonance(s) near twice the eigenfrequency of a bending vibration mode of the cylindrical shell (i.e. an axi-asymmetrical vibration mode). However, the results presented in Chapter 7 indicate that the dynamic stability analysis of harmonically axially excited cylindrical shells with a relatively high top mass and thus with a relatively low frequent axi-symmetrical vibration mode should be concentrated around the corresponding resonance peak. The dynamic stability results as presented in Chapter 7 are not observed in previous numerical studies of dynamically axially loaded cylindrical shells, since these studies did not include the effect of a top mass.

In Chapter 8 (part two of the last case study), the dynamic stability of a base-excited thin-cylindrical shell with top mass is examined using the realized experimental setup (i.e. the same setup as used in Chapter 6 for the experiments with the base-excited thin beam with top mass). To be able to compare the experimental results with semi-analytical results, also here a coupled shaker/structure model derived. At the experimental setup, the cylindrical shell with top mass is supported by the shaker which has a relatively low support stiffness in axial direction. Nevertheless, also in this case a low frequent resonance dominated by axi-symmetrical shell vibrations occurs. In analogy with the results presented in Chapter 7, semi-analytical results indicate again that in the top of this peak the stability of the harmonic response may be lost and severe out-of-plane beating responses may appear instead if the excitation amplitude is increased above some threshold. Experiments qualitatively confirm the dynamic response predicted by the semi-analytical model (including the shaker dynamics). It has been illustrated that the differences between the experimental results and the semi-analytical results for the cylindrical shell may be due to the strong dependency of the results with respect to the geometrical imperfections present in the shell.

In summary, with the adopted semi-analytical approach, for four case studies new insights and results have been obtained. For each case study, the semi-analytical models are validated through a comparison with results obtained using FEM analysis. Furthermore, for the last two cases, semi-analytical results have been compared with experimental results and good (quantitative and/or qualitative) correspondences have been obtained. In conclusion, it has been shown that the semi-analytical approach is a valuable tool in the (pre-) design process of thin-walled structures under dynamic loading.

## 9.2 Recommendations

In this thesis, a semi-analytical approach to study in a computational effective manner the dynamic buckling of thin-walled structures is proposed. Furthermore, an experimental setup has been realized to test base-excited structures carrying a top mass. The semi-analytical approach in combination with experiments is used in this thesis to predict and verify the dynamic buckling a thin beam and a thin cylindrical shell subjected to a harmonic base-excitation. Base-excited thin-walled structures with top mass represent an important class of structures in structural and aerospace engineering. It is, therefore, recommended to exploit the powerful combination of the semi-analytical approach and the experimental setup to study also other structures (e.g. plate, frame or panel type of structures and/or initially buckled structures) and also to consider other types of base-excitation (e.g. shock loading, stochastic loading or combined types of loading).

As for example shown in Chapter 7 and 8 for the base-excited thin cylindrical shell with top mass, dynamic buckling loads for shell type structures may be very sensitive to initial imperfections. In this thesis, only geometric imperfections are considered. However, imperfections in the loading and/or the boundary conditions may also be important. Therefore, it is recommended to also study the effect of such imperfections. Furthermore, to validate the imperfection sensitivity of dynamic buckling loads, several similar structures with different geometric imperfections (different shape and/or amplitude) may be examined experimentally. Especially the determination of worst-case imperfection shapes (i.e. the imperfection shape with a predefined maximum amplitude for which the dynamic buckling load is minimal) is of interest. To be able to make a good quantitative comparison with numerical and experimental results it is important to measure the geometric imperfections so that these can be included in the semi-analytical model.

With respect to the experimental setup it is recommended to extend the measurement system such that vibrations of two dimensional structures (i.e. plates and shells) can be characterized better. This is important since for a good correspondence between semi-analytical results and experimental results, the discretization used for the semi-analytical model must be able to approximately describe the experimentally observed vibration/buckling patterns. Furthermore, it would be of interest to apply a feedback control strategy for the shaker such that a prescribed harmonic base-acceleration can be realized accurately. In this manner, the results become more generally applicable and no coupled structure/shaker model has to be applied to be able to make a comparison with experimental results. However, given the nonlinear behaviour observed for the base-excited structures with top mass (i.e. softening, period doubling, beating, etc.), designing a controller suitable for this purpose is not trivial.

# A

## *Modelling of the electrodynamic shaker*

In Chapters 5 and 7, two structures subjected to harmonic base-acceleration are considered. To validate the semi-analytical results for these two cases, experiments are performed. At the experimental setup, the base-acceleration is realized by an electrodynamic shaker system, see Fig. A.1. The shaker system consists of a laptop in combination with a data acquisition and control system (TUEDACs AQI), a power amplifier (LDS PA1000L), an electrodynamic shaker (LDS V455) and an accelerometer with charge amplifier (Bruell and Kjaer 4367) to measure the acceleration of the armature of the shaker. For model identification purposes, the mass of the armature will be varied by mounting an additional known mass ( $m_{add}$ ) on top of the armature (see Fig. A.1). At the laptop, input signals for the shaker are generated and sensor signals are stored using MATLAB/Simulink. No active feedback is used to control the acceleration of the shaker armature. Consequently, the resulting acceleration of the shaker will be determined by the dynamics of the electro/mechanical shaker system with on top the structure under test (SUT) (i.e. the structures as considered in Chapters 5 and 7). To be able to compare the experimental results with the semi-analytical results, the equations of motion for the thin-walled structure have to be coupled with a model of the electrodynamic shaker

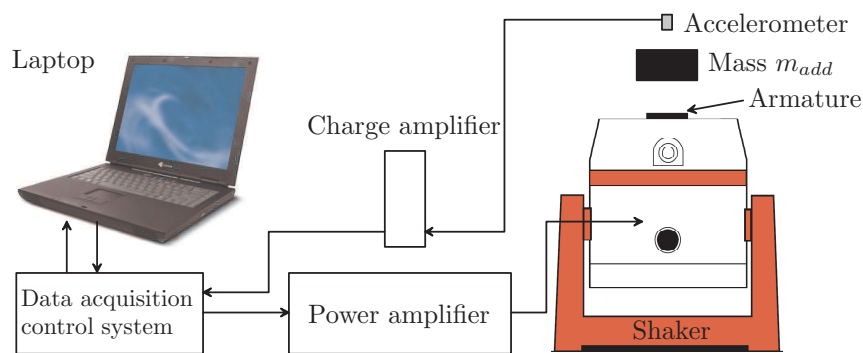


Figure A.1: Overview shaker system.

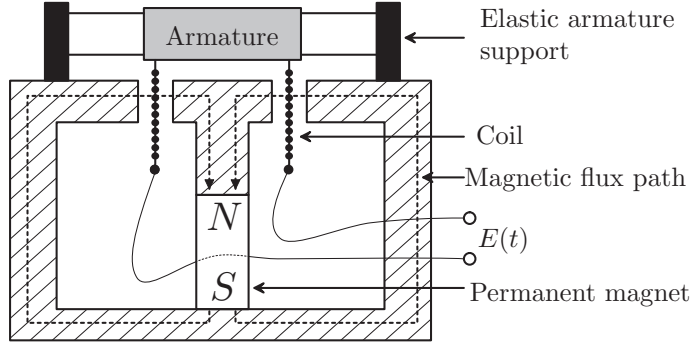


Figure A.2: Cross section of the electrodynamic shaker with permanent magnet.

system. The modelling of the electromagnetic shaker and the approach to obtain the final coupled total set of equations of motion will be discussed in this appendix.

The electrodynamic shaker is constructed as schematically shown in Fig. A.2, i.e. it consists of a fixed massive exciter base with a permanent magnet and a moving armature which is elastically suspended. The coil which is attached to the bottom of the armature is driven by a voltage  $E(t)$ . Due to this voltage, a current will run through the coil resulting in an electromagnetic force ( $F_{emf}(t)$ ) in the axial direction of the armature. The resulting force is

$$F_{emf}(t) = \kappa_c I(t). \quad (\text{A.1})$$

The current-to-force constant  $\kappa_c$  depends on the strength of the magnetic field that exists across the gap (due to the permanent magnet), the diameter, and the number of windings of the coil [88]. Due to the electromagnetic force, the armature will move in axial direction resulting in a relative motion between the coil and the magnetic field. When a coil moves in a magnetic field, a voltage will be induced. For the electrodynamic shaker, this voltage is called back voltage (or back electromotive force) and has a similar dissipative nature as mechanical viscous damping. The back voltage equals

$$E_{back} = -\kappa_c \dot{U}_{\mathbf{b}}, \quad (\text{A.2})$$

where  $\dot{U}_{\mathbf{b}}$  is the axial velocity of the armature and  $\kappa_c$  is the same force-to-current constant as in Eq. (A.1).

A model of the complete shaker system is depicted in Fig. A.3, where the electrical part and the mechanical part are presented separately. All parts of the



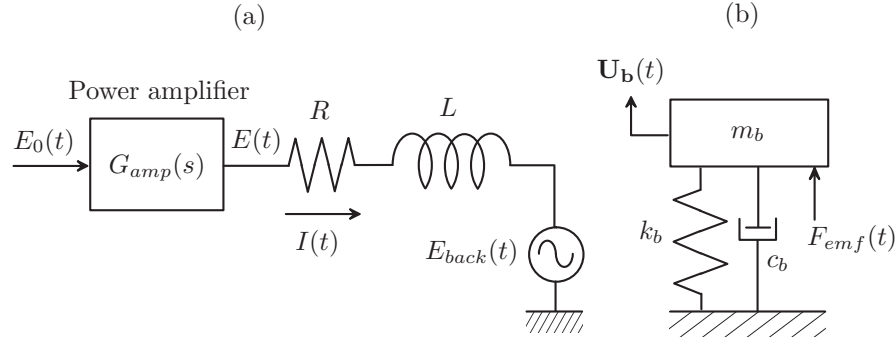


Figure A.3: Model of the electromagnetic shaker (electrical part (a) and mechanical part (b)).

shaker system are assumed to behave as be linear components. The electrical part of the model (Fig. A.3-a), consists of the power amplifier ( $G_{amp}(s)$ ), the coil resistance  $R$ , the coil inductance  $L$  and back voltage voltage  $E_{back}$  (which depends on the velocity of the armature, see Eq. (A.2)). The power-amplifier operates in a so-called voltage-mode [88]. Within the voltage-mode of operation, the output voltage  $E(t)$  is kept proportional to the input voltage  $E_0(t)$ . More specifically, in the frequency domain

$$E(s) = G_{amp}(s)E_0(s), \quad (\text{A.3})$$

where  $s = j\omega$  (with  $j^2 = -1$ ) and  $G_{amp}(s)$  is a frequency dependent amplifier gain. Unfortunately, details about sole amplifier characteristics (i.e.  $G_{amp}(s)$ ) are not available. Only the behaviour of the coupled amplifier/shaker system can be measured. It should be noted that (other) power amplifiers used for driving electrodynamic shakers may also operate in a so-called current-mode, i.e. the output current  $I(t)$  is kept proportional to the input voltage  $E_0(t)$  [88]. The influence of the type of operation of the amplifier (voltage-mode or current-mode) on the electrodynamic shaker dynamics is discussed in [88; 135].

The mechanical part of the model (Fig. A.3-b) corresponds to the elastically suspended armature which is excited by the electromagnetic force  $F_{emf}(t)$  (which depends on the current  $I$  through the electrical part, see Eq. (A.1)). This part is modelled as a linear structure with mass  $m_b$ , stiffness  $k_b$ , viscous damping  $c_b$  and single DOF  $\mathbf{U}_b$ . It should be noted that for the mechanical modelling of the shaker, the shaker base is assumed to be rigidly attached to the fixed world. If this assumption is not followed, the resulting mechanical

part of the shaker model would have more DOFs and unknown parameters which must be identified, see for example [143].

The coupled electro/mechanical dynamics of the shaker are described by the following set of ODEs [88]

$$\begin{aligned} L\dot{I} + RI + \kappa_c \dot{\mathbf{U}}_{\mathbf{b}} &= E(t), \\ m_o \ddot{\mathbf{U}}_{\mathbf{b}} + c_b \dot{\mathbf{U}}_{\mathbf{b}} + k_b \mathbf{U}_{\mathbf{b}} &= \kappa_c I, \end{aligned} \quad (\text{A.4})$$

where  $m_o = m_b + m_{add}$  and  $E(t)$  is related to  $E_0(t)$  by Eq. (A.3). From Eq. (A.4), the frequency response function from  $E_0$  to  $\mathbf{U}_{\mathbf{b}}$  follows to be

$$H_s(s) = \frac{\mathbf{U}_{\mathbf{b}}}{E_0} = \frac{h_1 G_{amp}(s)}{s^3 + h_2 s^2 + h_3 s + h_4}, \quad (\text{A.5})$$

where

$$h_1 = \frac{\kappa_c}{Lm_o}, \quad h_2 = \frac{Rm_o + Lc_b}{Lm_o}, \quad h_3 = \frac{Rc_b + Lk_b + \kappa_c^2}{Lm_o}, \quad h_4 = \frac{Rk_b}{Lm_o}. \quad (\text{A.6})$$

Next the procedure used for identifying the parameters of the shaker model will be discussed. The number of the physical parameters is equal to six ( $m_o = m_b + m_{add}$ ,  $c_b$ ,  $k_b$ ,  $L$ ,  $R$  and  $\kappa_c$ ), plus the number of parameters in  $G_{amp}(s)$ . The identification results hold for the bare shaker system as shown in Fig. A.1. At a later stage, it appeared that the armature suspension exhibited undesirable 'tilt' type of vibrational eigenmode(s) (see Fig. A.4) in the frequency domain of interest. To suppress these tilt vibrations in the frequency domain of interest, an additional linear sledge based on elastic hinges is added between the shaker and the SUT. The modelling and identification of the shaker system with this additional elastic support mechanism is, however, similar as discussed for the bare shaker system. Identification results for this case are reported at the end of this section.

The parameters of the shaker model will be identified using frequency domain techniques. Hereto, FRFs are measured by exciting the bare shaker system (i.e. no SUT attached) with a randomly varying input voltage  $E_0$  while measuring the acceleration of the armature  $\ddot{\mathbf{U}}_{\mathbf{b}}$ . To cancel measurement noise, the FRFs are averaged over at least five measurements. By dividing the measured FRFs in terms of  $\ddot{\mathbf{U}}_{\mathbf{b}}$  by  $-\omega^2$ , FRFs in terms of  $\mathbf{U}_{\mathbf{b}}$  are obtained (as in Eq. (A.5)). For model identification purposes, the mass of the armature will be varied by mounting additional mass(es) ( $m_{add}$ ) on top of the armature (see Fig. A.1). The result of this approach is depicted in Fig. A.5 for the reference situation, for an additional mass of 0.559 [kg] and for an additional mass of 2.184 [kg]. As can be noted, the shaker exhibits a heavily damped response. For the frequency range of interest (20 - 400 [Hz]), the FRF measurements show a good coherence

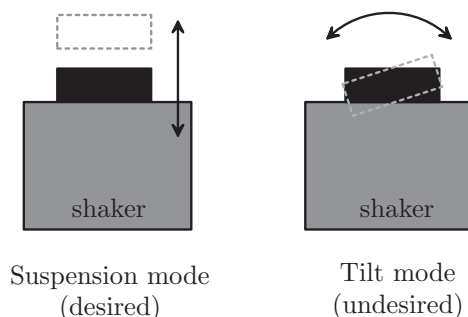


Figure A.4: Two types of vibration modes of a shaker.

(see the lowest graph in Fig. A.5).

Based on the measured FRF data, continuous-time transfer functions of the form

$$H(s) = \frac{b_1 s^n + b_2 s^{n-1} + \dots + b_{n+1}}{s^m + a_1 s^{m-1} + \dots + a_m}, \quad (\text{A.7})$$

are estimated using the function `invfreqs`, which is part of the MATLAB signal processing toolbox. This function determines the  $n + 1$  coefficients of the nominator ( $b_j$ ) and the  $m$  coefficients of the denominator ( $a_i$ ) such that Eq. (A.7) fits in a least squares sense to complex FRF data over a specified frequency range ( $m$  and  $n$  are parameters which must be supplied by the user). To be able to determine the order of the numerator ( $n$ ) and denominator ( $m$ ) of the model Eq. (A.5),  $G_{amp}(s)$  must be specified first. First a constant amplifier gain is assumed (i.e.  $G_{amp}(s) = P_{amp}$ ). For this case, the order of the nominator and denominator Eq. (A.5) are  $n = 0$  and  $m = 3$ , respectively. With these settings, however, a good fit could not be obtained. As an example, the fit is compared with the measured FRF for  $m_{add} = 0$  [kg] (see Fig. A.7) in Fig. A.7 (for the other two values of  $m_{add}$  similar results are obtained). Note that to elucidate the mismatch between the model and the experiments, the FRFs are now depicted in terms  $\ddot{U}_b/E_0$  (i.e. acceleration instead of position as output).

By introducing a frequency dependency of the amplifier gain as

$$G_{amp}(s) = P_{amp}(b_{amp} s + 1), \quad (\text{A.8})$$

an additional free parameter for the fitting procedure is introduced. This increases the order of the nominator of Eq. (A.5) to  $n = 1$ ) and results in a much better fit with the experimental results, see Fig. A.6. Note that for Eq. (A.8), the time domain version of Eq. (A.3) becomes  $E(t) = P_{amp}(b_{amp}\dot{E}_0(t) + E_0(t))$ . Since  $E_0$  is a known function of time, this expression can be implemented

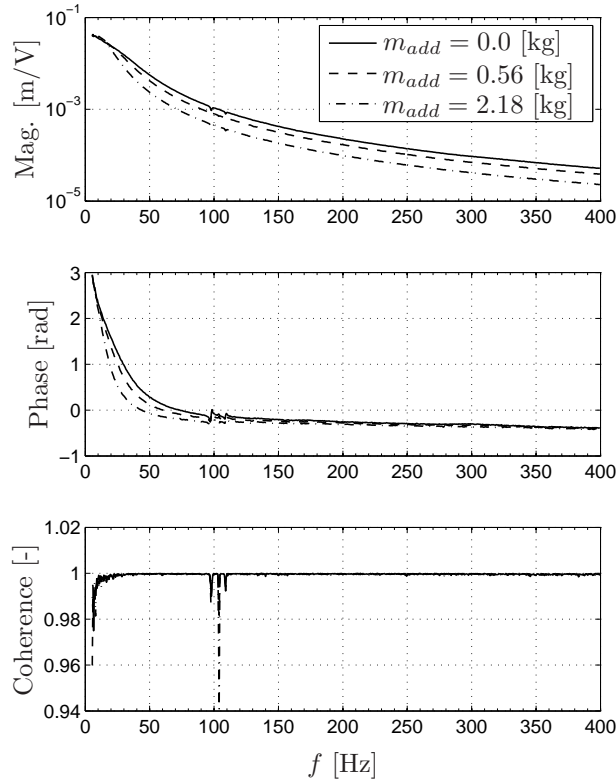


Figure A.5: Three measured FRFs of the bare shaker system.

without increasing the computational complexity of the shaker model (see Eq. (A.4)). It must be stressed that the frequency dependency of the amplifier gain as in Eq. (A.8) is simply a way to include an additional fit parameter allowing obtain a better fit for the frequency range of interest. The actual frequency characteristics of the amplifier are unknown and may be different from Eq. (A.8). For example, a better fit could (possibly) also have been obtained by including more DOFs in the mechanical part of the shaker model (as done in [143]). However, this would have resulted in a more computationally demanding shaker model (i.e. due to the increase of DOFs) with more unknown parameters to be identified.

With Matlab's `invfreqs` function, the five coefficients  $a_i$  and  $b_j$  of Eq. (A.7)

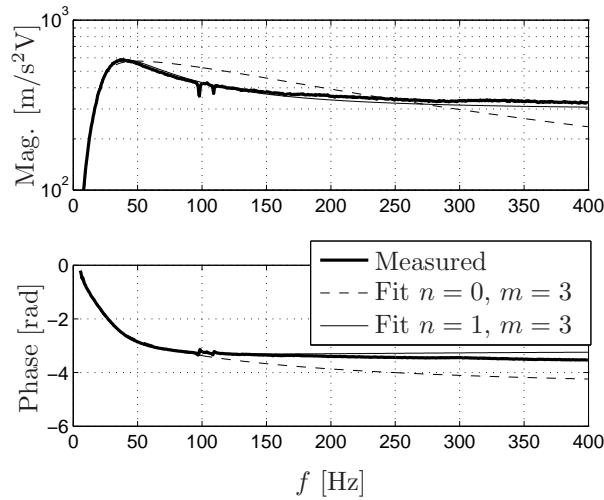


Figure A.6: Fitting of measured FRF data for two orders of numerator ( $n = 0$  and  $n = 1$ ),  $m = 3$  and  $m_{add} = 0$  [kg].

can be determined, resulting in a good correspondence with the experimental results. In this way, however, the values of the parameters present in the shaker model (see Eq. (A.4)) are not determined yet. The coil resistance is provided by the shaker manufacturer ( $R = 0.9$  [ $\Omega$ ]). Determining the five coefficients  $a_i$  and  $b_j$  of Eq. (A.7) for two values of  $m_{add}$  and setting for each case the resulting of coefficients of Eq. (A.7) equal to the corresponding coefficients of Eq. (A.5), results in ten equations in terms of the unknown seven parameters  $m_o = m_b + m_{add}$ ,  $c_b$ ,  $k_b$ ,  $L$ ,  $\kappa_c$ ,  $b_{amp}$ , and  $P_{amp}$ . This set of equations is numerically solved, considering  $m_{add} = 0$  [kg] and  $m_{add} = 0.56$  [kg] and resulted in an good fit of the original determined coefficients (i.e. the relative differences between the coefficients determined by `invfreqs` and the coefficients of Eq. (A.5) are less than 1.5%).

The identified parameter values are listed in Table A.1. The FRFs of the resulting model are compared with the two experimentally determined FRFs for  $m_{add} = 0$  [kg] and for  $m_{add} = 0.56$  [kg] (i.e. the ones which are used for the identification of the parameter values) in Fig. A.7. As can be noted, a good correspondence is obtained. For further validation, the FRF of the identified model and the measured FRF for the largest additional mass ( $m_{add} = 2.18$  [kg]) are compared in Fig. A.8. The measurements for  $m_{add} = 2.18$  [kg] are not used to identify the parameters, but the model still predicts the experiments with good accuracy. This supports the assumption that the shaker dynamics

Table A.1: Parameters shaker model (bare shaker configuration).

$c_b$	=	273	[kg/s]	$L$	=	$2.7 \cdot 10^{-3}$	[H]
$m_b$	=	1.7	[kg]	$\kappa_c$	=	8.7	[N/A]
$k_b$	=	$3.2 \cdot 10^3$	[N/m]	$R$	=	0.9	[ $\Omega$ ]
$P_{amp}$	=	-119	[-]	$b_{amp}$	=	$1.3 \cdot 10^{-3}$	[s <sup>-1</sup> ]

Table A.2: Parameters shaker model (shaker with additional elastic support mechanism).

$c_b$	=	278	[kg/s]	$L$	=	$2.6 \cdot 10^{-3}$	[H]
$m_b$	=	3.0	[kg]	$\kappa_c$	=	11.5	[N/A]
$k_b$	=	$5.28 \cdot 10^4$	[N/m]	$R$	=	0.9	[ $\Omega$ ]
$P_{amp}$	=	-88.3	[-]	$b_{amp}$	=	$1.4 \cdot 10^{-3}$	[s <sup>-1</sup> ]

---

may be captured with sufficient accuracy using a *linear* model.

As stated before, at a later stage an additional elastic support mechanism is mounted between the fixed world and the shaker armature to increase the rotational stiffness of the moving part of the shaker in order to avoid tilt (see Fig. A.4). The additional support mechanism is illustrated in Fig. 6.1 and Fig. 8.3. The dynamics of the shaker system with additional elastic support mechanism is captured with the same shaker model as used for the bare shaker (see Eq. (A.4)). The parameters are identified using the same procedure as discussed above for the bare shaker. The resulting parameters are listed in Table A.2. As expected, the additional elastic support mechanism significantly increases the stiffness  $k_b$  and mass  $m_b$ . Further comparison of Table A.1 and Table A.2 reveals that for both cases the obtained values for  $c_b$ ,  $L$ , and  $b_{amp}$  differ very little while the obtained values for  $P_{amp}$  and  $\kappa_c$  differ significantly. However, the product  $P_{amp} \cdot \kappa_c$  (which appears in the numerator of Eq. (A.5)), differs less than 1%. Apparently, with the adopted identification procedure, these two parameters can not be accurately identified separately from each other. Nevertheless, with the current identification procedure also for the shaker with additional elastic support mechanism, a satisfactory fit result is obtained, see Fig. A.9.

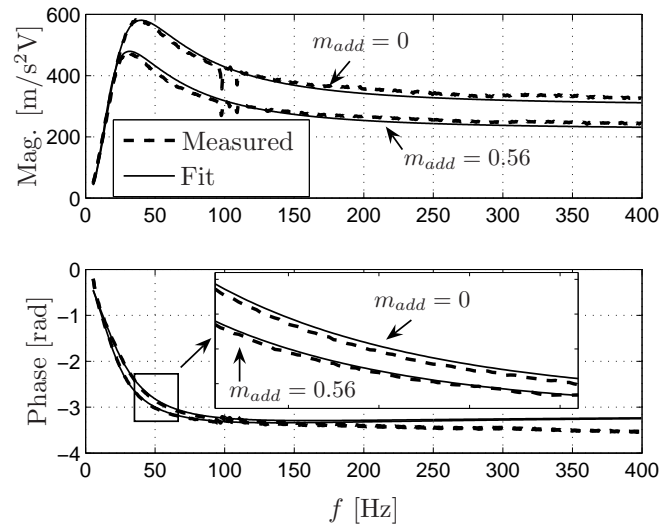
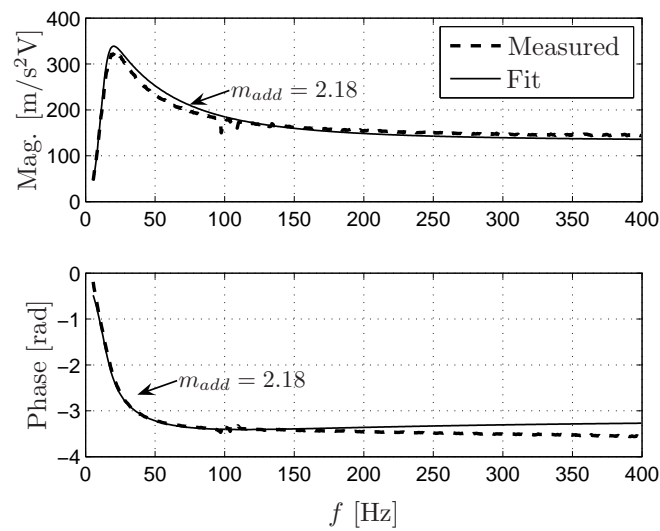


Figure A.7: Fit results.

Figure A.8: Validation of shaker model for bare shaker with  $m_{add} = 2.18$  [kg].

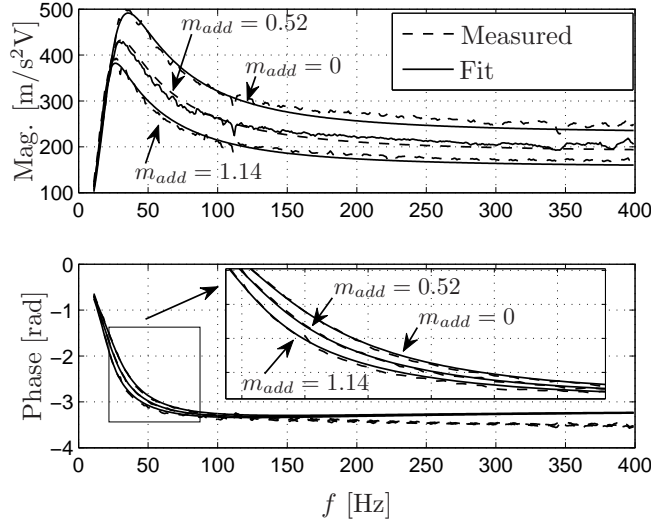


Figure A.9: Validation fit results for shaker with additional elastic support mechanism.

## A.1 The coupled shaker-structure model

After the determination of the parameters of the shaker model, the shaker model must be coupled with the model of the SUT (e.g. the beam structure as considered in Chapter 5 or the cylindrical shell structure as considered in Chapter 7). The coupled electro/mechanical equations of motion will be derived by following a charge/displacement formulation of Lagrange's equations [113]. In this formulation, energy and work expressions of the complete structure are formulated in terms of mechanical DOF and (in this case) one additional *charge* coordinate  $q$  which time derivative constitutes the current through the electrical part of the shaker model (i.e.  $\dot{q} = I$ ).

The total set of DOFs is collected in the column

$$\mathbf{Q}^* = [\mathbf{Q}_1, \mathbf{Q}_2, \dots, \mathbf{Q}_N, \mathbf{U}_b, q]^T, \quad (\text{A.9})$$

where the  $N$  DOF  $\mathbf{Q}_i$  are the generalized DOFs of the structure and  $\mathbf{U}_b$  is the axial motion of the shaker (see Fig. A.3).

The kinetic energy, potential energy and Rayleigh dissipation function of the SUT are denoted by  $\mathcal{T}_{SUT}$ ,  $\mathcal{V}_{SUT}$ ,  $\mathcal{R}_{SUT}$ , respectively. In the model of the SUT, the motions of the SUT are defined with respect to the base motion  $\mathbf{U}_b$  (see



Section 5.1 and Section 7.1). Consequently, the energy and work expressions for the coupled shaker/SUT system may be expressed as

$$\begin{aligned}
\mathcal{M} &= \frac{1}{2}L\dot{q}^2 + \kappa_c \dot{q} \mathbf{U}_{\mathbf{b}}, \\
\mathcal{T} &= \mathcal{T}_{SUT} + \frac{1}{2}m_b \dot{\mathbf{U}}_{\mathbf{b}}, \\
\mathcal{V} &= \mathcal{V}_{SUT} + \frac{1}{2}k_b \mathbf{U}_{\mathbf{b}}^2, \\
\mathcal{R} &= \mathcal{R}_{SUT} + \frac{1}{2}c_b \dot{\mathbf{U}}_{\mathbf{b}}^2 + \frac{1}{2}RI^2, \\
\delta\mathcal{W}_{nc} &= E(t)\delta q,
\end{aligned} \tag{A.10}$$

where  $\mathcal{M}$  is the magnetic energy of the moving coil of the shaker and  $\delta\mathcal{W}_{nc}$  is the virtual work of the voltage source  $E(t)$  [113]. Defining the Lagrangian  $\mathcal{L}$  of the complete system by  $\mathcal{L} = \mathcal{T} + \mathcal{M} - \mathcal{V}$ , the final coupled set of equations of motion can be determined

$$\frac{d}{dt}\mathcal{L}_{,\dot{\mathbf{Q}}^*} - \mathcal{L}_{,\mathbf{Q}^*} + \mathcal{R}_{,\dot{\mathbf{Q}}^*} = \mathbf{b}E(t), \tag{A.11}$$

where  $\mathbf{b} = [0, \dots, 0, 1]^T$  is an  $N + 2$  dimensional column.

Since during the modelling of the SUT, the motions of the SUT are defined with respect to the an arbitrary base motion  $\mathbf{U}_{\mathbf{b}}$ . For the coupled shaker/SUT system,  $\mathbf{U}_{\mathbf{b}}$  corresponds to the axial motion of the shaker. Consequently, the equations of motion for the SUT are not altered with respect to the case where the base motion is directly prescribed (i.e. as in Eq. (5.17) and in Eq. (7.20)). However, now  $\mathbf{U}_{\mathbf{b}}$  follows from

$$\begin{aligned}
L\dot{I} + RL + \kappa_c \dot{\mathbf{U}}_{\mathbf{b}} &= P_{amp}(b_{amp}\dot{E}_0(t) + E_0(t)), \\
(m_o + m_t)\ddot{\mathbf{U}}_{\mathbf{b}} + c_b \dot{\mathbf{U}}_{\mathbf{b}} + k_b \mathbf{U}_{\mathbf{b}} &= \kappa_c I + F_{SUT},
\end{aligned} \tag{A.12}$$

where  $m_t$  is the axial inertia of the SUT structure (which is in fact the mass of the top mass since the axial inertia of the supporting beam or cylindrical shell is neglected compared to the axial inertia of the top mass) and  $F_{SUT}$  is an inertial force due to the relative axial acceleration of the SUT. For example, for the single-mode third model model of the thin-beam with top mass (see Eq. (5.17)),

$$F_{SUT} = \frac{m_t \pi^2}{L} \left[ (he_1 + 2\mathbf{Q}_1) \ddot{\mathbf{Q}}_1 + 2\dot{\mathbf{Q}}_1^2 \right], \tag{A.13}$$

while for the 4 DOF model of the cylindrical shell with top mass (see Eq. (7.20))

$$F_{SUT} = m_t \ddot{\mathbf{U}}_{\mathbf{t}}. \tag{A.14}$$

Coupling of Eq. (5.17) with Eq. (A.12) results in the so-called 1-MODE model used in Chapter 6.



## ***B***

### ***Stepped sine procedure***

At the experimental setup, the steady-state response of the structure under test will be analysed using stepped sine sweeps. Sine sweep tests are also often used in engineering practise to determine experimentally the dynamic steady-state behaviour of a structure. The details of the stepped sine procedure are discussed in this appendix. Furthermore, also the way how averaged response measures are computed from the obtained stepped sine experiments is addressed.

The excitation is considered to be a known sinusoidal function of time

$$E_0(t) = v_d \sin(2\pi ft + \phi), \quad (\text{B.1})$$

where  $v_d$  is the excitation amplitude,  $f$  is the excitation frequency and  $\phi$  the phase of the excitation. Since Eq. (B.1) is generated using a PC,  $t$  is discrete time. During the stepped sine procedure, one of the excitation parameters (i.e.  $v_d$  or  $f$ ) is incrementally increased or decreased. After each incremental update of the excitation parameter, the measurement signals are saved during  $N_e$  excitation periods after which the excitation parameter is adapted again. If the excitation frequency is adapted, also the phase of the excitation  $\phi$  is altered to obtain a continuous excitation force. The purpose of the stepped sine experiment is to assess the steady-state response of the structure. Consequently, the updating of the excitation parameters must be carried out using sufficiently small increments while the number of  $N_e$  excitation periods should be selected sufficiently large. In general, the stepped sine process is performed both for an incrementally increasing excitation parameter (sweep up) and for an incrementally decreasing excitation parameter (sweep down). For nonlinear systems, the sweep-up response may differ (very much) from the sweep-down response.

During the stepped sine experiment, one or multiple measurement signals will be stored. Based on these measurements, response plots (i.e. excitation-frequency versus response-amplitude plots or excitation-amplitude versus response-amplitude plots) will be constructed 'step by step'. Each step corresponds to a data set of measurement signals  $m^j(t)$ , where  $j$  is the  $j^{\text{th}}$  measurement signal. These signals are stored during the time interval  $t_i \leq t \leq t_i + N_e T$ , where  $t_i$  [s] is the time instance at which one of the

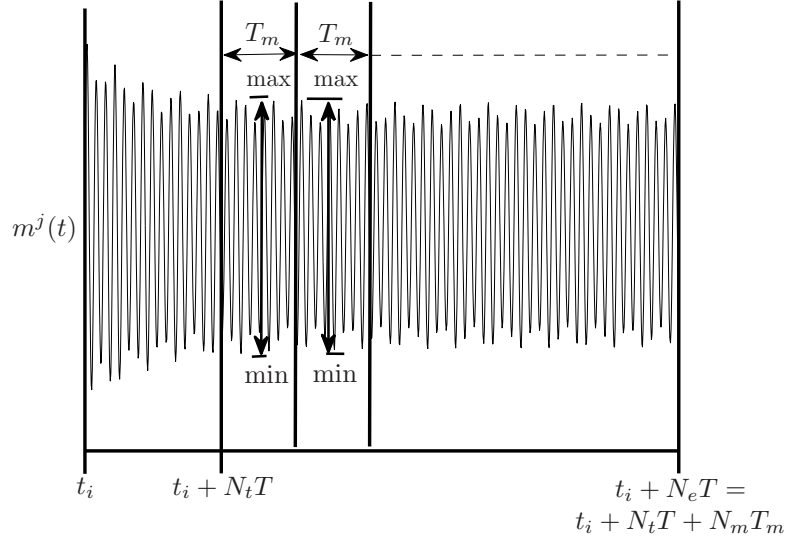


Figure B.1: Averaging procedure of measurement data.

excitation parameters is incrementally updated,  $i$  the step number,  $T_i = 1/f_i$  [s], and  $N_e$  is a positive integer, see Fig. B.1. To minimize transient effects, the measurement data during the first  $N_t < N_e$  periods is discarded. The rest of the data is divided in  $N_m = N_e - N_t$  equal parts with length  $T_m \geq T$  [s]. Subsequently, the following averaged response measures are determined

$$\tilde{M}_m^j = \frac{1}{N_m} \left( \sum_{k=0}^{N_m-1} \max_{T_m} m^j(t_i + kT_m) - \min_{T_m} m^j(t_i + kT_m) \right), \quad (\text{B.2})$$

where  $\tilde{M}_m^j$  is the scalar measure of the measurement signal  $m^j(t)$  during the  $i^{\text{th}}$  step of the stepped sine experiment.

# C

## *In-plane fields cylindrical shell model*

This appendix is part of the modelling procedure of the cylindrical shell with top mass as discussed in Chapter 7. First, the solution procedure of the expressions for the in-plane fields ( $u$  and  $v$ , see Fig. 7.2) corresponding to a given discretized out-of-plane displacement field ( $w$ ) and radial imperfection shape ( $w_0$ ) is discussed. Subsequently, as an example, the resulting expressions for  $u$  and  $v$  are presented for a 3-DOF discretization of  $w$ .

### *C.1 Solving the in-plane fields*

Using the assumed expressions for  $w$  (Eq. (7.14)) and  $w_0$  (Eq. (7.15)), the in-plane equilibrium equations (Eqs. (7.9)-(7.10)) consist of a set of linear inhomogeneous PDEs in terms of  $u$  and  $v$ . Consequently, the solutions for  $u$  and  $v$  can be written as

$$\begin{aligned} u(t, x, \theta) &= u_p(t, x, \theta) + u_h(t, x, \theta), \\ v(t, x, \theta) &= v_p(t, x, \theta) + v_h(t, x, \theta), \end{aligned} \quad (\text{C.1})$$

where  $u_p$  and  $v_p$  are the particular solutions and  $u_h$  and  $v_h$  the homogenous solutions (i.e. for  $w = w_0 = 0$ ) of Eq. (7.9) and Eq. (7.10), respectively. First the particular solutions are found. As out-lined in [34], the in-plane equilibrium equations (Eqs. (7.9) and (7.10)) can be decoupled into two linear inhomogeneous fourth order differential equations as follows. By applying first  $\frac{\partial^2}{\partial x^2}$  and then  $\frac{\partial^2}{\partial \theta^2}$  to Eq. (7.9), solving in both cases the term involving  $v$  and substituting these two expressions in the equation obtained by applying  $\frac{\partial^2}{\partial x \partial \theta}$  to (7.10), a fourth order differential equation in  $u$  is obtained

$$\beta_1 u_{,xxxx} + \eta u_{,xx\theta\theta} + \frac{1}{R^4} u_{,\theta\theta\theta\theta} = F_u(w, w_0, w_{,x}, w_{,\theta}, \dots). \quad (\text{C.2})$$

where  $\beta_1 = E_x/E_\theta$ ,  $\beta_2 = G_{x\theta}/E_\theta$  and

$$\eta = \frac{\beta_1 - \nu_x (\nu_x + 2\beta_2 (1 - \nu_x \nu_\theta))}{(1 - \nu_x \nu_\theta) \beta_2 R^2}. \quad (\text{C.3})$$

Similarly, by applying  $\frac{\partial^2}{\partial x^2}$  and  $\frac{\partial^2}{\partial \theta^2}$  to (7.10), solving in both cases the term involving  $u$  and substituting these two expressions in (7.9) after applying  $\frac{\partial^2}{\partial x \partial \theta}$ ,

a fourth order differential equation in  $v$  is obtained

$$\beta_1 v_{,xxxx} + \eta v_{,xx\theta\theta} + \frac{1}{R^4} v_{,\theta\theta\theta\theta} = F_v(w, w_0, w_x, w_\theta, \dots). \quad (\text{C.4})$$

The right-hand-sides of these equations,  $F_u(\cdot)$  and  $F_v(\cdot)$ , are long expressions in terms of  $w$  and  $w_0$  and their spatial derivatives (up to fourth order) and are not reported here explicitly for the sake of brevity. The decoupled equilibrium equations (Eqs. C.2-C.4) allow to solve  $u_p$  and  $v_p$  independent from each other. Using symbolic computations [87], the expansions for the particular solutions are derived. Introducing the abbreviations  $s_{j\theta} = \sin(jn\theta)$ ,  $c_{j\theta} = \cos(jn\theta)$ ,  $s_{ix} = \sin(\lambda_i x)$  and  $c_{ix} = \cos(\lambda_i x)$ , these expansions read

$$\begin{aligned} u_p(t, x, \theta) = & \sum_{i=1}^N \sum_{j=0}^M [\mathbf{A}_{ij}^u s_{j\theta} + \mathbf{B}_{ij}^u c_{j\theta}] c_{ix} + \\ & \sum_{i=1}^N \sum_{j=1}^N \sum_{k=l=0}^M [\mathbf{C}_{ijkl}^u s_{l\theta} s_{k\theta} + \mathbf{D}_{ijkl}^u c_{l\theta} c_{k\theta}] s_{ix} c_{jx} + \\ & \sum_{i=1}^N \sum_{j=1}^N \sum_{k=1}^M \sum_{l=0}^M \mathbf{E}_{ijkl}^u s_{k\theta} c_{l\theta} s_{ix} c_{ix}, \end{aligned} \quad (\text{C.5})$$

and

$$\begin{aligned} v_p(t, x, \theta) = & \sum_{i=1}^N \sum_{j=1}^M [\mathbf{A}_{ij}^v s_{j\theta} + \mathbf{B}_{ij}^v c_{j\theta}] s_{ix} + \\ & \sum_{i=j}^N \sum_{j=1}^N \sum_{k=l=1}^M (\mathbf{C}_{ijkl}^v s_{l\theta} s_{k\theta} + \mathbf{D}_{ijkl}^v c_{l\theta} c_{k\theta}) s_{ix} s_{jx} + \\ & \sum_{i=1}^N \sum_{j=1}^N \sum_{k=1}^M \sum_{l=0}^M (\mathbf{E}_{ijkl}^v s_{ix} s_{jx} + \mathbf{H}_{ijkl}^v c_{ix} c_{jx}) c_{l\theta} s_{k\theta} + \\ & \sum_{i=j}^N \sum_{j=1}^N \sum_{k=l=1}^M (\mathbf{F}_{ijkl}^v s_{l\theta} s_{k\theta} + \mathbf{G}_{ijkl}^v c_{l\theta} c_{k\theta}) c_{ix} c_{jx} + \\ & \sum_{i=j}^N \sum_{j=1}^N \sum_{k=1}^M (\mathbf{D}_{ijk0}^v s_{ix} s_{jx} + \mathbf{G}_{ijk0}^v c_{ix} c_{jx}) c_{k\theta}, \end{aligned} \quad (\text{C.6})$$

where  $\mathbf{F}_{iikk}^v = \mathbf{0}$ . The coefficients  $\mathbf{A}_{ij}^{u,v}$ ,  $\mathbf{B}_{ij}^{u,v}$ ,  $\mathbf{C}_{ijkl}^{u,v}$ ,  $\mathbf{D}_{ijkl}^{u,v}$ ,  $\mathbf{E}_{ijkl}^{u,v}$ ,  $\mathbf{F}_{ijkl}^{u,v}$ ,  $\mathbf{G}_{ijkl}^v$ ,  $\mathbf{H}_{ijkl}^v$  (for readability the time dependency of these coefficients is omitted) depend on the DOFs  $\mathbf{Q}_{ij}^{s,c}(t)$  from Eq. (7.14), the imperfection parameters  $e_i$  from Eq. (7.15) and the constants as present in Eqs. (7.14)-(7.15). These coefficients are solved by substituting Eq. (C.5) and Eq. (C.6) into Eq. (C.2) and

Eq. (C.4), respectively, and setting the coefficients of each unique combination of (goniometric) functions present in the resulting expressions to zero. For illustration, the particular solutions for an expansion of  $w$  with  $N = M = 1$  (see Eq. (7.14)) and  $w_0 = 0$  [m] are supplied in Appendix C.2.

The particular solutions (Eqs. (C.5) and (C.6)) do not yet satisfy the boundary conditions Eq. (7.5). Therefore, additionally the homogeneous solutions ( $u_h$  and  $v_h$ ) are solved such, that the total solutions Eqs. (C.1) satisfy exactly the boundary conditions. The homogeneous solutions are determined by considering the coupled in-plane equilibrium equations (Eqs. (7.9- 7.10)) for  $w = w_0 = 0$  [m];

$$\begin{aligned} u_{,xx} + \frac{\beta_2(1 - \nu_x \nu_\theta)}{\beta_1 R^2} u_{,\theta\theta} + \frac{\nu_x + \beta_2(1 - \nu_x \nu_\theta)}{\beta_1 R} v_{,\theta x} &= 0, \\ \frac{\beta_2(1 - \nu_x \nu_\theta)}{\beta_1} v_{,xx} + \frac{1}{\beta_1 R^2} v_{,\theta\theta} + \frac{\nu_x + \beta_2(1 - \nu_x \nu_\theta)}{\beta_1 R} u_{,\theta x} &= 0. \end{aligned} \quad (\text{C.7})$$

The homogeneous solutions consist of two parts,  $u_h = u_h^I + u_h^{II}$  and  $v_h = v_h^I + v_h^{II}$ . The first parts ( $u_h^I$  and  $v_h^I$ ) correct for the boundary conditions in  $u$ , the second part ( $u_h^{II}$  and  $v_h^{II}$ ) corrects for the boundary conditions in  $v$ . Evaluating Eq. (C.5) at  $x = 0$  and  $x = L$  results in expressions in terms of  $\mathbf{A}_{ij}^u$  and  $\mathbf{B}_{ij}^u$ . The homogeneous solutions which cancel out these terms, read

$$u_h^I(t, x, \theta) = \sum_{j=0}^M [f_j^u(x) \sin(jn\theta) \mathbf{A}_j + g_j^u(x) \cos(jn\theta) \mathbf{B}_j], \quad (\text{C.8})$$

$$v_h^I(t, x, \theta) = \sum_{j=0}^M [g_j^v(x) \sin(jn\theta) \mathbf{B}_j + f_j^v(x) \cos(jn\theta) \mathbf{A}_j], \quad (\text{C.9})$$

where  $\mathbf{A}_j = \sum_{i=1}^N \mathbf{A}_{ij}^u$ ,  $\mathbf{B}_j = \sum_{i=1}^N \mathbf{B}_{ij}^u$  and  $f_j^{u,v}(x)$  and  $g_j^{u,v}(x)$  are unknown axial distributions which satisfy

$$\begin{array}{c|cc} & x = 0 & x = L \\ \hline f_j^u, g_j^u & -1 & -\cos(i\pi) \\ f_j^v, g_j^v & 0 & 0 \end{array}. \quad (\text{C.10})$$

Substituting Eqs. (C.8)-(C.9) in Eq. (C.7), and setting each coefficient of  $\mathbf{A}_j$  and  $\mathbf{B}_j$  to zero, results in coupled sets of ODEs in terms of  $f_j^{u,v}(x)$  and  $g_j^{u,v}(x)$ . These sets of ODEs in combination with the boundary conditions Eq. (C.10) are solved using the symbolic ODE solver `dsolve` [87]. An important feature of the homogeneous solution  $u_h^I$  is that it includes a first order polynomial in

$x$  (see Eq. (C.8))

$$u_h^I(t, x, \theta) = u_h^{Ia}(t, x, \theta) + \sum_{i=1}^N \mathbf{B}_{i0}^u + \left[ \sum_{i=1}^N \mathbf{B}_{i0}^u (\cos(i\pi) - 1) + \mathbf{U}_t(t) \right] \frac{x}{L}, \quad (\text{C.11})$$

where  $u_h^{Ia}(t, x, \theta)$  is the axi-asymmetrical part of Eq. (C.8) and  $\mathbf{U}_t(t)$  is a newly introduced DOF corresponding to the (unknown) axial displacement of the top mass relative with respect to  $\mathbf{U}_b(t)$ , i.e.

$$\mathbf{U}_t(t) = u(t, L, \theta). \quad (\text{C.12})$$

Evaluating Eq. (C.6) at  $x = 0$  and  $x = L$  results in expressions in terms of  $\mathbf{F}_{ijkl}^v$ ,  $\mathbf{G}_{ijkl}^v$  and  $\mathbf{H}_{ijkl}^v$  terms. The homogeneous solutions which cancel out these terms, read

$$\begin{aligned} u_h^{II}(t, x, \theta) &= \sum_{k=l}^M \sum_{l=1}^M [q_{kl}^u(x) \sin((l-k)n\theta) \mathbf{A}_{kl}^{II} + \\ &\quad r_{kl}^u(x) \sin((l+k)n\theta) \mathbf{B}_{kl}^{II} s_{kl}^u(x) \cos((l-k)n\theta) \mathbf{C}_{kl}^{II} + \\ &\quad t_{kl}^u(x) \cos((l+k)n\theta) \mathbf{D}_{kl}^{II} + p_{k0}^u(x) \sin(kn\theta) \mathbf{E}_{k0}^{II}], \\ v_h^{II}(t, x, \theta) &= \sum_{k=l}^M \sum_{l=1}^M [q_{kl}^v(x) \cos((l-k)n\theta) \mathbf{A}_{kl}^{II} + \\ &\quad r_{kl}^v(x) \cos((l+k)n\theta) \mathbf{B}_{kl}^{II} + s_{kl}^v(x) \sin((l-k)n\theta) \mathbf{C}_{kl}^{II} + \\ &\quad t_{kl}^v(x) \sin((l+k)n\theta) \mathbf{D}_{kl}^{II} + p_{k0}^v(x) \cos(kn\theta) \mathbf{E}_{k0}^{II}], \end{aligned} \quad (\text{C.13})$$

where  $\mathbf{A}_{kl}^{II} = \frac{1}{2} \sum_{i=j}^N \sum_{j=1}^N \mathbf{F}_{ijkl}^v + \mathbf{G}_{ijkl}^v$ ,  $\mathbf{B}_{kl}^{II} = \frac{1}{2} \sum_{i=j}^N \sum_{j=1}^N \mathbf{G}_{ijkl}^v - \mathbf{F}_{ijkl}^v$ ,  $\mathbf{C}_{kl}^{II} = \mathbf{D}_{kl}^{II} = \frac{1}{2} \sum_{i=1}^N \sum_{j=1}^N \mathbf{H}_{ijkl}^v$ ,  $\mathbf{E}_{k0}^{II} = \sum_{i=j}^N \sum_{j=1}^N \mathbf{G}_{ijk0}^v$  and the unknown axial distributions satisfy

$$\begin{array}{c|cc} & x=0 & x=L \\ \hline p_{k0}^u, q_{kl}^u, r_{kl}^u, s_{kl}^u, t_{kl}^u & 0 & 0 \\ p_{k0}^v, q_{kl}^v, r_{kl}^v, s_{kl}^v, t_{kl}^v & -1 & -\cos(i\pi) \cos(j\pi) \end{array}. \quad (\text{C.14})$$

For illustration, the homogeneous solutions for an expansion of  $w$  with  $N = M = 1$  (see Eq. (7.14)) and  $w_0 = 0$  [m] are supplied in appendix C.2. Adding the homogenous solutions to the particular solutions

$$u(t, x, \theta) = u_p(t, x, \theta) + u_h^I(t, x, \theta) + u_h^{II}(t, x, \theta), \quad (\text{C.15})$$

$$v(t, x, \theta) = v_p(t, x, \theta) + v_h^I(t, x, \theta) + v_h^{II}(t, x, \theta), \quad (\text{C.16})$$

results in expressions for the in-plane fields which satisfy exactly the in-plane equilibrium equations (Eqs. (7.9)-(7.10)) and the in-plane boundary conditions (Eq. (7.5)). Moreover, the continuity in  $\theta$  for all displacement fields is satisfied.



## C.2 Expressions in-plane fields for $N = M = 1$

For illustration, the particular solutions for  $u$  and  $v$  are reported here for the expansion of  $w$  with  $N = M = 1$  and for the case without initial radial imperfection ( $w_0 = 0$  [m]). Adopting the same abbreviations as used in Eqs. (C.5)-(C.6), the expression for  $w$  takes the form

$$w(t, x, \theta) = \mathbf{Q}_{10}^c s_{1x} + \mathbf{Q}_{11}^s s_{1x} s_{1\theta} + \mathbf{Q}_{11}^c s_{1x} c_{1\theta}. \quad (\text{C.17})$$

The corresponding particular solutions of Eq. (C.2) and Eq. (C.2) read

$$\begin{aligned} u_p(t, x, \theta) = & \mathbf{A}_{11}^u c_{1x} s_{1\theta} + \mathbf{B}_{10}^u c_{1x} + \mathbf{B}_{11}^u c_{1x} c_{1\theta} + \mathbf{C}_{1111}^u s_{1\theta}^2 c_{1x} s_{1x} + \\ & \mathbf{D}_{1100}^u c_{1x} s_{1x} + \mathbf{D}_{1110}^u c_{1\theta} c_{1x} s_{1x} + \mathbf{D}_{1111}^u c_{1\theta}^2 c_{1x} s_{1x} + \\ & \mathbf{E}_{1110}^u s_{1\theta} c_{1x} s_{1x} + \mathbf{E}_{1111}^u s_{1\theta} c_{1\theta} c_{1x} s_{1x}, \end{aligned} \quad (\text{C.18})$$

$$\begin{aligned} v_p(t, x, \theta) = & \mathbf{A}_{11}^v s_{1\theta} s_{1x} + \mathbf{B}_{11}^v c_{1\theta} s_{1x} + \mathbf{C}_{1111}^v s_{1\theta}^2 s_{1x}^2 + \mathbf{D}_{1110}^v c_{1\theta} s_{1x}^2 + \\ & \mathbf{D}_{1111}^v c_{1\theta}^2 s_{1x}^2 + \mathbf{E}_{1110}^v s_{1\theta} s_{1x}^2 + \mathbf{E}_{1111}^v s_{1\theta} c_{1\theta} s_{1x}^2 + \mathbf{G}_{1110}^v c_{1\theta} c_{1x}^2 + \\ & \mathbf{G}_{1111}^v c_{1\theta}^2 c_{1x}^2 + \mathbf{H}_{1110}^v s_{1\theta} c_{1x}^2 + \mathbf{H}_{1111}^v s_{1\theta} c_{1\theta} c_{1x}^2, \end{aligned} \quad (\text{C.19})$$

with

$$\begin{aligned} \mathbf{A}_{11}^u &= u_1 \mathbf{Q}_{11}^s, & \mathbf{B}_{10}^u &= u_2 \mathbf{Q}_{10}^c, \\ \mathbf{C}_{1111}^u &= u_4 (\mathbf{Q}_{11}^s)^2 + u_5 (\mathbf{Q}_{11}^c)^2 + u_6 (\mathbf{Q}_{11}^s)^2, & \mathbf{B}_{11}^u &= u_3 \mathbf{Q}_{11}^c, \\ \mathbf{D}_{1100}^u &= u_7 (\mathbf{Q}_{10}^c)^2, & \mathbf{D}_{1110}^u &= u_8 \mathbf{Q}_{10}^c \mathbf{Q}_{11}^c, \\ \mathbf{D}_{1111}^u &= u_9 (\mathbf{Q}_{11}^s)^2 + u_{10} (\mathbf{Q}_{11}^c)^2 + u_{11} (\mathbf{Q}_{11}^c)^2, & \mathbf{E}_{1110}^u &= u_{12} \mathbf{Q}_{10}^c \mathbf{Q}_{11}^s, \\ \mathbf{E}_{1111}^u &= u_{13} \mathbf{Q}_{11}^s \mathbf{Q}_{11}^c, & & \\ \\ \mathbf{A}_{11}^v &= v_1 \mathbf{Q}_{11}^c, & \mathbf{B}_{11}^v &= v_2 \mathbf{Q}_{11}^s, \\ \mathbf{C}_{1111}^v &= v_3 \mathbf{Q}_{11}^s \mathbf{Q}_{11}^c, & \mathbf{D}_{1110}^v &= v_4 \mathbf{Q}_{11}^s \mathbf{Q}_{10}^c, \\ \mathbf{D}_{1111}^v &= v_5 \mathbf{Q}_{11}^s \mathbf{Q}_{11}^c, & \mathbf{E}_{1110}^v &= v_6 \mathbf{Q}_{11}^c \mathbf{Q}_{10}^c, \\ \mathbf{E}_{1111}^v &= v_7 (\mathbf{Q}_{11}^c)^2 + v_8 (\mathbf{Q}_{11}^s)^2 + v_9 (\mathbf{Q}_{11}^c)^2, & \mathbf{G}_{1110}^v &= v_{10} \mathbf{Q}_{11}^s \mathbf{Q}_{10}^c, \\ \mathbf{G}_{1111}^v &= v_{11} \mathbf{Q}_{11}^s \mathbf{Q}_{11}^c, & \mathbf{H}_{1110}^v &= v_{12} \mathbf{Q}_{11}^c \mathbf{Q}_{10}^c, \\ \mathbf{H}_{1111}^v &= v_{13} (\mathbf{Q}_{11}^c)^2 + v_{14} (\mathbf{Q}_{11}^s)^2, & & \end{aligned} \quad (\text{C.20})$$

where  $u_i$  and  $v_i$  are constants depending on  $L$ ,  $n$ ,  $\nu$  and  $R$ . These constants are not reported here for the sake of brevity.

The homogeneous solutions of Eq. (C.7) read

$$\begin{aligned}
u_h(t, x, \theta) = & (u_{14}s_{1\theta}\mathbf{A}_{11}^u + u_{15}c_{1\theta}\mathbf{B}_{11}^u + u_{16}s_{1\theta}\mathbf{G}_{1110}^v + u_{17}c_{1\theta}\mathbf{H}_{1110}^v) e^{\left(\frac{nx}{R}\right)} + \\
& (u_{18}s_{1\theta}\mathbf{A}_{11}^u + u_{18}c_{1\theta}\mathbf{B}_{11}^u + u_{19}s_{1\theta}\mathbf{G}_{1110}^v + u_{10}c_{1\theta}\mathbf{H}_{1110}^v) e^{-\left(\frac{nx}{R}\right)} + \\
& (u_{20}s_{2\theta}\mathbf{G}_{1111}^v + u_{21}c_{2\theta}\mathbf{H}_{1111}^v) e^{\left(\frac{2nx}{R}\right)} + u_{22}s_{2\theta}\mathbf{G}_{1111}^v + \\
& u_{23}c_{2\theta}\mathbf{H}_{1111}^v e^{-\left(\frac{2nx}{R}\right)} - \mathbf{B}_{10}^u + (\mathbf{U}_t - 2\mathbf{B}_{10}^u)x/L, \\
v_h(t, x, \theta) = & (v_{15}c_{1\theta}\mathbf{A}_{11}^u + v_{16}s_{1\theta}\mathbf{B}_{11}^u + v_{17}\mathbf{G}_{1110}^v c_{1\theta} + v_{10}\mathbf{H}_{1110}^v s_{1\theta}) e^{\left(\frac{nx}{R}\right)} + \\
& (v_{18}c_{1\theta}\mathbf{A}_{11}^u + v_{19}s_{1\theta}\mathbf{B}_{11}^u + v_{20}\mathbf{G}_{1110}^v c_{1\theta} + v_{11}\mathbf{H}_{1110}^v s_{1\theta}) e^{-\left(\frac{nx}{R}\right)} + \\
& (v_{21}c_{2\theta}\mathbf{G}_{1111}^v + v_{22}s_{2\theta}\mathbf{H}_{1111}^v) e^{-\left(\frac{2nx}{R}\right)} + (v_{23}c_{2\theta}\mathbf{G}_{1111}^v \\
& + v_{24}s_{2\theta}\mathbf{H}_{1111}^v) e^{\left(\frac{2nx}{R}\right)},
\end{aligned}$$

where  $u_i$  and  $v_i$  are constants depending on  $L$ ,  $n$ ,  $\nu$  and  $R$  (similar as in Eq. (C.20)). Again, these constants are not reported here for the sake of brevity.

## *Bibliography*

- [1] J. Albus, S. Dieker, H. Öry, and A. Rittweger. Parametric instability of pressurized propellant tanks. *Acta Astronautica*, 62(1-2):212–223, 2008.
- [2] M. Amabili. A comparison of shell theories for large-amplitude vibrations of circular cylindrical shells: Lagrangian approach. *J. of Sound and Vibr.*, 264(5):1091–1125, 2003.
- [3] M. Amabili. Nonlinear vibrations of circular cylindrical shells with different boundary conditions. *AIAA J.*, 41(6):1119–1130, 2003.
- [4] M. Amabili. Theory and experiments for large-amplitude vibrations of empty and fluid-filled circular cylindrical shells with imperfections. *J. of Sound and Vibr.*, 262(4):921–975, 2003.
- [5] M. Amabili and R. Garziera. A technique for the systematic choice of admissible functions in the Rayleigh-Ritz method. *J. of Sound and Vibr.*, 224(3):519–539, 1999.
- [6] M. Amabili and M.P. Païdoussis. Review of studies on geometrically nonlinear vibrations and dynamics of circular cylindrical shells and panels, with and without fluid-structure interaction. *Applied Mechanics Reviews*, 56(4):349–356, 2003.
- [7] T.J. Anderson, A.H. Nayfeh, and B. Balachandran. Experimental verification of the importance of the nonlinear curvature in the response of a cantilever beam. *ASME J. Vibr. and Acoustics*, 118(21):21–27, 1996.
- [8] J. Arbocz and J.H. Starnes. Future directions and challenges in shell stability analysis. *Thin-Walled Structures*, 40(9):729–754, 2002.
- [9] Arianespace, [www.arianespace.com](http://www.arianespace.com). *Vega Users Manual*, third edition, March 2006.
- [10] S. Atluri. Nonlinear vibrations of a hinged beam including nonlinear inertia effects. *ASME J. Appl. Mech.*, 40(1):121–126, 1973.
- [11] P. Aubert and B. Rousselet. Sensitivity computation and shape optimization for a non-linear arch model with limit-points instabilities. *Int. J. Numer. Meth. Eng.*, 42(1):15–48, 1998.
- [12] Z.P. Bazant and L. Cedolin. *Stability of Structures: Elastic, Inelastic, Fracture, and Damage Theories*. Oxford University Press, Oxford, 1991.

- 
- [13] C. Bisagni. Dynamic buckling of fiber composite shells under impulsive axial compression. *Thin-Walled Structures*, 43(3):499–514, 2005.
- [14] C. Bisagni and R. Zimmerman. Buckling of axially compressed fiber composite cylindrical shells due to impulsive loading. In *Proc. European conf. on spacecraft structures, materials and mechanical testing*, pages 557–562, Braunschweig, Germany, 1998. ESA.
- [15] V.V. Bolotin. *The Dynamic Stability of Elastic Systems*. Holden-Day, San Francisco, 1964.
- [16] A.A. Bondarenko and P.I. Galaka. Parametric instability of cylindrical glass-plastic cylindrical shells. *Soviet Applied Mechanics*, 13:411–414, 1977.
- [17] D.O. Brush and B.O. Almroth. *Buckling of Bars, Plates and Shells*. McGraw-Hill, 1975.
- [18] L. Buchaillot, O. Millet, E. Quévy, and D. Collard. Post-buckling dynamic behavior of self-assembled 3D microstructures. *Microsyst. Technol.*, 14:69–78, 2007.
- [19] B. Budiansky. Dynamic buckling of elastic structures: criteria and estimates. In *Dynamic Stability of Structures*, Ed. G. Herrmann, Pergamon Press, pages 83–106, 1967.
- [20] B. Budiansky. Theory of buckling and post-buckling behavior of elastic structures. *Advances in applied mechanics*, 14:1–66, 1974.
- [21] B. Budiansky and J.W. Hutchinson. Dynamic buckling of imperfection-sensitive structures. In *Proc. of the 11th Int. Congress of Applied Mechanics*, pages 421–446, Berlin, 1964.
- [22] B. Budiansky and R.S. Roth. Axisymmetric dynamic buckling of clamped shallow spherical shells. pages 597–606, 1962.
- [23] D. Bushnell. *Computerized buckling analysis of shells*. Kluwer academic publishers, Dordrecht, 1989.
- [24] G. Catellani, F. Pellicano, D. Dall’Asta, and M. Amabili. Parametric instability of a circular cylindrical shell with geometric imperfections. *Computers and Structures*, 82(31-32):2635–2645, 2004.
- [25] B. Charlot, W. Sun, K. Yamashita, H. Fujita, and H. Toshiyoshi. Bistable nanowire for micromechanical memory. *J. Micromech. and Microeng.*, 18(4):1–7, 2008.

- [26] J.-S. Chen and C.-Y. Liao. Experiment and analysis on the free dynamics of a shallow arch after impact load at the end. *ASME J. Appl. Mech.*, 72:54–61, 2005.
- [27] J.-S. Chen and J.-S. Lin. Dynamic snap-through of a shallow arch under a moving point load. *ASME J. Vibr. and Acoustics*, 126:514–519, 2004.
- [28] L. Chevalier. Influence of microstructure evolution on mechanical strength of blown poly(ethylene terephthalate). *Plastics, Rubber and Composites*, 28(8):385–392, 1999.
- [29] R.D. Cook, D.S. Malkus, and M.E. Plesha. *Concepts and applications of finite element analysis*. Wiley, Toronto, third edition, 1989.
- [30] J.G.A. Croll and A.C. Walker. *Elements of structural stability*. Macmillan, London, 1972.
- [31] L.J.A. de Boer. Modal analysis of a thin cylindrical shell with top mass. Technical Report DCT 2007.086, Eindhoven University of Technology, 2007.
- [32] R. Degenhardt, H. Klein, A. Kling, and R. Zimmermann. *Buckling and postbuckling analysis of shells under quasi-static and dynamic loads*. DLR institute of structural mechanics, www.dlr.de, 2002.
- [33] E. Doedel, R.C. Paffenroth, A.R. Champneys, T.F. Fairgrieve, Y.A. Kuznetsov, B.E. Oldeman, B. Sandstede, and X. Wang. *AUTO97: Continuation and bifurcation software for ordinary differential equations (with HOMCONT)*. Technical Report, Concordia University, 1998.
- [34] L.H. Donnell. *Beams, Plates and Shells*. McGraw-Hill, 1976.
- [35] E.H. Dowell. *Aeroelasticity of Plates and Shells*. Noordhoff International Publishing, 1975.
- [36] S.A. Emam and A.H. Nayfeh. On the nonlinear dynamics of a buckled beam subjected to a primary-resonance excitation. *Nonlinear Dynamics*, 35:1–17, 2004a.
- [37] S.A. Emam and A.H. Nayfeh. On the nonlinear responses of buckled beams to subharmonic-resonance excitations. *Nonlinear Dynamics*, 35:105–122, 2004b.
- [38] D.A. Evensen. *Nonlinear flexural vibrations of thin-walled cylindrical cylinders*. NASA TN D4090, 1967.
- [39] R. Feng and R.J. Farris. Linear thermoelastic characterization of anisotropic poly(ethylene terephthalate) films. *J. of Applied Polymer Science*, 86(12):2937 – 2947, 2002.

- 
- [40] R.H.B. Fey. *Steady-state behaviour of reduced dynamic systems with local nonlinearities*. PhD thesis, Eindhoven University of Technology, 1992.
- [41] M. Fukuyama, M. Nakagawa, K. Ishihama, Y. Hagiwara, Y. Toyoda, and H. Akiyama. Dynamic buckling experiments of fluid-structure-coupled co-axial thin cylinder. *Nuclear Engineering and Design*, 188:13–26, 1999.
- [42] Y.C. Fung and A. Kaplan. *Buckling of low arches or curved beams*. NASA TN 2840, 1952.
- [43] C.G. Gibson. *Elementary geometry of differentiable curves: An Undergraduate Introduction*. Cambridge University Press, 2001.
- [44] L.A. Godoy. *Theory of Elastic Stability, Analysis and Sensitivity*. Taylor & Francis, Philadelphia, 2000.
- [45] P.B. Gonçalves, D. Pamplona, P.B.C. Teixeira, R.L.C. Jerusalmi, I.A. Cestari, and A.A. Leirner. Dynamic non-linear behavior and stability of a ventricular assist device. *Int. J. Solids and Struct.*, 40(19):5017–5035, 2003.
- [46] P.B. Gonçalves and Z.J.G.N. Del Prado. Nonlinear oscillations and stability of parametrically excited cylindrical shells. *Meccanica*, 37(6):569–597, 2002.
- [47] P.B. Gonçalves and Z.J.G.N. Del Prado. Low-dimensional Galerkin models for nonlinear vibration and instability analysis of cylindrical shells. *Nonlinear Dynamics*, (41):129–145, 2005.
- [48] J.A. Gottwald, L.N. Virgin, and E.H. Dowell. Routes to escape from an energy well. *J. of Sound and Vibr.*, 187(1):133–144, 1995.
- [49] L. Gunawan. *Experimental study of nonlinear vibrations of thin-walled cylindrical shells*. PhD thesis, Delft University of Technology, 1998.
- [50] G.A. Hegemier and F. Tzung. Influence of damping on the snapping of a shallow arch under a step pressure load. *AIAA J.*, 7(8):1494–1499, 1969.
- [51] N.J. Hoff and V.G. Bruce. Dynamic analysis of the buckling of laterally loaded flat arches. *J. Math. Phys. C*, 32:276–288, 1954.
- [52] J. Horák, G.J. Lord, and M.A. Peletier. Cylinder buckling: the mountain pass as an organizing center. *SIAM J. Appl. Math.*, 66(5):1793–1824, 2006.
- [53] C.S. Hsu. On dynamic stability of elastic bodies with prescribed initial conditions. *Int. J. Eng. Sci.*, 4:1–21, 1966.

- [54] C.S. Hsu. The effects of various parameters on the dynamic stability of a shallow arch. *ASME J. Appl. Mech.*, 34(2):349–356, 1967.
- [55] <http://www.tuedacs.nl/>. TUE DACS/1 Advanced Quadrature / analog / digital Interface (AQI). 2008.
- [56] J.S. Humphreys. On dynamic snap buckling of shallow arches. *AIAA J.*, 4(5):878–886, 1966.
- [57] G. Hunt, G.J. Lord, and M. Peletier. Cylindrical shell buckling: a characterization of localization and periodicity. *Discrete and Continuous Dynamical Systems - B*, 3(4):505–518, 2003.
- [58] E.L. Jansen. Non-stationary flexural vibration behaviour of a cylindrical shell. *Int. J. Non-Linear Mech.*, 37(4-5):937–949, 2002.
- [59] E.L. Jansen. Dynamic stability problems of anisotropic cylindrical shells via simplified analysis. *Nonlinear Dynamics*, 39(4):349–367, 2005.
- [60] J.C. Ji and C.H. Hansen. Non-linear response of a post-buckled beam subjected to a harmonic axial excitation. *J. of Sound and Vibr.*, 237(2):303–318, 2000.
- [61] J. Jiang and E. Mockensturm. A novel motion amplifier using an axially driven buckling beam. In *Proc. of the 2003 ASME IMECE*, 2003.
- [62] E.R. Johnson. The effect of damping on dynamic snap-through. *ASME J. Appl. Mech.*, 47(3):601–606, 1980.
- [63] E.R. Johnson and I. K. McIvor. The effect of spatial distribution on dynamic snap-through. *ASME J. Appl. Mech.*, 45(3):612–618, 1978.
- [64] K.N. Karagiozis, M.P. Païdoussis, and A.K. Misra. Transmural pressure effects on the stability of clamped cylindrical shells subjected to internal fluid flow: Theory and experiments. *Int. J. Non-Linear Mech.*, 42(1):13–23, 2007.
- [65] T. Koga. Effects of boundary conditions on the free vibrations of circular cylindrical shells. *AIAA J.*, 26(11):1387–1394, 1988.
- [66] W.T. Koiter. *Over de stabiliteit van het elastisch evenwicht*. PhD thesis, Delft University of Technology. 1945 (in Dutch), Translated by E. Riks (1970): On the stability of elastic equilibrium, Tech. Report AFFDL TR 70-25.
- [67] A.N. Kounadis. Chaoslike phenomena in the non-linear dynamic stability of discrete damped or undamped systems under step loading. *Int. J. Non-Linear Mech.*, 26:301–311, 1991.

- [68] A.N. Kounadis and W.B. Krätzig (Editors). *Nonlinear stability of structures, theory and computational techniques*. Springer-Verlag, New York, 1995.
- [69] A.N. Kounadis, C.J. Gantes, and I.G. Raftoyiannis. A geometric approach for establishing dynamic buckling loads of autonomous potential n-degree-of-freedom systems. *Int. J. Non-Linear Mech.*, 39(10):1635–1646, 2004.
- [70] A.N. Kounadis and J. Raftoyiannis. Dynamic stability criteria of nonlinear elastic damped/undamped systems under step loading. *AIAA J.*, 28(7):1217–1223, 1990.
- [71] C.S. Kraaij. A semi-analytical buckling approach: modeling and validation. Technical Report DCT 2008.095, Eindhoven University of Technology, 2008.
- [72] W. Kreider and A.H. Nayfeh. Experimental investigation of single-mode responses in a fixed-fixed buckled beam. *Nonlinear Dynamics*, 15:155–177, 1998.
- [73] W. Lacarbonara, A.H. Nayfeh, and W. Kreider. Experimental validation of reduction methods for nonlinear vibrations of distributed-parameter systems: Analysis of a buckled beam. *Nonlinear Dynamics*, 17:95–117, 1998.
- [74] D. S. Lee. Nonlinear dynamic buckling of orthotropic cylindrical shells subjected to rapidly applied loads. *J. Eng. Math.*, 38:141–154, 2000.
- [75] X. Li and Y. Chen. Transient dynamic response analysis of orthotropic circular cylindrical shell under external hydrostatic pressure. *J. of Sound and Vibr.*, 257(5):967–976, 2002.
- [76] J.-S. Lin and J.-S. Chen. Dynamic snap-through of a laterally loaded arch under prescribed end motion. *Int. J. Solids and Struct.*, 40:4769–4787, 2003.
- [77] H.E. Lindberg and A.L. Florence. *Dynamic pulse buckling*. Martinus Nijhoff publishers, Dordrecht, 1987.
- [78] D.K. Liu. *Nonlinear vibrations of imperfect thin-walled cylindrical shells*. PhD thesis, Delft University of Technology, 1988.
- [79] M.H. Lock. Snapping of a shallow sinusoidal arch under a step pressure load. *AIAA J.*, 4(7):1249–1256, 1966.
- [80] M.H. Lock. Experiments on the snapping of a shallow dome under a step pressure load. *AIAA J.*, 6(7):1320–1326, 1968.



- 
- [81] N.J. Mallon, R.H.B. Fey, and H. Nijmeijer. Dynamic stability of a base-excited thin beam with top mass. In *Proc. of the 2006 ASME IMECE*, Nov. 5-10, pages 1–10, Chicago, USA, 2006. Paper 13148.
- [82] N.J. Mallon, R.H.B. Fey, and H. Nijmeijer. Dynamic buckling of a base-excited thin cylindrical shell carrying a top mass. In *Proc. 2007 Arctic Summer Conference on Dynamics, Vibrations and Control*, pages 1–14, Ivalo, Finland, 2007.
- [83] N.J. Mallon, R.H.B. Fey, and H. Nijmeijer. Experiments on the dynamic stability of a base-excited thin beam with top mass. In *Proc. of the Euromech Colloquium 483 'Geometrically Non-linear Vibrations of Structures'*, July 9-11, pages 81–84, Porto, Portugal, 2007.
- [84] N.J. Mallon, R.H.B. Fey, and H. Nijmeijer. Dynamic stability of a thin cylindrical shell with top mass subjected to harmonic base-acceleration. *Int. J. Solids and Struct.*, 45(6):1587–1613, 2008. doi:10.1016/j.ijsolstr.2007.10.011.
- [85] N.J. Mallon, R.H.B. Fey, H. Nijmeijer, and G.Q. Zhang. Drop-shock stability of a thin shallow arch considering the effects of variations in shape. In *Proc. of the Fifth EUROMECH Nonlinear Dynamics Conference*, pages 2457–2466, ID 22–120, Eindhoven, The Netherlands, 7-12 August 2005.
- [86] N.J. Mallon, R.H.B. Fey, H. Nijmeijer, and G.Q. Zhang. Dynamic buckling of a shallow arch under shock loading considering the effects of the arch shape. *Int. J. Non-Linear Mech.*, 41(9):1065–1075, 2006.
- [87] Maplesoft. *Maple R11*. Waterloo Maple Inc., 2007.
- [88] K.G. McConnell. *Vibration testing, Theory and Practice*. Wiley, 1995.
- [89] The MathWorks Inc. *MATLAB R14*, 2005.
- [90] L. Meirovitch. *Principles and techniques of vibrations*. Prentice-Hall International, London, 1997.
- [91] L. Meirovitch. *Fundamentals of vibrations*. McGraw-Hill, 2001.
- [92] E. Mettler. *Dynamic buckling*. In: *Handbook of engineering mechanics (Flügge, W., ed.)*. McGraw-Hill, 1962.
- [93] MSC.Software. *MSC.Marc manual Volume B, Element Library*. MSC.Software corporation, 2005.
- [94] MSC.Software. *MSC.Marc Mentat 2005r2*. MSC.Software corporation, 2005.

- 
- [95] D.W. Murray. Local buckling, strain localization, wrinkling and postbuckling response of line pipe. *Engineering Structures*, 19(5):360–371, 1997.
- [96] NAG. *Fortran Library Manual Mark 20*. The Numerical Algorithms Group, Limited, 2002.
- [97] A.H. Nayfeh and D.T. Mook. *Nonlinear Oscillations*. Wiley-Interscience, 1979.
- [98] T.Y. Ng and K.Y. Lam. Effects of boundary conditions on the parametric resonance of cylindrical shells under axial loading. *Shock and Vibration*, 5:343–354, 1998.
- [99] S.P.M. Noijen, R.H.B. Fey, N.J. Mallon, H. Nijmeijer, and G.Q. Zhang. New results in steady-state analysis of a transversally excited buckled beam. In *Proc. of the Fifth EUROMECH Nonlinear Dynamics Conference*, pages 2467–2476, Eindhoven, The Netherlands, 7-12 August 2005.
- [100] S.P.M. Noijen, N.J. Mallon, R.H.B. Fey, H. Nijmeijer, and G.Q. Zhang. Periodic excitation of a buckled beam using a higher order semi-analytic approach. *Nonlinear Dynamics*, 50(1-2):325–339, 2007.
- [101] N. Olhoff and R.H. Plaut. Bimodal optimization of vibrating shallow arches. *Int. J. Solids and Struct.*, 19(6):553–570, 1983.
- [102] L.J. Ovenshire and I.K. McIvor. On the dynamic snap-through of a shallow cylindrical shell subject to nearly symmetric impulsive loading. *Int. J. Solids and Struct.*, 7:585–601, 1971.
- [103] M.P. Païdoussis. *Fluid-structure interactions: slender structures and axial flow. Vol. 1*. Academic press, 1998.
- [104] M.P. Païdoussis. *Fluid-structure interactions: slender structures and axial flow. Vol. 2*. Academic press, 2004.
- [105] T. S. Parker and L. O. Chua. *Practical Numerical Algorithms for Chaotic Systems*. Springer-Verlag, 1988.
- [106] F. Pellicano. Experimental analysis of seismically excited circular cylindrical shells. In *Proc. of the Fifth EUROMECH Nonlinear Dynamics Conference*, Eindhoven, The Netherlands, 7-12 August 2005.
- [107] F. Pellicano. Vibrations of circular shells: Theory and experiments. *J. of Sound and Vibr.*, 303(1-2):154–170, 2007.

- [108] F. Pellicano and M. Amabili. Stability and vibration of empty and fluid-filled circular shells under static and periodic axial loads. *Int. J. Solids and Struct.*, 40(13-14):3229–3251, 2003.
- [109] F. Pellicano and M. Amabili. Dynamic instability and chaos of empty and fluid-filled circular cylindrical shells under periodic axial loads. *J. of Sound and Vibr.*, 293(1-2):227–252, 2006.
- [110] F. Pellicano and K.V. Avramov. Linear and nonlinear dynamics of a circular cylindrical shell connected to a rigid disk. *Comm. in Nonlinear Science and Numerical Simulation*, 12(4):496–518, 2007.
- [111] M. Pignataro, N. Rizzi, and A. Luongo. *Stability, bifurcation and postcritical behaviour of elastic structures*. Elsevier Science Publishers, Amsterdam, 1991.
- [112] R.H. Plaut and N. Olhoff. Optimal forms of shallow arches with respect to vibration and stability. *J. Struc. Mech*, 11(1):81–100, 1983.
- [113] A. Preumont. *Mechatronics, dynamics of electromechanical and piezoelectric systems*. Springer, 2006.
- [114] J. Qiu, J.H. Lang, and A.H. Slocum. A curved-beam bistable mechanism. *J. of Microelectromechanical Systems*, 13(2):137–146, 2004.
- [115] E. Quévy, P. Bigotte, D. Collard, and L. Buchailot. Large stroke actuation of continuous membrane for adaptive optics by 3D self-assembled microplates. *Sensors and Actuators A*, 95:183–195, 2002.
- [116] P. Ribeiro and R. Carneiro. Experimental detection of modal interactions in the non-linear vibration of a hinged-hinged beam. *J. of Sound and Vibr.*, 277(4-5):943–954, 2003.
- [117] F. Schilder, J. Rübél, J. Starke, H. Osinga, B. Krauskopf, and M. Inagaki. Efficient computation of quasiperiodic oscillations in nonlinear systems with fast rotating parts. *Nonlinear Dynamics*, 51(4):529–539, 2008.
- [118] R. Scholte, I. Lopez, and B. Roozen. Quantitative and qualitative verification of pressure and velocity based planar nearfield acoustic holography. In *Proc. of the thirteenth int. congress on sound and vibration, ICSV13*, Vienna, Austria, 2006.
- [119] K. Schweizerhof, R. Hauptmann, T. Rottner, and M. Raabe. Silo buckling analyses considering nonuniform filling - dynamic versus static analyses using ls-dyna. In *Proc. 5th Int. LS-DYNA Conf.*, Southfield, Michigan, 1998.

- 
- [120] R. Seydel. *From equilibrium to chaos*. Elsevier Science Publishers Co., Inc., New York, 1988.
- [121] G.J. Simitses. *Dynamic stability of suddenly loaded structures*. Springer-Verlag, New York, 1990.
- [122] M.S. Soliman and P.B. Gonçalves. Chaotic behaviour resulting in transient and steady state instability of pressure-loaded shallow spherical shells. *J. of Sound and Vibr.*, 259(3):497–512, 2003.
- [123] H.B. Stewart, J.M.T. Thompson, Y. Ueda, and A.N. Lansbury. Optimal escape from potential wells - patterns of regular and chaotic bifurcation. *Physica D: Nonlinear Phenomena*, 85:259–295, 1995.
- [124] Y.S. Tamura and C.D. Babcock. Dynamic stability of cylindrical shells under step loading. *ASME J. Appl. Mech.*, 42(1):190–194, 1975.
- [125] L.T. Tan and S. Pellegrino. Ultra thin deployable reflector antennas. In *Proc. 45th AIAA/ASME/ASCE/AHS/ASC Structures, Structural Dynamics and Materials Conference*, pages 1–10, Palm Springs, 19-22 April, 2004.
- [126] J.M.T. Thompson and G.W. Hunt. *A general theory of elastic stability*. John Wiley and Sons Ltd., London, 1973.
- [127] J.M.T. Thompson and G.W. Hunt. *Elastic instability phenomena*. John Wiley and Sons Ltd., London, 1984.
- [128] J.M.T. Thompson and H.B. Stewart. *Nonlinear dynamics and chaos*. Chichester, Wiley, 2nd edition, 2002.
- [129] J.J. Thomsen. *Vibrations and Stability, Advanced Theory, Analysis and Tools*. Springer-Verlag, second edition, 2003.
- [130] A. Tondl, T. Ruijgrok, F. Verhulst, and R. Nabergoj. *Autoparametric Resonance in Mechanical Systems*. Cambridge University Press, Cambridge, UK, 2000.
- [131] B.H. Tongue. *Principles of vibration*. Oxford University Press, Inc., New York, 1996.
- [132] H. Troger and C.S. Hsu. Response of a nonlinear system under combined parametric and forcing excitation. *ASME J. Appl. Mech.*, 44:179–181, 1977.
- [133] CH. Tsitouras and S. N. Papakostas. Cheap error estimation for runge-kutta methods. *SIAM J. Sci. Comput.*, 20(6):2067–2088, 1999.

- [134] J. Tyrrell, J. Cremers, and J. Wijker. Buckling analysis and qualification static load testing of VEGA interstage 1/2 structure. In *proc. 1st CEAS European Air and Space Conference*, Berlin, 10-13 Sept. 2007. DLRG.
- [135] P.S. Varoto and L.P.R. De Oliveira. On the interaction between the vibration exciter and the structure under test in vibration testing. In *Proc. IMAC-XIX: A Conference on Structural Dynamics*, pages 640–647, Kissimmee Florida, 2001.
- [136] J.C. Virella, L.A. Godoy, and L.E. Suárez. Dynamic buckling of anchored steel tanks subjected to horizontal earthquake excitation. *J. of Constructional Steel Research*, 62(6):521–531, 2006.
- [137] J. Wijker. *Mechanical Vibrations in Spacecraft Design*. Springer-Verlag, New York, 2004.
- [138] J. Winterflood, T. Barber, and D.G. Blair. Using Euler buckling springs for vibration isolation. *Classical and Quantum Gravity*, 19(7):1639–1645, 2002.
- [139] J. Winterflood and D.G. Blair. High performance vibration isolation using springs in Euler column buckling mode. *Phys. Letters A*, submitted, 2001.
- [140] L. Wullschleger and H.R. Meyer-Piening. Buckling of geometrical imperfect cylindrical shells - definition of a buckling load. *Int. J. Non-Linear Mech.*, 37(4–5), 2002.
- [141] W.C. Xie. *Dynamic Stability of Structures*. Cambridge University Press, 2006.
- [142] J. Xu, H. Huang, P. Zhang, and J. Zhou. Dynamic stability of shallow arch with elastic supports - application in the dynamic stability analysis of inner winding of transformer during short circuit. *Int. J. Non-Linear Mech.*, 37:909–920, 2002.
- [143] X. Xu, E. Pavlovskaia, M. Wiercigroch, F. Romeo, and S. Lenci. Dynamic interactions between parametric pendulum and electro-dynamical shaker. *Z. Angew. Math. Mech. (ZAMM)*, 87(2):172–186, 2007.
- [144] H. Yabuno, Y. Ide, and N. Aoshima. Nonlinear analysis of a parametrically excited cantilever beam (effect of the tip mass on stationary response). *JSME Int. J.*, 41(3):555–562, 1998.
- [145] H. Yabuno, M. Okhuma, and W. Lacarbonara. An experimental investigation of the parametric resonance in a buckled beam. In *Proceedings of the ASME DETC'03*, pages 2565–2574, Chicago, USA, 2-6 September 2003.

- 
- [146] N. Yamaki. *Elastic stability of circular cylindrical shells*. Elsevier science publishers, Amsterdam, 1987.
- [147] C.L. Zaretzky and M.R.M. Crespo da Silva. Experimental investigation of non-linear modal coupling in the response of cantilever beams. *J. of Sound and Vibr.*, 174(2):145–167, 1994.
- [148] L.D. Zavodney and A.H. Nayfeh. The non-linear response of a slender beam carrying a lumped mass to a principal parametric excitation: theory and experiment. *Int. J. Non-Linear Mech.*, 24(2):105–125, 1989.
- [149] J. Zhang, D.H. van Campen, G.Q. Zhang, V. Bouwman, and J.W. ter Weeme. Dynamic stability of doubly curved orthotropic shallow shells under impact. *AIAA J.*, 39(5):956–961, 2001.
- [150] S.L. Zhang and J.C.M. Li. Anisotropic elastic moduli and Poisson's ratios of a poly(ethylene terephthalate) film. *J. of Polymer Science Part B: Polymer Physics*, 42(3):260–266, 2003.

## *Summary*

Buckling refers to a sudden large increase in the deformation of a structure due to a small increase of some external load. If this external load has a dynamic nature, (e.g. a harmonic load, shock load, a step load and/or a random load), such a sudden increase in deformations is denoted as dynamic buckling. Thin-walled structures are often met in engineering practice due to their favourable mass-to-stiffness ratio. Such structures are very susceptible to buckling and are often subjected to dynamic loading. However, fast (pre-) design tools for obtaining detailed insight in the dynamic response and the stability of thin-walled structures subjected to dynamic loading are still lacking. One of the research objectives of this thesis is, therefore, to develop (fast) modelling and analysis tools which give insight in the behaviour of dynamically loaded thin-walled structures.

To illustrate and to test the abilities of the developed tools, a number of case studies are examined. The tools are developed for structures with a relatively simple geometry. The geometric simplicity of the structures allows to derive models with a relative low number of degrees of freedom which are, therefore, very suitable for extensive parameter studies (as essential during the design process of thin-walled structures). These models are symbolically derived using a Ritz method in combination with assumptions regarding geometric nonlinear (strain-displacement) relations and the effects of (in-plane) inertia. The resulting models, obtained from energy expressions, are sets of coupled ordinary differential equations which include stiffness nonlinearities and (sometimes) inertia and damping nonlinearities. The modelling approach is implemented in a generic manner in a symbolic manipulation software package, so that model variations can be easily performed. Furthermore, a set of designated numerical tools is combined (e.g. continuation tools for equilibria, periodic solutions and bifurcations, and numerical integration routines) to solve the analytically derived models in a computationally efficient manner.

Using this semi-analytical (i.e. analytical-numerical) approach four case studies are performed which include the dynamic buckling of an arch type of structure due to shock loading, snap-through behaviour of a transversally, harmonically excited pre-buckled beam, and the dynamic buckling of a beam and a cylindrical shell structure, both with top mass, which are harmonically loaded in axial direction at their base. For all cases, the effects of several parameter variations are illustrated, including the effect of small deviations from the nominal geometry (i.e. geometric imperfections).

For validation, the semi-analytical results are compared with results obtained using the computationally much more demanding finite element modelling technique. However, more important, for two cases (i.e. the axially excited beam and cylindrical shell structures carrying a top mass), the semi-analytical results are also compared with experimentally obtained results. For this purpose, a dedicated experimental set-up has been realized. For the beam structure, the experimental results are in good agreement with the semi-analytical results whereas for the cylindrical shell structure, a qualitative match is obtained. It has been illustrated that the differences between the experimental results and the semi-analytical results for the cylindrical shell may be due to the strong dependency of the results with respect to the geometrical imperfections present in the shell.

Next to the specific new insights obtained for each case considered, the major result of the thesis is the illustrated power of the semi-analytical approach to obtain practical relevant insights in the phenomena of dynamic buckling of thin-walled structures. In conclusion it can be stated that the semi-analytical approach is a valuable tool in the (pre-) design process of thin-walled structures under dynamic loading.



## *Samenvatting*

Knik komt overeen met een plotselinge toename van de deformatie van een constructie ten gevolge van een kleine verandering van de externe kracht welke werkt op de constructie. Indien deze externe kracht dynamisch van aard is (bijv. een harmonische belasting, een schokbelasting, een stapbelasting, een stochastische belasting of een algemene tijdsafhankelijke belasting), wordt zonn plotselinge toename aangeduid als dynamische knik. Dunwandige constructies worden vaak toegepast vanwege hun gunstige massa-stijfheidsverhouding. Een ander kenmerk van dunwandige constructies is dat ze erg gevoelig voor (dynamische) knik kunnen zijn. Echter, snelle (voor-)ontwerpgereedschappen (software) voor het verkrijgen van inzicht in het dynamische gedrag en de dynamische stabiliteit van dynamisch belaste, dunwandige constructies zijn nog niet beschikbaar. Een belangrijke onderzoeksdoelstelling van dit proefschrift is, daarom, het ontwikkelen van efficiënte modellerings- en analysegereedschappen, waarmee inzicht verkregen kan worden in het gedrag van dynamisch belaste dunwandige constructies.

De gereedschappen zijn ontwikkeld voor constructies met een relatief simpele geometrie. Voor dit soort constructies is het mogelijk om nauwkeurige modellen op te stellen met een relatief klein aantal vrijheidsgraden. Zulk soort modellen zijn, in tegenstelling tot eindige-elementenmodellen, zeer goed bruikbaar voor grootschalige parameterstudies (zoals uitgevoerd dienen te worden tijdens het ontwerpproces van dunwandige constructies). De modellen worden symbolisch afgeleid middels een Ritz methode in combinatie met aannames met betrekking tot de geometrisch niet-lineaire rek/verplaatsingsrelaties en de traagheid in het vlak van de constructieelementen. De resulterende modellen, afgeleid van energie-uitdrukkingen, zijn stelsels van gewone differentiaalvergelijkingen en bevatten naast niet-lineaire stijfheidstermen soms ook niet-lineaire traagheids- en dempingstermen. De modelleringaanpak is geïmplementeerd op een generieke manier in een software pakket dat uitermate geschikt is voor het symbolisch manipuleren van vergelijkingen. Op deze manier kunnen model variaties snel en eenvoudig worden uitgevoerd. Tevens zijn er een aantal specifieke gereedschappen voor numerieke analyse gecombineerd. Dit betreft software voor de berekening van (takken van) statische evenwichtspunten en periodieke oplossingen en hun stabiliteit, software voor de berekening van (takken van) bifurcaties en (standaard) numerieke integratie routines. Met deze gereedschappen kan het statisch en dynamisch gedrag van de analytisch afgeleide modellen op een snelle en efficiënte manier worden onderzocht.

Gebruik makend van deze semi-analytische aanpak (waarin analytische modellen numeriek worden geanalyseerd) worden vier casestudies uitgevoerd. De eerste casestudie betreft de dynamische knik van een boogvormige constructie onder schokbelasting. Vervolgens wordt het doorknikken van een initieel geknikte balk, die harmonisch wordt belast in transversale richting, onderzocht. Tenslotte worden de dynamische knik van een balk- en van een cilindrische schaalconstructie, die beide een topmassa dragen, onderzocht. Beide constructies worden via de bodem harmonisch geëxciteerd in axiale richting. Voor alle casestudies zijn de effecten van een groot aantal parametervariëaties geïllustreerd, waaronder het effect van kleine afwijkingen ten opzichte van de nominale geometrie (beter bekend als geometrische imperfecties).

Ter validatie worden de semi-analytische resultaten vergeleken met resultaten verkregen via eindige elementen analyses, die een veel langere rekentijd vragen dan de semi-analytische aanpak. Daarnaast worden, en dit is van groter belang, voor de laatste twee casestudies (d.w.z. voor de in axiale richting, harmonisch belaste balk- en cilindrische schaalconstructie met top massa), de semi-analytische resultaten vergeleken met experimentele resultaten. Voor dit doel is een specifieke experimentele opstelling gerealiseerd. Voor de balkconstructie zijn de experimentele en semi-analytische resultaten in zeer goede overeenstemming. Voor de meer complexe cilindrische schaalconstructie komen de experimentele en semi-analytische resultaten in kwalitatieve zin overeen. Geïllustreerd wordt dat de verschillen tussen de experimentele en semi-analytische resultaten veroorzaakt kunnen worden door de extreme gevoeligheid van de resultaten met betrekking tot geometrische imperfecties in de schaal.

Eén van de belangrijkste resultaten van dit proefschrift is, naast de verkregen specifieke nieuwe inzichten voor elke casestudy, de illustratie van de mogelijkheden van de semi-analytische aanpak voor het verkrijgen van praktisch relevante inzichten in dynamische knikverschijnselen van dunwandige constructies. Er kan dus worden geconcludeerd dat de in dit proefschrift uitgewerkte semi-analytische aanpak een waardevolle methode is in het (voor-)ontwerpproces van dynamisch belaste dunwandige constructies.

## *Acknowledgments*

This thesis would not have been written without the help of many people. First of all I want to thank my promotor Henk Nijmeijer for giving me the opportunity to work on this project and for his support during the project. I also want to thank my copromotor Rob Fey, for his help, support and all the careful reading and correction work. Andre de Boer, Dick van Campen and Kouchi Zhang are acknowledged for their work as members of the reading committee.

I want to thank STW for their financial support for this project and the members of the STW users committee for the fruitful discussions and valuable input during the users committee meetings. Pieter van Hoof is gratefully acknowledged for his indispensable help during the realization of the experimental setup. Rens Kodde, Peter Hamels and Harrie van de Loo also helped me a lot with practical issues for which I want to thank them. I want to thank Eelco Jansen for helping me with the research related to cylindrical shells. Tom Engels is acknowledged for helping me with the characterization of the cylindrical shell PET material. The students who have performed their traineeship or master thesis project in the scope of my research, Sander Noijen, Maarten Leijen, Leonard de Boer and Stefan Kraaij, are also gratefully acknowledged for their work. I like to thank all my former colleagues for the fun and support during my pleasant stay at the TU/e. In particular, I want to mention Apostolos, Dennis, Ewout, Francois, Jan-Kees, Jeroen, Joris, Ines, Lia, Lyosha, Matthijs, Marieke, Nathan, Nenad, Niels, René, Rick, Rob, Theo, Wilbert and Wouter.

Two people who also supported me (and my family) a lot during my PhD period are my parents Hans and Cobie. Thank very much for your unconditional love and support. To my grandmother Nel, your optimism and perseverance have been a great inspiration for me. I also want to thank my parents in law, Annette and Geert, for their support and interest during my PhD project.

Finally, I want to thank the three most important people in my life. Evi and Finne (my two beautiful daughters), I love you and I'm proud to be your father. Meja, without your support this thesis would definitely not be finished and my life would not be so joy full.



## *Curriculum vitae*

Niels Mallon was born on July 20, 1975 in Boxmeer, the Netherlands. After finishing his lower vocational education (LBO), intermediate vocational education (MBO) and higher vocational education (HBO), he started his academic education (WO) in September 2000 at Eindhoven University of Technology in Eindhoven, the Netherlands. He received his M.Sc. degree in Mechanical Engineering in November 2003. The title of his Master Thesis project was Reduced Observer Based Friction Compensation for a One-Link Robot. In the period from November 2003 till January 2008, he worked on his Ph.D. project in the Dynamics and Control group at the department of Mechanical Engineering of Eindhoven University of Technology. The topic of his research project was dynamic stability of thin-walled structures and the results of this research are presented in this thesis. Since January 2008, he is working for the Netherlands Organisation for Applied Scientific Research (TNO) at the Center for Mechanical and Maritime Structures (CMC) in Delft, the Netherlands.